



## **Geomechanical characterization of sedimentary and crystalline geothermal reservoirs**

**Martin Potten**

Vollständiger Abdruck der von der Ingenieur fakultät Bau Geo Umwelt der Technischen Universität München zur Erlangung des akademischen Grades eines

**Doktor-Ingenieurs (Dr.-Ing.)**

genehmigten Dissertation.

Vorsitzender: Prof. Dr.-Ing. Christoph Gehlen  
Prüfer der Dissertation: 1. Prof. Dr. rer. nat. Kurosch Thuro  
2. Prof. Dr. mont. Robert Galler  
3. Prof. Dr. Michael Drews

Die Dissertation wurde am 21.07.2020 bei der Technischen Universität München eingereicht und durch die Ingenieur fakultät Bau Geo Umwelt am 29.10.2020 angenommen.



*“Part of the Power that would  
Always wish Evil, and always works the Good.[...]  
I am the spirit, ever, that denies!  
And rightly so: since everything created,  
in turn deserves to be annihilated:  
Better if nothing came to be.  
So all that you call Sin, you see,  
destruction, in short, what you’ve meant  
by Evil is my true element.”*

Citation from Faust: A Tragedy, verse 1336 ff.

Johann Wolfgang von Goethe (1749–1832)

german poet, dramatist and scientist

The Ph.D. supervisor's description of the Ph.D. student's laboratory activities in the course of this work.



## Abstract

To use geothermal energy in Bavaria even more, a precise knowledge of the underground, which serves as a reservoir, is essential. The present work examines the most promising areas within Bavaria. It concerns the North Alpine Foreland Basin, SE Germany in the area around Munich and the Franconian Basin in NE Bavaria.

In the North Alpine Foreland Basin, SE Germany the carbonates of the Upper Jurassic are already successfully used as a reservoir (also known as Malm aquifer) for hydrothermal geothermal energy. For the characterization of the Upper Jurassic aquifer eleven core drillings were investigated. A total of 449 core samples were taken from depths ranging from 243 m to 5,225 m. The drill cores originated from different stratigraphic intervals, and have different lithologies and facies. In the north-east of Bavaria, petrothermal geothermal energy should be used in the future.

In the Franconian Basin there is a demonstrable anomaly with elevated underground temperatures. The reservoir rocks are probably granites below the Franconian Basin, which could be the origin of the geothermal anomaly. Due to the absence of samples from this area, sample material similar to the reservoir rock was examined from twelve outcrops in the Fichtelgebirge. A total of 358 analogue samples were produced. These rocks are considered the closest analogue material for the rocks below the Franconian Basin.

Drill cores and analogue samples were prepared for laboratory investigations. The resulting test samples were characterized geomechanically using both non-destructive as well as destructive testing methods. The non-destructive laboratory investigations were ultrasonic tests. The destructive laboratory investigations included Uniaxial Compression Tests, Brazilian Tensile Tests, Point Load Tests, Cerchar Abrasivity Tests and LCPC Abrasivity Tests. All testing results are listed in the appendix of the thesis.

The wells/borehole and outcrops are described individually and the most important characteristic values are listed in each case. In addition, the testing results are summarised for the respective reservoir. The testing results of the Upper Jurassic aquifer are classified according to their stratigraphy, lithology and facies. The testing results of the granites from the Fichtelgebirge are classified according to their age of intrusion (G types) and their orientation.

The results for the North Alpine Foreland Basin, SE Germany show that the Upper Jurassic aquifer has very heterogeneous geomechanical characteristics. No directional dependences of the parameter examined over the different stratigraphic units as well as lithologies was found. For the types of facies in each lithology, most of the values decrease with the increasing particle size. The results of the analogue samples show that if applicable granites present below the Franconian Basin in NE Bavaria have very homogeneous geomechanical characteristics. It is not possible to identify G type and orientation based on the data from the laboratory investigations. In destructive laboratory tests, characteristic value ranges were found.

In this thesis the determined characteristic values serve as input parameters for various scenarios in the numerical simulation of the borehole stability. For both locations a stress distribution in the near-field of the borehole was carried out with the program RS2 from Rocscience. The depth of failure around the borehole was also determined.

In the North Alpine Foreland Basin, SE Germany for all lithologies, borehole stability decreases with increasing depth. The depth of failure around the borehole hardly differs between the individual lithologies when considering the UCS mean values.

In NE Bavaria the borehole stability is found to be very low for all G types for all UCS values. If the calculated values for the stress field are correct, a successful drilling in NE Bavaria is unlikely.

The determined parameter ranges can be used in the future to check existing models and also create new models. They allow for a more precise understanding of the sedimentary and crystalline reservoirs and a more effective use of geothermal energy in Bavaria.

## Zusammenfassung

Um die Geothermie in Bayern noch stärker nutzen zu können, ist eine genaue Kenntnis des Untergrunds, welcher als Reservoir dient, zwingend notwendig. Die vorliegende Arbeit untersucht die beiden aussichtsreichsten Gebiete in Bayern. Es handelt sich um das nördliche Vorlandbecken der Alpen, SO Deutschland in dem Gebiet um München und um das Fränkische Becken in NO Bayern.

Im nördlichen Vorlandbecken der Alpen, SO Deutschland werden die Karbonate des Oberjura als Reservoir (auch bekannt als Malm Aquifer) für die hydrothermale Geothermie bereits erfolgreich genutzt. Für die Charakterisierung des oberjurassischen Karbonatreservoirs wurden elf Kernbohrungen untersucht. Es wurden 449 Bohrkerne über einen Tiefenbereich von 243 m bis 5225 m entnommen. Die Bohrkerne stammen aus unterschiedlichen stratigrafischen Intervallen und weisen unterschiedliche Lithologien und Fazies auf.

Im Nordosten von Bayern soll in Zukunft die petrothermale Geothermie genutzt werden. Im fränkischen Becken liegt nachweislich eine Anomalie mit erhöhten Untergrundtemperaturen vor. Bei den Reservoirgesteinen handelt es sich wahrscheinlich um Granite unterhalb des Fränkischen Beckens, die der Ursprung der geothermischen Anomalie sind. Da Proben aus diesem Gebiet nicht vorhanden sind, wurde dem Reservoirgestein ähnliches Probenmaterial aus zwölf Aufschlüssen im Fichtelgebirge untersucht. Insgesamt wurden 358 Analogproben hergestellt. Diese Gesteine gelten als das nächstliegende Analogmaterial für die Gesteine unterhalb des fränkischen Beckens.

Bohrkerne und Analogproben wurden für die Laboruntersuchungen präpariert. Die so erhaltenen Prüfkörper wurden sowohl mit zerstörungsfreien als auch zerstörenden Prüfmethode geomechanisch charakterisiert. Bei den zerstörungsfreien Laboruntersuchungen handelt es sich um Ultraschallversuche. Bei den zerstörenden Laboruntersuchungen handelt es sich um die Einaxialen Druckversuche, Spaltzugversuche, Punktlastversuche, Cerchar Abrasivitätsversuche sowie LCPC Abrasivitätsversuche. Alle Messergebnisse sind im Anhang der Arbeit aufgelistet.

Die Bohrungen und Aufschlüsse werden einzeln beschrieben und die wichtigsten Kennwerte jeweils genannt. Zudem werden die Messergebnisse für das jeweilige Reservoir zusammengefasst. Dabei werden die Messergebnisse des oberjurassischen Karbonatreservoirs nach ihrer Stratigraphie, Lithologie sowie Fazies klassifiziert. Die Messergebnisse der Granite aus dem Fichtelgebirge werden nach ihrem Intrusionsalter (G Typ) sowie ihrer Orientierung klassifiziert.

Die Ergebnisse für das nördliche Vorlandbecken der Alpen, SO Deutschland zeigen, dass das oberjurassische Karbonatreservoir sehr heterogene geomechanische Kennwerte aufweist. Es findet sich keine direkte Abhängigkeit der untersuchten Parameter über die verschiedenen stratigraphischen Einheiten sowie Lithologien. Für die Faziestypen in den einzelnen Lithologien nehmen die meisten Werte mit zunehmender Partikelgröße ab. Die Ergebnisse der Analogproben belegen, dass gegebenenfalls vorhandene Granite unter dem Fränkischen Becken in NO Bayern sehr homogene geomechanische Kennwerte aufweisen. Es ist nicht möglich, G Typ und Orientierung anhand der Daten aus den Laboruntersuchungen zu identifizieren. In zerstörenden Laborversuchen wurden charakteristische Wertebereiche gefunden.

Die ermittelten Kennwerte dienen in dieser Arbeit als Eingangsparameter für verschiedene Szenarien bei der numerischen Simulation der Bohrlochstabilität. Für beide Standorte wurde mit dem Programm RS2 von Rocscience eine Spannungsverteilung im Nahfeld des Bohrlochs ermittelt. Ebenso wurde die Auflockerungszone um das Bohrloch bestimmt.

Im nördlichen Vorlandbecken der Alpen, SO Deutschland nimmt die Bohrlochstabilität für alle Lithologien mit zunehmender Tiefe ab. Die Auflockerungszone um das Bohrloch herum unterscheidet sich unter Berücksichtigung der UCS-Mittelwerte zwischen den einzelnen Lithologien kaum.

Im NO Bayern ist die Bohrlochstabilität aller G Typen für alle UCS-Werte sehr gering. Wenn die berechneten Werte für das Spannungsfeld korrekt sind, ist eine erfolgreiche Bohrung im Nordosten Bayerns unwahrscheinlich.

Die ermittelten Parameterbereiche können zukünftig dazu verwendet werden bestehende geotechnische Modelle zu überprüfen und neue geotechnische Modelle zu erstellen. Sie ermöglichen damit eine genauere Kenntnis der sedimentären und kristallinen Reservoirs und eine effektivere Nutzung der Geothermie in Bayern.

## Acknowledgements

The creation of this Ph.D.-thesis was a truly life-changing experience, which pushed me to my limits. Without the support of many people and institutions this would not have been possible. I therefore want to take the opportunity to thank everyone who accompanied me on this journey, especially during the Corona crisis, for the experiences I have gained with their help.

Under the supervision of Prof. Dr. Kurosch Thuro, Chair of Engineering Geology at the Technical University of Munich this thesis was written. First of all, I want to thank him for allowing me to come to his chair, write this thesis and gain all these new experiences. He has continuously supported me during my research with inspiring discussions and valuable suggestions. He pushed me forward and was therefore an excellent supervisor for my doctorate, whom I can warmly recommend. Kurosch, thank you very much for allowing me to work on this exciting geothermal project. You have made me even more interesting for the experts as a self-proclaimed water heater.

Thank you Prof. Dr. Robert Galler for the co-supervision of this thesis. My special thanks go to Prof. Dr. Michael Drews for his co-supervision and review of this work, to which you made valuable contributions in the final phase. Thank you, Michael for your help with the sampling campaign in the Fichtelgebirge under not always optimal weather conditions.

I want to thank my mentor, Dr. Tina Menschik, very much. Due to her experience and support she made the transition to the Technical University of Munich very easy for me. I further want to thank Tina for reviewing my publications and for suggesting improvements.

My thanks also go to the Bavarian State Ministry of Education, Science and the Arts for the financial support within the context of the Geothermal-Alliance Bavaria project, from which this work emerged. With the help of GAB, drilling data and drill cores from the Bavarian Environment Agency, Neptune Energy Deutschland GmbH, Wintershall Holding GmbH, DEA Deutsche Erdöl AG could be examined. I thank the quarry owners who provided me with analogue samples and Stadtwerke München (SWM) for core samples from the "Schäftlarnstraße". Thank you all for your cooperation.

I would also like to thank all participants of the GAB with whom I have worked over the last three years. My special thanks go to two subproject teams in which I was involved. These are on the one hand, Dr. Kai Zosseder and his team from the subproject "Reservoir Characterization" and on the other hand Prof. Dr. Harald Stollhofen and his team from the subproject "PetroTherm". In the the subproject "PetroTherm" I would like to thank especially Dr. Wolfgang Bauer and my former fellow students Andreas Eberts and Katharina Popp who helped me with sampling during the field campaign.

As a project partner and good friend, I would like to thank Daniel Bohnsack from the Chair of Hydrogeology. With his unlimited willingness to do research, we were able to complete this laboratory program and its evaluation. I thank the project partner Philipp Wolpert for his help in the collection and facial as well as stratigraphic classification of the rock samples. I would also like to thank Dr. Robin Seithel for his outstanding good cooperation and the intensive discussion of the stress conditions in the North Alpine Foreland Basin, SE Germany.

I thank the head of the laboratory Dr. Heiko Käsling for all his practical support in the laboratory and the experience I gained while working on industrial projects. Heiko thank you very much organizing

the TechTalk session, where I could discuss my research with you and all Ph.D. students of the chair. I would also like to thank the technical assistant Friedrich Ettl, who prepared hundreds of samples for my laboratory program and former technical assistants Karen Helm-Knapp and Vladimir Ruttner, who also helped me with tips and tricks in my laboratory work.

I would also like to thank my two student assistants, Svenja Rau and Justin Mattheis, who did an extraordinary job in the laboratory. Without you two, Svenja and Justin, the large number of samples during the project phase could not have been processed in the laboratory.

Moreover, I thank all my colleagues at the Chair of Engineering Geology for their help, support and discussions during the past 3 years. Many thanks to my colleagues Matthias Brugger and Dr. Gerhard Lehrberger, who helped me with the internal formalities to prepare my thesis at the Chair of Engineering Geology. I would also like to thank the technical assistant Klaus Haas, who helped me with various figures for this thesis. My thanks also go to my office colleagues Dr. Elena Mraz, Georg Stockinger and Moritz Gamperl, who helped me with questions of all kinds. Elena, thank you very much, through your connections in the geothermal industry I quickly got to know the people who were essential in creating this thesis. Georg thank you very much for your help and your advice in the rock laboratory and for your cooperation in a branch where everybody tends to keep their knowledge secret. I would also like to thank Moritz for his constant help in creating the model based on the data collected for this work. I want to thank Dr. Florian Duschl from the Assistant Professorship of Geothermal Technologies, for his support in researching the scarce literature of the geology of north–east Bavaria.

Many thanks to my family and friends for the wonderful experience which helped me to recover and return refreshed to this work during the last 3 years. My friends Christina Obermair and Markus Brumm, with whom I and my wife Lisa spent relaxing holidays, had a big part in this. The three of them took care of the organization. Also “aunt” Monika Hock, who, as a hirer, made a great contribution to the success of this work. She made it possible for me and Lisa to live so beautiful in Perlach and to write this work in a nice and inspiring home office environment.

I would also like to thank my former laboratory manager from my student days, Dr. Emilia Jarochowska, who eased my transition from Erlangen to Munich with a letter of recommendation. I would also like to thank Thomas Brand for much needed support with the graphical evaluation of the laboratory results with the statistical program R. Many thanks to Dr. Barbara Seuß, who helped me in finding “non”-accessible literature. I would also like to thank one of my best friends, Felix Henriquez, for his help with the graphical implementation of the illustrations. Special thanks to my english native speaker friend Michael Prenkert for the review and the language improvement of this Ph.D.-thesis. Many thanks to my family in law Scharl (Thomas, Christine, Lukas, Christian and Martin), who welcomed me into their family more than 11 years ago and who supports me and Lisa with their help and advice.

I am deeply grateful to my family (Holger, Hedi, Helen, Sabine and our dog Luna), for accompanying me lovingly in every respect and my life. Many thanks! Also, thank you to Helen's boyfriend Niclas who assisted with Excel programming.

Finally, I am infinitely happy to have my best friend and wife Lisa at my side. During my work, you always stood beside me, believed in me and pushed me forward. No words can express my gratitude to you, my beloved wife.

## Contents

Abstract .....	I
Zusammenfassung.....	III
Acknowledgements .....	V
Contents .....	VII
List of figures .....	IX
List of tables .....	XV
List of acronyms and abbreviations.....	XVIII
List of symbols .....	XIX
List of formulas .....	XXI
<b>1 Introduction.....</b>	<b>1</b>
1.1 Classification of deep geothermal systems .....	4
1.2 Geomechanics in deep geothermal energy.....	7
1.3 Mission objectives .....	10
1.4 Scope of work and research objectives.....	11
1.5 Structure of the thesis .....	13
<b>2 Geomechanical reservoir characterization .....</b>	<b>14</b>
2.1 Methodology .....	15
2.1.1 Laboratory Testing.....	15
2.1.2 Numerical simulation .....	35
2.2 North Alpine Foreland Basin, SE Germany .....	40
2.2.1 State of the art .....	41
2.2.2 Geological setting .....	43
2.2.3 Data, study area and sampling .....	48
2.2.4 Results .....	51
2.2.5 Discussion .....	73
2.2.6 Conclusions.....	100
2.3 NE Bavaria .....	102
2.3.1 State of the art .....	103
2.3.2 Geological setting .....	104
2.3.3 Data, study area and sampling .....	111

---

2.3.4	Results .....	113
2.3.5	Discussion .....	138
2.3.6	Conclusions.....	158
2.4	Numerical simulations.....	160
2.4.1	North Alpine Foreland Basin, SE Germany .....	161
2.4.2	NE Bavaria.....	171
3	Summary .....	182
4	Outlook.....	185
	References.....	186
	URL references .....	204
	Appendix.....	206

## List of figures

Fig. 1: Mean investment cost distribution of a geothermal project mod. after BMU (2007).....	2
Fig. 2: Schematic diagram of a hydrothermal (left) and petrothermal geothermal energy system (right) mod. after WEBER & MOECK (2018). .....	5
Fig. 3: The relationship between the mud weight in the borehole, the borehole stability and the different rock failures that occur mod. after ZHANG (2013). .....	8
Fig. 4: Geomechanics through the life of a field mod. after ZOBACK (2016), the Reservoir Geomechanics course. ....	9
Fig. 5: Schematic representation of a geothermal project with the illustration of the five subprojects of the GAB mod. after FLECHTNER (2018).....	10
Fig. 6: Modelled subsurface temperature distribution in Bavaria at different depths mod. after AGEMAR et al. (2012). Additionally, the location of the geothermal anomaly in NE Bavaria was marked. ....	14
Fig. 7: Orientation of the drilling and testing directions from outcrop blocks after DREXL (2018).....	15
Fig. 8: Prepared samples for the Uniaxial Compression Test (UCT), the Brazilian Tensile Test (BTT) and the Point Load Test (PLT) after DREXL (2018).....	16
Fig. 9: Test setup of the ultrasonic measurements to determine the vP and the elastic parameters on the respective specimen mod. after MENSCHIK (2015). ....	20
Fig. 10: Sketch of the front view of the compression testing machine "ToniNorm" with a load frame with 2000 kN nominal load for UCT (1), a load frame with 200 kN nominal load (2) for BTT (top) or PLT(bottom), the control panel (3) and LVDT for radial (4) and axial strain measurements (5) mod. after WIESER (2016).....	23
Fig. 11: Schematic stress-strain curve of a test sample showing the determination of the uniaxial compressive strength $\sigma_u$ , the V-Modulus and the E-Modulus ( $\sigma_{cc}$ crack closure stress, $\sigma_{ci}$ crack initiation stress, $\sigma_{cd}$ crack damage stress). ....	24
Fig. 12: Sketch of the Brazilian tensile test and the applied forces for the determination of the Brazilian tensile strength $\sigma_t$ mod. after DGGT (2008). ....	28
Fig. 13: Sketch of the point load test, measured parameters & applied forces for the determination of the point load index IS mod. after DGGT (2010). ....	29
Fig. 14: Sketch of the Cerchar apparatus for the determination of the Cerchar Abrasivity Index (CAI) after DGGT (2016), mod. after WEST (1989).....	31
Fig. 15: Sketch of the abrasimeter for the determination of the LCPC Abrasivity Coefficient (LAC) and LCPC Breakability Coefficient (LBC) mod. after KÄSLING & THURO (2010). ....	33
Fig. 16: The three stress regimes (NF, SS, TF) according to the Anderson classification and the combination of these regimes (NS & TS) mod. and extended after HEIDBACH et al. (2018).....	35
Fig. 17: Geometry and used mesh architecture of the model (20 x 20 m) (left) in RS2 without interfaces or rock boundaries with the 6" diameter borehole under investigation (right).....	38
Fig. 18: The determined depth of failure plotted against the ratio of the maximum borehole wall stress to the uniaxial compressive strength after HOEK & MARTIN (2014). ....	39
Fig. 19: Cross section through the North Alpine Foreland Basin, SE Germany from www-23; www-24 (left) and StMWi (2019b), mod. after LEMCKE (1988) (right). ....	43
Fig. 20: Lithostratigraphic units of the Upper Jurassic important for geothermal energy mod. after COHEN et al. (2013; updated). ....	45

Fig. 21: An overview of existing data from the World Stress Map in the North Alpine Foreland Basin, SE Germany created with CASMO (www-22) and modified. ....	48
Fig. 22: Overview of the research of drill cores and the finally accessible core samples from the oil and gas industry for this work. ....	49
Fig. 23: Overview of the investigated core samples of the wells in the North Alpine Foreland Basin, SE Germany. ....	50
Fig. 24: Left: limestone (peloidal, fossiliferous grainstone (259 mTVD)); middle: dolomitic limestone (bioturbated wackestone (243 mTVD)); right: medium crystalline dolostone (464 mTVD). ....	52
Fig. 25: Example of a typical stress-strain curve (RW-1-30). ....	52
Fig. 26: $v_p$ - and $v_s$ -velocity (left) and UCS values (right) of differently saturated core samples (research well RW-1) versus depth. ....	53
Fig. 27: Left: limestone (peloidal, fossiliferous grainstone (1,146 mTVD)); middle: dolomitic limestone (floating rhombs, peloidal grainstone (1,299 mTVD)); right: medium crystalline dolostone (1,371 mTVD). ....	54
Fig. 28: Example of a typical stress-strain curve (RW-2-57.1). ....	54
Fig. 29: $v_p$ - and $v_s$ -velocity (left) and UCS values (right) of differently saturated core samples (research well RW-2) versus depth. ....	55
Fig. 30: Left: dolomitic limestone (peloidal, fossiliferous grainstone (1,400 mTVD); right: coarsely crystalline dolostone (1,456 mTVD). ....	56
Fig. 31: Example of a typical stress-strain curve (W-3-7.1). ....	56
Fig. 32: $v_p$ - and $v_s$ -velocity (left) and UCS values (right) of differently saturated core samples (well W-3) versus depth. ....	57
Fig. 33 Left: limestone (peloidal, fossiliferous, lithoclastic grainstone (1,484 mTVD); right: coarsely crystalline dolostone (1,478 mTVD). ....	58
Fig. 34: Example of a typical stress-strain curve (W-4-15). ....	58
Fig. 35: $v_p$ - and $v_s$ -velocity (left) and UCS values (right) of differently saturated core samples (well W-4) versus depth. ....	59
Fig. 36: Limestone (ooidal, peloidal, fossiliferous grainstone (2,440 mTVD). ....	60
Fig. 37: Example of a typical stress-strain curve (W-5-14). ....	60
Fig. 38: $v_p$ - and $v_s$ -velocity (left) and UCS values (right) of differently saturated core samples (well W-5) versus depth. ....	61
Fig. 39: Limestone (wackestone (2,692 mTVD)). ....	62
Fig. 40: Example of a typical stress-strain curve (W-6-1). ....	62
Fig. 41: $v_p$ - and $v_s$ -velocity (left) and UCS values (right) of differently saturated core samples (well W-6) versus depth. ....	63
Fig. 42: Limestone (peloidal, fossiliferous, lithoclastic packstone (2,671 mTVD). ....	64
Fig. 43: Example of a typical stress-strain curve (W-7-6). ....	64
Fig. 44: $v_p$ - and $v_s$ -velocity (left) and UCS values (right) of differently saturated core samples (well W-7) versus depth. ....	65
Fig. 45: Limestone (peloidal, fossiliferous, lithoclastic floatstone (2,674 mTVD). ....	66
Fig. 46: Example of a typical stress-strain curve (W-8-3). ....	66

Fig. 47: $v_p$ - and $v_s$ -velocity (left) and UCS values (right) of differently saturated core samples (well W-8) versus depth.....	67
Fig. 48: Limestone (fossiliferous wacke-stone (5,222 mTVD)). .....	68
Fig. 49: Example of a typical stress-strain curve (W-9-4.1). .....	68
Fig. 50: $v_p$ - and $v_s$ -velocity (left) and UCS values (right) of differently saturated core samples (well W-9) versus depth.....	69
Fig. 51: Left: limestone (ooidal, fossiliferous grainstone (2,895 mTVD)); middle: dolomitic limestone (mudstone (3,055 mTVD)); right: medium crystalline dolostone (3,154 mTVD). .....	70
Fig. 52: Left: limestone (peloidal, fossiliferous grainstone (2,526 mTVD)); middle: dolomitic limestone (laminated layer wackestone (2,440 mTVD)); right: medium crystalline dolostone (2,482 mTVD). ....	71
Fig. 53: Vertical $v_p$ (dry)-velocities plotted against vertical $v_p$ (sat.)-velocities (left) and $v_s$ (dry)-velocities plotted against $v_s$ (sat.)-velocities (right) to consider the influence of saturation of the carbonates from the Upper Jurassic aquifer.....	74
Fig. 54: Dynamic Young's Modulus plotted against static Young's Modulus (left) and dynamic Poisson's ratio plotted against static Poisson's ratio (right) to consider the difference between dynamic and static parameters. ....	74
Fig. 55: UCS plotted against $v_p$ -velocities of the carbonates from the Upper Jurassic aquifer.....	76
Fig. 56: UCS plotted against the porosity( $H_2O$ ) of the carbonates from the Upper Jurassic aquifer....	76
Fig. 57: UCS plotted against the bulk density of the carbonates from the Upper Jurassic aquifer. ....	76
Fig. 58: UCS plotted against the Young's Modulus and the V-Modulus of the carbonates from the Upper Jurassic aquifer. ....	78
Fig. 59: UCS plotted against the BTS (left) and static Young's Modulus plotted against the V-Modulus (right) and of the carbonates from the Upper Jurassic aquifer. ....	78
Fig. 60: UCS plotted against the static Poisson's ratio (right) of the carbonates from the Upper Jurassic aquifer. ....	78
Fig. 61: $v_p$ - (left) and $v_s$ -velocity (right) of differently saturated core samples versus stratigraphy. ..	81
Fig. 62: $v_p/v_s$ ratio (left) and dynamic Young's Modulus (right) of differently saturated core samples versus stratigraphy. ....	82
Fig. 63: Dynamic Poisson's ratio of differently saturated core samples versus stratigraphy. ....	83
Fig. 64: UCS (left) and BTS (right) of differently saturated core samples versus stratigraphy.....	84
Fig. 65: Static Young's Modulus and V-Modulus (left) and static Poisson's ratio (right) of differently saturated core samples versus stratigraphy. ....	86
Fig. 66: CAI versus stratigraphy. ....	87
Fig. 67: Bioturbated wackestones from well RW-1 (left) and well RW-2 (middle and right) demonstrate the varying grade of dolomitization which leads to an increasing porosity mod. after BOHNSACK et al. (2020). ....	88
Fig. 68: $v_p$ - and $v_s$ -velocities (left) and $v_p/v_s$ ratio (right) of differently saturated core samples versus lithology.....	88
Fig. 69: Dynamic Young's Modulus (left) and dynamic Poisson's ratio (right) of differently saturated core samples versus lithology. ....	90
Fig. 70: UCS of differently saturated core samples (left) and BTS (right) versus lithology. ....	90

Fig. 71: Static Young's Modulus and V-Modulus (left) and static Poisson's ratio (right) of differently saturated core samples versus lithology. ....	92
Fig. 72: CAI versus lithology. ....	92
Fig. 73: vp-velocities (left) and vs-velocities (right) of differently saturated core samples versus facies. ....	94
Fig. 74: vp/vs ratio (left) and dynamic Young's Modulus (right) of differently saturated core samples versus facies. ....	96
Fig. 75: Dynamic Poisson's ratio (left) and UCS (right) of differently saturated core samples versus facies. ....	97
Fig. 76: BTS (left) and static Young's Modulus and V-Modulus (right) versus facies. ....	98
Fig. 77: Static Poisson's ratio (left) and CAI (right) of differently saturated core samples versus facies. ....	99
Fig. 78: Expansion and temperature distribution (interpolated gradT map) of the Franconian Basin temperature anomaly in NE Bavaria, based on the analysis of temperature data from 18 wells after KÄMMLEIN et al. (2020). ....	102
Fig. 79: Schematic SW–NE cross-section through the Franconian Basin from www-23; www-24 (left) and mod. after KÄMMLEIN et al. (2020) (right). ....	105
Fig. 80: Map sketch of the late Hercynian granitoids of the Fichtelgebirge mod. after HECHT (1998). ....	108
Fig. 81: An overview of existing data from the World Stress Map in NE Bavaria, created with CASMO (www-22) and modified. ....	110
Fig. 82: Overview of the outcrops in the Fichtelgebirge and the finally accessible outcrops for sampling for this work. ....	111
Fig. 83: Overview of the investigated analogue samples of the outcrops in NE Bavaria mod. after HECHT (1998). ....	112
Fig. 84: Scan of a sample of TUM-001. ....	114
Fig. 85: Example of a typical stress-strain curve (TUM-001-01A-03). ....	114
Fig. 86: Scan of a sample of TUM-002. ....	116
Fig. 87: Example of a typical stress-strain curve (TUM-001-04A-01). ....	116
Fig. 88: Scans of samples of TUM-003 which were exposed to different weathering conditions. ....	118
Fig. 89: Example of a typical stress-strain curve (TUM-003-01I-05). ....	118
Fig. 90: Scan of a sample of TUM-004. ....	120
Fig. 91: Example of a typical stress-strain curve (TUM-004-01C-03). ....	120
Fig. 92: Scan of a sample of TUM-005. ....	122
Fig. 93: Example of a typical stress-strain curve (TUM-005-01A-04). ....	122
Fig. 94: Scan of samples of TUM-006. From left to right the colour changes from grey to pastel yellow. ....	124
Fig. 95: Example of a typical stress-strain curve (TUM-006-03A-10). ....	124
Fig. 96: Scan of a samples of TUM-007. Left: Reinersreuth granite; right: Reinersreuth Granitporphyr. ....	126
Fig. 97: Example of a typical stress-strain curve (TUM-007-01C-04). ....	126

---

Fig. 98: Scan of a sample of TUM-008.....	128
Fig. 99: Example of a typical stress-strain curve (TUM-008-01A-02).....	128
Fig. 101: Example of a typical stress-strain curve (TUM-009-04A-05).....	130
Fig. 100: Scan of samples of TUM-009 which were exposed to different weatherings (the degree of weathering increases from left to right). ....	130
Fig. 102: Scan of a sample of TUM-010.....	132
Fig. 103: Example of a typical stress-strain curve (TUM-010-G-02).....	132
Fig. 104: Scan of a sample of TUM-011.....	134
Fig. 105: Example of a typical stress-strain curve (TUM-011-02C-02).....	134
Fig. 106: Scan of a sample of TUM-012.....	136
Fig. 107: Example of a typical stress-strain curve (TUM-012-G-03).....	136
Fig. 108: Vertical $v_p$ (dry)-velocities plotted against vertical $v_p$ (sat.)-velocities (left) and $v_s$ (dry)-velocities plotted against $v_s$ (sat.)-velocities (right) to consider the influence of saturation. ....	139
Fig. 109: Dynamic Young's Modulus(dry) plotted against static Young's Modulus(dry.) (left) and dynamic Poisson's ratio(dry) plotted against static Poisson's ratio(dry.) (right) to consider the difference between dynamic and static parameters. ....	140
Fig. 110: UCS(dry) plotted against $v_p$ (dry)-velocities of the granites from the Fichtelgebirge. ....	140
Fig. 111: UCS(dry) plotted against the porosity( $H_2O$ ) (left) and against the bulk density (right) of the granites from the Fichtelgebirge.....	141
Fig. 112: UCS(dry) plotted against the Young's Modulus and the V-Modulus (left) and against the Brazilian tensile strength of the granites from the Fichtelgebirge. ....	142
Fig. 113: Static Young's Modulus(dry) plotted against the V-Modulus (left) and on the right UCS(dry) plotted against the static Poisson's ratio of the granites from the Fichtelgebirge.....	142
Fig. 114: $v_p$ - and $v_s$ -velocities of differently saturated samples versus type of granite. ....	144
Fig. 115: $v_p/v_s$ ratio of differently saturated samples versus type of granite.....	144
Fig. 116: Dynamic Young's Modulus of differently saturated samples versus type of granite.....	145
Fig. 117: Dynamic Poisson's ratio of differently saturated samples versus type of granite .....	146
Fig. 118: UCS(dry) (left) and BTS(dry) (right) versus type of granite.....	146
Fig. 119: Static Young's Modulus and V-Modulus versus type of granite.....	147
Fig. 120: Static Poisson's ratio (dry) (left) and CAI (dry) (right) versus type of granite.....	148
Fig. 121: LAC (left) and LBC (right) versus type of granite.....	148
Fig. 122: $v_p$ -velocities of differently saturated samples versus orientation.....	150
Fig. 123: $v_s$ -velocities of differently saturated samples versus orientation. ....	150
Fig. 124: $v_p/v_s$ ratio of differently saturated samples versus orientation. ....	152
Fig. 125: Dynamic Young's Modulus of differently saturated samples versus orientation. ....	152
Fig. 126: Dynamic Poisson's ratio of differently saturated samples versus orientation.....	154
Fig. 127: UCS (dry) versus orientation.....	154
Fig. 128: BTS versus orientation.....	155
Fig. 129: Static Young's Modulus and V-Modulus versus orientation.....	156

Fig. 130: Static Poisson's ratio(dry) versus orientation.....	156
Fig. 131: CAI versus orientation. ....	157
Fig. 132: Stresses before drilling in Upper Jurassic limestone (15.24 cm = 6" borehole diameter). Stress field in depths of 2 km (a), 3 km (b), 4 km (c) and 5 km (d). ....	161
Fig. 133: Stress patterns after drilling in Upper Jurassic limestone without hydrostatic water pressure ("dry"). Borehole diameter 6" = 15.24 cm. Stress field in depths of 2 km (a), 3 km (b), 4 km (c) and 5 km (d). ....	162
Fig. 134: Stress patterns including hydrostatic pressure in a borehole in Upper Jurassic limestone. Borehole diameter 6" = 15.24 cm. Stress field in depths of 2 km (a), 3 km (b), 4 km (c) and 5 km (d). ....	163
Fig. 135: Stress patterns including drilling mud in a borehole in Upper Jurassic limestone. Borehole diameter 6" = 15.24 cm. Stress field in depths of 2 km (a), 3 km (b), 4 km (c) and 5 km (d). ....	164
Fig. 136: Stress patterns in a borehole in Upper Jurassic limestone, hydrostatic pressure in depths of 2 km (a), 3 km (b), 4 km (c) and 5 km (d) with depth of failure after HOEK & MARTIN (2014), using the UCS mean value.....	165
Fig. 137: The depth of failure for the pessimistic failure criterion (left) and the differential stress for the optimistic failure criterion (right) versus depth of the borehole in the Upper Jurassic limestone. ...	167
Fig. 138: Stresses before drilling in G1 type (15.24 cm =6" borehole diameter). Stress field in depths of 2 km (a), 3 km (b), 4 km (c) and 5 km (d). ....	171
Fig. 139: Stress patterns after drilling in G1 type without hydrostatic water pressure ("dry"). Borehole diameter 6" = 15.24 cm. Stress field in depths of 2 km (a), 3 km (b), 4 km (c) and 5 km (d). ....	172
Fig. 140: Stress patterns including hydrostatic pressure in a borehole in G1 type. Borehole diameter 6" = 15.24 cm. Stress field in depths of 2 km (a), 3 km (b), 4 km (c) and 5 km (d). ....	173
Fig. 141: Stress patterns including drilling mud in a borehole in G1 type. Borehole diameter 6" = 15.24 cm. Stress field in depths of 2 km (a), 3 km (b), 4 km (c) and 5 km (d). ....	174
Fig. 142: Stress patterns in a borehole in G1 type, hydrostatic pressure in depths of 2 km (a), 3 km (b), 4 km (c) and 5 km (d) with depth of failure after HOEK & MARTIN (2014), using the UCS mean value. ....	175
Fig. 143: The depth of failure for the pessimistic failure criterion (left) and the differential stress for the optimistic failure criterion (right) versus depth of the borehole in the G1 type. ....	177

## List of tables

Tab. 1: Classification of abrasiveness with the CAI test (according to Cerchar (1986)).	32
Tab. 2: Classification of the LCPC Abrasivity Coefficient (LAC) according to the Cerchar Abrasivity Index (CAI) and related rock type examples mod. after THURO et al. (2006).	34
Tab. 3: Classification of the LCPC breakability coefficient (LBC), as defined by BÜCHI et al. (1995).	34
Tab. 4: Relative stress magnitudes and faulting regimes mod. after ZOBACK (2010).	35
Tab. 5: Overview of the tests performed in the North Alpine Foreland Basin, SE Germany.	51
Tab. 6: Characteristic values of the research well RW-1.	53
Tab. 7: Characteristic values of the research well RW-2.	55
Tab. 8: Characteristic values of well W-3.	57
Tab. 9: Characteristic values of the well W-4.	59
Tab. 10: Characteristic values of well W-5.	61
Tab. 11: Characteristic values of well W-6.	63
Tab. 12: Characteristic values of the well W-7.	65
Tab. 13: Characteristic values of the well W-8.	67
Tab. 14: Characteristic values of the well W-9.	69
Tab. 15: Characteristic values of the well W-10.	70
Tab. 16: Characteristic values of the borehole B-11.	71
Tab. 17: Overview of the tests performed in NE Bavaria.	113
Tab. 18: Characteristic values of the quarry TUM-001.	115
Tab. 19: Characteristic values of the quarry TUM-002.	117
Tab. 20: Characteristic values of the quarry TUM-003.	119
Tab. 21: Characteristic values of the quarry TUM-004.	121
Tab. 22: Characteristic values of the quarry TUM-005.	123
Tab. 23: Characteristic values of the quarry TUM-006.	125
Tab. 24: Characteristic values of the quarry TUM-007.	127
Tab. 25: Characteristic values of the geotope TUM-008.	129
Tab. 26: Characteristic values of the quarry TUM-009.	131
Tab. 27: Characteristic values of the geotope TUM-010.	133
Tab. 28: Characteristic values of the geotope TUM-011.	135
Tab. 29: Characteristic values of the quarry TUM-012.	137
Tab. 30: Overview of the parameters used for modelling the respective rocks.	160
Tab. 31: Overview of the stress field parameters and stress regime used for modelling in the respective area.	160
Tab. 32: Calculated and modelled maximum borehole wall stress after the drilling at the respective depth for the North Alpine Foreland Basin, SE Germany.	162

---

Tab. 33: Calculated and modelled maximum borehole wall stress with hydrostatic pressure at the respective depth for the North Alpine Foreland Basin, SE Germany.	163
Tab. 34: Calculated and modelled maximum wall stress including drilling mud at the respective depth for the North Alpine Foreland Basin, SE Germany.	164
Tab. 35: Calculated and modelled depth of failure at the respective depth for the Upper Jurassic limestone. Negative values indicate, that there are no borehole breakouts. Marked section indicates a reasonable scenario using UCS mean.	166
Tab. 36: Calculated and modelled differential stress at the respective depth for the Upper Jurassic limestone. Negative values indicate a stable borehole. Marked section indicates a reasonable scenario using the UCS mean value.	166
Tab. 37: Calculated and modelled depth of failure at the respective depth for the Upper Jurassic dolomitic limestone. Negative values indicate, that there are no borehole breakouts. Marked section indicates a reasonable scenario using UCS mean.	169
Tab. 38: Calculated and modelled differential stress at the respective depth for the Upper Jurassic dolomitic limestone. Negative values indicate a stable borehole. Marked section indicates a reasonable scenario using the UCS mean value.	169
Tab. 39: Calculated and modelled depth of failure at the respective depth for the Upper Jurassic dolostone. Negative values indicate, that there are no borehole breakouts. Marked section indicates a reasonable scenario using UCS mean.	170
Tab. 40: Calculated and modelled differential stress at the respective depth for the Upper Jurassic dolostone. Negative values indicate a stable borehole. Marked section indicates a reasonable scenario using the UCS mean value.	170
Tab. 41: Calculated and modelled maximum borehole wall stress after the drilling at the respective depth for NE Bavaria.	172
Tab. 42: Calculated and modelled maximum borehole wall stress with hydrostatic pressure at the respective depth for NE Bavaria.	173
Tab. 43: Calculated and modelled maximum wall stress including drilling mud at the respective depth for NE Bavaria.	174
Tab. 44: Calculated and modelled depth of failure at the respective depth for the G1 type. Marked section indicates a reasonable scenario using the UCS mean value.	176
Tab. 45: Calculated and modelled differential stress at the respective depth for the G1 type. Negative values indicate a stable borehole. Marked section indicates a reasonable scenario using the UCS mean value.	176
Tab. 46: Calculated and modelled depth of failure at the respective depth for the G2 type. Marked section indicates a reasonable scenario using the UCS mean value.	179
Tab. 47: Calculated and modelled differential stress at the respective depth for the G2 type. Negative values indicate a stable borehole. Marked section indicates a reasonable scenario using the UCS mean value.	179
Tab. 48: Calculated and modelled depth of failure at the respective depth for the G3 type. Marked section indicates a reasonable scenario using the UCS mean value.	180
Tab. 49: Calculated and modelled differential stress at the respective depth for the G3 type. Negative values indicate a stable borehole. Marked section indicates a reasonable scenario using the UCS mean value.	180
Tab. 50: Calculated and modelled depth of failure at the respective depth for the G4 type. Marked section indicates a reasonable scenario using the UCS mean value.	181

Tab. 51: Calculated and modelled differential stress at the respective depth for the G4 type. Negative values indicate a stable borehole. Marked section indicates a reasonable scenario using the UCS mean value.

## List of acronyms and abbreviations

Acronyms and abbreviations	Description
BMU	Federal Environment Agency
BTT	Brazilian Tensile Test
BTS	Brazilian tensile strength
BVEG	Bundesverband Erdgas, Erdöl und Geoenergie e.V.
CAIT	Cerchar Abrasivity Index Test
CAI	Cerchar abrasivity index
DEA	Deutsche Erdoel AG
DGGT	Deutsche Gesellschaft für Geotechnik
DIN	German Industrial Standard(s)
EEG	German Renewable Energy Source Act
FAU	Friedrich-Alexander University Erlangen-Nürnberg
FG	fracture gradient
FIT	formation integrity test
GAB	Geothermal-Alliance Bavaria
GeotIS	Geothermal Information System
HEP	Helium gas Expansion Porosimetry
IQR	interquartile range
ISRM	International Society for Rock Mechanics
KTB	German Continental Deep Drilling Program
LBEG	Landesamt für Bergbau, Energie und Geologie
LCPCT	Laboratoire Central des Ponts et Chaussées Test
LfU	Bavarian Environment Agency
LVDT	Linear Variable Differential Transformers
MSE	Munich School of Engineering
MW	mud weight
MW <sub>el</sub>	megawatt electrical
MW <sub>th</sub>	megawatt thermal
NE	north-east
NF	normal faulting regime
OIC	Older Intrusive Complex
PLT	Point Load Test
PP	pore pressure
R	receiver probe
SE	south-east
SFG	shear failure gradient
SS	strike-slip regime
StMWi	Bayerisches Staatsministerium für Wirtschaft, Landesentwicklung und Energie
SWM	Stadtwerke München
T	transmitter probe
TF	thrust faulting regime
TVD	true vertical depth
TUM	Technical University of Munich
TWh	Terawatt-hour
UBT	University of Bayreuth
UCS	Uniaxial compressive strength
UCT	Uniaxial Compression Test

Acronyms and abbreviations	Description
UT	Ultrasonic Test
VDI	Verein Deutscher Ingenieure
WIP	Water Immersion Porosimetry
WSM	World Stress Map
YIC	Younger Intrusive Complex

## List of symbols

Symbol	Description	Unit
A	cross-section area of the sample	[mm <sup>2</sup> ]
CAI	cerchar abrasiveness index	[-]
D <sub>e</sub> <sup>2</sup>	area of failure surface	[mm <sup>2</sup> ]
E	modulus of elasticity (Young's Modulus)	[GPa]
E <sub>dyn</sub>	dynamic modulus of elasticity	[GPa]
F <sub>max</sub>	failure load of the sample	[kN]
G <sub>dyn</sub>	dynamic shear modulus	[GPa]
I <sub>S</sub>	point load index	[MPa]
I <sub>S(50)</sub>	point load index for 50 mm edge length	[MPa]
K <sub>dyn</sub>	dynamic bulk modulus	[GPa]
L	length of the failure surface	[mm]
LAC	LCPC abrasivity coefficient	[g/t]
LBC	LCPC breakability coefficient	[%]
V	modulus of deformation (V-Modulus)	[GPa]
V <sub>b</sub>	bulk volume	[cm <sup>3</sup> ]
V <sub>g</sub> <sup>He</sup>	connected pore volume	[cm <sup>3</sup> ]
V <sub>p</sub> <sup>He</sup>	helium grain volume	[cm <sup>3</sup> ]
V <sub>p</sub> <sup>W</sup>	pore volume	[cm <sup>3</sup> ]
W	width of the failure surface	[mm]
Z	acoustic impedance	[kg/m <sup>2</sup> s]

Symbol	Description	Unit
a	borehole diameter	[cm]
c	correction factor	[-]
d	diameter of the sample	[mm]
d <sub>CAI</sub>	mean wear of the steel pin	[mm]
d <sub>f</sub>	depth of failure	[cm]
d <sub>0</sub>	original diameter of the sample	[mm]
d <sub>1</sub>	final diameter of the sample	[mm]
Δd	differential diameter of the sample	[mm]
g	Earth's gravitational acceleration	[m/s <sup>2</sup> ]
l	length of the sample	[mm]
l <sub>0</sub>	original length of the sample	[mm]
l <sub>1</sub>	final length of the sample	[mm]
Δl	differential length of the sample	[mm]
m <sub>d</sub>	dry mass of the sample	[g]
m <sub>F</sub>	mass of the metal impeller after the test	[g]
m <sub>F0</sub>	mass of the metal impeller prior the test	[g]
m <sub>s</sub>	saturated mass of the sample	[g]

Symbol	Description	Unit
$m_T$	total mass of the sample	[t]
$m_{1.6}$	mass fraction with grain size < 1.6 mm	[g]
$n$	number of tests	[-]
$t$	time	[s]
$\Delta t$	runtime of the ultrasonic wave in the sample	[s]
$v_{dw}$	dilatational wave velocity of the sample	[m/s]
$v_p$	p-wave velocity of the sample	[m/s]
$v_{pd}$	p-wave velocity of the sample (crosswise)	[m/s]
$v_{pl}$	p-wave velocity of the sample (lengthwise)	[m/s]
$v_s$	shear wave velocity of the sample	[m/s]
$z$	depth of interest	[m]

Symbol	Description	Unit
$\Delta$	difference	[ ]
$\varepsilon$	strain	[-]
$\varepsilon_l$	axial strain	[-]
$\Delta\varepsilon_l$	differential axial strain	[-]
$\Delta\varepsilon_l^{el}$	differential axial elastic strain	[-]
$\varepsilon_q$	radial strain	[-]
$\Delta\varepsilon_q$	differential radial strain	[-]
$\lambda$	wave length	[m]
$\mu$	coefficient of friction	[-]
$\nu$	poisson's ratio	[-]
$\nu_{dyn}$	dynamic poisson's ratio	[-]
$\rho$	density	[g/cm <sup>3</sup> ]
$\rho_b$	bulk density	[g/cm <sup>3</sup> ]
$\rho_g$	grain density	[g/cm <sup>3</sup> ]
$\rho_w$	purified water density	[g/cm <sup>3</sup> ]
$\sigma_{cc}$	crack closure stress	[MPa]
$\sigma_{cd}$	crack damage stress	[MPa]
$\sigma_{ci}$	crack initiation stress	[MPa]
$\sigma_h$	minimum horizontal stress	[MPa]
$\sigma_H$	maximum horizontal stress	[MPa]
$\sigma_m$	derived uniaxial compressive strength	[MPa]
$\sigma_{max}$	maximum borehole wall stress	[MPa]
$\sigma_t$	brazilian tensile strength	[MPa]
$\sigma_u$	uniaxial compressive strength	[MPa]
$\sigma_{u(2)}$	revised uniaxial compressive strength	[MPa]
$\sigma_v$	vertical stress	[MPa]
$\Delta\sigma$	differential axial stress	[MPa]
$\phi_{eff}^{He}$	effective porosity [He]	[%]
$\phi_{eff}^W$	effective porosity [W]	[%]

## List of formulas

Eqn. 1: Calculation of the bulk density ( $\rho_b$ ).	18
Eqn. 2: Calculation of the connected pore volume ( $V_{pHe}$ ).	18
Eqn. 3: Calculation of the grain density ( $\rho_g$ ).	18
Eqn. 4: Calculation of the effective porosity ( $\phi_{effHe}$ ).	19
Eqn. 5: Calculation of the effective porosity ( $\phi_{effW}$ ).	19
Eqn. 6: Calculation of the p-wave velocity ( $v_p$ ) lengthwise ( $v_{pl}$ ) and crosswise ( $v_{pd}$ ).	21
Eqn. 7: Calculation of the dynamic modulus of elasticity ( $E_{dyn}$ ).	22
Eqn. 8: Calculation of the dynamic shear modulus ( $G_{dyn}$ ).	22
Eqn. 9: Calculation of the dynamic bulk modulus ( $K_{dyn}$ ).	22
Eqn. 10: Calculation of the dynamic poisson's ratio ( $\nu_{dyn}$ ).	22
Eqn. 11: Calculation of the acoustic impedance ( $Z$ ).	23
Eqn. 12: Calculation of failure stress as compressive strength ( $\sigma_u$ ).	25
Eqn. 13: Calculation of adjusted compressive strength ( $\sigma_u(2)$ ).	25
Eqn. 14: Calculation of the modulus of deformation ( $V$ ).	25
Eqn. 15: Calculation of the uniaxial compressive strength ( $\sigma_u(1)$ ).	26
Eqn. 16: Calculation of the modulus of elasticity ( $E$ ).	26
Eqn. 17: Calculation of the poisson's ratio ( $\nu$ ).	27
Eqn. 18: Calculation of the Brazilian tensile strength ( $\sigma_t$ ).	28
Eqn. 19: Calculation of the point load index ( $I_s$ ).	30
Eqn. 20: Calculation of the point load index ( $IS(50)$ ) correlating to the standard edge length of 50 mm.	30
Eqn. 21: Calculation of uniaxial compressive strength ( $\sigma_m$ ) derived from ( $IS(50)$ ).	30
Eqn. 22: Calculation of the Cerchar Abrasiveness Index (CAI).	32
Eqn. 23: Calculation of the LCPC abrasivity coefficient (LAC).	33
Eqn. 24: Calculation of the LCPC breakability coefficient (LBC).	34
Eqn. 25: Calculation of the vertical stress ( $\sigma_V$ ).	36
Eqn. 26: Calculation of the depth of failure ( $df$ ) after HOEK & MARTIN (2014).	39
Eqn. 27: Calculation of the maximal horizontal stress $\sigma_H$ and the minimum horizontal stress $\sigma_h$ for NE Bavaria.	160



# 1 Introduction

“Geothermal energy is the most climate-friendly renewable energy which is available to us [...].

Without its use, Germany will miss its climate change objectives.” (www-01)

Christiane Lohse (Senior Scientific Advisor, Federal Environment Agency)

At the “Praxisforum 2018”, Mrs Lohse explained that Germany has an accessible potential, which could make Germany greenhouse neutral by 2050. With geothermal energy, a technical-ecological potential (50 terawatt-hours (TWh) in electricity generation and 100 TWh in heat supply) can be tapped annually (www-01). However, in order to achieve these values, 2,120 geothermal power plants would have to be built (THOMAS et al. 2010).

In combination with other renewable energies, the next step could be to abandon the use of nuclear energy and fossil fuels. Geothermal energy is the only renewable energy that is independent of day/night fluctuations, weather and seasonal variations and available 24 hours a day. This unique advantage makes it possible to stabilize the national grids and to reduce the consumption of fossil fuels. Therefore, geothermal energy can make a major contribution to cover the base load and thereby replace the old fossil fuel-fired power plants (BAUER et al. 2014; STOBER & BUCHER 2014). All this contributes essentially to a reduction of CO<sub>2</sub> emissions into the Earth’s atmosphere.

The unique aspect of this technology is that geothermal energy is actually not renewable, but practically inexhaustible (HUENGES et al. 2013) on a human scale. This market has been growing worldwide for the last 30 years, by generating energy from convective and conductive systems (BERTANI 2016). Through the use of geothermal energy, there is access to an almost unlimited source of heat and electricity (STOBER & BUCHER 2014).

The Free State of Bavaria is a leader in the use of deep geothermal energy in Germany (StMWi 2019b) and wants to penetrate in the geothermal energy market even more. In Bavaria, the Upper Jurassic reservoir (“Malm aquifer”) is geothermally used for district heating and, in some cases, for power generation (www-02). The Bavarian energy sector is striving to move away from fossil fuels and consistently making the switch to renewable energies. This switch to renewable energies is one of the biggest challenges for the energy market in its fight to counteract one of the most pressing issues of the time, global warming. However, in the Bavarian energy supply, deep geothermal energy use makes up only 1.0 % of the renewable sources that are utilized (StMWi 2019a; www-03). In comparison with all other energy sources, deep geothermal energy use makes up only 0.2 % of the total (StMWi 2019a; www-03).

Geothermal energy can help to hit the German Renewable Energy Source Act (EEG) targets and reach the climate protection goals of the COP 21 summit. Since the heating sector in particular is continuing to grow, geothermal energy offers a great opportunity to provide heat without emissions regardless of the time of year (AGEMAR et al. 2018). Although the greatest primary energy requirement is heat, the “Energiewende” continues to focus on renewable electricity generation (FALTENHAUSER 2018; WEBER & MOECK 2018).

Generating power from deep geothermal energy, is only 8 % to 13 % efficient (LfU 2016). This shows that only a small part of the heat energy can be used to generate electricity. Therefore, the remaining heat should be used for heating purposes if possible (LfU 2016). In order to achieve the climate protection goals, a rethink is needed and the focus must be on “Wärmewende”; production of heat instead of electricity. This step can be successful if the great development potential of deep geothermal energy, which has been little used to date, is better exploited (AGEMAR et al. 2018).

One downside of the enormous potential of geothermal energy, is that the geological development and exploration of geothermal energy projects are associated with high investments and risks (StMWi 2019b). The costs of drilling a well takes up the largest part of the investment in a geothermal project (Fig. 1).

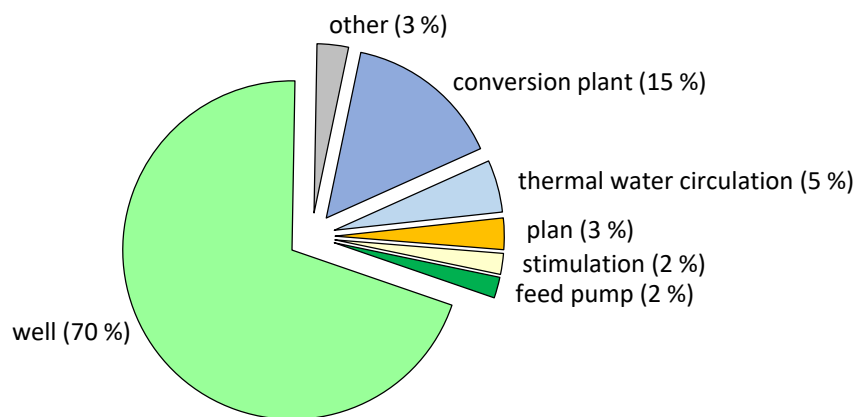


Fig. 1: Mean investment cost distribution of a geothermal project mod. after BMU (2007).

However, this phase in the project is still subject to uncertainties. In the end, the target formation may turn out to be unsuitable and the investments were worthless. Due to the different geological conditions in the deep surface, in contrast to other renewable energies, each geothermal project must be planned individually (AGEMAR et al. 2014b).

The progress of civilization is based on the availability of energy. The regional energy provider Stadtwerke München (SWM) is aware of this and has recognized the opportunities that geothermal energy can provide. Its goal is to be the first city in Germany to provide for the cities heating needs exclusively with renewable energies, most importantly from geothermal energy, by 2040 (SWM 2019). Such an aim can only be reached, however, because the North Alpine Foreland Basin, SE Germany in the area of Munich offers perfect conditions for deep geothermal energy (SWM 2019). Currently, the most comprehensive heating project in Central Europe is being developed in the “Schäftlarnstraße” in Munich (www-04). This means that, hydrothermal geothermal energy is used in an innovative way in Bavaria and outstanding technical expertise is built up.

In contrast, the unexplored and unused potential of petrothermal geothermal energy is mainly concentrated on the rocks below the Franconian Basin in the north–east (NE) of Bavaria. Crystalline rocks are assumed to be reservoir rocks (DREWS et al. 2019a). The Bavarian state government does not currently expect petrothermal geothermal energy to be relevant in Bavaria for the next few years. Petrothermal geothermal energy in Bavaria is currently still in the experimental stage (StMWi 2019b).

However, the petrothermal geothermal energy may have an enormous potential for the future and therefore extensive research is needed to finally realize it in Bavaria.

The release of microseismic events in the North Alpine Foreland Basin, SE Germany in the area of Munich (SEITHEL et al. 2019) caused public acceptance of geothermal energy to waver. This led to a reconsideration of the reservoir operation by including geomechanical concepts and showed that it is therefore important that geothermal energy projects receive scientific support (AGEMAR et al. 2018). For this reason, but also to accompany the increased expansion of hydrothermal geothermal energy in Bavaria, the research association Geothermal-Alliance Bavaria (GAB) was founded. This thesis was created within the framework of this research project and deals with geomechanical characterization of sedimentary and crystalline geothermal reservoirs in Bavaria.

The collected data as well as the modelling should help to understand the borehole and reservoir behaviour and thereby minimize unpredictable risks during drilling and operation. This helps to use the deep geothermal energy sustainably.

## 1.1 Classification of deep geothermal systems

The natural energy beneath the surface of the solid Earth, which is stored in the form of heat, is defined as geothermal energy (VDI 4640: 2010). This geothermal energy is generated in two different ways. 30 % of that energy is the residual gravitational heat. This heat is the result of the geological formation of the Earth about 4.5 billion years ago. The other 70 % can be attributed to the radioactive decay of potassium, thorium and uranium isotopes in the Earth's crust (STOBER et al. 2016). A mean temperature increase of about 3 K per 100 m can be observed within the continental crust (KALTSCHMITT et al. 2013). This geothermal gradient is expressed in K/m and can be explained by the heat flow from the Earth's interior to the Earth's surface. The mean heat flow in Bavaria is about 65 mW/m<sup>2</sup> (STOBER et al. 2016), but the heat is not uniformly distributed in the subsurface (AGEMAR et al. 2012).

Geothermal energy that can be used directly and can be accessed via deep wells is called deep geothermal energy (STOBER & BUCHER 2014). According to the definition of STOBER et al. (2016), deep geothermal energy begins at depths of more than 400 m and temperatures above 20 °C. It is more common to speak of deep geothermal energy at depths greater than 1,000 m and at temperatures above 60 °C. Depths between 400 m and 1,000 m are referred to as medium-depth geothermal projects (STOBER et al. 2016) but between the individual systems the transition is fluid (HOMUTH 2014).

To develop a geothermal project successfully a preliminary study is first carried out using data and literature from boreholes in the area surrounding the planned site (STOBER et al. 2016). After this detailed analysis and a positive feasibility study have been evaluated, a seismic campaign is usually carried out to explore the geological subsurface in detail. As soon as the data from the seismic campaign are obtained and combined with the previously known data, and if a conclusive picture can be seen, the drilling phase begins (AGEMAR et al. 2014b).

Exploration of deep geothermal energy takes place via a production and injection well, which is usually drilled from a single well site (StMWi 2019b). The most common systems used in Bavaria are the open systems. One type of this system is the hydrothermal system. Here, the hot water is pumped from the aquifer to the surface. Another type of system is the petrothermal system where water is injected underground. The water is then heated by the hot rock and pumped back to the surface. Both systems can be used for electricity generation as well as for local or district heating (BAUER et al. 2014; STOBER et al. 2016).

### Hydrothermal systems

To produce geothermal energy, the hot water from an aquifer (Fig. 2) is brought into a hydrothermal cycle. For this system, a production well is drilled so that the drilling path covers the aquifer or fault zone over a large area (STOBER et al. 2016). This allows a larger amount of water to be withdrawn from the aquifer (STOBER & BUCHER 2014). The hot water is pumped to the surface via a production well to a power plant. There, via a heat exchanger, the hot water transfers a substantial part of its thermal energy to a secondary power plant circuit or is used as local or district heating.

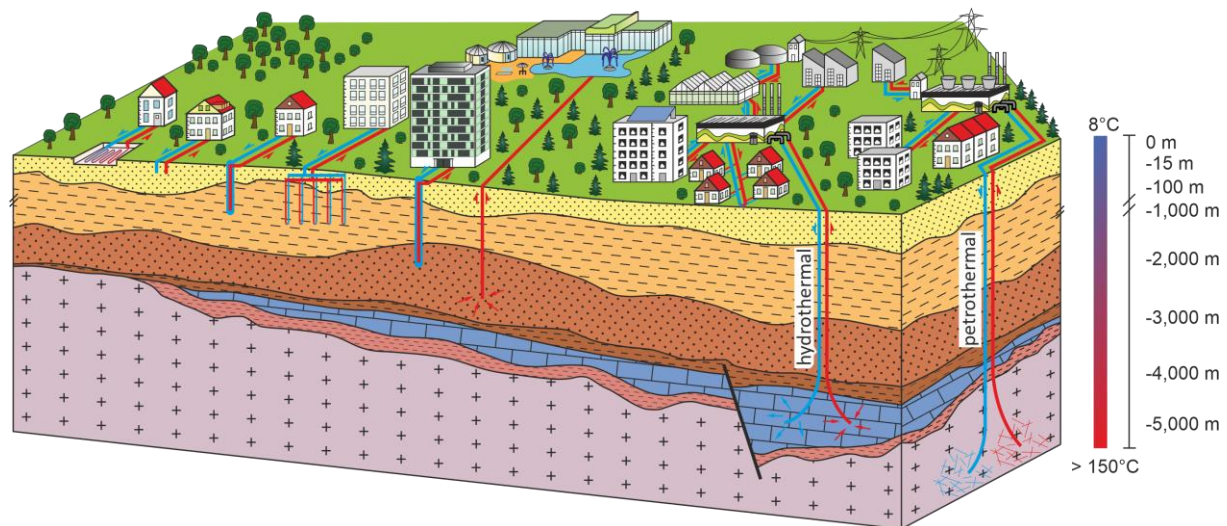


Fig. 2: Schematic diagram of a hydrothermal (left) and petrothermal geothermal energy system (right) mod. after WEBER & MOECK (2018).

Once the thermal water has been cooled down by the heat exchanger, the water is fed back into the ground via an injection well. This is necessary for several reasons. On the one hand, very large quantities of water are pumped. To ensure a steady water balance, the same quantity is returned to the aquifer (StMWi 2019b). On the other hand, the water could have a high mineralization and gas content which circulates in a closed hydrothermal cycle kept under pressure. If this water was relieved of its temperature and pressure, it would become supersaturated with certain minerals and precipitation would occur (STOBER et al. 2016).

These precipitates lead to disposal problems which can be buffered or avoided with hydrochloric acid or inhibitors (STOBER & BUCHER 2014; STOBER et al. 2016). Both measurements, however, unnecessarily burden the profitability of a project. In the North Alpine Foreland Basin, SE Germany the used water of the Upper Jurassic reservoir has often drinking water quality (STOBER 2014; WEBER et al. 2019) and the corrosion effects are minimal and scaling effects are manageable (WEBER et al. 2019). Overall, however, it is possible to drill several wells in different directions from one well site (HUENGES 2010) to improve the connection to the reservoir.

If no large reservoir can be developed directly, faults as tectonically disrupted zones should be drilled. These tectonically disrupted zones have a higher natural permeability and possibly higher temperatures if deeper thermal water conductors are reached and then connected (PASCHEN et al. 2003). At the beginning of geothermal exploration, these faults were the most important exploration target. The focus of exploration has shifted to lithofacial features, such as karst, since there is increased knowledge about the subsurface in the North Alpine Foreland Basin, SE Germany (BÖHM et al. 2011; BÖHM 2012; STIER & PRESTEL 1991).

To ensure long-term use and to avoid a hydraulic circuit, the production and injection wells should be drilled at a sufficient distance from each other (StMWi 2019b). The distance between injection and production wells must be dimensioned in such a way that no adverse temperature drops can occur in

the production well as a result of the cooled water being pumped into the useful horizon via the injection well (BAUER et al. 2014). Furthermore, the distance should not be oversized, as otherwise no permanent flow rate to the production well is guaranteed.

Therefore, the problem utilization horizons should be as powerful and laterally as wide as possible. The genesis of the fault, the recent stress conditions, the petrography of the disturbed rock, and also the geochemical processes, can influence the wells as well. Since the overburden pressure of the rock increases with increasing depth and the permeability, which is important for reservoir utilization, generally decreases with increasing depth due to decreasing fracture width, porosity and possibly karstification, the above-mentioned geological conditions are not present everywhere.

Nothing can be said of the prospects of the project success until the drilling is completed and longterm tests can be analysed. The chances of success for a hydrothermal geothermal projects can be determined by two parameters. On the one hand, whether the predicted volume flows are achieved and on the other hand, whether the necessary temperatures are reached (StMWi 2019b). If the measured parameters confirm the expected parameters, the power plant and the district heating network will be designed, built and then operated economically.

If the flow rate and/or temperatures are not reached, the drilling is considered unsuccessful. While a defined temperature is usually reached at the appropriate drilling depth, rock permeability that is too low and causes too little thermal water production considerably limits the number of possible sites. In order to practically exclude these non-productive wells, an improved system understanding of the reservoir is indispensable.

### **Petrothermal systems**

In contrast to hydrothermal geothermal energy, petrothermal geothermal energy does not use in situ water for heat and power generation. For this type of energy production, deep-lying and low-permeable (less than  $10^{-15}$  m<sup>2</sup>) and low-porous (less than 15 %) crystalline rocks are suitable (MOECK et al. 2019). Such rocks could be heat producing granites, which are probably present in NE Bavaria (DREWS et al. 2019a). These hot rocks of the crystalline bedrock can be used as a heat exchanger (STOBER et al. 2016). Water is injected underground via an injection well. The water acts as a heat transfer medium that can circulate through the slightly fissured crystalline bedrock like in an aquifer with low permeability (Fig. 2). The hot water is pumped to the surface via a production well to a power plant (StMWi 2019b). There, via a heat exchanger, the hot water transfers a substantial part of its thermal energy to a secondary power plant circuit.

By injecting water under higher pressures, the already existing fissure system can be widened. This will also help to create additional and better quality pathways (STOBER & BUCHER 2014). With petrothermal geothermal energy, no existing reservoir is developed directly. The reservoir is solely created through stimulation measures.

In Germany, two different stimulation measures are used: hydraulic and chemical stimulation. Hydraulic stimulation, is either stimulated directly with water or small amounts of additives are added to the

water. This is then pressed into the rock. This pressure must be higher than the rock strength to reactivate existing fracture systems and better connect the borehole to the reservoir. During the chemical stimulation, chemicals as e.g. diluted hydrochloric acid are added to the water. These are used to dissolve mud and residues in the borehole or the borehole edge area. The chemical stimulation is also used in hydrothermal geothermal energy systems to flush the borehole (BAUER et al. 2014).

The advantage of petrothermal geothermal energy is that it is largely independent of location and, as a future technology, it also makes it possible to build up new know-how in Bavaria and then export it.

## 1.2 Geomechanics in deep geothermal energy

Geomechanics investigates the mechanical behaviour of rock. It combines the knowledge of different disciplines as rock mechanics, geophysics, petrophysics and geology. In the subsurface, the rocks are exposed to various compressive stresses (ZOBACK 2010). The stress levels depend on three underground stresses and the pore pressure at different depths and the predominant tectonics in this area (FJÆR et al. 2008; ZOBACK 2010). These stresses as well as the strength properties of the rocks change over geological time periods, therefore these parameters are subject to alterations and differ at different locations.

The various stresses and forces in the underground are normally in apparent equilibrium. However, this can be changed by research or production activities. If the stresses applied to the rock exceed its strength, the rock will fail (ZOBACK 2010). The goal of geomechanics is to estimate the potential for failure and to evaluate the benefits and risks that may result.

Geomechanics is used in the exploration and production phases of geothermal projects to optimize the benefits and reduce the risks associated with mechanical failure of the deposit and surrounding formations (ZOBACK 2010). A geothermal reservoir is also affected by the stresses in the underground. For the geomechanical evaluation of such a reservoir, different reservoir characteristics (stress/strength/pressure) have to be analysed. A knowledge of the reservoir rock history is important too (FJÆR et al. 2008). In geothermal energy, to develop a petrothermal reservoir hydraulic fracturing is used and geomechanical monitoring is of crucial importance (www-25). The stress states that develop in the reservoir and in the surrounding geology as a result of hydraulic fracturing are analysed. But also the naturally existing cracks in the rock have a great influence on the productivity of the borehole. In order to develop the reservoir in the best possible way, an understanding of the different permeabilities (www-25) such as the existing matrix and fracture permeability as well as the induced fracture permeability is necessary.

Since the development of geothermal energy requires deeper and deeper drilling and the reservoirs are becoming more and more geologically challenging, the investigation of geomechanics in the areas where drilling is to be carried out plays an increasingly important role (WHALEY 2019).

The aim of these investigations is to predict the impact of drilling and production activities on the subsurface as soon as possible in order to identify and minimize restrictions on exploration and devel-

opment activities due to negative environmental impacts as quickly as possible. Geomechanical surveys are conducted throughout the exploration and production cycle. Characterization of the rock properties are prepared before drilling begins and used to model the in situ stresses (WHALEY 2019). During drilling, geomechanical investigations are used to ensure the stability of the borehole or to estimate the effects of hydraulic fracture (www-25).

Stability problems occur worldwide during the drilling process (FJÆR et al. 2008). Both the borehole and the drilling fluid create new stresses in the rock. The borehole wall fails if these new stresses exceed the existing rock strength. In order to prevent this, the boreholes are kept stable by analysing the mud weight window. The range of the permissible mud weight (MW) can be adjusted so that a stable drilling can be carried out (ZOBACK 2010; www-25). The minimum mud weight is the lower bound of the mud window used to obtain wellbore stability. If the mud weight is lower than the shear failure gradient (SFG) or the pore pressure gradient (PP) it comes to a collapse of the borehole (Fig. 3). The maximum mud weight is the upper bound of the mud window. If the mud weight is higher than the fracture gradient (FG) it results in a loss of circulation due to hydraulic fracturing of the rock (ZOBACK 2010; www-25).

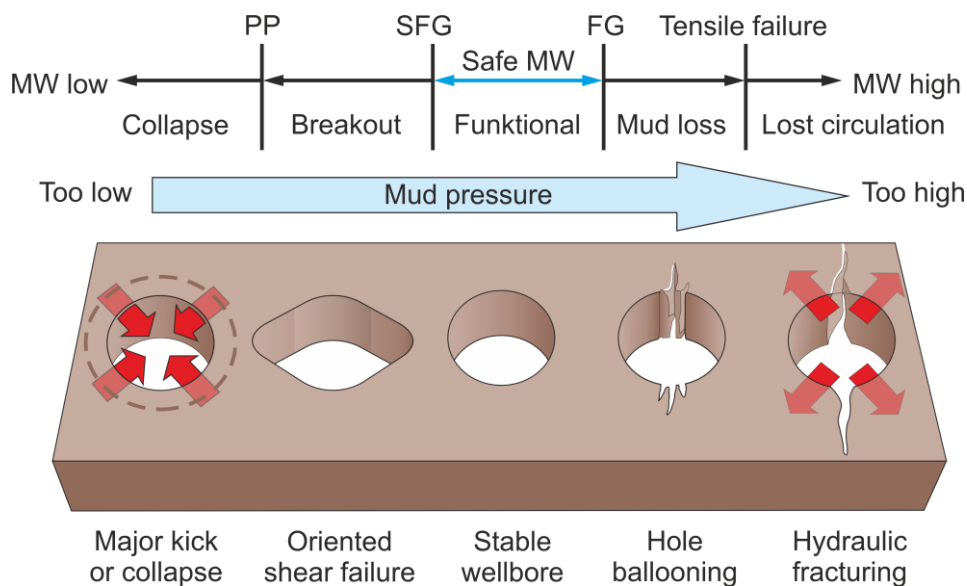


Fig. 3: The relationship between the mud weight in the borehole, the borehole stability and the different rock failures that occur mod. after ZHANG (2013).

When incidents such as “tight hole” or “stuck pipe” occur due to wellbore instability, the solution is time consuming and expensive (FJÆR et al. 2008). Geomechanical investigations can be used to measure the stress changes around a planned borehole. This can reduce the probability of borehole failure problems, circulation losses or stuck pipes.

Geomechanical models can be used to counter these effects and risks. For this purpose, the models must be fed with geomechanical data collected in the area prior to drilling. At the beginning of a geothermal project there are little data available. Throughout the lifetime of a reservoir, the geomechanical models will be better than in the beginning as more and more data are available (Fig. 4). This allows the model to be adjusted over time to solve any geomechanical problem that may arise. This will improve the understanding and prediction of how the reservoir properties will change during the lifetime

of the field. Geomechanics is also used to monitor the reservoir by different logging methods in real time, as the reservoir conditions change during the reservoir life-cycle (WHALEY 2019). On the one hand, the pressure is reduced by extracting water and the rock is subjected to higher pressure by the overburden. On the other hand, the water is returned to the deposit after energy extraction.

All these changes affect the reservoir and its surroundings. This can affect the stability of the borehole and thus lead to the collapse of the casing or affect the Earth's surface. A goal of geomechanics is to predict the occurrence of failure and reduce the risks during the life-cycle of a geothermal reservoir (ZOBACK 2010). The measured data can be used for further planned boreholes in the area.

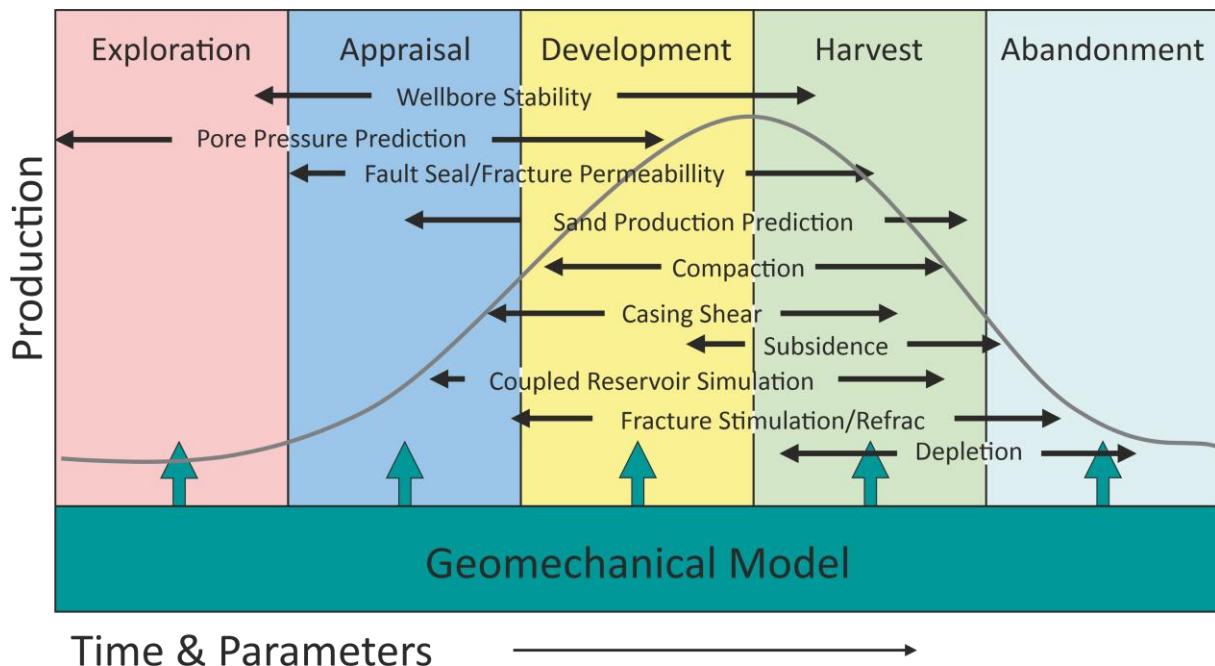


Fig. 4: Geomechanics through the life of a field mod. after ZOBACK (2016), the Reservoir Geomechanics course.

### 1.3 Mission objectives

This thesis was written within the framework of the GAB. The Bavarian State Ministry of Education, Science and the Arts was funding this joint research project for a project period of four years. Since 2016 three Bavarian universities have been participating in this research alliance: the Technical University of Munich (TUM), the Friedrich-Alexander University Erlangen-Nürnberg (FAU) and the University of Bayreuth (UBT). The main goal of the GAB is to improve geothermal energy as a renewable energy source for the domestic energy market and thereby achieve the CO<sub>2</sub> reduction targets (www-05). For this reason, the GAB project bundle, consisting of its five subprojects with a geological and engineering focus, was funded. In the following the five different subprojects are presented. It is also possible to see which universities were involved in the subproject and which objectives were pursued in each case.

- 1) Subproject “Reservoir Characterization” (TUM & FAU)  
Minimization of the exploration risk due to improved reservoir understanding
- 2) Subproject “PetroTherm” (FAU & TUM)  
Fundamental research in the field of petrothermal geothermal energy in NE Bavaria
- 3) Subproject “Operational safety for the thermal water cycle” (TUM)  
Investigation on scalings (thermal water circuit deposits) and an electric submersible pump
- 4) Subproject “Monitoring” (TUM)  
Development and implementation of an online monitoring system for geothermal plants
- 5) Subproject “Efficient and flexible power plants” (TUM & UBT)  
Improvement of profitability and efficiency of plant components on the surface

The interdisciplinary character of the necessary research and development work is evident from the five subprojects (Fig. 5). The present thesis deals with basic geological research of geomechanical reservoir characterization in the field of hydrothermal (“Reservoir Characterization”) geothermal energy in the North Alpine Foreland Basin, SE Germany and petrothermal (“PetroTherm”) geothermal energy in NE Bavaria. For this purpose, a parameter study was carried out on rare drill cores and on analogue material from outcrops.

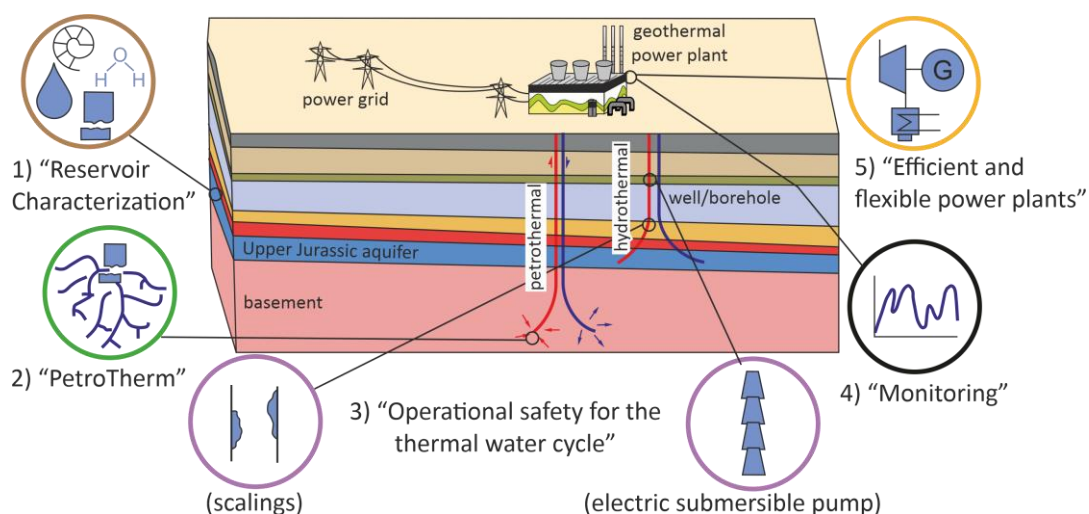


Fig. 5: Schematic representation of a geothermal project with the illustration of the five subprojects of the GAB mod. after FLECHTNER (2018).

## 1.4 Scope of work and research objectives

For the successful implementation of geothermal projects, a comprehensive knowledge of the subsurface lithology and structure is essential (SYMANK 2020). In the context of this thesis, the two areas which are important for geothermal energy in Bavaria were investigated geomechanically. One area investigated was the North Alpine Foreland Basin, SE Germany and the other was the Franconian Basin in NE Bavaria. The geological conditions for geothermal use in these two areas are completely different.

In the Northern Alpine Foreland Basin, SE Germany, hydrothermal geothermal energy is already being used successfully but the usage of the Upper Jurassic aquifer is to be improved and expanded. Here, the warm water from the Upper Jurassic aquifer is used but this reservoir has a very heterogeneous character due to the high variability in its depositional history. It is therefore assumed that the geomechanical properties of the Upper Jurassic aquifer are variable. However, in order to characterize the reservoir as well as possible, a better knowledge about distribution and diversity of geomechanical parameters is required.

Up to now, in the Northern Alpine Foreland Basin, SE Germany there are few borehole measurements. Many of these are incomplete because of the high costs or risks involved in their execution (BOHNSACK et al. 2020). Also, drill cores are usually not taken from the Upper Jurassic aquifer area of a geothermal well. Therefore, analogue samples similar to the aquifer rock in the borehole are used in projects (ALBER et al. 2019; THURO et al. 2019). Since there are only few geomechanical parameters for the Upper Jurassic aquifer from literature, analogue outcrops, or hydrocarbon/research wells, this parameter study was carried out. In the course of this research, it was possible to use rare drill cores from hydrocarbon wells in the Upper Jurassic aquifer. The main focus was on core samples in the area of Munich. Drill cores of eleven core drillings from the Upper Jurassic aquifer were examined using non-destructive as well as destructive laboratory experiments. Several core samples were taken per well, and thus the entire Upper Jurassic aquifer could be covered. This thesis characterizes the Upper Jurassic aquifer stratigraphically, lithologically and facially.

In NE Bavaria, petrothermal geothermal energy is still not being used. In this region, the geomechanical data, especially underground, are very limited. The heat-producing granites probably present in the subsurface of the Franconian Basin are to be used for petrothermal geothermal energy. As no deep drilling has ever reached the possible granitic basement in the area of the geothermal anomaly in the Franconian Basin, there are no granite drill cores. For this reason, no statement can be made about the geomechanical values from that area so far. Within the scope of this work, a parameter study was carried out using analogue reservoir rocks.

For this reason, the nearest granite outcrops were geomechanically investigated. The granites of the Fichtelgebirge serve as analogue material to the reservoir rock, which is assumed for petrothermal geothermal energy in NE Bavaria. A total of twelve outcrops were examined and the same laboratory experiments as in the North Alpine Foreland basin, SE Germany were carried out on the analogue samples from the outcrops of the Fichtelgebirge. This thesis helps to limit the uncertainties of the geothermal anomaly in the the Franconian Basin by improving the knowledge of the geological underground. If, during a possible exploration of the Franconian Basin, the reservoir rock is found to be granitic, first geomechanical analogue parameters were determined for this area.

Within the scope of this work, a small geomechanical model was created with the determined rock parameters of both areas to determine the excavation-damaged zone. This model helps to get a first overview of borehole stability in boreholes in the respective areas.

## 1.5 Structure of the thesis

The current situation of deep geothermal energy in Bavaria was explained in the “Introduction (1)”. In this thesis, the two areas which are important for geothermal energy in Bavaria were investigated geomechanically. The explanation of the two different geothermal systems can be found in the “Classification of deep geothermal systems (1.2)”. At the chapter “Geomechanics in deep geothermal energy (1.1)” the increasing role of geomechanics in deep geothermal energy is presented. A short overview of the GAB project including the different subprojects is summarised in the “Mission objectives (1.3)”. The introduction is completed with the chapters “Scope of work and research objectives (1.4)” and “Structure of the thesis (1.5)”.

In order to accurately characterize a hydrothermal or petrothermal reservoir, it is necessary to have the most comprehensive knowledge possible of the rock properties (Geomechanical reservoir characterization (2)). This chapter is again structured into three larger subchapters. The chapter “Methodology (2.1)” explains the methodological approach of the present work. On the one hand, the way the samples were prepared and then tested in the various geomechanical laboratory experiments is elaborated upon (Laboratory Testing (2.1.1)). For this purpose, non-destructive and destructive laboratory tests were performed. On the other hand, an introduction of the used simulation software and the different settings which were chosen in this thesis is discussed (Numerical simulation (2.1.2)). The following two chapters are divided into the two areas of investigation. The structure of the two chapters North Alpine Foreland Basin, SE Germany (2.2) and NE Bavaria (2.3) is identical. The respective chapter “State of the art (2.2.1/2.3.1)” explains the previous work in the respective areas. The chapter “Geological setting (2.2.2/2.3.2)” presents the respective working areas, the geological development and a brief description of the respective reservoirs. Furthermore, the situation of the local stress field in the respective area, which is needed for the final modelling, is described. To start, the existing database was searched for drillings and quarries in which the required rocks are present. Then, field and sampling campaigns were carried out in which drill cores and analogue material for the laboratory campaign were obtained (Data, study area (2.2.3/2.3.3)). In the laboratory campaign the various rocks from the two areas of interest were geomechanically examined. The results of the laboratory program used to create the present database and in which form the input parameters for the modelling can be obtained is covered in “Results (2.2.4/2.3.4)”. The correlations of these results as well as results of the modelling are described in the chapter “Discussion (2.2.5/2.3.5)”. The parameters and the modelling will therefore improve the understanding of the reservoirs as described in the “Conclusions (2.2.6/2.3.6)”. The results of the modelling are described in the chapter “Numerical simulation (2.4)”.

This is followed by a summary from both areas of interest (Summary (3)). This thesis concludes with the chapter “Outlook (4)” discussing what this work can be used for, what is currently in progress and what should be done in the future. Since chapter “Results (2.2.4/2.3.4)” mainly uses a graphical representation, a detailed tabular description of the results from the laboratory tests can be found in the Appendix.

## 2 Geomechanical reservoir characterization

Within a geothermal project many different disciplines work together. To successfully manage and complete a geothermal project, a comprehensive and accurate knowledge of the reservoir characteristics is essential. One important part of this knowledge relates to the geomechanical properties of the rock, which form the basis for the development of geomechanical models (see Fig. 4).

AGEMAR et al. (2012) published for the first time an underground temperature model of four different depths for Germany. In this thesis only the areas which are important for deep geothermal energy in Bavaria are shown (Fig. 6). The white areas represent regions where no underground data are available. In NE Bavaria the well temperature measurements of the German Continental Deep Drilling Program (KTB) are included whereas the geothermal anomaly of the Franconian Basin is not. No data are yet available for this anomaly at these depths, but the location of the anomaly has been plotted on the map for clarity.

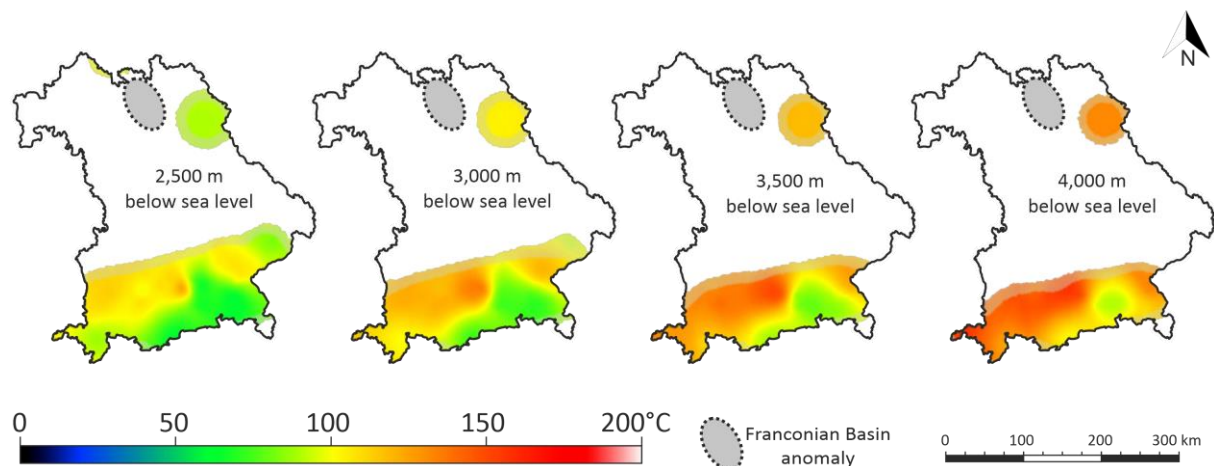


Fig. 6: Modelled subsurface temperature distribution in Bavaria at different depths mod. after AGEMAR et al. (2012). Additionally, the location of the geothermal anomaly in NE Bavaria was marked.

The areas of interest for hydrothermal and petrothermal geothermal energy in Bavaria were geomechanically investigated.

## 2.1 Methodology

In order to geomechanically describe the hydrothermal and petrothermal reservoirs in Bavaria, a workflow was developed (BOHNSACK et al. 2019; POTTEN et al. 2019b). A first step was to search for suitable core samples and analogue material in a sampling campaign. In a second step these samples were analysed in an extensive laboratory testing program. At the end, the determined characteristic values were processed for the near-field modelling of a borehole and the depth of failure was calculated.

### 2.1.1 Laboratory Testing

The sample preparation took place in the rock laboratories of the Chair of Engineering Geology at the TUM. First of all, samples had to be drilled from the outcrop blocks as well as the drill cores obtained from the oil and gas industry. All drill cores from the oil and gas industry were overdrilled similarly to those at the LfU. From the blocks, cores were obtained in different directions using a diamond drill and a diamond core bit with a diameter of 50 mm. The drilling was always performed vertically and, in most cases, also horizontally. In one case even the lateral direction could be determined due to the block size. The orientation of each drilled sample was marked with an arrow to orientate the sample in the rock block. Finally, cubes were sawn from the granite blocks, which were then used for the point load tests.

In order to take into account equally oriented test directions from outcrop blocks, the vertically drilled specimens for the uniaxial compression tests were compared with the horizontally drilled specimens for the Brazilian tensile strength tests (Fig. 7). This made it possible to obtain a direction-dependent comparison of the characteristic values in which the loading direction of the uniaxial compression test and the Brazilian tensile test were oriented in the same direction.

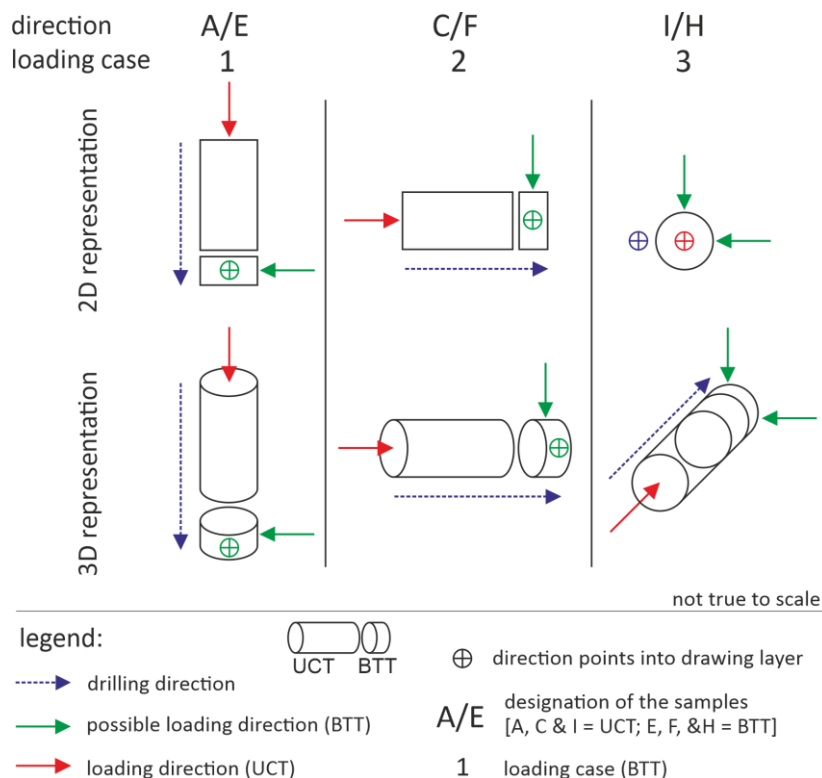


Fig. 7: Orientation of the drilling and testing directions from outcrop blocks after DREXL (2018).

Since Brazilian tensile strength (BTS) and Uniaxial compressive strength (UCS) were measured in different directions on the sample, the vertical direction for UCS determination corresponds to the horizontal direction for BTS determination and vice versa.

Two different sample geometries were created from the drawn cylindrical samples with a diameter of 50 mm. Cylindrical specimens with a length ( $l$ ) to diameter ( $d$ ) ratio of 2:1 as well as small slices with a  $l/d$  ratio of 1:2 were cut from the cores. Because the investigated wells were drilled almost vertically back then, the core samples could be prepared in such a way as to ensure that the angle between the layering and the upcoming loading is  $90^\circ$  (THURO 1996). The sawn cubes from the granite blocks had an edge length ratio of 1:1:1. The following Fig. 8 shows an example of the individual manufactured specimens with their respective geometries.

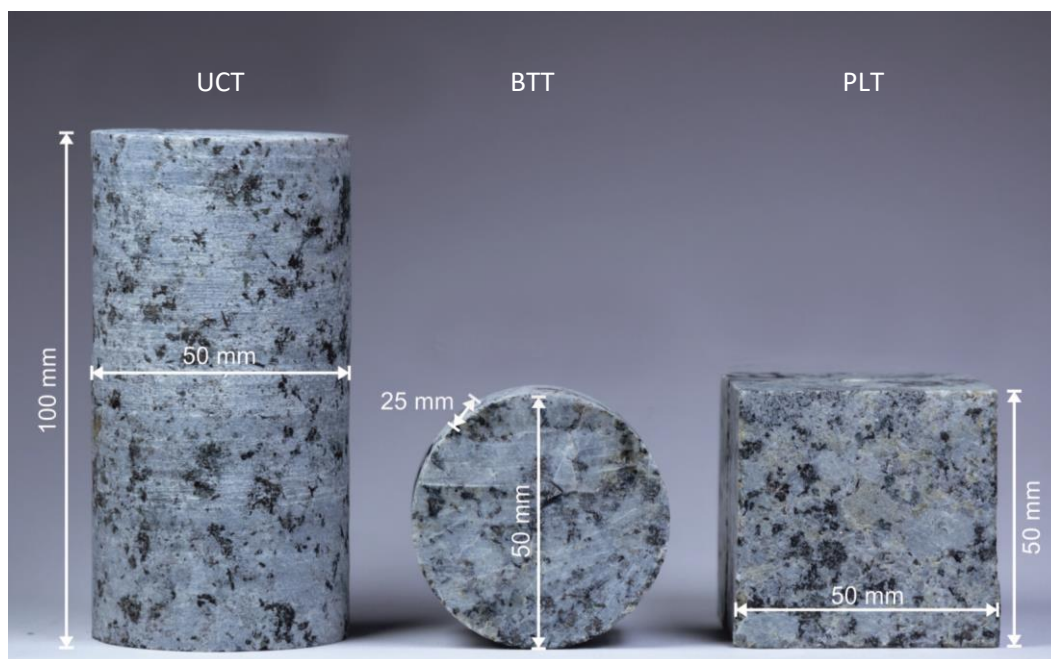


Fig. 8: Prepared samples for the Uniaxial Compression Test (UCT), the Brazilian Tensile Test (BTT) and the Point Load Test (PLT) after DREXL (2018).

After drilling, the cylindrical specimens were cut to a length of 100 mm with a diamond circular saw. Due to the drilled diameter of 50 mm, the  $l/d$  ratio of the specimens was 2:1. For small sampled drill cores or cores of poor sample quality after the drilling, the samples which did not have a 2:1 ratio were prepared with the largest possible sample geometry. The end surfaces of the specimens were ground flat with a diamond grinding machine. This allowed the production of optimal cylindrical specimens with parallelism of the two end faces and rectangularity of the end faces to the core axis according to the ASTM D4543-19 (2019). The correct smoothness and perpendicularity was finally checked with a straightedge. The specimens were then measured eight times lengthwise ( $l$ ) and six times crosswise ( $d$ ) with a digital caliper gauge to an accuracy of 0.01 mm.

After calibration, the test samples were oven dried at  $105^\circ\text{C}$  for 48 hours until mass constancy was achieved. A digital scale was used to obtain the dry mass of the sample ( $m_d$ ). Weighing was repeated five times to an accuracy of 0.01 g. After that, the saturation weight ( $m_s$ ) was measured. For this pur-

pose, the samples were placed in a desiccator and flushed with purified water until they were completely covered. A vacuum was then placed in the desiccator to release trapped air from the interconnected pores. The vacuum was maintained for at least 72 hours to ensure the best possible saturation. The saturation weight ( $m_s$ ) was then measured using the same principle as for the  $m_d$ -measurement. The non-destructive tests such as ultrasonic test and petrophysical investigations were first carried out on the samples prepared in this way. Afterwards the uniaxial compression tests were performed on these same test samples.

After drilling, the cylindrical specimens were also cut to a length of 25 mm with a diamond circular saw. Due to the drilled diameter of 50 mm, the  $l/d$  ratio of the specimens was 1:2. These slices were then measured two times lengthwise ( $l$ ) and crosswise ( $d$ ) with a digital caliper gauge to an accuracy of 0.01 mm. After the calibration, the test samples were oven dried at 105 °C for 48 h until mass constancy was achieved. A digital scale was used to obtain the dry mass of the sample ( $m_d$ ). Weighing was repeated five times to an accuracy of 0.01 g. The Brazilian tensile tests were performed on these test specimens. After the Brazilian tensile tests, the Cerchar abrasivity tests were carried out on the rough, fractured surfaces.

The sawn cubes had an edge length of 50 mm. The specimens were then measured two times lengthwise and crosswise with a digital caliper gauge to an accuracy of 0.01 mm. After the calibration, the test samples were oven dried at 105 °C for 48 hours until mass constancy was achieved. A digital scale was used to obtain the dry mass of the sample ( $m_d$ ). Weighing was repeated five times to an accuracy of 0.01 g. First point load tests were carried out on these cubes. Then the material was used for the LCPC abrasivity tests.

The LCPC abrasivity test requires 500 g  $\pm$  2 g of air-dried material. Therefore, the rock cubes from the point load test were put into a jaw crusher. If there were no cubes from the point load test for one outcrop, the remaining material from the sample preparation of the respective outcrop was used. Then the material was dry sieved until a sufficient sample material of the specified fraction (4–6.3 mm) was obtained.

The entire laboratory testing program was carried out in the rock laboratories at the Chair of Engineering Geology at the TUM. First the non-destructive and then the destructive laboratory tests were conducted on the prepared test samples. At the same time as the non-destructive laboratory tests at the Chair of Engineering Geology the project partner of the Chair of Hydrogeology started the petrophysical investigations on all the same drill cores of the GAB subproject "Reservoir Characterization".

As a result, the hydraulic properties of the drill samples were determined from the petrophysical properties. Using a helium expansion porosimeter (HEP) and water immersion porosimetry (WIP) the effective porosities for gas and water were measured (BOHNSACK et al. 2020). Since some of these parameters could be used for correlation in the results and discussion chapter, they are explained briefly here. A more detailed explanation as well as the complete range of all results obtained can be found in the Ph.D.-thesis of Daniel Bohnsack. With the previously determined dry mass of the sample ( $m_d$ ) and the measured values of the sample geometries ( $l$  &  $d$ ) for the bulk volume ( $V_b$ ), the bulk density ( $\rho_b$ ) was calculated (Eqn. 1).

Eqn. 1: Calculation of the bulk density ( $\rho_b$ ).

$$\rho_b = \frac{m_d}{V_b} \quad (\text{Eqn. 1})$$

with:	$\rho_b$	bulk density	[g/cm <sup>3</sup> ]
	$m_d$	dry mass of the sample	[g]
	$V_b$	bulk volume	[cm <sup>3</sup> ]

and

$$V_b = \pi \cdot \left(\frac{d}{2}\right)^2 \cdot l \quad (\text{Eqn. 1.1})$$

with:	$V_b$	bulk volume	[cm <sup>3</sup> ]
	$d$	diameter of the sample	[mm]
	$l$	length of the sample	[mm]

With the help of a helium pycnometer (Micromeritics, AccuPyc II 1340 Series), the helium grain volume  $V_g^{\text{He}}$  of the rock samples was determined according to Boyle's law by displacing known volumes of the injected gas (Micromeritics 2020). Therefore, using the  $V_b$ , it was possible to determine (Eqn. 2) the connected pore volume ( $V_p^{\text{He}}$ ).

Eqn. 2: Calculation of the connected pore volume ( $V_p^{\text{He}}$ ).

$$V_p^{\text{He}} = V_b - V_g^{\text{He}} \quad (\text{Eqn. 2})$$

with:	$V_p^{\text{He}}$	connected pore volume	[cm <sup>3</sup> ]
	$V_b$	bulk volume	[cm <sup>3</sup> ]
	$V_g^{\text{He}}$	helium grain volume	[cm <sup>3</sup> ]

Likewise with  $m_d$  and  $V_g^{\text{He}}$  the grain density ( $\rho_g$ ) was calculated according to the Eqn. 3.

Eqn. 3: Calculation of the grain density ( $\rho_g$ ).

$$\rho_g = \frac{m_d}{V_g^{\text{He}}} \quad (\text{Eqn. 3})$$

with:	$\rho_g$	grain density	[g/cm <sup>3</sup> ]
	$m_d$	dry mass of the sample	[g]
	$V_g^{\text{He}}$	helium grain volume	[cm <sup>3</sup> ]

The fraction of the interconnected non-solid volume that allows flow through the rock is defined as effective porosity  $\phi_{\text{eff}}$ . This was estimated (Eqn. 4) from  $V_g^{\text{He}}$  and  $V_b$ .

Eqn. 4: Calculation of the effective porosity ( $\phi_{eff}^{He}$ ).

$$\phi_{eff}^{He} = \left(1 - \frac{V_g^{He}}{V_b}\right) \cdot 100 \% \quad (\text{Eqn. 4})$$

with:	$\phi_{eff}^{He}$	effective porosity	[%]
	$V_g^{He}$	helium grain volume	[cm <sup>3</sup> ]
	$V_b$	bulk volume	[cm <sup>3</sup> ]

With the assumption of a constant known density of the absorbed water  $\rho_w$  (0.997 g/cm<sup>3</sup> at 24–26 °C) (WAGNER & PRUß 2002), and by using the pore volume  $V_p^W$ , the effective porosity  $\phi_{eff}^W$  was obtained (American Petroleum Institute 1998; ANOVITZ & COLE 2015; MCPHEE et al. 2015).

Eqn. 5: Calculation of the effective porosity ( $\phi_{eff}^W$ ).

$$\phi_{eff}^W = \left(\frac{V_p^W}{V_b}\right) \cdot 100 \% \quad (\text{Eqn. 5})$$

with:	$\phi_{eff}^W$	effective porosity	[%]
	$V_p^W$	pore volume	[cm <sup>3</sup> ]
	$V_b$	bulk volume	[cm <sup>3</sup> ]

and

$$V_p^W = \frac{(m_s - m_d)}{\rho_w} \cdot 1 \quad (\text{Eqn. 5.1})$$

with:	$V_p^W$	pore volume	[cm <sup>3</sup> ]
	$m_s$	saturated mass of the sample	[g]
	$m_d$	dry mass of the sample	[g]
	$\rho_w$	purified water density	[g/cm <sup>3</sup> ]

## Ultrasonic Test

The non-destructive laboratory test was an ultrasonic test. This test allows one to determine the sound wave velocity in a material. It is used to determine the different rock properties without destroying the sample under investigation. The ultrasonic test was performed on the same specimens that were subsequently used for uniaxial compression. The different wave types differ in their direction of movement. Primary waves ( $v_p$ ), also called compression waves, move longitudinally to the direction of propagation (REYNOLDS 2011). Secondary waves ( $v_s$ ), also called shear waves, move transversely to the direction of propagation (REYNOLDS 2011).

First, the  $v_p$ -velocity of the rock sample was determined in an ultrasonic transmission test (longitudinal wave) according to DIN EN 12504-4 (2004). With the help of this  $v_p$ -velocity, the elastic parameters were determined using  $v_s$ -velocity, the extensional wave method (www-06 and DIN EN 14146 (2004-06)). The ultrasonic tests were carried out with the complete system from Geotron Elektronik. This consists of an ultrasonic generator (USG-40), an oscilloscope (Scopemeter, PicoScope 4000), a transmitter probe (T) UPG-D 3083 and a receiver probe (R) UPE-D 3080 (www-07; www-08; www-09). This receiver probe allows simultaneous measurement of  $v_p$ - and  $v_s$ -waves. The oscilloscope was connected to a computer on which the respective software is installed. The sample to be tested was installed in a test frame. The test setup is shown in Fig. 9.

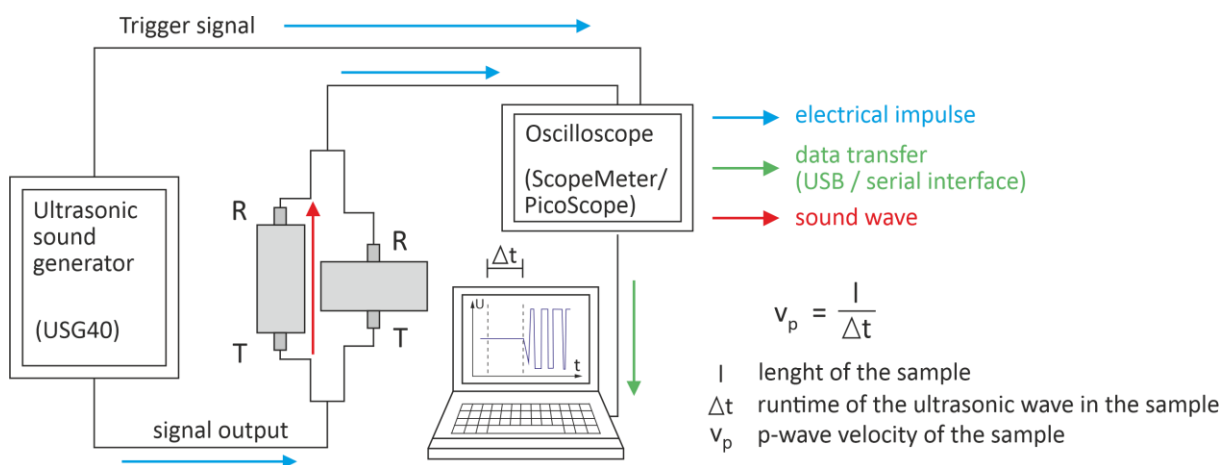


Fig. 9: Test setup of the ultrasonic measurements to determine the  $v_p$  and the elastic parameters on the respective specimen mod. after MENSCHIK (2015).

## Testing processes

Two probes were attached to the test frame. The test sample was placed on the lower probe which was the transmitter. Then the lever (Fig. 9) was released and the receiver was placed on top of the sample. The lever was locked and the test sample was fixed. The sample to be tested was then subjected to air pressure (2 bar) within the test frame to achieve better contact between the sample and the detector heads. Since the samples have been petrophysically tested by the Chair of Hydrogeology for permeability and porosity and the samples have to be returned to their owners after the laboratory program, no contact liquid was permitted to improve the contact area. The ultrasonic test was carried out under room conditions mainly on dry but also on saturated (sat.) samples. The results section,

therefore, distinguishes between dry non-destructive and sat. non-destructive tests. After the sample dimensions were entered and the correct probes were selected, the testing began.

During the test, the ultrasonic wave was generated by the ultrasonic generator (USG 40) and the probes were piezoelectrically stimulated. The wave was transmitted through the first head, then passed through the sample and subsequently detected by a second head. During the test the continuous trigger mode was active and the USG-40 with a frequency of 20 kHz was used. The electrical signal obtained was recorded at a sampling frequency of 10 MHz and amplified with 40 dB. This signal was fed to an oscilloscope, which converted the wave signal into a computer signal. From there, the data were sent to the connected computer. The samples were measured three times ( $v_{pl}$ ) lengthwise (l) and three times ( $v_{pd}$ ) crosswise (d) for the ultrasonic transmission test.

### Testing analysis

With the help of the Lighthouse UMPC software, the  $v_p$ -velocity was picked manually from the waveform (www-10). This was the range in the ultrasonic signal where the first onset (the first “kink” of the signal from the zero line) was suspected. Care had to be taken that the amplitude was properly scaled to determine the running time  $\Delta t$  correctly.

*Eqn. 6: Calculation of the p-wave velocity ( $v_p$ ) lengthwise ( $v_{pl}$ ) and crosswise ( $v_{pd}$ ).*

$$v_{pl} = \frac{l}{\Delta t} \quad \text{or} \quad v_{pd} = \frac{d}{\Delta t} \quad (\text{Eqn. 6})$$

with:	$v_p$	p-wave velocity of the sample	[m/s]
	l	length of the sample	[mm]
	d	diameter of the sample	[mm]
	$\Delta t$	runtime of the ultrasonic wave in the sample	[s]

The elastic properties were determined with the Lighthouse DW software (www-11). Since the dilatational wave ( $v_{dw}$ ) can only be measured on cylindrical specimens, only two measurements were made on the end faces of the samples. After entering the sample sizes and checking the reference standard, the previously measured  $v_p$ -velocity was picked again. Then the natural frequency was determined automatically and then the different dynamic parameters were released.

Using the following calculations (Eqn. 7–Eqn. 11) the dynamic parameters of the non-destructive tests were determined. The dynamic moduli were determined in the non-destructive ultrasonic tests and the static moduli were determined in the uniaxial compression tests. The meaning of all measured moduli is also briefly explained.

The modulus of elasticity (E) is defined according to SCHÖN (2015) “as the ratio of stress to strain in a uniaxial stress state”.

Eqn. 7: Calculation of the dynamic modulus of elasticity ( $E_{dyn}$ ).

$$E_{dyn} = \rho \cdot v_{dw}^2 \quad (\text{Eqn. 7})$$

with:	$E_{dyn}$	dynamic modulus of elasticity	[GPa]
	$\rho$	density of the sample	[g/cm <sup>3</sup> ]
	$v_{dw}$	dilatational wave velocity of the sample	[m/s]

The Shear modulus (G) is defined according to SCHÖN (2015) “as the ratio of shear stress to shear strain”.

Eqn. 8: Calculation of the dynamic shear modulus ( $G_{dyn}$ ).

$$G_{dyn} = \rho \cdot v_s^2 \quad (\text{Eqn. 8})$$

with:	$G_{dyn}$	dynamic shear modulus	[GPa]
	$\rho$	density of the sample	[g/cm <sup>3</sup> ]
	$v_s$	shear wave velocity of the sample	[m/s]

The bulk modulus (K) is defined according to SCHÖN (2015) “as the ratio of hydrostatic stress to volumetric strain”.

Eqn. 9: Calculation of the dynamic bulk modulus ( $K_{dyn}$ ).

$$K_{dyn} = \rho \cdot \left( v_p^2 - \left( \frac{4}{3} \right) \cdot v_s^2 \right) \quad (\text{Eqn. 9})$$

with:	$K_{dyn}$	dynamic bulk modulus	[GPa]
	$\rho$	density of the sample	[g/cm <sup>3</sup> ]
	$v_p$	p-wave velocity of the sample	[m/s]
	$v_s$	shear wave velocity of the sample	[m/s]

The poisson’s ratio ( $\nu$ ) is defined according to SCHÖN (2015) “as the (negative) ratio of lateral strain to axial strain in a uniaxial stress state”.

Eqn. 10 Calculation of the dynamic poisson’s ratio ( $\nu_{dyn}$ ).

$$\nu_{dyn} = \frac{3 \cdot K_{dyn} - E_{dyn}}{6 \cdot K_{dyn}} \quad (\text{Eqn. 10})$$

with:	$\nu_{dyn}$	dynamic poisson’s ratio	[-]
	$K_{dyn}$	dynamic bulk modulus	[MPa]
	$E_{dyn}$	dynamic modulus of elasticity	[MPa]

The acoustic impedance ( $Z$ ) according to SCHÖN (2015) “of the materials (geological layers) can be calculated after from P [...] reflectivities by inversion”.

Eqn. 11 Calculation of the acoustic impedance ( $Z$ ).

$$Z = \rho \cdot v_p \quad (\text{Eqn. 11})$$

with:	$Z$	acoustic impedance	$[10^6 \text{ kg/m}^2\text{s}]$
	$\rho$	density of the sample	$[\text{g/cm}^3]$
	$v_p$	p-wave velocity of the sample	$[\text{m/s}]$

A summary of all test results is given in the Appendix.

### Uniaxial Compression Test

The uniaxial compression tests were carried out on the cylindrical sample cores according to the German recommendation no. 1 for uniaxial compression tests with free lateral propagation DGGT (2004). By selecting the test option 6, the desired parameters could be achieved. All compression tests were performed in the servo-controlled hydraulic testing machine Toni-Norm from Zwick/Roell. This machine has two load frames with a nominal load of 2000 kN for uniaxial compression tests (UCT) and 200 kN for Brazilian tensile tests (BTT) and point load tests (PLT) (Fig. 10).

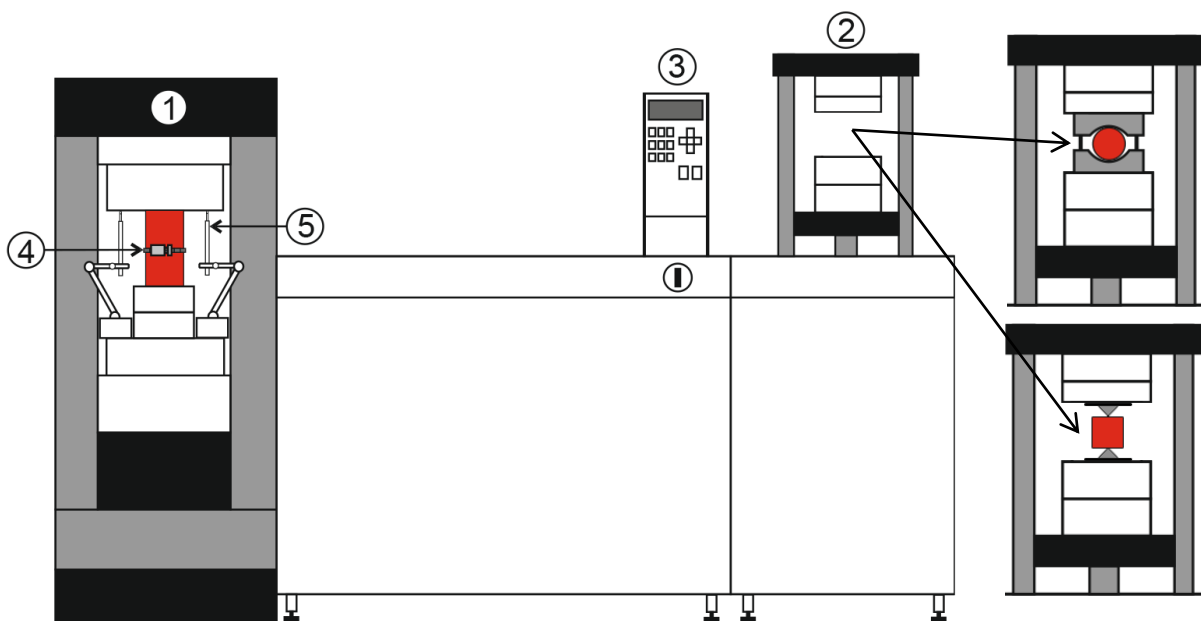


Fig. 10: Sketch of the front view of the compression testing machine "ToniNorm" with a load frame with 2000 kN nominal load for UCT (1), a load frame with 200 kN nominal load (2) for BTT (top) or PLT (bottom), the control panel (3) and LVDT for radial (4) and axial strain measurements (5) mod. after WIESER (2016).

### Testing processes

The prepared test samples were loaded and the actual load was measured continuously until the final failure of the specimen. The compression tests were performed with the large load frame, which can have a nominal load of 2000 kN ((1) in Fig. 10). According to class 1 of the German standard DIN 51220

(2003) as well as DIN EN ISO 7500-1 (2018), the machine used meets the high accuracy requirements. The samples were tested in axial deformation controlled mode at a constant deformation rate of 0.06 mm/min until complete failure of the rock.

The lower plate of the machine is movable and exerts the load by pressing the test sample against the upper steel plate. The upper steel plate has a spherical seat and can therefore compensate non-parallel end faces by aligning the plate to the test sample. Once the test sample is captured between the plates, rotation and movement of the plates is impossible.

During the testing, the axial deformation was recorded with three digital inductive displacement transducers (HBM W5TK) connected in parallel to determine the stress-strain curve. These Linear Variable Differential Transformers (LVDT) are installed evenly around the test samples. In this thesis the axial deformation was measured between the two load plates and not on the test samples itself. To document the radial (lateral) deformation of the test sample, a strain measurement chain with a lateral displacement transducer (RDP group D6) was connected in parallel to determine the stress-strain curves. The measuring chain used, with an integrated LVDT, was installed at the middle height of the rock sample. After the test sample dimensions were entered and the transducers worked correctly, the test began.

With a sampling rate of 5 MHz, the “ToniTrol” control unit recorded the load and strain. All data were processed by a computer with Zwick’s “TestXpert” software. This software was used to document the time, the deformation and the currently applied force, to perform all further calculations and to create the final documentation of the test. In this study, the uniaxial compressive strength ( $\sigma_u$ ), the deformation-/V-Modulus ( $V$ ) and the elasticity-/Young’s Modulus ( $E$ ) were measured with this software. The control system detects the breakage by a defined decrease in load. An overview of the ranges in which the parameters are determined in the stress-strain curve is shown in Fig. 11.

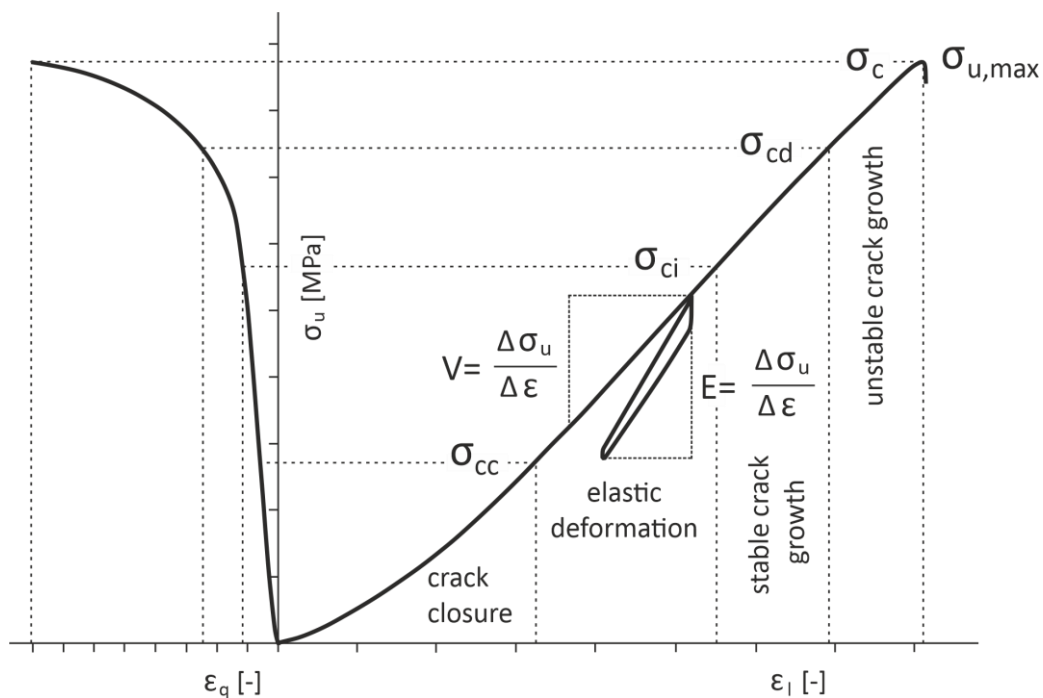


Fig. 11: Schematic stress-strain curve of a test sample showing the determination of the uniaxial compressive strength  $\sigma_u$ , the V-Modulus and the E-Modulus ( $\sigma_{cc}$  crack closure stress,  $\sigma_{ci}$  crack initiation stress,  $\sigma_{cd}$  crack damage stress).

### Testing analysis

Two different types of uniaxial compression tests were carried out. A number of tests were performed in which the test sample was simply loaded until the rock failed completely. In these so-called preliminary tests, the deformation modulus  $V$  in the slope of the first load branch and the maximum uniaxial compressive strength  $\sigma_u$  were determined. These tests served to better characterize the rocks and to determine in which range the linear range of the respective rock was to lie. They served as preliminary tests for the main tests in which the modulus of elasticity  $E$  was to be determined.

The uniaxial compressive strength  $\sigma_u$  is defined from the stress-strain curve as the maximum force  $F_{\max}$  applied to the initial end face surfaces  $A$  of the investigated sample (Eqn. 12).

*Eqn. 12: Calculation of failure stress as compressive strength ( $\sigma_u$ ).*

$$\sigma_u = \frac{F_{\max}}{A} \quad (\text{Eqn. 12})$$

with:	$\sigma_u$	uniaxial compressive strength	[MPa]
	$F_{\max}$	failure load of the sample	[kN]
	$A$	cross-section area of the sample	[mm <sup>2</sup> ]

If the test sample  $l/d$  ratio was less than 2, the compressive strength  $\sigma_u$  had to be corrected to follow the existing recommendations and standards. The revised compressive strength  $\sigma_{u(2)}$  was adjusted according to the equation (Eqn. 13) from OBERT & DUVALL (1967).

*Eqn. 13: Calculation of adjusted compressive strength ( $\sigma_{u(2)}$ ).*

$$\sigma_{u(2)} = \frac{8 \cdot \sigma_u}{7 + 2 \cdot \frac{d}{l}} \quad (\text{Eqn. 13})$$

with:	$\sigma_{u(2)}$	revised uniaxial compressive strength	[MPa]
	$\sigma_u$	uniaxial compressive strength	[MPa]
	$d$	diameter of the sample	[mm]
	$l$	length of the sample	[mm]

The deformation modulus  $V$  was determined in the linear section of the stress-strain curve as the quotient of axial stress and strain change (Eqn. 14).

*Eqn. 14: Calculation of the modulus of deformation ( $V$ ).*

$$V = \frac{\Delta\sigma}{\Delta\varepsilon_1} \quad (\text{Eqn. 14})$$

with:	$V$	modulus of deformation (V-Modulus)	[GPa]
	$\Delta\sigma$	differential axial stress	[MPa]
	$\Delta\varepsilon_1$	differential axial strain	[-]

and

$$\varepsilon_1 = \frac{l_1 - l_0}{l_0} = \frac{\Delta l}{l_0} \quad (\text{Eqn. 14.1})$$

with:	$\varepsilon_1$	axial strain	[-]
	$l_1$	final length of the sample	[mm]
	$l_0$	original length of the sample	[mm]
	$\Delta l$	differential length of the sample	[mm]

After the preliminary tests had been carried out, the range for running the unloaded and loaded loop to determine the modulus of elasticity  $E$  of the main tests was determined. Since the carbonates of this work are not isotropic, the ranges for the  $E$ -Moduli were determined for each rock. Since no correlation between uniaxial compressive strength and facies could be established, the linear dependence of the uniaxial rock compressive strength on the acoustic impedance was used. For this purpose the acoustic impedance  $Z$  of all  $v_p$ -measurements ( $v_{pl}$  &  $v_{pd}$ ) was calculated.

The uniaxial compressive strength ( $\sigma_{u(1)}$ ) was calculated for each sample using the equation (Eqn. 15) according to MÜLLER & PIPPING (2011):

*Eqn. 15: Calculation of the uniaxial compressive strength ( $\sigma_{u(1)}$ ).*

$$\sigma_{u(1)} = 7.947158777 \cdot Z + 6.956724986 \quad (\text{Eqn. 15})$$

with:	$\sigma_{u(1)}$	calculated uniaxial compressive strength	[MPa]
	$Z$	acoustic impedance	[kg/m <sup>2</sup> s]

The  $\sigma_{u(1)}$  were then compared with the  $\sigma_u$  of the preliminary tests. The linear part of the stress-strain curve from the preliminary tests was noted. This range was transferred to the main tests individually using  $Z$  and the  $\sigma_{u(1)}$  and  $\sigma_u$ . For the investigated granites, the linear part of the curve was determined by the preliminary tests of the respective quarry. In this area, the modulus of elasticity was then determined for all granites in the quarry in the main tests.

In the main tests the test sample was run in a loop. The sample was pre-loaded, unloaded and loaded again in the linear-elastic range until the rock failed completely. The modulus of elasticity  $E$  was determined in the reloading curve of the linear section of the stress-strain curve in accordance with the standards in addition to the modulus of deformation  $V$  and maximum uniaxial compressive strength  $\sigma_u$  (Eqn. 16).

*Eqn. 16: Calculation of the modulus of elasticity ( $E$ ).*

$$E = \frac{\Delta \sigma}{\Delta \varepsilon_1^{el}} \quad (\text{Eqn. 16})$$

with:	$E$	modulus of elasticity (Young's Modulus)	[GPa]
	$\Delta \sigma$	differential axial stress	[MPa]
	$\Delta \varepsilon_1^{el}$	differential axial elastic strain	[-]

and

$$\varepsilon_1^{el} = \frac{l_1 - l_0}{l_0} = \frac{\Delta l}{l_0} \quad (\text{Eqn. 16.1})$$

with:	$\varepsilon_1^{el}$	axial elastic strain	[-]
	$l_1$	final length of the sample	[mm]
	$l_0$	original length of the sample	[mm]
	$\Delta l$	differential length of the sample	[mm]

If the change in radial strain to the specimen axis was measured at the same time, the poisson's ratio  $\nu$  was determined (Eqn. 17).

*Eqn. 17: Calculation of the poisson's ratio ( $\nu$ ).*

$$\nu = \frac{\Delta \varepsilon_q}{\Delta \varepsilon_1} \quad (\text{Eqn. 17})$$

with:	$\nu$	poisson's ratio	[-]
	$\Delta \varepsilon_q$	differential radial strain	[-]
	$\Delta \varepsilon_1$	differential axial strain	[-]

and

$$\varepsilon_q = \frac{d_1 - d_0}{d_0} = \frac{\Delta d}{d_0} \quad (\text{Eqn. 17.1})$$

with:	$\varepsilon_q$	radial strain	[-]
	$d_1$	final diameter of the sample	[mm]
	$d_0$	original diameter of the sample	[mm]
	$\Delta d$	differential diameter of the sample	[mm]

Some test samples from the North Alpine Foreland Basin, SE Germany were also measured saturated to investigate the influence of complete saturation on the parameters of the uniaxial compression tests. None of the test samples from NE Bavaria were measured in a saturated condition. These rocks have such a low porosity that this porosity has no influence on the measurement.

A summary of all test results is given in the Appendix.

### Brazilian Tensile Test

The Brazilian tensile strength test was carried out in accordance with the German recommendation no. 10 of the DGGT (2008) for the indirect tensile test. The prepared disc-shaped cylinder had a  $l/d$  ratio of 0.5.

### Testing processes

The small loading frame of the servo-controlled hydraulic testing machine Toni-Norm by Zwick/Roell with a nominal load of 200 kN was used to load and measure the failure load. The machine meets the accuracy requirements of class 1 in the German standard DIN 51220 (2003) as well as DIN EN ISO 7500-

1 (2018). This system was used to measure the indirect tensile strength of a rock by loading the cylindrical sample surface line. For this purpose, the loading frame of the “ToniNorm” testing machine is equipped with a frame yoke which fixes the sample in the correct position pins as shown in the schematic illustration in Fig. 12.

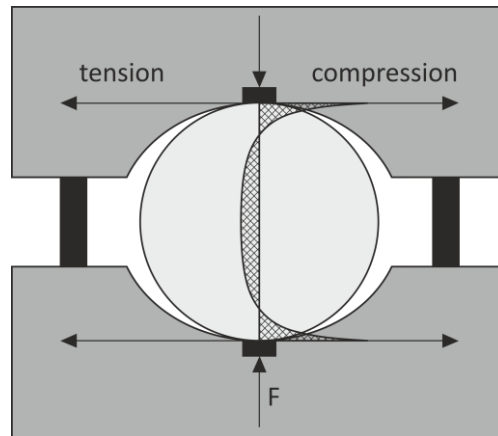


Fig. 12: Sketch of the Brazilian tensile test and the applied forces for the determination of the Brazilian tensile strength  $\sigma_t$  mod. after DGGT (2008).

After the sample dimensions were entered, the test began and the samples were loaded with a constant stress rate of 0.07 kN/s. The load was applied to the sample surface line with two curved loading jaws. The loading direction was taken into account with regard to its anisotropies, specimen orientation and bedding. As can be seen in Fig. 12 the load causes compressive stresses at the area where the force is generated, and leads to tensile stresses in excess of about 70 % of the sample diameter DGGT (2008). All data were processed by a computer using Zwick's “TestXpert” software. This software was used to document the time and the currently applied force, perform all further calculations and produce the final documentation of the test.

### Testing analysis

Transverse tensile stresses inside the test sample induce the failure by forming a sharp vertical crack. The failure load  $F_{\max}$  was recorded with the software TestXpert and the Brazilian tensile strength  $\sigma_t$  was determined (Eqn. 18).

Eqn. 18: Calculation of the Brazilian tensile strength ( $\sigma_t$ ).

$$\sigma_t = \frac{2 \cdot F_{\max}}{\pi \cdot d \cdot l} \quad (\text{Eqn. 18})$$

with:	$\sigma_t$	Brazilian tensile strength	[MPa]
	$F_{\max}$	failure load of the sample	[kN]
	d	diameter of the sample	[mm]
	l	length of the sample	[mm]

A summary of all test results is given in the Appendix.

## Point Load Test

In accordance with the test recommendation of DGGT (2010), the point load test was carried out. The point load index ( $I_S$ ) was calculated, which is used as an indirect method to define the uniaxial compressive strength of rock samples. The prepared rock cubes had a standardized edge length of 50 mm and during the sample preparation, great care was taken to obtain samples with a minimum of discontinuities.

### Testing processes

The point load test was also performed with the servo-controlled hydraulic press from ToniNorm by Zwick/Roell. As in the Brazilian tensile test, the small load frame (200 kN nominal load) was also used for the point load test in order to measure the failure load that occurred. The machine meets the accuracy requirements of class 1 in the German standard DIN 51220 (2003) as well as DIN EN ISO 7500-1 (2018). For this test, the loading frame was equipped with point load test pins as shown in the schematic illustration in Fig. 13.

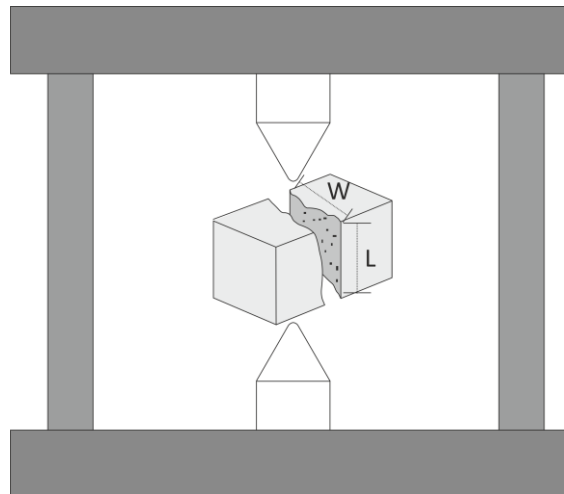


Fig. 13: Sketch of the point load test, measured parameters & applied forces for the determination of the point load index  $I_S$  mod. after DGGT (2010).

After the sample dimensions were entered, the test could begin and the specimens were loaded at a constant stress rate of 3 kN/s until the complete failure of the specimen occurred. All data were processed by a computer using Zwick's "TestXpert" software. This software was used to document the time and currently applied force, perform all further calculations and produce the final documentation of the test. After the test, the exact geometry of the failure surface  $D_e^2$  of the samples was measured with a digital caliper gauge by two perpendicular measurements (Fig. 13). At least ten rock cubes from one block were tested to calculate a mean value of  $I_S$ .

### Testing analysis

The point load index  $I_S$  was calculated using the failure load and the area of the failure surface from each of the cube samples (Eqn. 19). The calculation of the area of failure surface does not comply with the ISRM (1985) recommendation, as it relies on a diametric test on cylindrical samples.

Eqn. 19: Calculation of the point load index ( $I_S$ ).

$$I_S = \frac{F_{\max}}{D_e^2} \quad (\text{Eqn. 19})$$

with:	$I_S$	point load index	[MPa]
	$F_{\max}$	failure load of the sample	[kN]
	$D_e^2$	area of failure surface	[mm <sup>2</sup> ]

and

$$D_e^2 = W \cdot L \quad (\text{Eqn. 19.1})$$

with:	$D_e^2$	area of failure surface	[mm <sup>2</sup> ]
	$W$	width of the failure surface	[mm]
	$L$	length of the failure surface	[mm]

Due to the fact that the point load index  $I_S$  is strongly affected by the sample size, the scale effect has to be considered. Because of this, BROOK (1993) proposed the below correction factor to convert  $I_S$  to a cube with 50 mm edge length (Eqn. 20).

Eqn. 20: Calculation of the point load index ( $I_{S(50)}$ ) correlating to the standard edge length of 50 mm.

$$I_{S(50)} = \left( \frac{D_e^2}{2500} \right)^{0.225} \quad (\text{Eqn. 20})$$

with:	$I_{S(50)}$	point load index for 50 mm edge length	[MPa]
	$D_e^2$	area of failure surface	[mm <sup>2</sup> ]
	$I_S$	point load index	[MPa]

and

$$D_e^2 = W \cdot L \quad (\text{Eqn. 20.1})$$

with:	$D_e^2$	area of failure surface	[mm <sup>2</sup> ]
	$W$	width of the failure surface	[mm]
	$L$	length of the failure surface	[mm]

The uniaxial compressive strength  $\sigma_m$  was obtained from the  $I_{S(50)}$  with the correction factor  $c$ . This factor is an empirically defined constant. Based on the results of various studies, the factor  $c$  was previously fixed at  $\sim 20$ . Within this thesis  $c$  is given for each test (Eqn. 21).

Eqn. 21: Calculation of uniaxial compressive strength ( $\sigma_m$ ) derived from ( $I_{S(50)}$ ).

$$\sigma_m = c \cdot I_{S(50)} \quad (\text{Eqn. 21})$$

with:	$\sigma_m$	derived uniaxial compressive strength	[MPa]
	$c$	correction factor	[-]
	$I_{S(50)}$	point load index for 50 mm edge length	[MPa]

A summary of all test results is given in the Appendix.

## Cerchar Abrasivity Test

The Cerchar abrasivity test was carried out on the rough fracture surfaces of the samples from the Brazilian tensile tests in accordance with the test recommendation of the Centre d'Etudes et Recherches de Charbonnages de France (Cerchar 1986; ALBER et al. 2014; DGGT 2016). The Cerchar Abrasivity Index (CAI), was established as an indicator of the abrasiveness of rocks that cause wear on excavation tools.

### Testing processes

The test apparatus which was used in the laboratory (Fig. 14) is the modified Cerchar apparatus according to WEST (1989).

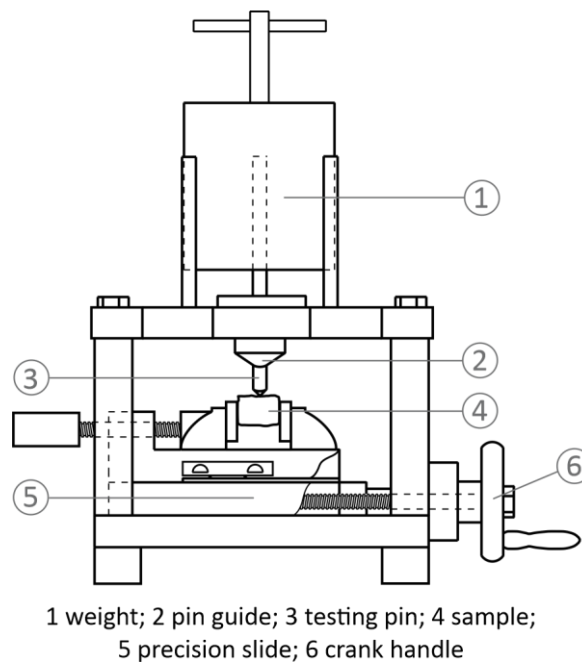


Fig. 14: Sketch of the Cerchar apparatus for the determination of the Cerchar Abrasivity Index (CAI) after DGGT (2016), mod. after WEST (1989).

The Brazilian tensile test sample was placed in the precision slide with the rough fracture surface facing upwards. Under a static load of 7 kg the inserted steel pin was loaded. During the test, the steel pin was scratched with a defined geometry and quality (HRC 54–56) over 10 mm of the rough, fractured surfaces of the specimen. Every test sample was scratched five times according to this pattern. The testing direction for anisotropic or inhomogeneous rocks was perpendicular to anisotropies, specimen orientation and bedding.

### Testing analysis

For the testing analysis, the resulting wear on the steel pins was examined with an incident light binocular microscope. A measuring scale was used to determine the diameter of the flattened area with an accuracy of 0.02 mm. Each steel pin was read in four perpendicular directions. Then all results of one steel pin were averaged. Using the following equation (Eqn. 22) and the wear on the steel pin ( $d_{CAI}$ ), the Cerchar Abrasivity Index (CAI) was calculated.

Eqn. 22: Calculation of the Cerchar Abrasiveness Index (CAI).

$$CAI = d_{CAI} \cdot 10 \quad (\text{Eqn. 22})$$

with: CAI Cerchar Abrasiveness Index [-]  
 $d_{CAI}$  mean wear of the steel pin [mm]

The abrasiveness of each sample was evaluated according to the Tab. 1.

Tab. 1: Classification of abrasiveness with the CAI test (according to Cerchar (1986)).

CAI [-]	Classification
0.0–0.3	not abrasive
0.3–0.5	not very abrasive
0.5–1.0	slightly abrasive
1.0–2.0	medium abrasive
2.0–4.0	very abrasive
4.0–6.0	extremely abrasive

A summary of all test results is given in the Appendix.

### LCPC Abrasivity Test

The LCPC abrasivity test was carried out according to the French Standard (THURO & KÄSLING 2009; WILLIAMS 2010; NF P 18-579: 2013; KÄSLING & THURO 2010). This test was developed by the Laboratoire Central des Ponts et des Chaussées (LCPC) for the definition of the abrasiveness (LCPC Abrasivity Coefficient (LAC)) and breakability (LCPC Breakability Coefficient (LBC)) of hard rock.

#### Testing processes

The LCPC abrasivity test was carried out with an abrasivity test apparatus (“abrasimeter”), which is shown in Fig. 15. The rectangular steel impeller with standardized dimensions (5 x 25 x 50 mm) and a Rockwell hardness of B 60–75 was weighed with an accuracy of 0.01 g. After weighing, the impeller was mounted on the abrasimeter and the sample container was closed. 500 g of the dried, broken sample was filled into the sample container via a funnel on top of the machine. After sealing the funnel, the machine was started. Then the wheel rotated at a speed of 4,500 rpm for five minutes in the sample container. After the test, the sample container with the tested sample was carefully disassembled to obtain all the crushed test material and the impeller is disassembled.

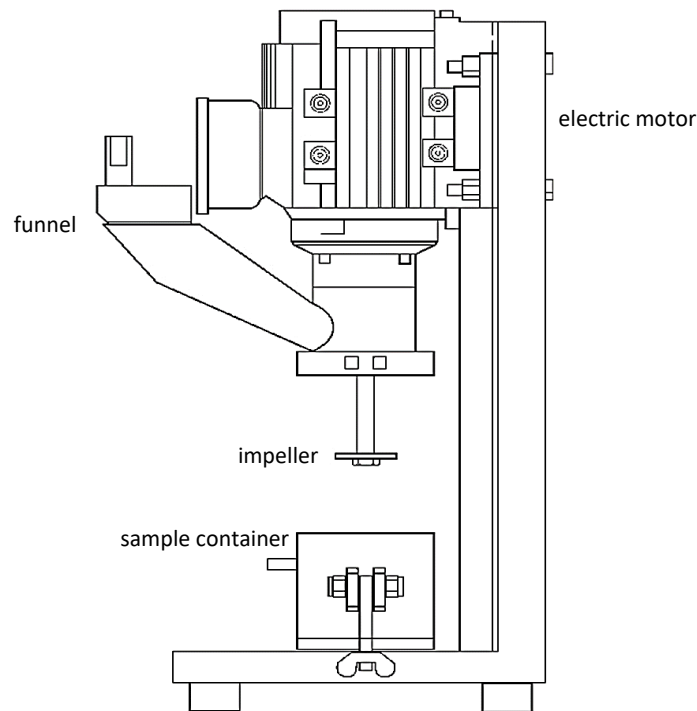


Fig. 15: Sketch of the abrasimeter for the determination of the LCPC Abrasivity Coefficient (LAC) and LCPC Breakability Coefficient (LBC) mod. after KÄSLING & THURO (2010).

### Testing analysis

The rotation of the impeller during the abrasion test caused the steel to wear and erode on the edges and surfaces. This made the impeller lighter. The examined rock material was also worn and the grains were crushed within the sample container. The LCPC Abrasivity Coefficient (LAC) was investigated by the loss of mass of the metal impeller during this test (Eqn. 23).

Eqn. 23: Calculation of the LCPC abrasivity coefficient (LAC).

$$LAC = \frac{m_{F0} - m_F}{m_T} \quad (\text{Eqn. 23})$$

with:	LAC	LCPC abrasivity coefficient	[g/t]
	$m_{F0}$	mass of the metal impeller prior the test	[g]
	$m_F$	mass of the metal impeller after the test	[g]
	$m_T$	total mass of the sample	[t]

The LAC for rocks ranges from 0 to 2,000 g/t typically. The LAC range is defined by 6 classes and can be correlated with the CAI-classification (see Tab. 2:). The CAI shows an almost linear correlation to the LAC (THURO et al. 2006; THURO & KÄSLING 2009).

Tab. 2: Classification of the LCPC Abrasivity Coefficient (LAC) according to the Cerchar Abrasivity Index (CAI) and related rock type examples mod. after THURO et al. (2006).

LAC [g/t]	CAI [-]	Classification	Rock type examples
0–50	0.0–0.3	not abrasive	wood, turf
50–100	0.3–0.5	not very abrasive	clay-silt stone, marl
100–250	0.5–1.0	slightly abrasive	schist, sandstone (fine grained, argillaceous cement), limestone (pure), marble (pure)
250–500	1.0–2.0	medium abrasive	limestone (sandy), marble (containing quartz) sandstone (calcareous cement)
500–1,250	2.0–4.0	very abrasive	sandstone (siliceous cement), porphyry, andesite, basalt, phyllite, mica schist, some amphibolites
1,250–2,000	4.0–6.0	extremely abrasive	(vein-) quartz, granite, quartzite, eclogite, gneiss, some amphibolites

By sieving the analysed sample material and measuring the fraction below 1.6 mm, it is possible to determine the (LCPC Breakability Coefficient (LBC) (Eqn. 24).

Eqn. 24: Calculation of the LCPC breakability coefficient (LBC).

$$LBC = \frac{100 \cdot m_{1.6}}{m_T} \quad (\text{Eqn. 24})$$

with:	LBC	LCPC breakability coefficient	[%]
	$m_{1.6}$	mass fraction with grain size < 1.6 mm	[g]
	$m_T$	total mass of the sample	[t]

The LBC is classified according to BÜCHI et al. (1995) (Tab. 3).

Tab. 3: Classification of the LCPC breakability coefficient (LBC), as defined by BÜCHI et al. (1995).

LBC [%]	Classification
0–25	very poor
25–50	medium poor
50–75	medium
75–100	medium high
> 100	very high

A summary of all test results is given in the Appendix.

### 2.1.2 Numerical simulation

In order to get a first rough overview of the possibly prevailing conditions in a borehole, models are used. These are then refined during the course of the project with data from the underground. In this thesis a model was created to show the stress distribution in the near-field of a borehole and the depth of failure. The input parameters for the numerical modelling are the rock parameters determined in the parameter study. However, in order to be able to depict the stress conditions in the subsurface, in addition to the specific laboratory parameters, the in situ stresses from the regional stress field are also important for the stress models.

### Tectonic stress field

The Earth’s crust stress field is composed of the different magnitudes and directions of the three orthogonal to each other principal stress components (FJÆR et al. 2008): vertical stress ( $\sigma_V$ ), minimum horizontal stress ( $\sigma_h$ ) and maximum horizontal stress ( $\sigma_H$ ) (ZANG & STEPHANSSON 2010). The general approach is to assume a vertical-horizontal stress field, meaning that one principal stress is vertical ( $\sigma_V$ ) and the other two principal stresses are horizontal ( $\sigma_H$  &  $\sigma_h$ ) (FJÆR et al. 2008).

The orientation and magnitude of the stresses are influenced by the prevailing geology and tectonics and can therefore assume different stress states (maximum principal stress ( $\sigma_1$ ), intermediate principal stress ( $\sigma_2$ ) and minimum principal stress ( $\sigma_3$ )) according to ANDERSON (1951). In a normal faulting regime (NF), the vertical stress is the maximum principle stress. In a strike-slip regime (SS), the vertical stress is the intermediate principle stress. In a thrust faulting regime (TF), the vertical stress is the minimum principle stress (Tab. 4) (ZOBACK 2010).

Tab. 4: Relative stress magnitudes and faulting regimes mod. after ZOBACK (2010).

Regime	Stress		
	$\sigma_1$	$\sigma_2$	$\sigma_3$
NF	$\sigma_V$	$\sigma_H$	$\sigma_h$
SS	$\sigma_H$	$\sigma_V$	$\sigma_h$
TF	$\sigma_H$	$\sigma_h$	$\sigma_V$

The three categories of the Anderson faulting are shown in Fig. 16 and according to ZOBACK (1992) additionally a combination of the three types (NF with SS is NS and TF with SS is TS) were listed.

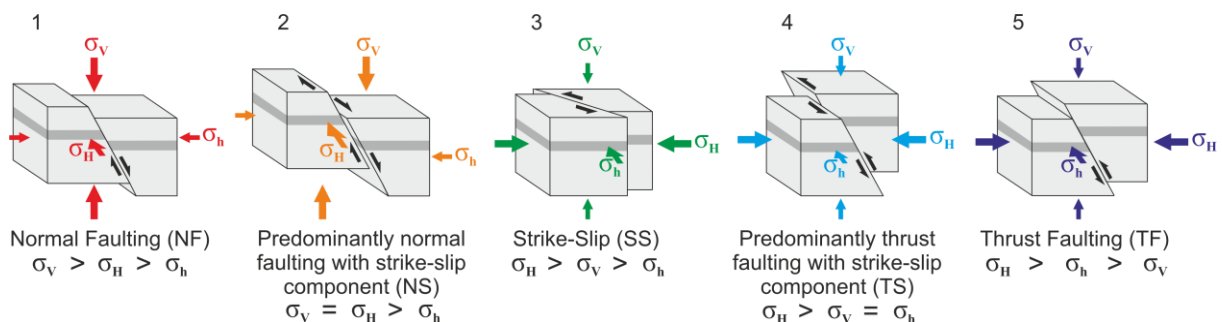


Fig. 16: The three stress regimes (NF, SS, TF) according to the Anderson classification and the combination of these regimes (NS & TS) mod. and extended after HEIDBACH et al. (2018).

The aim in subsurface construction, as in geothermal energy, is to identify the simplest and safest drilling path. This can be achieved by drilling through high strength rock that is only slightly stressed. In this way, the problems of stress concentration and the associated failure can be minimized (ZANG & STEPHANSSON 2010).

To achieve this, the determination of different in situ stress magnitudes and directions play a major important role. Integrating a density log over the vertical depth enables the estimation of the overburden stress (FJÆR et al. 2008; ZOBACK 2010). For density logs active gamma ray tools are needed which use the Compton scattering of gamma rays. This allows the electron density to be measured for each formation. Using lithological adjustments, the electron density is then transformed into rock density (FJÆR et al. 2008).

In this thesis the density of the rocks was determined by laboratory experiments (chapter 2.1.1). The magnitude of  $\sigma_V$  can be calculated (Eqn. 25) by integrating the bulk density with the particular true vertical depth (TVD)  $z$  of the core samples:

*Eqn. 25: Calculation of the vertical stress ( $\sigma_V$ ).*

$$\sigma_V = \int_0^z \rho_b \cdot g \cdot z \quad (\text{Eqn. 25})$$

with:	$\sigma_V$	vertical stress	[MPa]
	$\rho_b$	bulk density	[g/cm <sup>3</sup> ]
	$g$	Earth's gravitational acceleration	[m/s <sup>2</sup> ]
	$z$	depth of interest	[m]

In the hydrocarbon industry as well as in geothermal industry the horizontal stress directions are determined by well logs. It should be noted that well logs are used to document breakouts on the borehole wall after drilling and before logging.

A caliper log provides a presentation of the well diameter and therefore the shape of the well (ZOBACK 2010). With the help of the caliper tool the horizontal stress directions are estimated from the breakout orientations (FJÆR et al. 2008). This allows the identification of areas along the borehole wall that have been damaged.

The image log provides a complete, 360° picture of the borehole wall (FJÆR et al. 2008). This allows the different aspects of the borehole's geometry, such as fine structures like stratigraphic planes and the fracture network, to be identified (natural fractures and borehole induced fractures) (FJÆR et al. 2008).

In a vertical borehole where different horizontal stresses prevail ( $\sigma_H > \sigma_h$ ), two different failure modes are determined: compressive and tensile failure. Compressive failure is induced at low borehole pressure in the direction parallel to the lowest horizontal stress ( $\sigma_h$ ). This causes breakouts and an ovalization of the borehole. Tensile failure occurs at high borehole pressures in the direction parallel to the greatest horizontal stress ( $\sigma_H$ ). This will induce a fracture (FJÆR et al. 2008).

To determine the minimum horizontal stress ( $\sigma_h$ ), the pressure at the formation of a fracture as well as the pressure at which the fracture closes is recorded. The condition for this type of determination is that the fracture produced has penetrated far into the formation. This is to ensure that the formation

has only felt the horizontal stress occurring in situ. The determination of the maximum horizontal stress ( $\sigma_H$ ) is not as straight forward. One possibility is to determine this horizontal stress by means of a repeated fracture test. However, since the pressure to trigger this fracture is often lost in reality, this method is uncertain. Another possibility is an extended leak-off test. There, the pressure in the borehole is increased by increasing the volume at a constant rate. This yields a straight line of pressure versus volume (time), with the slope of the line given by the compressibility of the system (primarily the drilling fluid). The point where the pressure response starts to deviate from this straight line is defined as the leak-off point. This is actually the point where a fracture is starting to form.

The largest database for stress data is the World Stress Map. This contains 42,870 data points. This is a global compilation of information on current crustal in situ stress (HEIDBACH et al. 2010; HEIDBACH et al. 2016; HEIDBACH et al. 2018). To characterize the stress pattern of the crust and to understand the causes for these tensions is the goal of the World Stress Map (HEIDBACH et al. 2019). The stress information is mainly obtained from earthquake focal mechanism, borehole breakouts and borehole-induced tensile fractures as well as in situ stress measurements (HEIDBACH et al. 2019).

### Model geometry and meshing

In this thesis the numerical modelling was performed using the 2D finite element code RS2 from Rocscience. This program is used for a wide range of engineering projects such as the design and analysis of tunnels in soil and rock. Under the simple assumption that a vertical geothermal borehole is a tunnel, the currently available code (RS2 2019) was used. The model is a 2D section perpendicular to the drilling path.

In the “Geometry” tab, a model space of 20 x 20 m (Fig. 17, left) was selected for near-field modelling. In the center of the square a circle with a diameter of 15.24 cm (6”) (Fig. 17, right) was excavated. This represents the borehole. The size of the diameter was chosen analogous to the diameter in the open-hole section in the reservoir area from the project “Dolomitkluft” (THURO et al. 2019).

In the “Materials & Staging” tab, the material properties were defined for each scenario. The Initial Element Loading with “Field Stress Only” was selected as the initial condition for each scenario. The Stiffness Type is “Isotropic”. As Failure Criterion for all scenarios “Generalized Hoek-Brown” was selected.

In the “Loading” tab, the in situ stress field was created under the “Filed Stress Properties”. “Constant” was set as field stress type to generate an in situ stress field that is not variable with position or depth. This is the best way to check the respective rock properties per set depth. The maximum horizontal stress is “Sigma 1”, the minimum horizontal stress is “Sigma 3” and “Sigma Z” indicates the vertical stress. With the help of the “Angle” the direction of the maximum horizontal stress was fixed. This is measured counterclockwise between the positive x axis and the direction of “Sigma 1”. Likewise, with “Add Uniform Load” a water pressure or mud weight was generated inside the borehole. A magnitude of 9.8067 MN/m<sup>2</sup> was determined for different stages. This makes it possible to simulate an increase in water pressure or mud weight with depth, which acts against the applied in situ stress field.

In the “Mesh” tab the same mesh setup was set for all scenarios. The mesh type is “Graded” and the element type is “6 Noded Triangles”. The “Graduation Factor” is “0.02” and the “Default Number of Nodes on All Excavations” is “50”. This setting creates a tight mesh in the near-field of the borehole and increases the distance between the nodes in the far field. This eliminates an unnecessarily large number of elements and reduces the calculation time. The generated model has a 6 noded triangles count of 3,512 and a total of 7,312 nodes.

In the “Restraints” tab the outer edges were mechanically fixed. This is to prevent movements of the model's outer nodes that could affect the model.

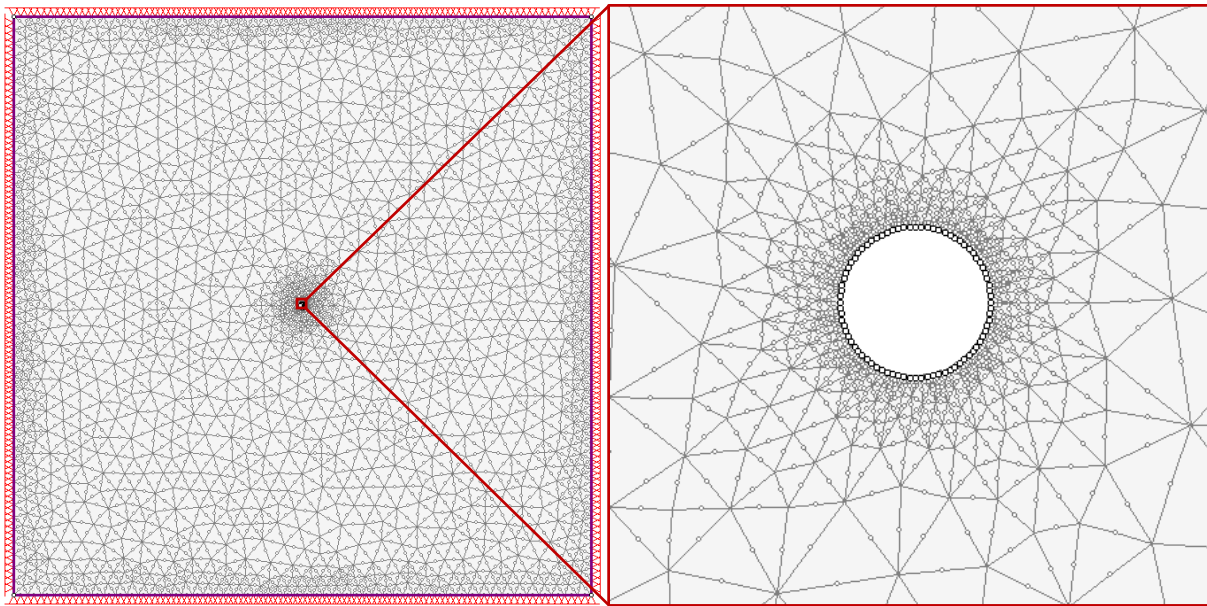


Fig. 17: Geometry and used mesh architecture of the model (20 x 20 m) (left) in RS2 without interfaces or rock boundaries with the 6" diameter borehole under investigation (right).

### Determination of the depth of failure

As wells are drilled deeper in geothermal energy projects, the process of brittle fracturing, which leads to borehole breakouts, is becoming increasingly important. In the Canadian Underground Research Laboratory (URL Mine-by experiment), the spalling in granite in an experimental tunnel was investigated using in situ stress measurements (MARTINI et al. 1997). It was found that spalling occurred during excavation and when these spillings were removed, further new spillings occurred. This can be explained by the stress changes during the drilling process by reducing the minimum horizontal stress in the wall to zero and increasing the maximum horizontal stress in the wall. MARTIN & CHRISTIANSSON (2009) recognized that the crack initiation stress can be taken as the lower limit for the spalling resistance. To determine the depth of failure, MARTIN et al. (1999) found out that it depends on the ratio of the maximum wall stress to the mean uniaxial compressive strength. It has been found that shallow fractures are generally associated with tensile failure, where thin fragments detach the tunnel surface. The maximum depth of fracture is reached when there is no change in the stress field. Since HOEK & MARTIN (2014) the calculation of the depth of failure was slightly changed in comparison to MARTIN et al. (1999), Eqn. 26 was taken from the later paper for further calculations.

Eqn. 26: Calculation of the depth of failure ( $d_f$ ) after HOEK & MARTIN (2014).

$$\left(\frac{d_f}{a}\right) = 1.25 \cdot \left(\frac{\sigma_{\max}}{\sigma_u}\right) - 0.51 \tag{Eqn. 26}$$

with:  $d_f$  depth of failure [cm]  
 $a$  borehole diameter [cm]  
 $\sigma_{\max}$  maximum borehole wall stress [MPa]  
 $\sigma_u$  uniaxial compressive strength [MPa]

and

$$\sigma_{\max} = 3 \cdot \sigma_H - \sigma_h \tag{Eqn. 26.1}$$

with:  $\sigma_{\max}$  maximum borehole wall stress [MPa]  
 $\sigma_H$  maximum horizontal stress [MPa]  
 $\sigma_h$  minimum horizontal stress [MPa]

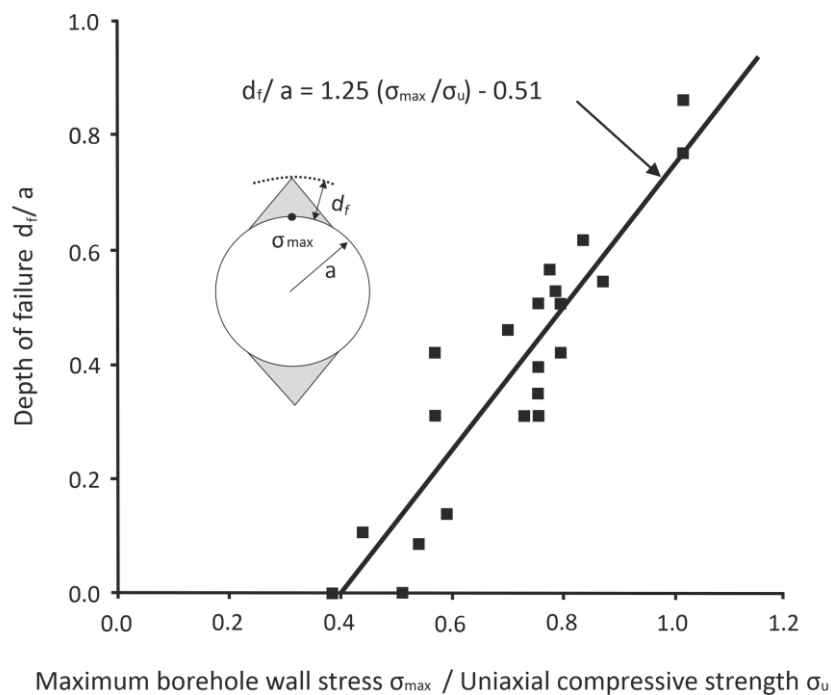


Fig. 18: The determined depth of failure plotted against the ratio of the maximum borehole wall stress to the uniaxial compressive strength after HOEK & MARTIN (2014).

The concept of the depth of failure shows, that borehole breakouts already occur, when the maximum stress level in a certain borehole depth reaches about 50 % of the uniaxial compressive strength. This typically correlates with the crack initiation point  $\sigma_{ci}$  of the stress-strain curve during uniaxial compression testing (Fig. 11).

Since this correlation was established in large diameter tunnel excavations rather than in small diameter boreholes and in crystalline rocks rather than in brittle carbonate rock types, it is not really sure if this concept is really applicable in geothermal wells. Nevertheless, it was also used by VALLEY (2007) to explain borehole breakouts in Soultz-sous-Forêts, but also in crystalline rock types.

## 2.2 North Alpine Foreland Basin, SE Germany

The most important thermal aquifer in Central Europe are the carbonates of the Upper Jurassic (“Malm”) in the North Alpine Foreland Basin, SE Germany (PASCHEN et al. 2003). This foreland basin is characterized by faults and fractures as well as by litho- and biofacies (MOECK 2014). The reservoir targets are faults and reef complexes (CACACE et al. 2013). This fractured and karstified aquifer forms a large contiguous hydrothermally accessible reservoir, which has been the site of the majority of hydrothermal geothermal development in Germany. The hydraulic properties of the Upper Jurassic aquifer change over the entire North Alpine Foreland Basin, SE Germany (BIRNER et al. 2012).

In Bavaria, the North Alpine Foreland Basin, SE Germany has been explored in recent decades through the drilling of water, hydrocarbon, thermal and geothermal wells (MRAZ 2019). With the Erding hydrocarbon well, the development of geothermal projects began in 1998 (AGEMAR et al. 2014a; DUSSEL et al. 2016). This well is now used as a source of geothermal energy. Since the first geothermal project in Unterschleißheim in 2003 many further wells were drilled (DUSSEL et al. 2016). At depths of about 2–3 km, the Upper Jurassic aquifer hosts waters with temperatures ranging between 65–130 °C (AGEMAR et al. 2014b). Besides temperature, the flow rate of hot water in the aquifer is also important for hydrothermal systems in the North Alpine Foreland Basin, SE Germany. In the Munich area high flow rates up to 140 l/s can be reached (AGEMAR et al. 2014b).

For this reason, Malm is extremely important for both heat supply and electricity generation (SCHULZ & THOMAS 2012). Megawatts electrical ( $MW_{el}$ ) refers to the electrical power produced by a generator, while megawatts thermal ( $MW_{th}$ ) refers to the thermal power produced by a generator. Currently, 25 successful geothermal projects in Bavaria extract heat from the reservoir and feed mostly district heating systems. Three of these geothermal projects are just electricity projects (www-12). These have a total capacity of 330  $MW_{th}$ . The ongoing project “Schäftlarnstraße” of the SWM is supposed to supply an additional 50  $MW_{th}$  (www-04). In addition, 34.7  $MW_{el}$  of electrical installed capacity is currently being fed into the grid (www-02).

### 2.2.1 State of the art

Knowledge about the Upper Jurassic strata in Bavaria is mainly based on outcrops in the Franconian and Swabian Alb (LEMCKE 1988). Since the 1950s and 1980s, the rocks of the North Alpine Foreland Basin, SE Germany have undergone intensive investigation during hydrocarbon exploration (BACHMANN et al. 1981; LEMCKE 1979). During the course of geothermal exploration, interest in these carbonate rocks of the Upper Jurassic has been reawakened. Due to the increased exploration activities for the economic use of the Upper Jurassic aquifer, various studies on reservoir characterization have been conducted in the past (BÖHM et al. 2010; 2011; 2012; 2013; BIRNER et al. 2012; KOCH et al. 2009; KOCH et al. 2010; MRAZ et al. 2018).

For this purpose, in various research projects, intact rocks from outcrops in the Franconian and Swabian Alb in southern Germany as well as drill cuttings and a few drill cores have already been petrophysically examined to better characterize the carbonate reservoir rock of the North Alpine Foreland Basin, SE Germany (BACKERS et al. 2017; KOCH et al. 2009; SCHNEIDER 2012; SCHULZ & THOMAS 2012; THURO et al. 2019; WOLFGRAMM et al. 2018). In this thesis only projects are mentioned which were mainly concerned with a geomechanical reservoir characterization in the North Alpine Foreland Basin, SE Germany.

“Since BARTON et al. (1995) found that critical fractures are more often hydraulically active than uncritically stressed fractures, the geomechanical reservoir parameters describing the field of tension are important for the exploration of geothermal projects” (POTTEN et al. 2019b). Nevertheless, the geomechanical parameters of the Upper Jurassic, were not sufficiently recorded. A few parameter studies were carried out and they are explained in the following.

In the Mauerstetten hydrothermal well the carbonate rocks of the Upper Jurassic aquifer didn't show sufficient permeability. This well should be converted into a petrothermal project within the framework of the “Allgäu 2.0” research project (AMRO et al. 2014). TONDERA et al. (2013) carried out the laboratory experiments on three analogue materials from the southern Franconian Alb to develop an adapted stimulation concept to improve the hydraulic pathways (AMRO et al. 2014). In addition to strength parameters (uniaxial, triaxial as well as Brazilian tensile tests) the petrophysical properties (porosity and permeability) of the rocks were examined. The parameter study showed that the permeability of the rock and thus the reservoir production in Mauerstetten can be increased by shear fractures (TONDERA et al. 2013).

In the extensive outcrop analogue study of the Upper Jurassic reservoir (HOMUTH & SASS 2014; HOMUTH et al. 2015), mainly petrophysical properties were determined. Several samples from outcrops and shallow boreholes in the Swabian and Franconian Alb, as well as deep boreholes from Malm reservoir were investigated (Moosburg SC 4, Geretsried GEN 1) (HOMUTH 2014). With the help of the developed value ranges of the thermophysical and hydraulic rock parameters, a statistically validated database was created (HOMUTH 2014). This allows a more reliable reservoir prognosis when different models (tectonic, hydraulic and thermofacial) are combined (HOMUTH et al. 2015). In total, 51 samples were also subjected to uniaxial compression tests on analogue material. The mud- and wackestones showed a mean value of 182 MPa and the rud-, float- and grainstone samples showed a mean value of 119 MPa

(HOMUTH 2014). It was also found that the processed samples had the highest compressive strengths on mean in Malm alpha to gama and lower compressive strengths in Malm Delta to Malm Zeta. In the lithofacial classification of the results it was determined that the bench limestones show greater variations than the dolostones (HOMUTH 2014). These results were correlated with the determined porosities and were attributed to them. Overall HOMUTH (2014) concluded that due to the small number of samples only a limited interpretation is possible.

In the research project “PrognosPermae” (ALBER et al. 2019) analogue material (dolostone and limestone) from two outcrops from the southern Franconian Alb were investigated (HEDTMANN & ALBER 2017; HEDTMANN & ALBER 2018). Analogue material to the Kirchweihdach well was investigated because no drill cores were taken. The aim was to determine hydrogeomechanical parameters of carbonates of the Upper Jurassic (Malm) of the North Alpine Foreland Basin, SE Germany. HEDTMANN (2020) performed ultrasonic tests, uniaxial compression tests (45 limestone and 40 dolostone samples) and the Brazilian tensile tests (44 limestone and 42 dolostone samples). The aim was to determine the possible impact of scale on the rock properties. To that aim, the experiments were performed with different sample sizes (HEDTMANN 2020) The laboratory study showed that the hydrogeomechanical properties of the carbonates are size independent and that an extrapolation of the laboratory results to in situ conditions is possible (HEDTMANN 2020).

In the context of the joint project “Dolomitkluft” analogue samples were examined sedimentologically, petrophysically and also geomechanically (THURO et al. 2019). The investigated analogue samples should be comparable by the lithology and facies to the carbonate reservoir rocks of the Upper Jurassic to the geothermal well Geretsried GEN 1 ST (MRAZ et al. 2018). The analogue samples were taken from eleven quarries and outcrops in the southern Franconian Alb, the south–eastern Swabian Alb and at the Kanisfluh in Vorarlberg. One aim of the project was to determine geomechanical parameters of both analogue samples from the Upper Jurassic and cores from the newly drilled sidetrack GEN-1ST-A1 (STOCKINGER et al. 2019). A total of 109 uniaxial compression tests, 124 Brazilian tensile tests and ultrasonic tests were carried out on the analogue carbonates (THURO et al. 2019). Only eight of the cores that had been drawn could be subjected to ultrasonic tests (THURO et al. 2019). The cores had been disassembled during the drilling and pulling process (THURO et al. 2019). It was found that the strength is influenced by porosity and small fractures. The uniaxial compressive strengths are between 80 MPa and 250 MPa and the Brazilian tensile strengths are between 5 MPa and 11 MPa. The investigated carbonates all showed very brittle fracture behaviour (THURO et al. 2019). Using geomechanical modelling it was determined that cracks occur in a radius of 50 cm around the borehole. There is almost no shear offset, which, in addition to the facies present, is responsible for the low water inflow in the well (THURO et al. 2019).

In the above-mentioned studies, mainly analogue outcrop samples and drill cuttings of some boreholes were examined. Only a few selected core samples of the buried reservoir were petrophysically examined for reservoir characterization. The common goal of these studies was to correlate the petrophysical properties of cuttings/drill core or outcrop samples of a single stratigraphic layer to different areas of the aquifer within the North Alpine Foreland Basin, SE Germany. However, the high heterogeneity

in the depositional sequences of Malm is the major problem when it comes to correlating these data with the entirety of the Upper Jurassic aquifer.

## 2.2.2 Geological setting

In total, the entire wedge-shaped North Alpine Foreland Basin extends more than 1,000 km in an East–West direction North of the Alps. The North Alpine Foreland Basin, SE Germany is part of this basin. At its widest point in Bavaria, the North Alpine Foreland Basin, SE Germany has a North–South extension of 130 km and stretches 250 km East to West. The North Alpine Foreland Basin, SE Germany is bounded to the North by the Swabian–Franconian Alb. In the South, it is bounded by the mountain ranges of the Alps (HOMUTH 2014) and the Folded Molasse. To the West and East, the boundaries of the North Alpine Foreland Basin, SE Germany are formed by the French Folded Jura and the Bohemian Massif (BACHMANN et al. 1987). The boundaries of the North Alpine Foreland Basin, SE Germany to the Bohemian Massif in the East and the Alps in the South are fault systems (LEMCKE 1988).

The carbonate reservoir of the Upper Jurassic lies above the crystalline basement (KUHLEMANN & KEMPF 2002) is overlaid by Cenozoic sediments. As can be seen from the asymmetric basin (BACHMANN et al. 1987) (Fig. 19), the Upper Jurassic rocks, which are important for geothermal energy, dip slightly to the South with an inclination of about 2.5° (SYMANK 2020). These strata are exposed to the North and out-crop to the surface in the Swabian–Franconian Alb (HENNINGSEN & KATZUNG 2011; LEMCKE 1988). At the northern edge of the Alps, the Mesozoic layers can reach depths of approximately 5,000 m (BACHMANN et al. 1987).

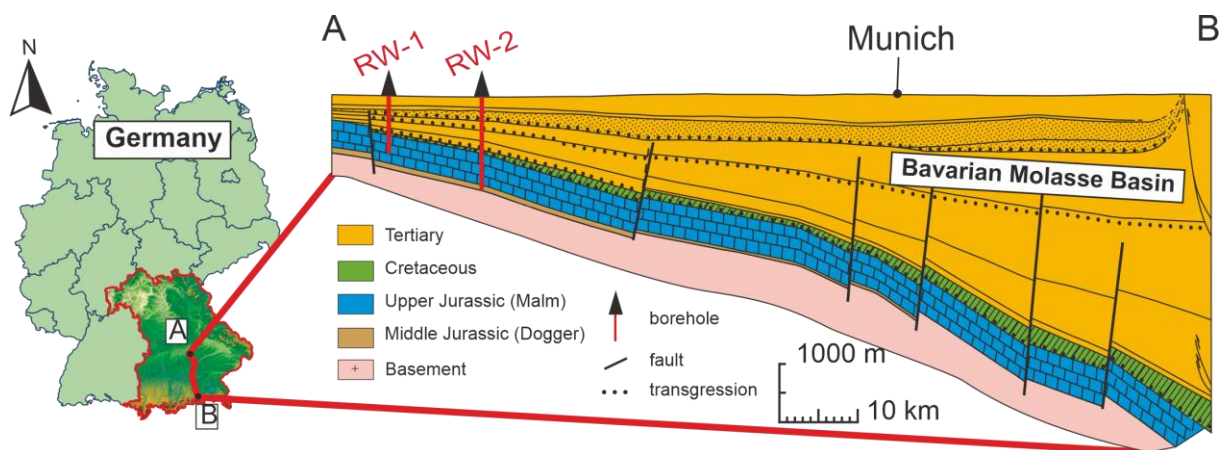


Fig. 19: Cross section through the North Alpine Foreland Basin, SE Germany from *www-23*; *www-24* (left) and *StMWi* (2019b), mod. after LEMCKE (1988) (right).

The stratigraphy of the deeper parts of the North Alpine Foreland Basin, SE Germany can be grouped into three separate deposition phases. The classification of these phases is according to the age of origin and the lithology existing at that time. The deepest part is occupied by the Paleozoic basement, which consists mainly of crystalline rocks of the Bohemian Massif and sediments of the Upper Carboniferous and Permian (BACHMANN & MÜLLER 1996). In the period between the Upper Carboniferous and the end of the Middle Permian, the Hercynian basement was eroded. The resulting continental land with few ridges is called Vindelician ridge (LEMCKE 1988). Then there was a marine transgression from

the North at the end of the Permian, where primarily carbonates and claystones were sedimented (BACHMANN et al. 1987).

The second phase is formed by the deposition of Mesozoic sediments. From early Triassic to Jurassic periods the deposition fluctuated constantly between terrestrial, shallow marine and marine environments (WALTER & DORN 2007). The slowly sinking Vindelician Ridge was successively covered with Mesozoic sediments. Gradually the sea encroached from the NW and covered the land. At the beginning of the Lower Triassic the mainland was not flooded and fluvial sediments were deposited (DOPPLER et al. 2004). At the beginning of the Upper Triassic, sandstone, mudstone and dolomite were deposited as the proportion of continental Vindelician ridge increased. Afterwards gypsum and evaporation of anhydrite took place and claystone, marlstone and sandstone were deposited (DOPPLER et al. 2004). During the Lower Jurassic, the shallow sea slowly flooded from North to East (BACHMANN et al. 1987) and clayey marls and clays were deposited (LEMCKE 1988).

During the Middle Jurassic, the sea continuously advanced further and limestone as well as sandstone layers, were deposited (DOPPLER et al. 2004). During the Upper Jurassic, an up to 600 m in thick limestone–marl sequence was deposited (BACHMANN et al. 1987; MEYER & SCHMIDT-KALER 1989; MEYER & SCHMIDT-KALER 1996) which has become key for the geothermal use of the North Alpine Foreland Basin, SE Germany.

The Upper Jurassic aquifer is a reservoir for thermal water stored in pore spaces and fractures (BIRNER 2013). In southern Germany, the stratigraphic term “Malm” according to OPPEL (1858) is no longer valid. In geothermal energy, however, it is still used for the geological period of the Upper Jurassic as well as for the deposited rocks of this period (BÖHM 2012). The term Upper Jurassic aquifer includes Purbeck Formation and the underlying carbonate rocks of the Upper Jurassic (BIRNER 2013).

Purbeck is a common term for an interbedded strata of mudstone, limestone and evaporite. The beginning of the deposition was at the end of the Tithonian (www-13; PIENKOWSKI et al. 2008). In northern Germany, the Upper Jurassic is subdivided according to the ammonite biostratigraphic units (Lias, Dogger and Malm). This categorization is also used for the lithostratigraphic division of southern Germany and is additionally subdivided into Malm Alpha ( $\alpha$ ) through Malm Zeta ( $\zeta$ ) according to QUENSTEDT (1858) (Fig. 20). For comparability with the academic literature, all these terms are used in this thesis.

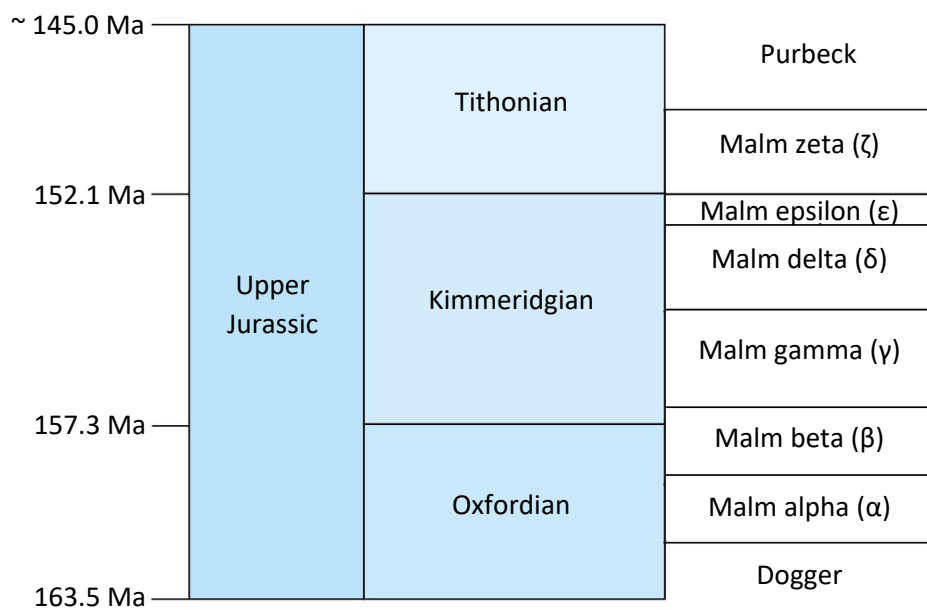


Fig. 20: Lithostratigraphic units of the Upper Jurassic important for geothermal energy mod. after COHEN et al. (2013; updated).

During the Upper Jurassic, the encroachment of the shallow sea ceased leaving the entire area and the southern Vindelician ridge flooded. The most recent deposit of the Malm is the Malm  $\alpha$ . Within the North Alpine Foreland Basin, SE Germany, the Franconian–South Bavarian platform began to develop. East of this platform, a NW–SE oriented sponge bed formed (MEYER & SCHMIDT-KALER 1989).

In a calm and shallow sea, thick carbonate layers were deposited during Malm  $\beta$  to Malm  $\delta$  (MEYER & SCHMIDT-KALER 1989). The reef development reached its peak at the end of Malm  $\delta$ . This is due to the sea level gradually receding. A margin consisting of debris from corals and reefs developed in the East of the Franconian–South Bavarian platform (MEYER & SCHMIDT-KALER 1989). Inner basin-like areas with stratified carbonates were formed as the sea level continued to fall during Malm  $\epsilon$ . During Malm  $\zeta$  high carbonate layers formed and the corals were replaced by sponges. The depositional environment changed into brackish sea ended in the Upper Jurassic with a maximum regression surface. In Purbeck the reefs died off and the typical fine dolomite layers were deposited. These layers are very similar to the carbonates of Malm  $\zeta$ .

Then the flooding of the North Alpine Foreland Basin, SE Germany ended and the basin was exposed to weathering. This can be seen today in erosion and karst formation (LEMCKE 1988). Both, the erosion intensity and the karst level decrease from the northern to the southern part of the basin due to the longer exposure time of the northern area. For this reason, the thermal water mainly flows through the local fault systems and the permeability decreases towards the Alps. Diagenesis and the existing karst phenomena ensure good conductivity and productivity of Malm carbonates. The total thickness of Malm formation, the reservoir depth, and the water temperatures increase from North to South (LEMCKE 1988).

Malm carbonates can be subdivided into two main facies classes: the bedded facies and the massive facies. The classification is made according to the depositional environment and main organisms found

there (MEYER & SCHMIDT-KALER 1989). The bedded facies was mainly sedimented in the basin as limestone with alternating layers of marlstone (MRAZ 2019). The limestones and dolomitic sediments of the massive facies are more susceptible to karstification and can be distinguished by reefs, patch reefs and mud mound-building organisms (KOCH et al. 1994; MEYER 1994).

At the end of the Cretaceous, a transgression from the South with the deposition of sandstone, marlstone and claystone took place. These sediments are preserved in karst caves and tectonic depressions (DOPPLER et al. 2004; RICHTER 1985).

The third phase is defined by the sedimentation of Molasse deposits. At the end of the Upper Cretaceous, the collision of the European and Adriatic plates is directly related to the origin of the Molasse (SCHMID et al. 2004). Due to Alpine orogeny the North Alpine Foreland Basin, SE Germany was reshaped into a foreland basin during the Palaeogene and Neogene. In two major cycles terrestrial and marine sediments were deposited. These are the marine Molasse and the freshwater Molasse. This stratification is the result of the synergy of basin subsidence, transgression and regression of the Paratethys sea and sediment transport (LEMCKE 1988; WOLFGRAMM et al. 2015).

### **Tectonic stress field**

In addition to the described lithology of the Upper Jurassic aquifer, the tectonic stress field, with its acting forces, also has a major influence on the productivity of a geothermal project. The tectonic stress regime around a well is characterized based on the relationship of the three principal stresses to each other. In the North Alpine Foreland Basin, SE Germany, the stress regime varies locally, on different scales and over different time periods. It is therefore uncertain (REINECKER et al. 2010; SEITHEL et al. 2015; ZIEGLER et al. 2016; DREWS et al. 2018) and currently under discussion (ZIEGLER & HEIDBACH 2020). Evidence for this is provided by various borehole data as well as structural geological interpretations and depth/lithology dependent changes (BACHMANN et al. 1987; HERGERT et al. 2015; UNGER 1999).

Older studies suggested from the derivation of geotechnical in situ stress measurements (ILLIES & GREINER 1978) that the current tectonic regime is situated between strike-slip and thrust faulting (LEMCKE 1988). However, the determined stress field is not representative of the undeformed Foreland Molasse because these measurements were made in the area between the Folded Molasse and the Foreland Molasse (DREWS et al. 2018). Some authors prefer normal faulting regime (BACHMANN et al. 1987; DREWS et al. 2018; 2019c; 2020; REINECKER et al. 2010) whereas other authors assume a normal faulting to strike-slip regime (BUDACH et al. 2018; BACKERS et al. 2017) or a strike-slip regime (MEGIES & WASSERMANN 2014; SEITHEL et al. 2015).

By analysing the focal mechanisms of induced seismicity in the crystalline basement of the North Alpine Foreland Basin, SE Germany, MEGIES & WASSERMANN (2014) proposed a strike-slip stress regime. The previously published stress regime indicators which suggest a strike-slip to normal faulting regime are from the Swiss part of the North Alpine Foreland Basin (HEIDBACH & REINECKER 2013; ZIEGLER et al. 2016). With the help of evaluating borehole data within the World Stress Map Project (HEIDBACH et al. 2018; REINECKER et al. 2010) and determining borehole breakouts, the stress regime was deviated and

a  $\sigma_H$ -orientation perpendicular to the Alpine thrust front was specified (HEIDBACH & REINECKER 2013; REINECKER et al. 2010).

Overall, there is a high degree of agreement for the approximate directions of the principal horizontal stress component (DREWS et al. 2018). The magnitudes of the principal horizontal stresses were estimated only by formation integrity tests and with the help of the stress polygon according to ZOBACK et al. (2003) (SEITHEL et al. 2015). Furthermore, with the help of image log interpretation it was found that there may be different stress regimes for the Mesozoic in the area south–east of Munich (SEITHEL et al. 2015). By using the image log database of ten wells, SEITHEL (2019) analysed the distribution of borehole failure mechanisms of the Upper Jurassic reservoir. SEITHEL (2019) derived stress field information and interpreted a strike-slip stress regime with  $1.1 < \sigma_H/\sigma_V < 1.56$  (SEITHEL 2019).

DREWS et al. (2019c) summarised the current knowledge of the stress regime in the North Alpine Foreland Basin, SE Germany and noticed that it varies. The Cenozoic basin fill is characterized by a normal-faulting regime (DREWS et al. 2019c). A normal-faulting to strike-slip stress regime is dominating in the Mesozoic sediments (BUDACH et al. 2018; SEITHEL et al. 2015). According to MEGIES & WASSERMANN (2014) there is a strike-slip stress regime in the crystalline basement. By using a formation integrity test and a leak-off test as well as cementation pressure from 46 deep geothermal boreholes the  $\sigma_H$ -magnitude was determined. It was noted that there is a change of the  $\sigma_H$ -gradient and the frictional equilibrium (DREWS et al. 2019c):

- clay-rich Cenozoic layers:  $\sigma_H$  of 16.5 MPa/km, frictional equilibrium with  $0.2 < \mu < 0.4$
- limestone to marl dominated Purbeck:  $\sigma_H$  of 15.5 MPa/km,  $\mu_i$ : with  $0.4 < \mu < 0.6$
- Upper Jurassic:  $\sigma_H$  of 14 MPa/km,  $\mu_i$ :  $0.4 < \mu < 0.6$ .

This shows that the sedimentological composition per lithology determines the  $\sigma_H$  magnitude (DREWS et al. 2019c).

With decreasing distance from the Alpine thrust front and with increasing depth, the overpressure potential increases (DREWS et al. 2018; MÜLLER et al. 1988). South–east of Munich there is overpressure in the overlying rock of the North Alpine Foreland Basin, SE Germany (DREWS et al. 2018). In the Upper Jurassic, the pore pressure conditions change to “under”-hydrostatic reservoir conditions (BIRNER et al. 2012).

An overview of the available data from the World Stress Map is shown in Fig. 21. The created World Stress Map (www-22) shows, the current data in this area from the WSM database edition (HEIDBACH et al. 2016). The selected data quality of the map is A to C.

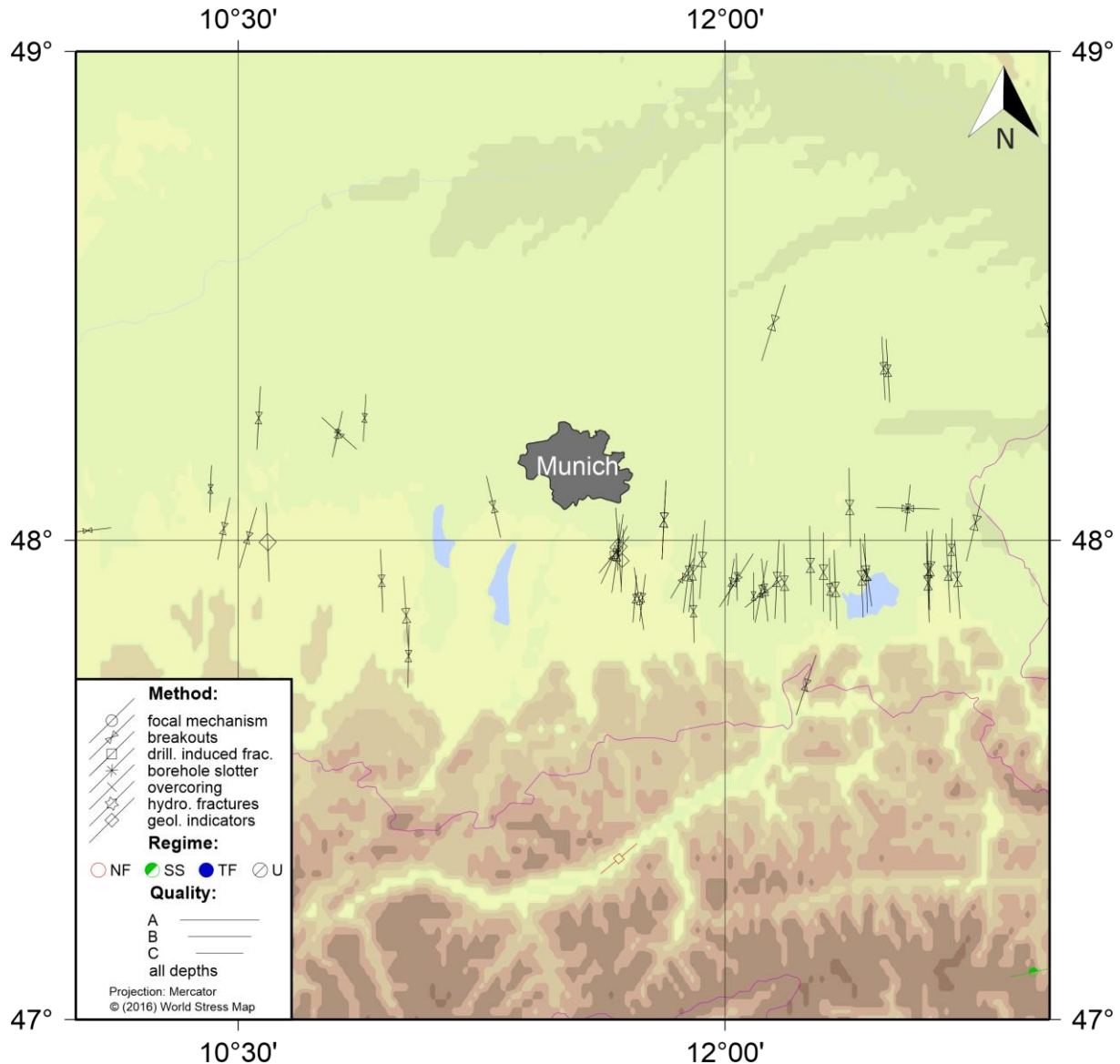


Fig. 21: An overview of existing data from the World Stress Map in the North Alpine Foreland Basin, SE Germany created with CASMO (www-22) and modified.

### 2.2.3 Data, study area and sampling

Rare drill cores from the area of the hydrothermal reservoir close to Munich were sought. For this purpose, the open-access verification data list “Bohrungen\_ETRS89” of the Landesamt für Bergbau, Energie und Geologie (LBEG) with 20,996 drilled boreholes (Fig. 22, left) and wells in Germany was evaluated (BRAUNER & HOSE 2019).

The coordinates of the boreholes and wells were used to locate where in Bavaria the drillings were sunk (Fig. 22, middle). Then the boreholes that were located were compared with the metadata of the Geothermal Information System (GeotIS) and extended by these (AGEMAR et al. 2014a; www-02). By using the online map service “UmweltAtlas Bayern” of the Bavarian Environment Agency (LfU) with the subject area “geology” and the content “drilling and springs” it was verified whether or not drill cores from different depths were available in the LfU drill core archive (LfU 2018; www-12). In addition,

a list of all Bavarian drill cores from the Upper Jurassic was requested from the LfU. Together with the requests of the other project partners, the project coordination of the GAB enquired collectively at the LfU as well as with the owners of old oil and gas wells via the Bundesverband Erdgas, Erdöl und Geoenergie e.V. (BVEG). This agreement gave GAB access to drill samples (Fig. 22, right), drilling reports and geophysical measurements (logs). Furthermore, it granted access to additional data at the South Bavaria Mining Office.

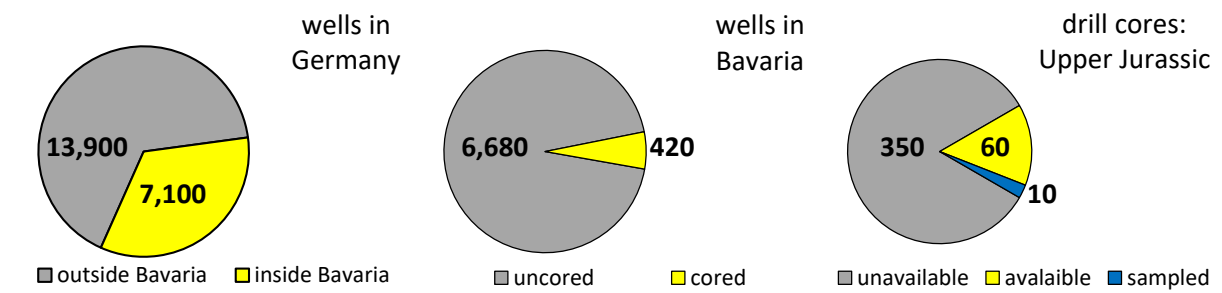


Fig. 22: Overview of the research of drill cores and the finally accessible core samples from the oil and gas industry for this work.

The research project “GeoMaRe” being conducted with SWM’s ongoing geothermal energy project “Schäftlarnstraße” enabled investigations on drill cores from the centre of Munich.

Drill cores of the Upper Jurassic were taken from two rare cored boreholes in the drill core archive of the LfU in Hof on five different days (02.03./03.04./18.05./02.08./03.08.2017). Seven other cored former oil and gas wells were investigated in a sampling campaign on 04.02.2019 and 05.02.2019 at the DEA drill core archive in Wietze. The plugs from the last oil and gas well were examined at the end of February 2019. Those were supplied by the company Neptune Energy GmbH for non-destructive testing. It was also possible to analyse non-destructively the latest cored drill samples from the two side-wall coring runs from the drilling site “Schäftlarnstraße” (SWM).

General information and the geological descriptions of the different wells/borehole are summarised in the following chapter of the respective well/borehole. The Upper Jurassic reservoir rocks were sampled and geomechanically investigated at depths ranging from 243 m to 5,225 m. Eleven cored wells are being processed for reservoir characterization of the Upper Jurassic (Fig. 83). Two of these cored wells are research wells (RW-1 & RW-2) located north-east of Munich. Eight of the wells being investigated are wells from the oil and gas industry. Two wells are located north of Munich: W-3 and W-4. Four other wells are located southwest of Munich: W-5, W-6, W-7 and W-8. The well (W-9) is located southwest of the Peisenberg and one well (W-10) from the eastern molasse is located north of Garching an der Alz. In addition, the SWM allowed borehole samples (B-11) from the ongoing geothermal energy project “Schäftlarnstraße” to be examined in association with the research project GeoMaRe. As can be seen from the position of the wells, it should be possible to establish a correlation between the individual wells. This correlation will be completed with the latest SWM drill cores from the centre of Munich. The two wells which are not located in the Munich area were selected for the following reasons. The W-9 well was chosen to get material properties from a deep well in Bavaria. The W-10 well was selected in order to obtain material with characteristic properties also from the Eastern Molasse in the interesting area around the new geothermal well Garching an der Alz. The following figure (Fig. 23) shows an overview of the location of the examined wells/borehole.

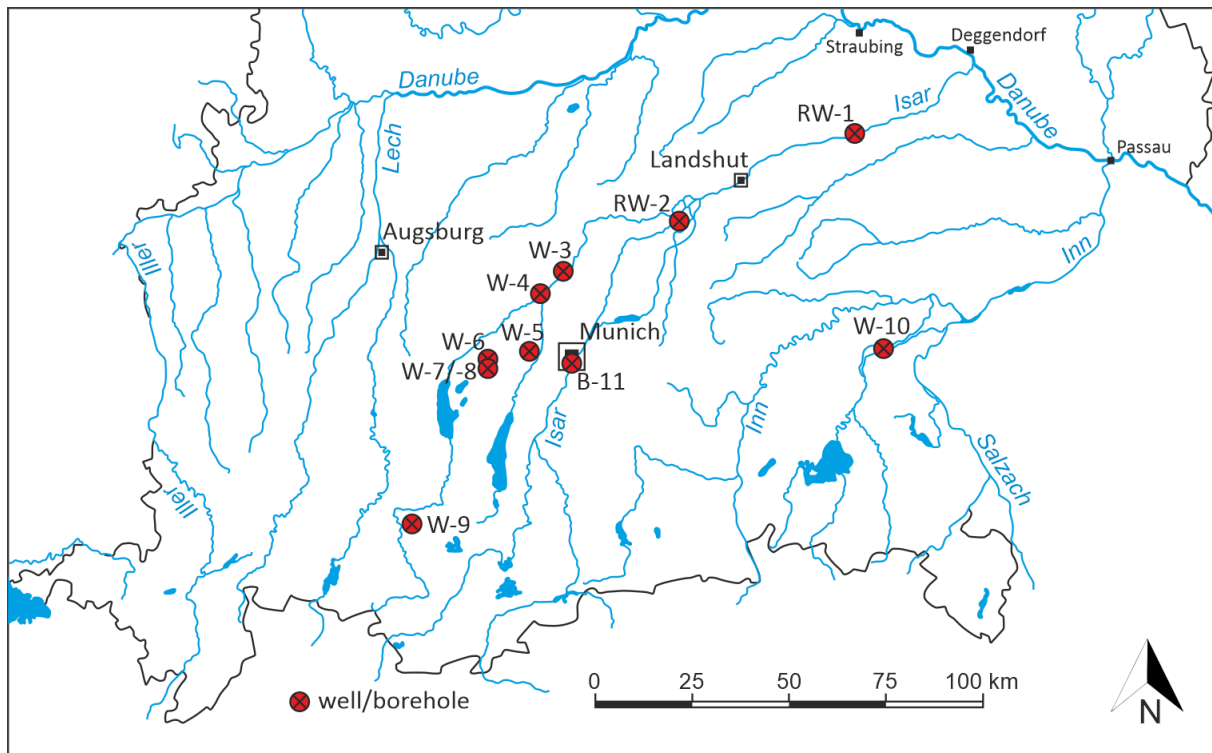


Fig. 23: Overview of the investigated core samples of the wells in the North Alpine Foreland Basin, SE Germany.

After the acquisition of the drill cores, the project partner from the Eberhard Karls University of Tübingen described the sequence stratigraphy, lithology and microstructures of the complete drill core material. The facies description and a detailed characterisation of each individual core sample was carried out with the project partner the Chair of Hydrogeology of the TUM. In addition to this description, the components, pore types and other characteristics of the samples were determined in this cooperation. These characteristics can be grouped in five different groups; open fissures/fractures, healed fissures/fractures, small vugs, large vugs and stylolites.

To obtain a representative dataset for the entire Upper Jurassic reservoir, the core samples were collected from varying stratigraphic intervals, lithologies and facies along the drill cores. Nevertheless, the sample intervals had to be adapted to the quality of the drill core yield and the presence of drill sample fragmentation and dinking. From the original drill core, the test core samples were drilled parallel to its vertical axis. The drilled samples have a diameter of 50 mm (BOHNSACK et al. 2019).

The LfU overdrilled the selected drill cores in its laboratory, located in the drill core archive in Hof, and provided them for further processing. The selected core samples released from the wells of the BVEG were delivered intact to the TUM for further sample preparations. Before and after overdrilling all drill cores were examined. The top and bottom of each core sample was marked with an arrow pointing to the bottom. Since all drill cores were not sampled oriented at the time of the drilling, at least one axis could be determined in this way.

All drill samples were stored and will be returned to the respective owners and stored there after completion of this thesis. These samples are representative of the reservoir rocks and the most reliable source of information for reservoir research (TAVAKOLI 2018).

## 2.2.4 Results

It should be noted that not all laboratory tests could be performed on all core samples taken. Only non-destructive tests could be carried out on well W-10 and borehole B-11. These samples were returned to the owners completely intact. Due to the uniqueness of all the core samples of the Upper Jurassic aquifer, no destructive LCPCT were conducted. As a result, the core samples have been crushed in such a way that no one would be able to perform a new analysis in the future. In addition, no PLT could be carried out as all drill cores examined were drilled with a small drill bit. As a result, the drill cores examined were too small in calibre to be able to perform this type of test.

For the determination of the V-Moduli of the North Alpine Foreland Basin, SE Germany core samples from a small range of the pre-loaded linear stress-strain curve were selected. This was also applied to the E-Moduli in the linear reloaded range of the curve. This small determined range is an important part of the linear-elastic range of the stress-strain curve when determining the respective moduli. This is to ensure that the non-linear part of the stress-strain curve is not included in the determination of the V-Moduli or the E-Moduli.

The porosities have to be divided based on wettability. The HEP measured porosities represent the maximum effective porosity and the WIP measured porosities represent the minimum effective porosity of the core samples (BOHNSACK et al. 2020). Likewise, the densities of all the core samples were provided and used for this thesis.

To start, every well/borehole is characterized individually. A short synopsis about the drilled well/borehole location as well as a description of the examined core samples is provided. Furthermore, there is a figure of a stress-strain curve of a characteristic sample of the borehole and a short description of it. For each well/borehole, the key parameters (min., mean, med. & max.) are listed in a table and two figures show the distribution of relevant parameters per depth. This is intended to provide a first overview of the parameters determined in the area of the drilled well/borehole and to get a rough parameters overview of the conditions and distribution in the desired area for future geothermal projects.

The number of tests which could be performed for the North Alpine Foreland Basin, SE Germany in each well/borehole is listed in Tab. 5.

Tab. 5: Overview of the tests performed in the North Alpine Foreland Basin, SE Germany.

Well/borehole	Number n (samples)	UT ( $v_p$ )	UT ( $v_s$ )	UCT	BTT	PLT	CAIT	LCPCT
RW-1	49	588	196	28	21	-	21	-
RW-2	249	2,970	992	164	191	-	191	-
W-3	22	132	44	13	23	-	23	-
W-4	27	162	54	19	16	-	16	-
W-5	13	78	26	12	13	-	13	-
W-6	5	30	10	2	4	-	4	-
W-7	11	66	22	8	5	-	5	-
W-8	16	96	32	10	11	-	11	-
W-9	9	54	18	7	16	-	16	-
W-10	26	156	52	-	-	-	-	-
B-11	22	132	44	-	-	-	-	-
Number n (total)	449	4,464	1,490	263	300	-	300	-

## Research well RW-1

The research well RW-1 was drilled in 2014 and is located in the district town Dingolfing. This well has a total vertical depth of 473 m (www-12) and was part of a project for the storage of thermal energy in the reservoir section (BOHNSACK et al. 2020; UECKERT & BAUMANN 2019). Malm aquifer was cored in several intervals and in this thesis the drill samples between 243 m and 472 m were examined. 49 samples were stratigraphically prepared from Malm  $\zeta$  4–5 to Malm  $\delta$ . The most common characteristics found in the samples are open fissures and small vugs. Dolomitized limestones and limestones can be found in the top and dolostones in the rest of Malm aquifer section. The facies of the dolomitized limestones is wackestone with bioturbation components (Fig. 24). The facies of the limestones is grainstone with peloidal and fossiliferous components. The crystalline dolostones vary in their appearance at the bottom of the well and show changes in their crystal size (idio-xenomorph).

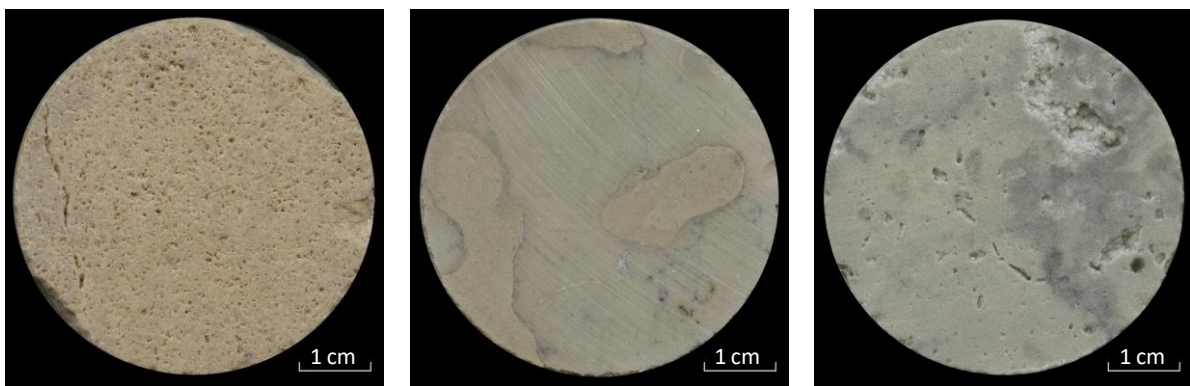


Fig. 24: Left: limestone (peloidal, fossiliferous grainstone (259 mTVD)); middle: dolomitic limestone (bioturbated wackestone (243 mTVD)); right: medium crystalline dolostone (464 mTVD).

Fig. 25 shows a typical stress-strain curve of the well RW-1. Clearly visible is the long linear course of the axial strain and the very low lateral strain. At about 95 % of the axial strain a slight curvature is formed and the failure is spontaneous. In this well, the mode of failure is mostly axial splitting which is characterized by some vertical cracks splitting the sample.

A total of 49 UT, 28 UCT (0 preliminary tests and 28 main tests), 21 BTT as well as 21 CAIT were carried out from the prepared core samples.

Tab. 6 shows the determined key parameter values of the tests performed.

Fig. 26 illustrates the distribution of ultrasonic velocity and UCS values of differently saturated core samples at different depths.

A summary of all test results of the well RW-1 is given in the Appendix.

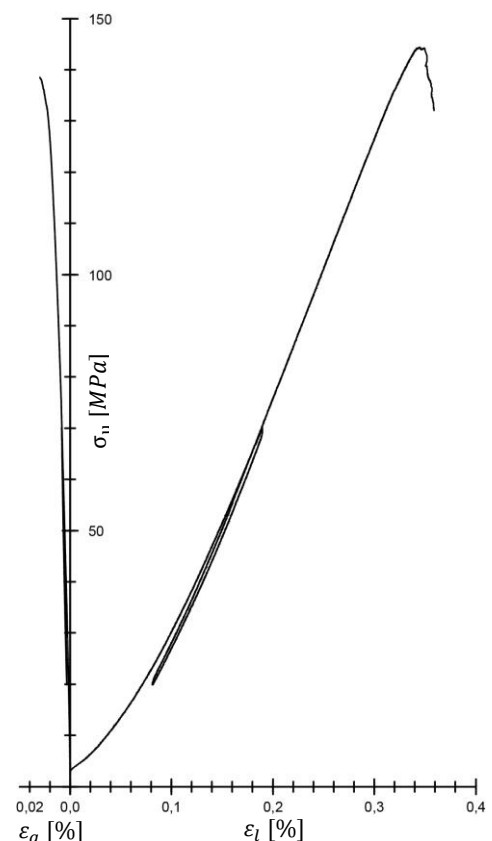


Fig. 25: Example of a typical stress-strain curve (RW-1-30).

Tab. 6: Characteristic values of the research well RW-1.

Research well	State	Parameter	Units	min.	mean	med.	max.	n
RW-1	dry	$v_{pl}$	[m/s]	3,123.3	<b>5,411.4</b>	5,516.8	6,564.6	49
		$v_{pd}$	[m/s]	2,639.3	<b>5,535.4</b>	5,830.8	6,965.4	
		$v_s$	[m/s]	1,376.0	<b>2,862.4</b>	3,004.0	3,413.5	
		$E_{dyn}$	[GPa]	13.52	<b>57.21</b>	59.24	81.37	
		$G_{dyn}$	[GPa]	4.90	<b>22.13</b>	23.47	31.24	
		$K_{dyn}$	[GPa]	17.70	<b>48.75</b>	47.70	74.25	
		$\nu_{dyn}$	[-]	0.21	<b>0.30</b>	0.30	0.39	
		Z	[ $10^6$ kg/m <sup>2</sup> s]	7.80	<b>14.17</b>	14.60	17.80	
	sat.	$v_{pl}$	[m/s]	3,656.3	<b>5,906.2</b>	6,108.9	6,683.7	49
		$v_{pd}$	[m/s]	3,139.3	<b>5,871.5</b>	6,129.5	6,605.4	
		$v_s$	[m/s]	1,309.0	<b>2,790.7</b>	2,938.0	3,472.5	
		$E_{dyn}$	[GPa]	13.06	<b>59.30</b>	63.16	86.77	
		$G_{dyn}$	[GPa]	4.53	<b>21.42</b>	22.70	32.32	
		$K_{dyn}$	[GPa]	38.85	<b>90.46</b>	94.70	123.65	
		$\nu_{dyn}$	[-]	0.34	<b>0.39</b>	0.38	0.45	
		Z	[ $10^6$ kg/m <sup>2</sup> s]	10.85	<b>17.60</b>	18.45	20.70	
	dry	$\sigma_u$	[MPa]	56.1	<b>106.3</b>	106.2	209.5	15
		V	[GPa]	22.75	<b>40.88</b>	43.27	49.47	12
		E	[GPa]	35.78	<b>47.70</b>	51.27	56.66	
		$\nu$	[-]	0.04	<b>0.12</b>	0.09	0.28	11
		$\sigma_t$	[MPa]	5.1	<b>8.7</b>	6.5	7.9	
		CAI	[-]	1.1	<b>1.5</b>	1.4	1.5	
	sat.	$\sigma_u$	[MPa]	44.8	<b>99.4</b>	98.2	220.7	13
		V	[GPa]	26.49	<b>39.23</b>	42.22	47.28	10
E		[GPa]	31.64	<b>49.32</b>	52.38	56.97		
$\nu$		[-]	0.04	<b>0.16</b>	0.12	0.50		
dry	$\Phi_{eff}^{He}$	[%]	1.63	<b>6.69</b>	5.46	15.6	49	
sat.	$\Phi_{eff}^W$	[%]	1.40	<b>5.56</b>	3.99	14.49		
dry	$\rho_b$	[g/cm <sup>3</sup> ]	2.29	<b>2.61</b>	2.64	2.79		
		$\rho_g$	[g/cm <sup>3</sup> ]	2.67	<b>2.80</b>	2.80	2.98	

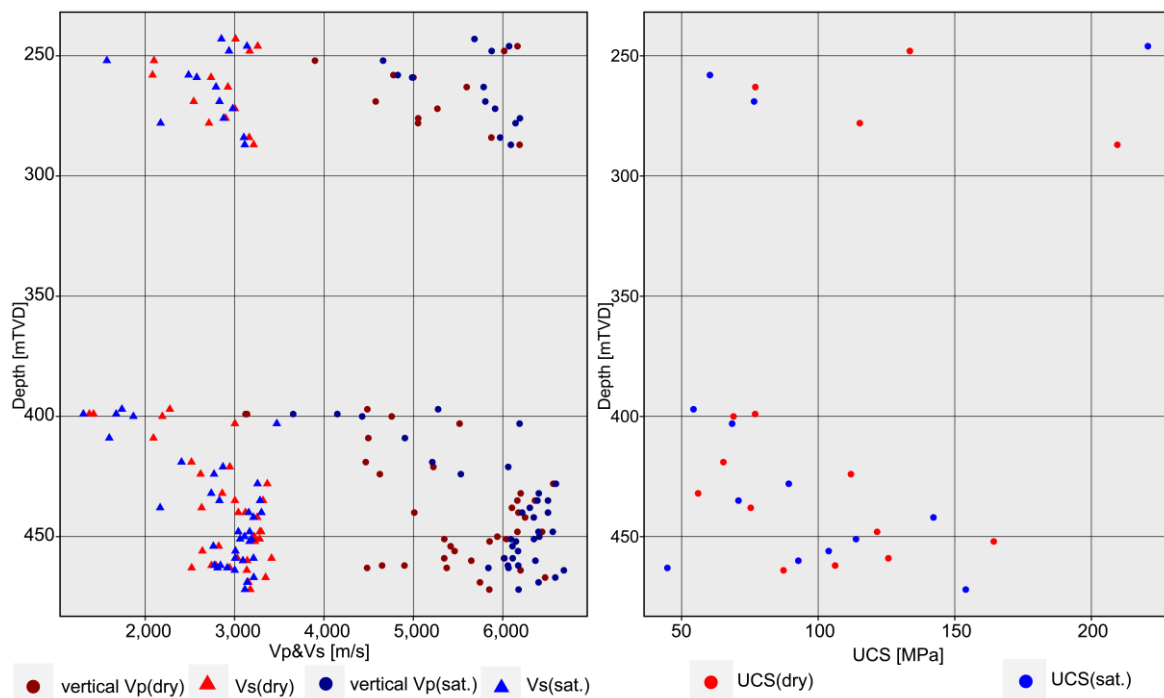


Fig. 26:  $v_p$ - and  $v_s$ -velocity (left) and UCS values (right) of differently saturated core samples (research well RW-1) versus depth.

## Research well RW-2

The research well RW-2 is located near the city of Moosburg. The well was drilled in 1990 to a total vertical depth of 1,585 m (www-12). Malm aquifer was cored completely (453 m) (BÖHM et al. 2011; BÖHM 2012; MEYER 1994) and the drill samples between 989 m and 1,584 m were examined (POTTEN et al. 2018; POTTEN et al. 2019a) in this thesis. A total of 249 samples were stratigraphically prepared from Purbeck, the complete Malm to the upper Dogger. In this well all characteristics (open and healed fissures/fractures, small and large vugs as well as stylolites) could be determined. Malm aquifer is composed of an alternation of limestones, dolomitized limestones and dolostones (BOHNSACK et al. 2020). In the top and bottom parts of the well there is limestone, whereas dolostone is mostly in the middle part of the research well. Throughout the borehole, limestone, dolomitized limestone and dolostones vary in their appearance (facies and crystal size) (Fig. 27).

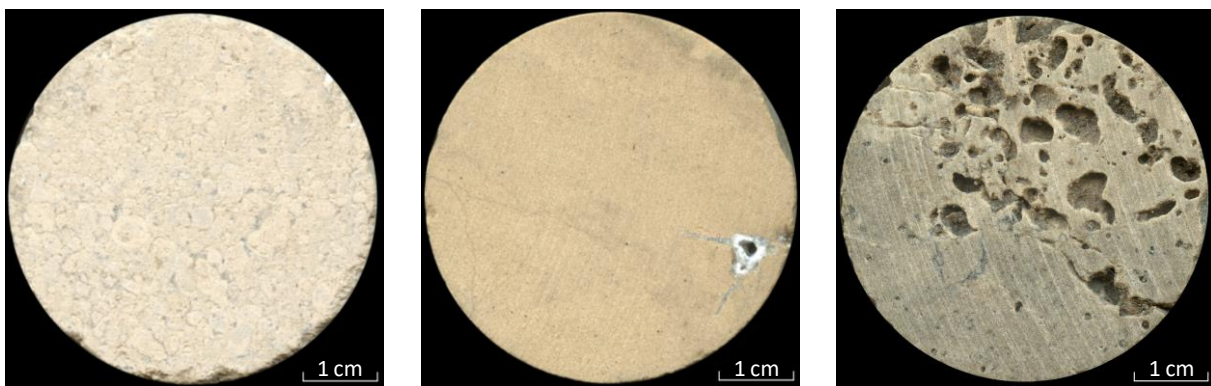


Fig. 27: Left: limestone (peloidal, fossiliferous grainstone (1,146 mTVD)); middle: dolomitic limestone (floating rhombs, peloidal grainstone (1,299 mTVD)); right: medium crystalline dolostone (1,371 mTVD).

Fig. 28 shows a typical stress-strain curve of the well RW-2. Clearly visible is the linear course of the axial strain and the low lateral strain. The curve has a small nonlinear shape where the cracks were closed. After the crack closure point the linear elastic region of the curve begins. At about 80 % of the axial strain the linear shape of the curve ends and the visible nonlinear curve shape with plastic deformation begins. In this well, the mode of failure is mostly conjugate shear planes and sometimes with splitting at the surface area of the sample.

A total of 248 UT, 164 UCT (58 preliminary test and 106 main tests), 191 BTT as well as 191 CAIT were performed from the prepared samples. Tab. 7 shows the determined key parameter values of the tests performed.

Fig. 29 illustrates the distribution of ultrasonic velocity and UCS values of differently saturated core samples at different depths. A summary of all test results of the well RW-2 is given in the Appendix.

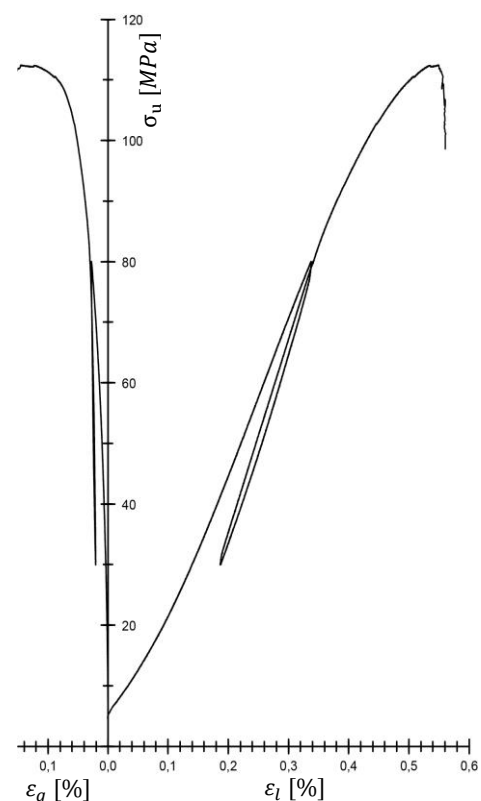


Fig. 28: Example of a typical stress-strain curve (RW-2-57.1).

Tab. 7: Characteristic values of the research well RW-2.

Research well	State	Parameter	Units	min.	mean	med.	max.	n
RW-2	dry	$v_{pl}$	[m/s]	1,397.1	<b>5,348.1</b>	5,590.2	7,200.3	247
		$v_{pd}$	[m/s]	2,616.8	<b>5,876.1</b>	6,086.7	9,533.4	
		$v_s$	[m/s]	417.0	<b>2,789.9</b>	2,960.5	3,721.0	
		$E_{dyn}$	[GPa]	1.30	<b>55.80</b>	60.61	100.76	
		$G_{dyn}$	[GPa]	1.78	<b>21.44</b>	23.29	38.49	
		$K_{dyn}$	[GPa]	4.40	<b>51.08</b>	55.00	103.50	
		$\nu_{dyn}$	[-]	0.09	<b>0.31</b>	0.31	0.45	
		Z	[ $10^6$ kg/m <sup>2</sup> s]	3.60	<b>14.06</b>	15.00	19.70	
	sat.	$v_{pl}$	[m/s]	2,851.9	<b>5,545.0</b>	5,900.1	6,911.0	248
		$v_{pd}$	[m/s]	2,828.3	<b>5,610.7</b>	5,901.2	6,958.5	
		$v_s$	[m/s]	1,127.5	<b>2,748.1</b>	2,944.3	3,656.0	
		$E_{dyn}$	[GPa]	7.29	<b>57.32</b>	64.34	102.0	
		$G_{dyn}$	[GPa]	2.66	<b>20.88</b>	23.17	37.34	
		$K_{dyn}$	[GPa]	9.40	<b>78.75</b>	85.50	140.05	
		$\nu_{dyn}$	[-]	0.06	<b>0.37</b>	0.37	0.45	
		Z	[ $10^6$ kg/m <sup>2</sup> s]	1.90	<b>16.46</b>	17.70	22.20	
	dry	$\sigma_u$	[MPa]	27.0	<b>131.1</b>	113.5	313.1	134
		V	[GPa]	9.21	<b>38.53</b>	40.87	127.07	63
		E	[GPa]	18.48	<b>43.46</b>	47.0	66.52	
		$\nu$	[-]	0.01	<b>0.14</b>	0.13	0.48	119
		$\sigma_t$	[MPa]	2.2	<b>9.7</b>	10.1	23.0	
		CAI	[-]	0.5	<b>1.2</b>	1.1	2.1	
	sat.	$\sigma_u$	[MPa]	55.0	<b>140.8</b>	122.3	284.7	33
		V	[GPa]	10.18	<b>41.50</b>	43.06	56.20	30
E		[GPa]	23.16	<b>46.72</b>	47.64	76.84		
$\nu$		[-]	0.04	<b>0.16</b>	0.12	0.50		
dry	$\Phi_{eff}^{He}$	[%]	0.22	<b>5.97</b>	4.56	22.22	247	
	sat.	$\Phi_{eff}^W$	[%]	0.30	<b>4.86</b>	3.12		19.18
dry	$\rho_b$	[g/cm <sup>3</sup> ]	2.12	<b>2.59</b>	2.63	2.79		
	$\rho_g$	[g/cm <sup>3</sup> ]	2.65	<b>2.75</b>	2.75	2.85		

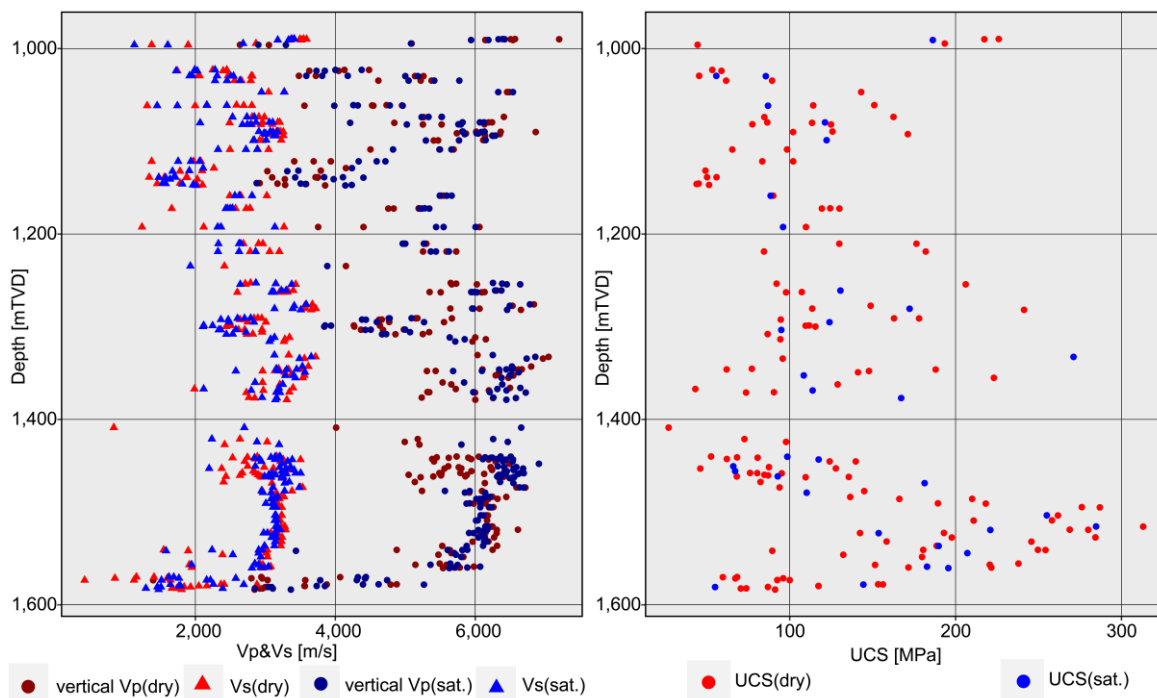


Fig. 29:  $v_p$ - and  $v_s$ -velocity (left) and UCS values (right) of differently saturated core samples (research well RW-2) versus depth.

### Well W-3

The oil/gas exploration well W-3 is located 10 km north of the city boundary of Munich. The well was drilled in 1987 to a total vertical depth of 1,460 m (www-12). The Upper Jurassic aquifer was cored in three intervals and in this thesis the drill samples between 1,392 m and 1,457 m were examined. A total of 22 samples were stratigraphically prepared from Purbeck and Malm  $\zeta$  4–5. The most common characteristics observed in the samples are open/healed fissures and especially small vugs. Dolomitized limestones can be found in the top part of the well and dolostones in the bottom part of the well. The facies of the dolomitized limestones are mainly grainstone with peloids and fossiliferous components (Fig. 30). The facies of the dolomitized limestones in the transition to the dolostone is pack-grainstone with the same components and glauconite. The crystalline dolostones vary in their appearance at the bottom of the well and show changes in their crystal size.

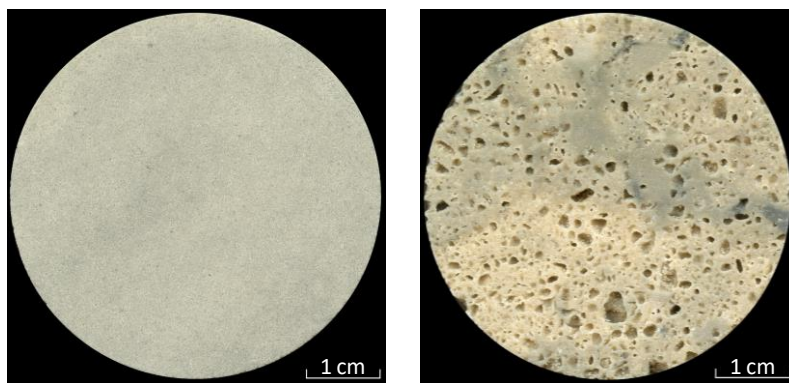


Fig. 30: Left: dolomitic limestone (peloidal, fossiliferous grainstone (1,400 mTVD)); right: coarsely crystalline dolostone (1,456 mTVD).

Fig. 31 shows a typical stress-strain curve of the well W-3. Clearly visible is the long path of the axial strain and a lower lateral strain. The curve has a small nonlinear shape with elastic deformation where the cracks were closed. The linear elastic region and a stable crack growth take place until a small visible crack in the sample is closed. At this point the stable crack growth ends and the unstable crack growth begins. In this well the failure is spontaneous and the failure mode builds mostly conjugate pairs of shear failure surfaces sometimes with a lot of float pieces.

A total of 22 UT, 13 UCT (1 preliminary test and 12 main tests), 23 BTT as well as 23 CAIT were performed from the prepared samples.

Tab. 8 shows the determined key parameter values of the tests performed.

A summary of all test results of the well W-3 is given in the Appendix.

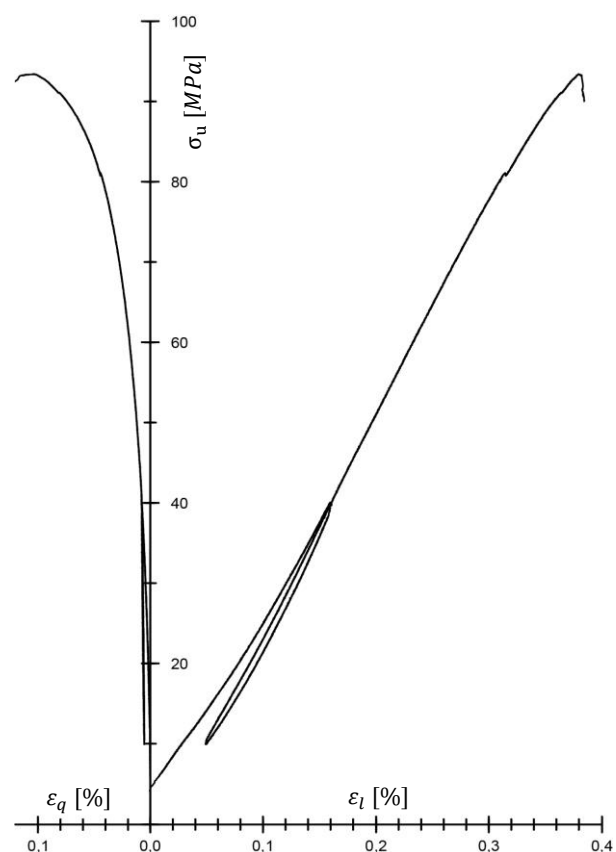


Fig. 31: Example of a typical stress-strain curve (W-3-7.1).

Tab. 8: Characteristic values of well W-3.

Well	State	Parameter	Units	min.	mean	med.	max.	n	
W-3	dry	$v_{pl}$	[m/s]	3,747.0	<b>4,987.5</b>	4,656.6	7,016.4	22	
		$v_{pd}$	[m/s]	4,165.0	<b>5,284.1</b>	5,026.2	7,038.9		
		$v_s$	[m/s]	2,223.5	<b>2,831.1</b>	2,618.0	3,500.0		
		$E_{dyn}$	[GPa]	28.26	<b>49.63</b>	36.79	87.84		
		$G_{dyn}$	[GPa]	11.06	<b>19.70</b>	15.03	33.22		
		$K_{dyn}$	[GPa]	14.60	<b>35.51</b>	26.68	82.20		
		$\nu_{dyn}$	[-]	0.18	<b>0.25</b>	0.25	0.32		
		Z	[10 <sup>6</sup> kg/m <sup>2</sup> s]	8.20	<b>11.86</b>	9.88	19.0		
	dry	$\sigma_u$	[MPa]	32.4	<b>76.7</b>	62.6	160.0	8	
		V	[GPa]	14.87	<b>35.71</b>	23.08	91.17	6	
		E	[GPa]	23.08	<b>45.57</b>	33.80	92.90		
		$\nu$	[-]	0.05	<b>0.13</b>	0.13	0.20	14	
		$\sigma_t$	[MPa]	4.0	<b>7.6</b>	7.4	16.0		
		CAI	[-]	0.1	<b>0.6</b>	0.4	1.5		
	sat.	$\sigma_u$	[MPa]	46.0	<b>90.1</b>	73.5	144.1	5	
		V	[GPa]	17.96	<b>34.31</b>	30.91	50.67	4	
		E	[GPa]	22.29	<b>40.27</b>	43.02	52.74		
		$\nu$	[-]	0.07	<b>0.20</b>	0.19	0.38		
	dry	$\Phi_{eff}^{He}$	[%]	2.50	<b>17.42</b>	19.83	29.35	22	
		sat.	$\Phi_{eff}^W$	[%]	2.10	<b>15.75</b>	18.57		25.79
			$\rho_b$	[g/cm <sup>3</sup> ]	2.01	<b>2.34</b>	2.29		2.71
		dry	$\rho_g$	[g/cm <sup>3</sup> ]	2.78	<b>2.84</b>	2.84		2.85

Fig. 32 illustrates the distribution of ultrasonic velocity and UCS values of differently saturated core samples at different depths.

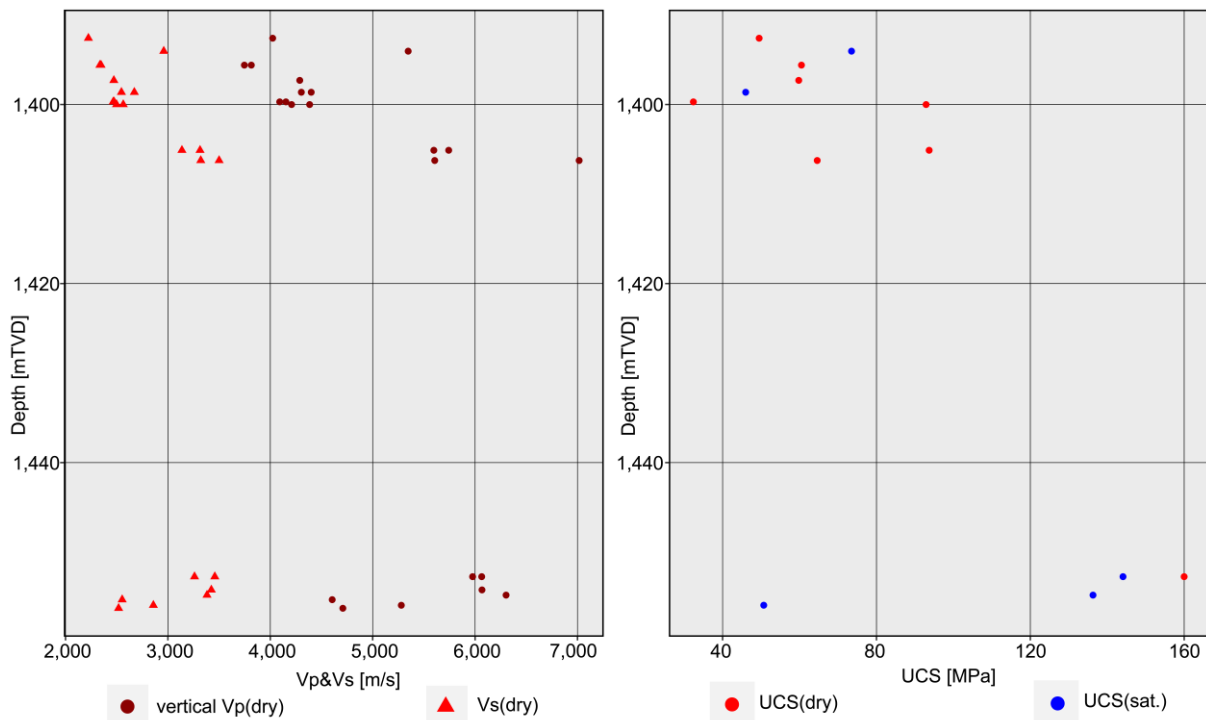


Fig. 32:  $v_p$ - and  $v_s$ -velocity (left) and UCS values (right) of differently saturated core samples (well W-3) versus depth.

## Well W-4

The oil/gas exploration well W-4 is located 5 km north–northwest of the city boundary of Munich. The well was drilled in 1981 to a total vertical depth of 2,071 m (www-02). The Upper Jurassic aquifer was cored in eight intervals and in this thesis the drill samples between 1,449 m and 1,484 m were examined. A total of 27 samples were stratigraphically prepared from Purbeck and Malm  $\zeta$  4–5. The most prevalent characteristics appearing in the samples are healed fissure, small vugs and stylolites. Limestones can be found in the top part of the well and an alternation of limestones and dolostones is found in the bottom part of the well. The facies of the limestones are from wackestone to floatstone. The facies in the transition to the dolostone is pack–grainstone. The limestones have peloidal, fossiliferous and lithoclastic components. The crystalline dolostones vary in their appearance at the bottom of the well and show changes in their crystal size (hyp–idiomorphic) (Fig. 33).

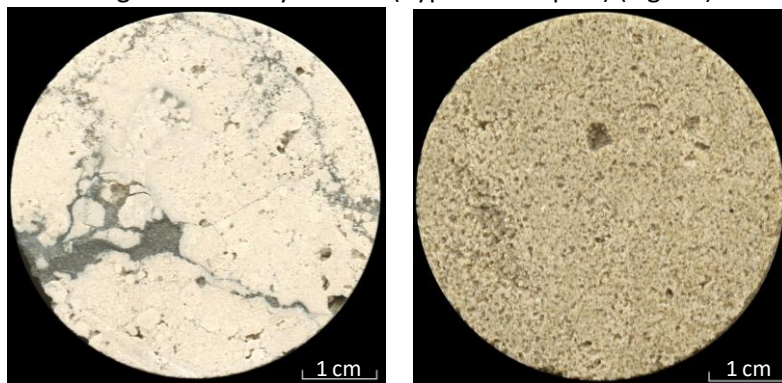


Fig. 33 Left: limestone (peloidal, fossiliferous, lithoclastic grainstone (1,484 mTVD); right: coarsely crystalline dolostone (1,478 mTVD).

Fig. 34 shows a typical stress-strain curve of the well W-4. Clearly visible is the short path of the axial strain and a lateral strain. The stress-strain curve of this sample shows a post failure range of the axial strain with no further axial strain. The mode of failure of this core sample is a shear failure which runs along an open, and in some places healed, quartz fissure. In this well, the mode of failure is mostly axial splitting which is characterized by some vertical cracks splitting the sample and smaller cracks forming parallel to the sample axis. The failure is mostly spontaneous. Overall, all the samples from this well do not withstand very much stress.

A total of 27 UT, 19 UCT (0 preliminary test and 12 main tests), 16 BTT as well as 16 CAIT were performed from the prepared samples.

Tab. 9 shows the determined key parameter values of the tests performed.

A summary of all test results of the well W-4 is given in the Appendix.

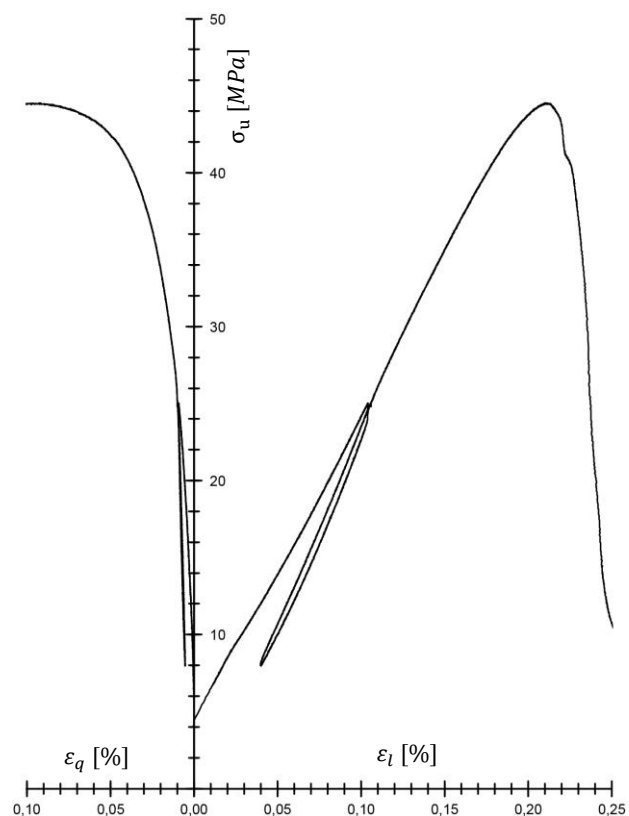


Fig. 34: Example of a typical stress-strain curve (W-4-15).

Tab. 9: Characteristic values of the well W-4.

Well	State	Parameter	Units	min.	mean	med.	max.	n	
W-4	dry	$v_{pl}$	[m/s]	2,223.5	<b>4,487.0</b>	4,412.7	6,759.5	27	
		$v_{pd}$	[m/s]	2,456.2	<b>4,827.2</b>	4,629.0	6,886.9		
		$v_s$	[m/s]	1,407.0	<b>2,396.8</b>	2,274.0	3,700.0		
		$E_{dyn}$	[GPa]	10.21	<b>38.31</b>	33.23	96.39		
		$G_{dyn}$	[GPa]	4.38	<b>14.82</b>	12.55	37.45		
		$K_{dyn}$	[GPa]	5.10	<b>32.39</b>	31.70	75.40		
		$\nu_{dyn}$	[-]	0.15	<b>0.29</b>	0.29	0.37		
		Z	[ $10^6$ kg/m <sup>2</sup> s]	4.90	<b>11.04</b>	11.10	18.50		
	dry	$\sigma_u$	[MPa]	23.8	<b>69.0</b>	74.7	118.5	9	
		V	[GPa]	11.56	<b>26.10</b>	26.82	42.72	8	
		E	[GPa]	23.58	<b>39.78</b>	38.16	65.98		
		$\nu$	[-]	0.10	<b>0.17</b>	0.13	0.40	11	
		$\sigma_t$	[MPa]	1.6	<b>5.1</b>	4.2	11.0		
		CAI	[-]	0.2	<b>0.8</b>	1.0	1.3		
	sat.	$\sigma_u$	[MPa]	14.7	<b>61.2</b>	50.8	171.4	10	
		V	[GPa]	5.36	<b>26.46</b>	21.98	59.14	4	
		E	[GPa]	39.48	<b>53.53</b>	56.43	61.79		
		$\nu$	[-]	0.05	<b>0.20</b>	0.27	0.36		
	dry	$\phi_{eff}^{He}$	[%]	0.90	<b>11.22</b>	8.24	26.96	27	
		sat.	$\phi_{eff}^W$	[%]	0.52	<b>10.22</b>	7.20		24.73
		dry	$\rho_b$	[g/cm <sup>3</sup> ]	2.01	<b>2.43</b>	2.52		2.74
			$\rho_g$	[g/cm <sup>3</sup> ]	2.71	<b>2.74</b>	2.72		2.85

Fig. 35 illustrates the distribution of ultrasonic velocity and UCS values of differently saturated core samples at different depths.

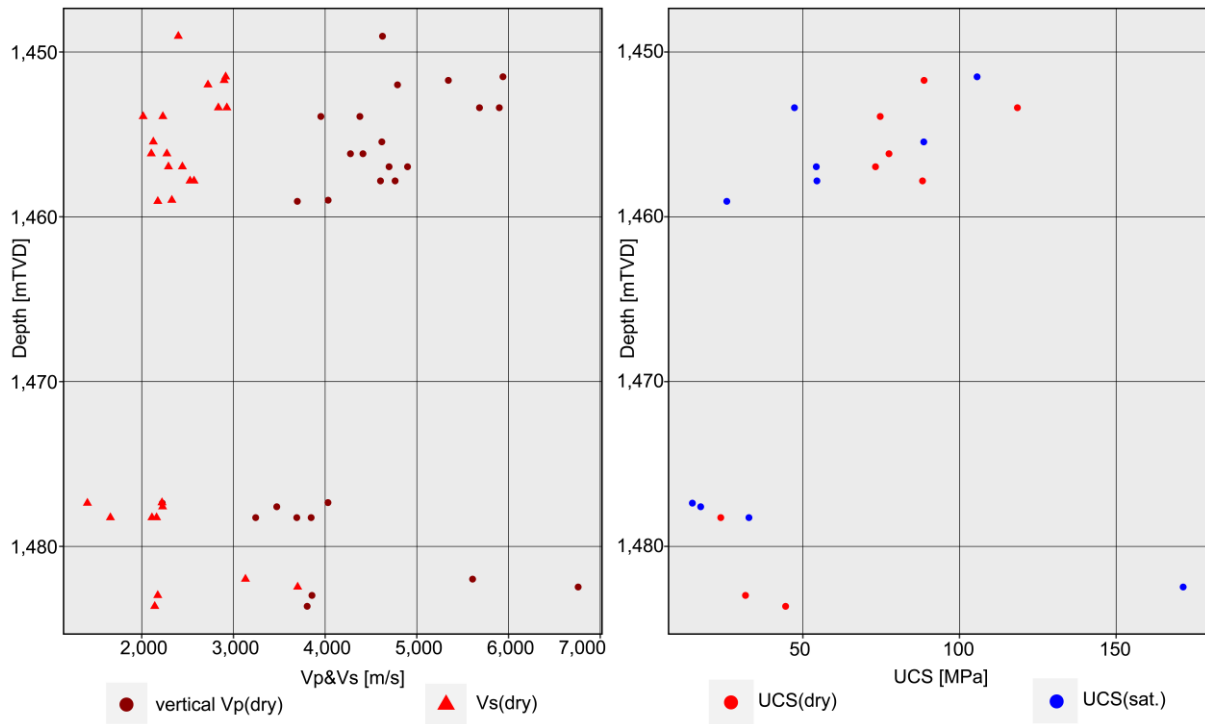


Fig. 35:  $v_p$ - and  $v_s$ -velocity (left) and UCS values (right) of differently saturated core samples (well W-4) versus depth.

## Well W-5

The oil/gas exploration well W-5 is located 5 km southwest of the city boundary of Munich. The well was drilled in 1956/1957 to a total vertical depth of 2,440 m (www-02). The Upper Jurassic aquifer was cored in 19 intervals and was examined at depths between 2,409 m and 2,440 m. A total of 13 samples were stratigraphically prepared from the Priabonian and Purbeck. The most common characteristics of these samples in the upper part of the well are healed fissures and stylolites. Limestones can be found throughout the entirety of the whole well with one layer of dolomitic limestone (wackestone). The facies of the Priabonian limestone are a mudstone and a bindstone with algal mats, lithoclasts and peloidal components. The facies of Purbeck limestones are from wackestone to grainstone with ooidal, peloidal, fossiliferous and dasycladaceans components (Fig. 36).

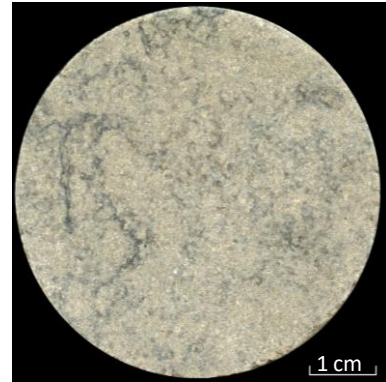


Fig. 36: Limestone (ooidal, peloidal, fossiliferous grainstone (2,440 mTVD).

Fig. 37 shows a typical stress-strain curve of the well W-5. Clearly visible is the long path of the nonlinear section of the curve and a short section of linear axial strain. The V- and E-Modulus was established in the upper part of the axial strain. Afterwards some small steps are observed in the curve where old microfractures were probably reactivated and then closed. A post-failure part is existent. The lateral strain is very small compared to the axial strain. This sample shows, that the lateral strain can only absorb 1/16 of the axial strain. In this well, the mode of failure is mostly axial splitting which is characterized by some vertical cracks splitting the sample.

A total of 13 UT, 12 UCT (0 preliminary test and 12 main tests), 13 BTT as well as 13 CAIT were performed from the prepared samples.

Tab. 10 shows the determined key parameter values of the tests performed.

A summary of all test results of the well W-5 is given in the Appendix.

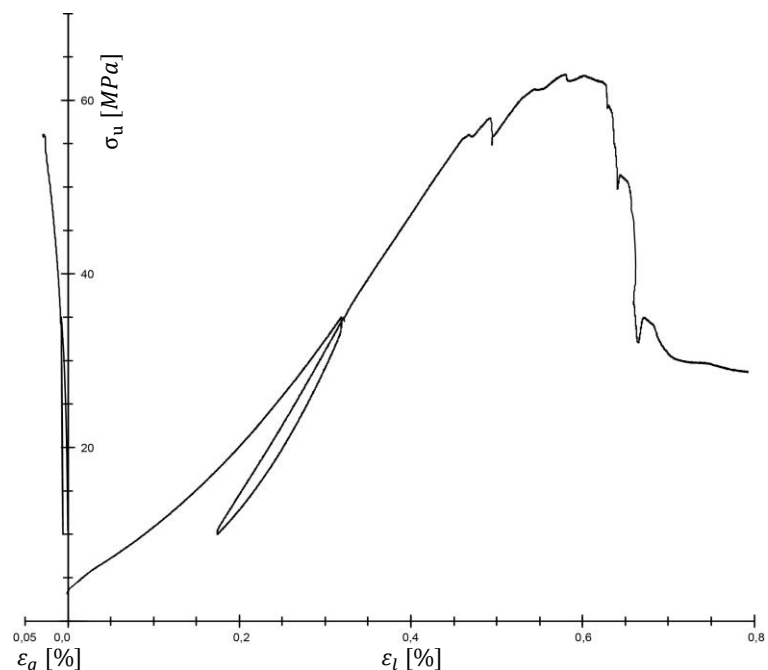


Fig. 37: Example of a typical stress-strain curve (W-5-14).

Tab. 10: Characteristic values of well W-5.

Well	State	Parameter	Units	min.	mean	med.	max.	n
W-5	dry	$v_{pl}$	[m/s]	3,193.2	<b>4,302.6</b>	4,167.8	5,966.3	13
		$v_{pd}$	[m/s]	3,962.6	<b>4,958.9</b>	5,004.8	6,530.3	
		$v_s$	[m/s]	1,719.0	<b>2,287.7</b>	2,263.0	2,904.0	
		$E_{dyn}$	[GPa]	21.38	<b>35.86</b>	35.42	59.78	
		$G_{dyn}$	[GPa]	7.98	<b>13.94</b>	13.12	22.51	
		$K_{dyn}$	[GPa]	12.60	<b>29.91</b>	27.0	57.90	
		$\nu_{dyn}$	[-]	0.21	<b>0.29</b>	0.27	0.38	
		Z	[10 <sup>6</sup> kg/m <sup>2</sup> s]	7.90	<b>11.08</b>	10.95	15.90	
	dry	$\sigma_u$	[MPa]	59.5	<b>88.7</b>	85.8	128.3	5
		V	[GPa]	13.66	<b>19.08</b>	15.77	26.93	4
		E	[GPa]	19.74	<b>26.58</b>	22.38	41.82	
		$\nu$	[-]	0.04	<b>0.06</b>	0.06	0.08	4
		$\sigma_t$	[MPa]	6.3	<b>9.2</b>	7.7	15.3	
		CAI	[-]	0.7	<b>1.1</b>	1.1	1.6	
	sat.	$\sigma_u$	[MPa]	54.4	<b>90.7</b>	87.9	132.2	7
		V	[GPa]	17.89	<b>24.04</b>	21.56	32.33	7
		E	[GPa]	23.35	<b>31.18</b>	31.23	40.39	
	dry	$\phi_{eff}^{He}$	[%]	0.67	<b>6.84</b>	7.14	11.73	13
		sat.	$\phi_{eff}^W$	[%]	1.02	<b>5.15</b>	5.27	
	dry	$\rho_b$	[g/cm <sup>3</sup> ]	2.41	<b>2.57</b>	2.57	2.67	
		$\rho_g$	[g/cm <sup>3</sup> ]	2.69	<b>2.76</b>	2.75	2.83	

Fig. 38 illustrates the distribution of ultrasonic velocity and UCS values of differently saturated core samples at different depths.

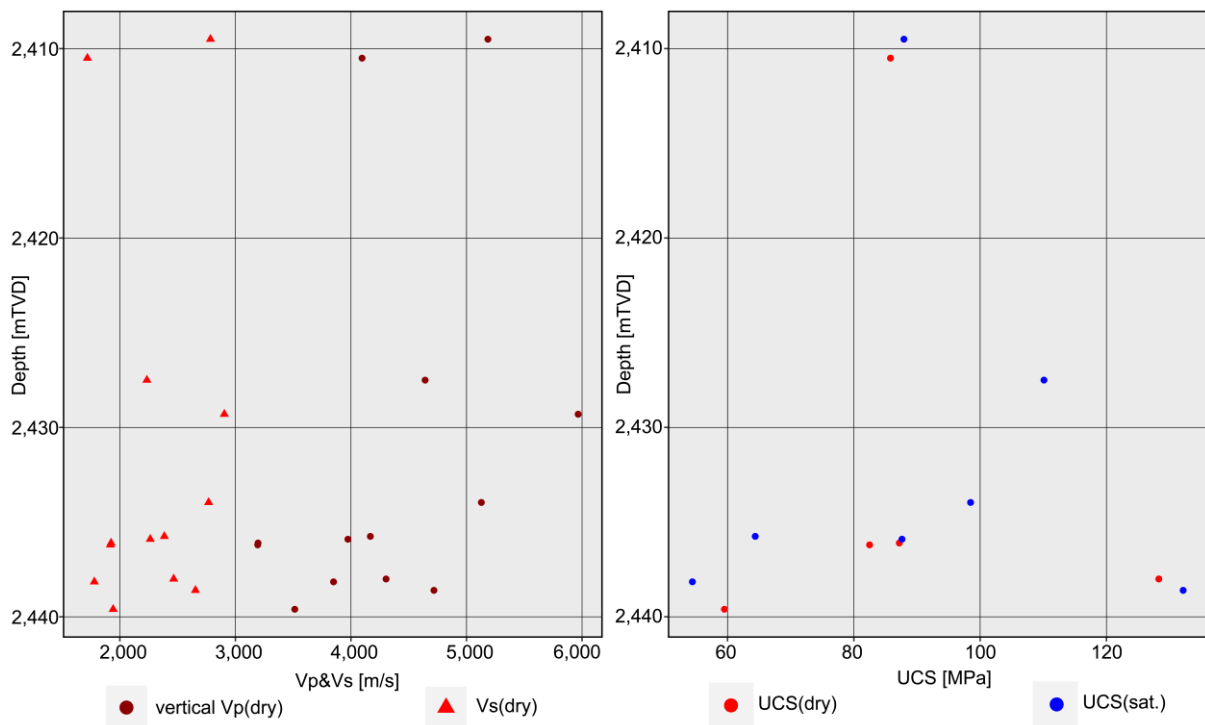


Fig. 38:  $v_p$ - and  $v_s$ -velocity (left) and UCS values (right) of differently saturated core samples (well W-5) versus depth.

## Well W-6

The oil/gas exploration well W-6 is located 7 km southwest of the city boundary of Munich. The well was drilled in 1955 to a total vertical depth of 2,706 m (www-02; www-12). The Upper Jurassic aquifer was cored in three intervals and was examined between 2,692 m and 2,698 m. A total of 5 samples were prepared from Malm ζ 4–5 stratigraphy. The most prevalent characteristic of the samples is stylolites. Limestones can be found in the top part of the well and a dolostone in the bottom part of the well. The facies of the limestones is wackestone (Fig. 39). The crystal size of the dolostone is fine crystalline with a hypidiomorphic morphology of the dolomite crystals.

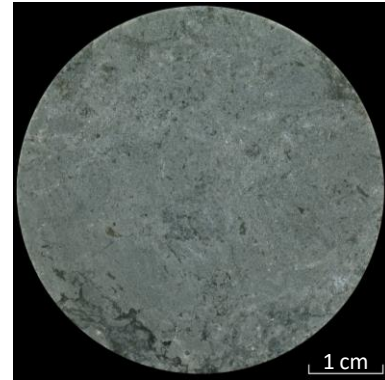


Fig. 39: Limestone (wackestone (2,692 mTVD)).

Fig. 40 shows a typical stress-strain curve of the well W-6. Clearly visible is the axial as well as the lateral strain on the sample. In this sample, after reaching the uniaxial compressive strength, a post-failure range without further strain is visible. The curve has a long nonlinear shape with elastic deformation where the cracks were closed. The V- and E-Modulus was established in the upper part where the elastic strain begins. The elastic-plastic deformation is only a small part of the curve. In this well, the mode of failure is mostly axial splitting which is characterized by some vertical cracks splitting the sample and smaller cracks forming parallel to the sample's axis. The failure is mostly spontaneous. Overall, these samples do not withstand very much stress.

A total of 5 UT, 2 UCT (8 preliminary tests and 2 main tests), 4 BTT as well as 4 CAIT were performed from the collected sample material.

Tab. 11 shows the determined key parameter values of the tests performed.

A summary of all test results of the well W-6 is given in the Appendix.

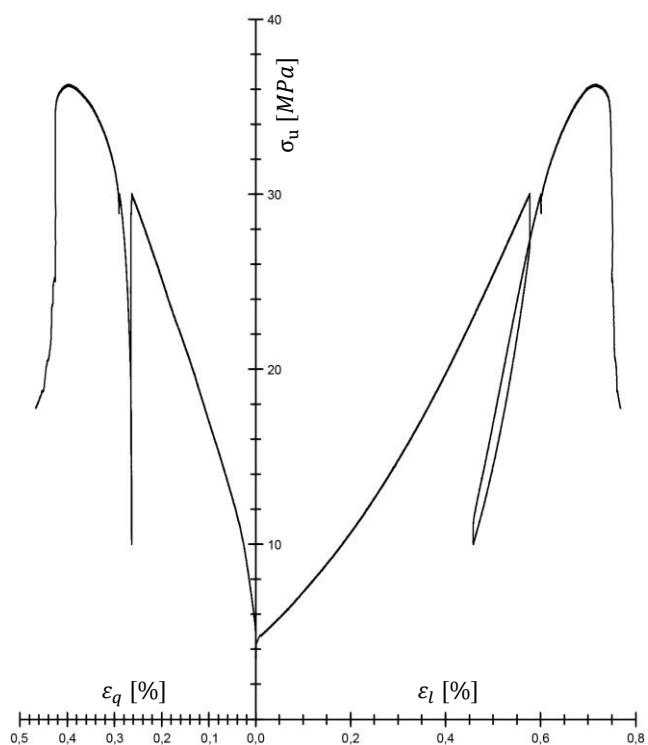


Fig. 40: Example of a typical stress-strain curve (W-6-1).

Tab. 11: Characteristic values of well W-6.

Well	State	Parameter	Units	min.	mean	med.	max.	n
W-6	dry	$v_{pl}$	[m/s]	2,305.4	<b>3,623.2</b>	3,231.6	5,941.5	5
		$v_{pd}$	[m/s]	3,292.0	<b>3,966.0</b>	3,507.3	5,911.7	
		$v_s$	[m/s]	1,003.0	<b>1,850.7</b>	1,509.5	3,334.0	
		$E_{dyn}$	[GPa]	7.28	<b>27.78</b>	16.38	74.32	
		$G_{dyn}$	[GPa]	2.63	<b>10.76</b>	6.02	29.33	
		$K_{dyn}$	[GPa]	10.60	<b>24.13</b>	18.65	53.20	
		$\nu_{dyn}$	[-]	0.26	<b>0.33</b>	0.36	0.39	
		Z	[ $10^6$ kg/m <sup>2</sup> s]	6.05	<b>9.53</b>	8.55	15.60	
	sat.	$\sigma_t$	[MPa]	2.7	<b>7.4</b>	3.0	16.5	3
		CAI	[-]	0.5	<b>0.7</b>	0.6	0.9	
	sat.	$\sigma_u$	[MPa]	14.6	<b>25.4</b>	25.4	36.3	2
		V	[GPa]	1.40	<b>3.69</b>	3.69	5.98	
		E	[GPa]	9.08	<b>10.28</b>	10.28	11.49	
		$\nu$	[-]	0.42	<b>0.42</b>	0.42	0.42	
	dry	$\Phi_{eff}^{He}$	[%]	2.45	<b>3.73</b>	3.27	6.37	5
sat.	$\Phi_{eff}^W$	[%]	2.60	<b>4.15</b>	4.45	6.27		
dry	$\rho_b$	[g/cm <sup>3</sup> ]	2.61	<b>2.63</b>	2.63	2.64		
	$\rho_g$	[g/cm <sup>3</sup> ]	2.71	<b>2.73</b>	2.71	2.82		

Fig. 41 illustrates the distribution of ultrasonic velocity and UCS values of differently saturated core samples at different depths.

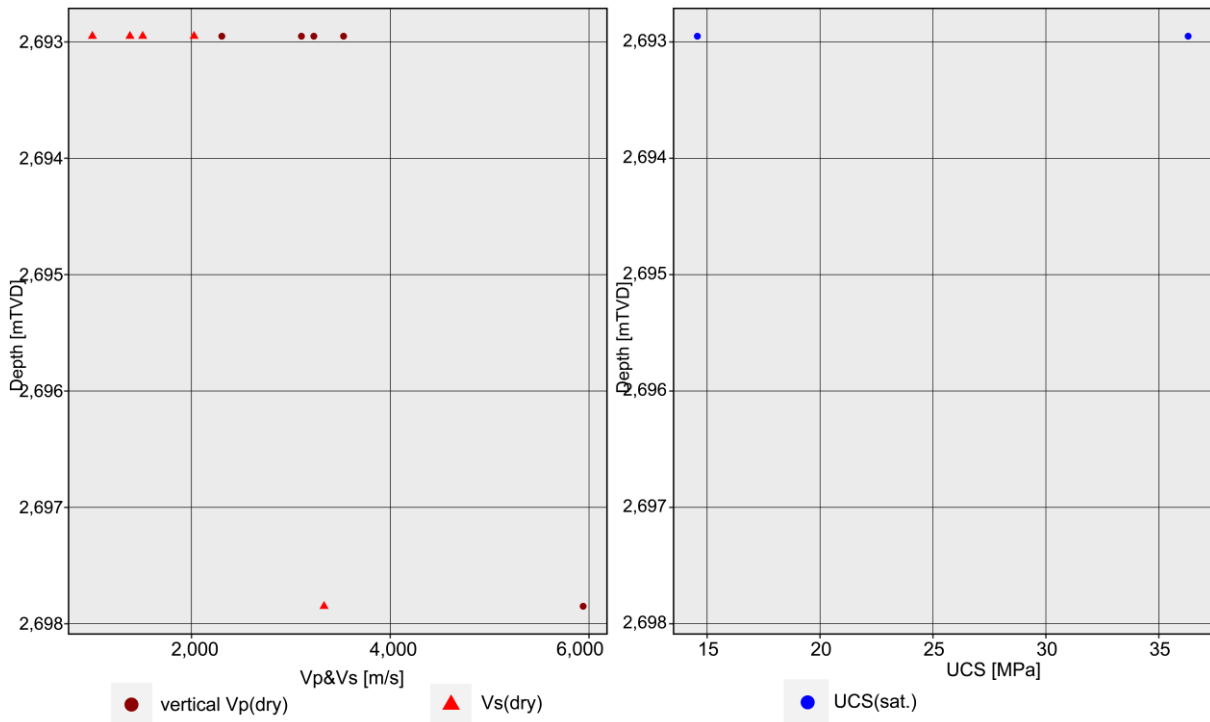


Fig. 41:  $v_p$ - and  $v_s$ -velocity (left) and UCS values (right) of differently saturated core samples (well W-6) versus depth.

### Well W-7

The oil/gas exploration well W-7 is located 9 km southwest of the city boundary of Munich. The well was drilled in 1956/1957 to a total vertical depth of 2,676 m (www-02; www-12). The Upper Jurassic aquifer was cored in one interval and was examined between 2,655 m and 2,698 m. A total of 11 samples were stratigraphically prepared from Purbeck, Malm  $\zeta$  4–5 and further unclassified Malm. The most common characteristics of the samples are healed fissures and stylolites. Only limestones can be found in whole well. The facies of the limestones in the top of the well W-7 is mudstone to bindstone with algal mats, peloidal, fossiliferous and, lithoclastic components (Fig. 42). In the bottom part of the well W-7 it is only grainstone with peloidal, fossiliferous, and lithoclastic components.

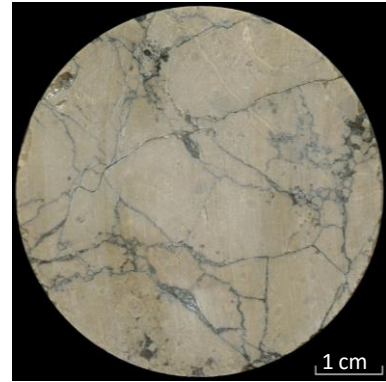


Fig. 42: Limestone (peloidal, fossiliferous, lithoclastic packstone (2,671 mTVD).

Fig. 43 shows a typical stress-strain curve of the well W-7. Clearly visible is the axial as well as a smaller lateral strain of the sample. The stress strain curve begins with a visible nonlinear shape. This part of the curve where the cracks were closed makes up approximately 24 % of the entire curve. The elastic part of the stress-strain curve continues until a small crack in the sample was closed. At this point the stable crack growth ends and the unstable crack growth begins. In this well, the mode of failure is mostly axial splitting which is characterized by some vertical cracks splitting the sample and smaller cracks forming parallel to the sample's axis. The failure is mostly spontaneous. Overall, these samples also do not withstand very much stress.

A total of 11 UT, 8 UCT (0 preliminary test and 8 main tests), 5 BTT as well as 5 CAIT were performed from the collected samples.

Tab. 12 shows the determined key parameter values of the tests performed.

A summary of all test results of the well W-7 is given in the Appendix.

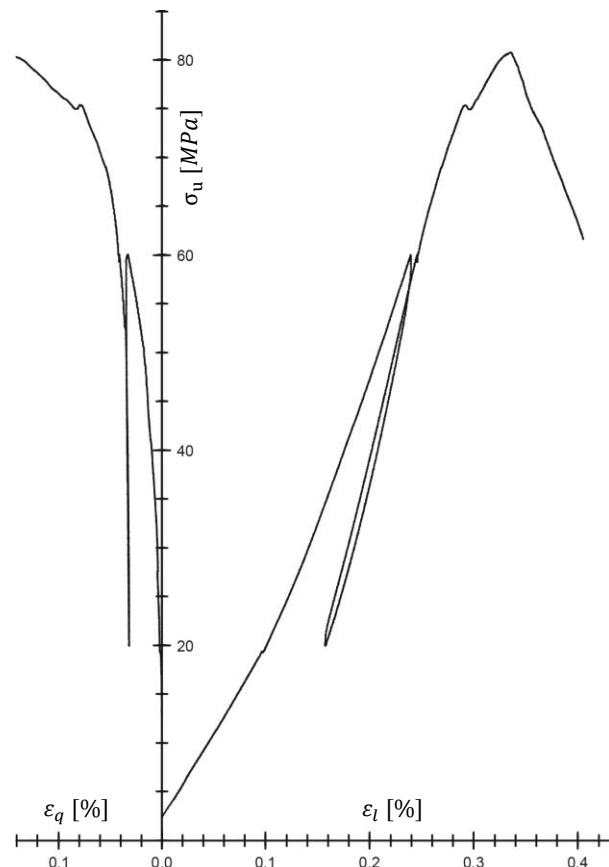


Fig. 43: Example of a typical stress-strain curve (W-7-6).

Tab. 12: Characteristic values of the well W-7.

Well	State	Parameter	Units	min.	mean	med.	max.	n
W-7	dry	$v_{pl}$	[m/s]	4,668.0	<b>5,692.3</b>	5,863.2	6,640.3	11
		$v_{pd}$	[m/s]	5,066.3	<b>5,612.0</b>	5,267.6	6,508.2	
		$v_s$	[m/s]	1,680.0	<b>2,595.3</b>	2,595.3	2,973.0	
		$E_{dyn}$	[GPa]	21.01	<b>48.89</b>	49.70	64.28	
		$G_{dyn}$	[GPa]	7.37	<b>18.14</b>	18.92	23.63	
		$K_{dyn}$	[GPa]	36.75	<b>61.45</b>	61.0	90.80	
		$\nu_{dyn}$	[-]	0.27	<b>0.36</b>	0.36	0.43	
		Z	[10 <sup>6</sup> kg/m <sup>2</sup> s]	12.15	<b>14.93</b>	15.30	17.20	
	dry	$\sigma_u$	[MPa]	67.9	<b>110.6</b>	103.9	166.7	4
		V	[GPa]	24.57	<b>30.32</b>	28.77	39.17	
		E	[GPa]	29.46	<b>53.58</b>	59.19	66.47	4
		$\nu$	[-]	0.09	<b>0.18</b>	0.10	0.45	3
		$\sigma_t$	[MPa]	3.9	<b>4.7</b>	4.4	5.9	
		CAI	[-]	0.9	<b>0.9</b>	0.9	1.0	
	sat.	$\sigma_u$	[MPa]	69.0	<b>78.4</b>	72.5	99.8	4
		V	[GPa]	19.38	<b>26.12</b>	26.37	32.35	3
		E	[GPa]	42.03	<b>47.35</b>	45.47	54.55	
	dry	$\nu$	[-]	0.06	<b>0.26</b>	0.24	0.49	11
		$\Phi_{eff}^{He}$	[%]	0.40	<b>3.03</b>	3.64	6.45	
	sat.	$\Phi_{eff}^W$	[%]	1.11	<b>2.98</b>	3.59	6.15	
	dry	$\rho_b$	[g/cm <sup>3</sup> ]	2.53	<b>2.62</b>	2.61	2.69	
$\rho_g$		[g/cm <sup>3</sup> ]	2.70	<b>2.70</b>	2.70	2.71		

Fig. 44 illustrates the distribution of ultrasonic velocity and UCS values of differently saturated core samples at different depths.

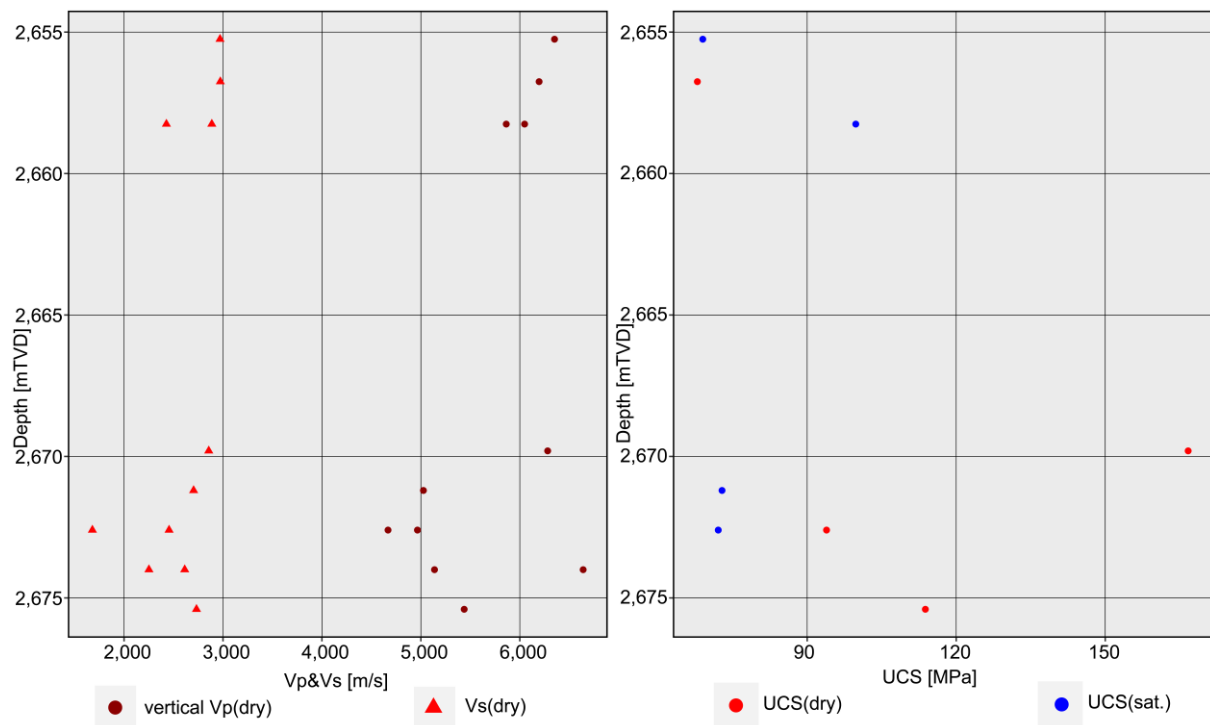


Fig. 44:  $v_p$ - and  $v_s$ -velocity (left) and UCS values (right) of differently saturated core samples (well W-7) versus depth.

## Well W-8

The oil/gas exploration well W-8 is located 9 km southwest of the city boundary of Munich. The well was drilled in 1957 to a total vertical depth of 2,675 m. The Upper Jurassic aquifer was cored in one interval and was examined between 2,655 m and 2,698 m. A total of 16 samples were stratigraphically prepared from Purbeck and further unclassified Malm. The most common characteristics found in the samples are healed fissures and stylolites.

Only limestones can be found throughout the well. The facies of the limestones in the top of the well W-8 is packstone to bindstone. In the bottom part of the well W-8 it is grainstone to floatstone (Fig. 45). All investigated samples are constructed with peloidal, fossiliferous, and lithoclastic components.



Fig. 45: Limestone (peloidal, fossiliferous, lithoclastic floatstone (2,674 mTVD).

Fig. 46 shows a typical stress-strain curve of the well W-8. Clearly visible is the long path of the axial strain and a smaller path of the lateral strain. The curve has a small nonlinear shape with elastic deformation where the cracks were closed. After the closure the curve shows some small steps where old microfractures were probably reactivated and then closed. The V- and E-Modulus was established in the upper part where the elastic strain begins. The lateral strain is recorded undisturbed up to these steps. At about 95 % of the axial strain a slight curvature is formed and the failure is spontaneous. In this well, the mode of failure is mostly axial splitting which is characterized by some vertical cracks splitting the sample and smaller cracks forming parallel to the sample's axis.

A total of 16 UT, 10 UCT (0 preliminary test and 10 main tests), 11 BTT as well as 11 CAIT were performed from the collected samples.

Tab. 13 shows the determined key parameter values of the tests performed.

A summary of all test results of the well W-8 is given in the Appendix.

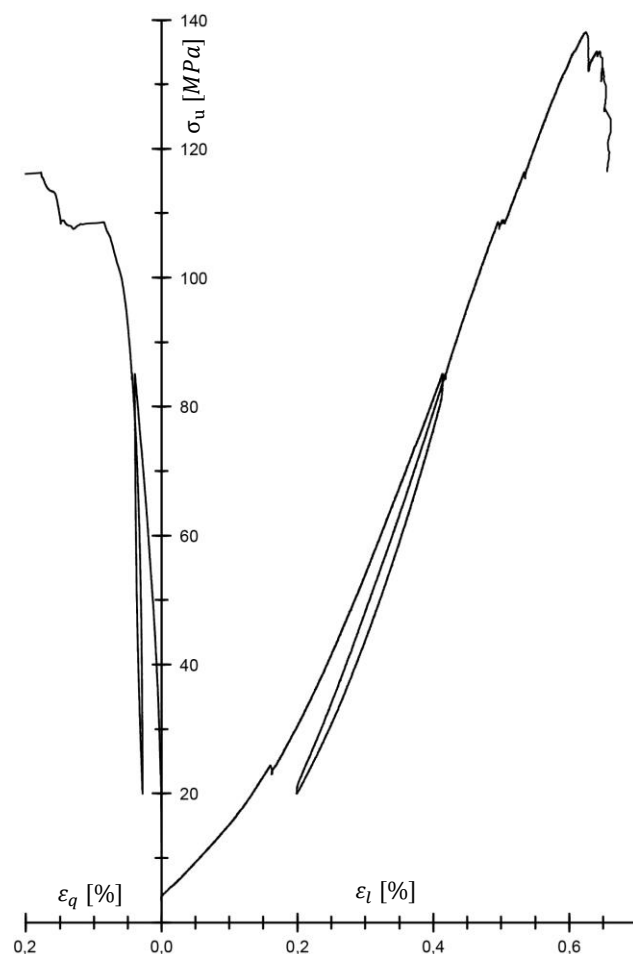


Fig. 46: Example of a typical stress-strain curve (W-8-3).

Tab. 13: Characteristic values of the well W-8.

Well	State	Parameter	Units	min.	mean	med.	max.	n
W-8	dry	$v_{pl}$	[m/s]	3,156.7	<b>5,044.6</b>	5,168.3	6,468.3	16
		$v_{pd}$	[m/s]	4,605.4	<b>5,323.0</b>	5,293.8	6,547.6	
		$v_s$	[m/s]	1,462.0	<b>2,573.8</b>	2,487.5	4,285.5	
		$E_{dyn}$	[GPa]	15.25	<b>46.28</b>	43.22	105.62	
		$G_{dyn}$	[GPa]	5.60	<b>18.24</b>	16.16	47.89	
		$K_{dyn}$	[GPa]	18.60	<b>42.96</b>	42.50	69.85	
		$\nu_{dyn}$	[-]	0.10	<b>0.31</b>	0.34	0.39	
		Z	[ $10^6$ kg/m <sup>2</sup> s]	8.25	<b>13.01</b>	13.20	16.90	
	dry	$\sigma_u$	[MPa]	60.8	<b>83.7</b>	70.3	127.1	5
		V	[GPa]	18.39	<b>22.98</b>	20.52	29.72	5
		E	[GPa]	28.24	<b>49.66</b>	51.32	67.31	
		$\nu$	[-]	0.01	<b>0.26</b>	0.28	0.47	6
		$\sigma_t$	[MPa]	3.2	<b>4.6</b>	4.2	6.2	
		CAI	[-]	0.8	<b>0.9</b>	0.9	1.0	
	sat.	$\sigma_u$	[MPa]	59.8	<b>78.0</b>	68.7	121.9	4
		V	[GPa]	15.86	<b>21.48</b>	21.48	28.48	5
		E	[GPa]	36.25	<b>44.87</b>	41.27	59.74	
	$\nu$	[-]	0.07	<b>0.13</b>	0.12	0.21	16	
	dry	$\Phi_{eff}^{He}$	[%]	0.61	<b>4.74</b>	4.34		9.82
	sat.	$\Phi_{eff}^W$	[%]	0.77	<b>4.55</b>	3.77		9.53
	dry	$\rho_b$	[g/cm <sup>3</sup> ]	2.44	<b>2.58</b>	2.59		2.69
$\rho_g$		[g/cm <sup>3</sup> ]	2.70	<b>2.71</b>	2.71	2.73		

Fig. 47 illustrates the distribution of ultrasonic velocity and UCS values of differently saturated core samples at different depths.

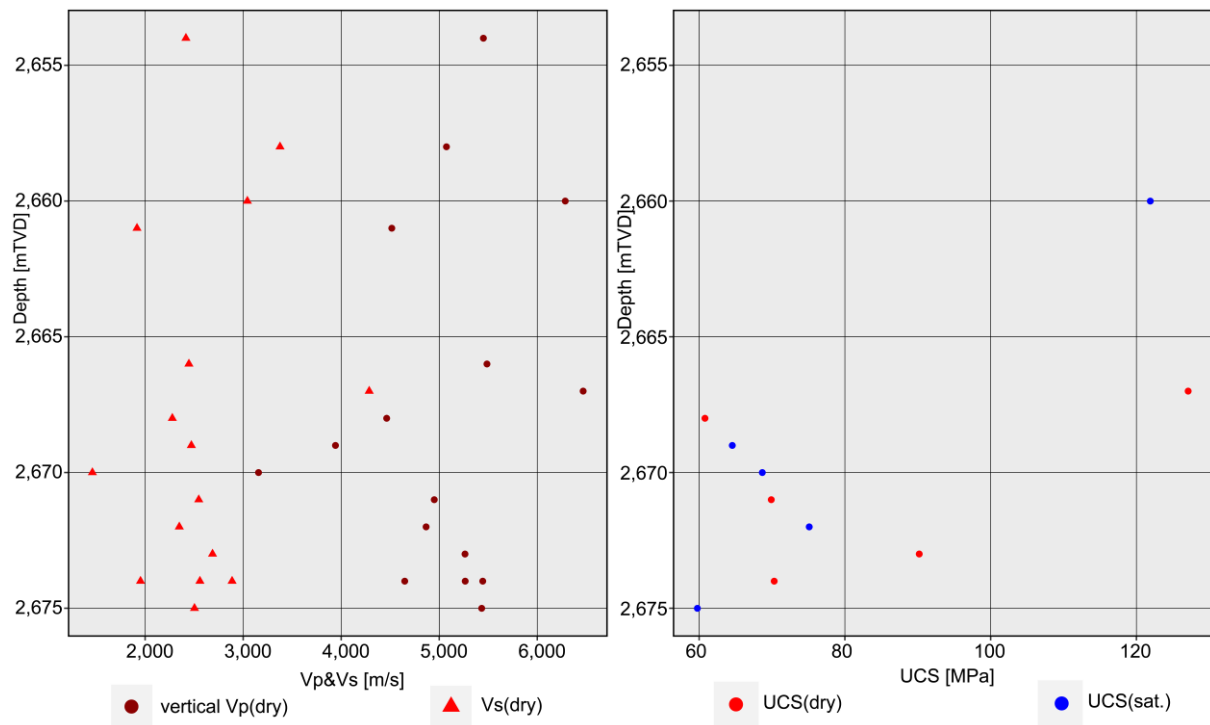


Fig. 47:  $v_p$ - and  $v_s$ -velocity (left) and UCS values (right) of differently saturated core samples (well W-8) versus depth.

## Well W-9

The gas exploration well W-9 is located 3 km southwest of the town boundary of Peißenberg. The well was drilled in 1989/1990 to a total vertical depth of 5,514 m (www-02; www-12). The Upper Jurassic aquifer was cored in one interval and was examined between 5,217 m and 5,225 m. A total of 9 samples were stratigraphically prepared from Malm ζ 4–5. The most prevalent characteristics of the samples are healed fissures and stylolites. Only limestones can be found in whole well. The facies of the limestones is wackestone with fossiliferous components (Fig. 48).



Fig. 48: Limestone (fossiliferous wackestone (5,222 mTVD)).

Fig. 49 shows a typical stress-strain curve of the well W-9. Clearly visible is the long path of the longitudinal deformation and a low transverse deformation. The curve has a relatively long path of nonlinear shape where the cracks were closed. The V- and E-Modulus was established in the upper part where the elastic strain begins. Then there is the elastic deformation which continues until a small crack of the sample was closed. At this point the stable crack growth ends and the unstable crack growth begins. The lateral strain is recorded undisturbed up to this step. In this well the failure is spontaneous and the failure mode is mostly axial splitting which is characterized by some vertical cracks splitting the sample.

A total of 9 UT, 7 UCT (0 preliminary test and 7 main tests), 16 BTT as well as 16 CAIT were performed from the collected samples.

Tab. 14 shows the determined key parameter values of the tests performed.

A summary of all test results of the well W-9 is given in the Appendix.

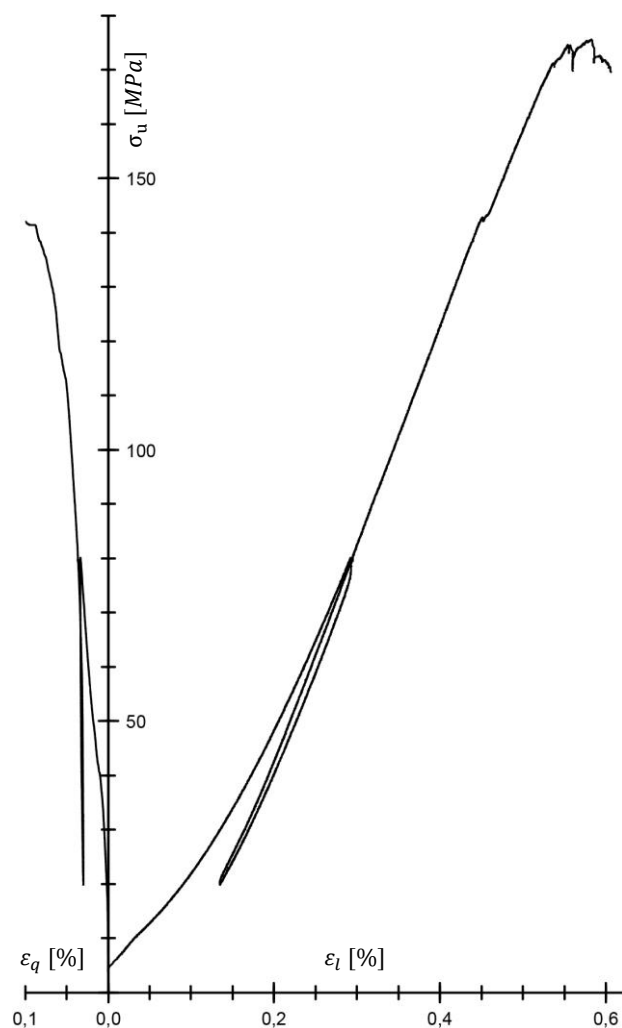


Fig. 49: Example of a typical stress-strain curve (W-9-4.1).

Tab. 14: Characteristic values of the well W-9.

Well	State	Parameter	Units	min.	mean	med.	max.	n
W-9	dry	$v_{pl}$	[m/s]	2,384.6	<b>2,725.1</b>	2,594.4	3,428.1	9
		$v_{pd}$	[m/s]	4,938.8	<b>5,453.8</b>	5,414.5	5,966.0	
		$v_s$	[m/s]	744.0	<b>1,031.2</b>	997.5	1,438.0	
		$E_{dyn}$	[GPa]	4.31	<b>8.47</b>	7.58	16.26	
		$G_{dyn}$	[GPa]	1.49	<b>3.09</b>	2.67	6.50	
		$K_{dyn}$	[GPa]	12.90	<b>15.44</b>	14.15	26.75	
		$\nu_{dyn}$	[-]	0.33	<b>0.41</b>	0.42	0.45	
		Z	[10 <sup>6</sup> kg/m <sup>2</sup> s]	6.40	<b>7.21</b>	6.90	9.15	
	dry	$\sigma_u$	[MPa]	71.7	<b>102.8</b>	83.1	159.7	5
		V	[GPa]	23.16	<b>27.94</b>	24.82	35.86	
		E	[GPa]	44.10	<b>57.95</b>	51.48	73.77	5
		$\nu$	[-]	0.15	<b>0.21</b>	0.17	0.33	5
		$\sigma_t$	[MPa]	5.1	<b>6.4</b>	6.5	7.9	
		CAI	[-]	1.1	<b>1.3</b>	1.4	1.5	
	sat.	$\sigma_u$	[MPa]	65.0	<b>77.9</b>	77.9	90.7	2
		V	[GPa]	30.43	<b>33.07</b>	33.07	35.71	
		E	[GPa]	41.76	<b>41.76</b>	41.76	41.76	1
		$\nu$	[-]	0.50	<b>0.50</b>	0.50	0.50	2
	dry	$\Phi_{eff}^{He}$	[%]	0.15	<b>0.53</b>	0.43	1.46	9
	sat.	$\Phi_{eff}^W$	[%]	0.27	<b>0.58</b>	0.49	1.47	8
dry	$\rho_b$	[g/cm <sup>3</sup> ]	2.67	<b>2.69</b>	2.69	2.70	9	
	$\rho_g$	[g/cm <sup>3</sup> ]	2.71	<b>2.71</b>	2.71	2.71		

Fig. 50 illustrates the distribution of ultrasonic velocity and UCS values of differently saturated core samples at different depths.

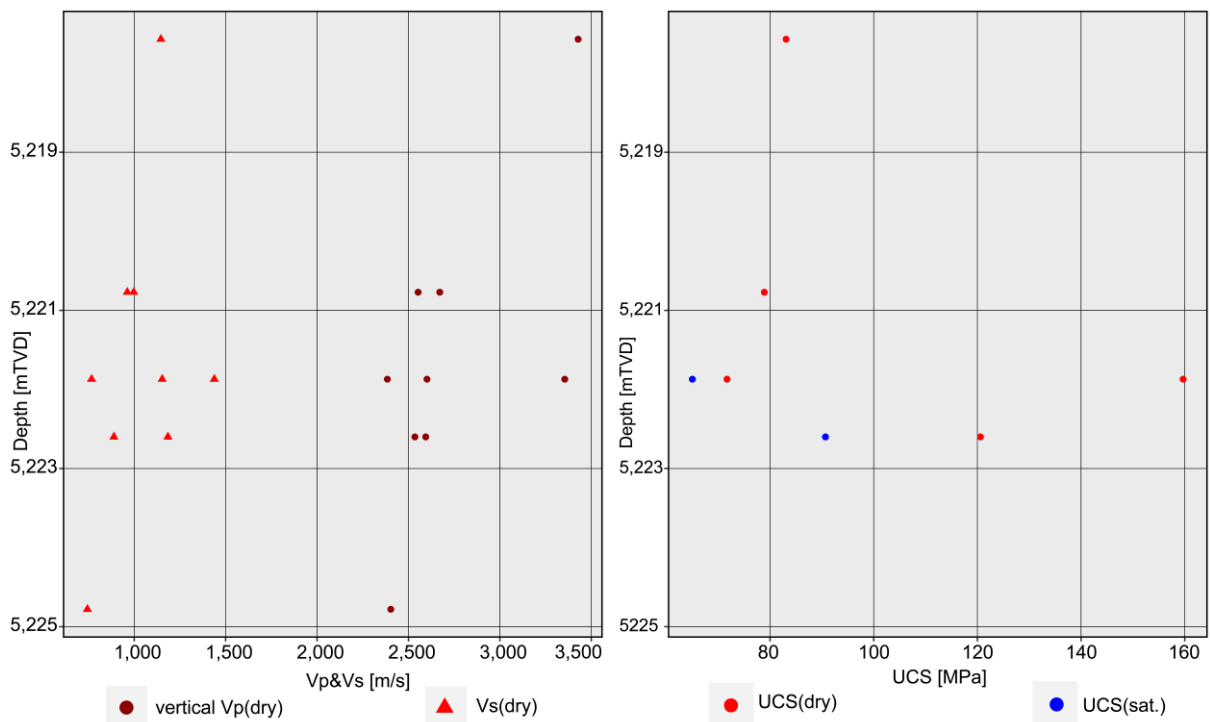


Fig. 50:  $v_p$ - and  $v_s$ -velocity (left) and UCS values (right) of differently saturated core samples (well W-9) versus depth.

## Well W-10

The gas exploration well W-10 is located ~0.5 km north of the city boundary of Garching an der Alz. The well was drilled in 1985 (www-12) to a total vertical depth of 3,182 m (www-02). The Upper Jurassic aquifer was cored and examined between 2,892 m and 3,156 m. A total of 26 plugs were sent for non-destructive investigations from the Lower Cretaceous, Purbeck and Malm  $\zeta$  stratigraphy.

The most common characteristics of the samples are open and healed fissures as well as small vugs. Limestones can be found in the top part of the well, whereas the middle part consists of dolomitized limestones and the bottom part consists of dolostone. The facies of the limestones are grainstone to bindstone with lithoclastic, ooidal, peloidal, fossiliferous and algal mats components. The dolomitized limestones are packstone and mudstone with peloidal, fossiliferous and lithoclastic components. The crystalline dolostones vary in their appearance at the bottom of the well and show a hypidiomorphic morphology of the dolomite crystals (Fig. 51).

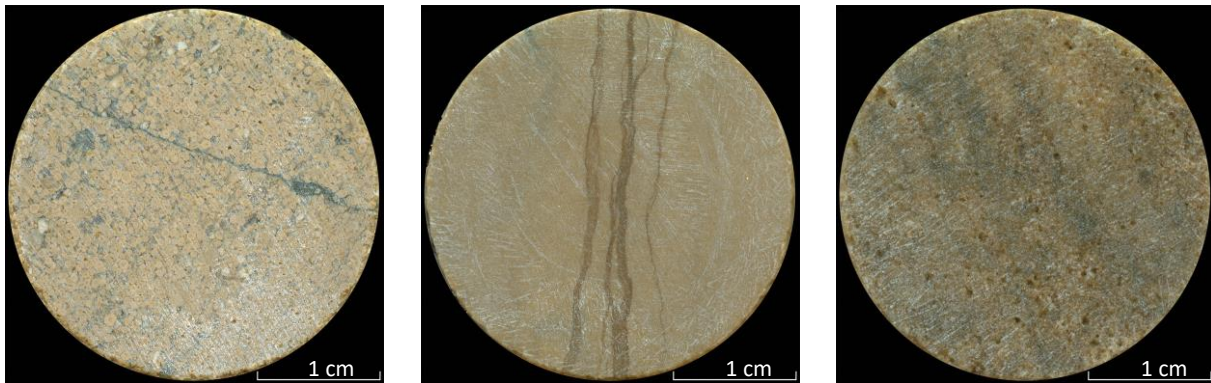


Fig. 51: Left: limestone (ooidal, fossiliferous grainstone (2,895 mTVD)); middle: dolomitic limestone (mudstone (3,055 mTVD)); right: medium crystalline dolostone (3,154 mTVD).

A total of only 26 UT were performed on the donated samples.

Tab. 15 shows the determined key parameter values of the tests performed.

A summary of all test results of the well W-10 is given in the Appendix.

Tab. 15: Characteristic values of the well W-10.

Well	State	Parameter	Units	min.	mean	med.	max.	n
W-10	dry	$v_{pl}$	[m/s]	3,791.3	<b>5,790.8</b>	6,040.5	7,057.2	26
		$v_{pd}$	[m/s]	3,755.1	<b>5,693.7</b>	5,943.6	6,806.6	
		$v_s$	[m/s]	1,502.0	<b>2,985.2</b>	3,156.0	3,508.0	
		$E_{dyn}$	[GPa]	16.80	<b>65.14</b>	70.11	92.35	
		$G_{dyn}$	[GPa]	5.97	<b>24.77</b>	27.13	35.63	
		$K_{dyn}$	[GPa]	26.40	<b>60.13</b>	62.20	93.30	
		$\nu_{dyn}$	[-]	0.27	<b>0.32</b>	0.31	0.41	
		Z	[ $10^6$ kg/m <sup>2</sup> s]	10.0	<b>15.76</b>	16.15	18.90	
	dry	$\phi_{eff}^{He}$	[%]	0.22	<b>2.14</b>	1.88	4.73	
	sat.	$\phi_{eff}^W$	[%]	0.22	<b>2.29</b>	2.23	5.04	
	dry	$\rho_b$	[g/cm <sup>3</sup> ]	2.60	<b>2.71</b>	2.72	2.89	
		$\rho_g$	[g/cm <sup>3</sup> ]	2.67	<b>2.77</b>	2.79	2.90	

**Borehole B-11**

The ongoing geothermal exploration well B-11 is located in the city center of Munich. The borehole was drilled in 2019 to a total vertical depth of ~3,000 m. The Upper Jurassic aquifer was cored and examined between 2,424 m and 2,775 m. A total of 22 plugs were sent for non-destructive investigations from Purbeck to Malm ε stratigraphy. This well has all five determined characteristics (open and healed fissures/fractures, small and large vugs as well as stylolites) distributed throughout the well.

Malm is composed of an alternation of limestones, dolomitized limestones, and dolostones. All three lithologies can be found in the top part of the well, whereas in the rest of the well there is only limestone and dolostone. The facies of the limestones are mudstone to grainstone with peloidal, fossiliferous and lithoclastic components. The dolomitized limestones shows a wackestone to packstone facies with peloidal, fossiliferous, lithoclastic and dolomite rhombohedron components. The crystalline dolostones vary in their appearance (Fig. 52).

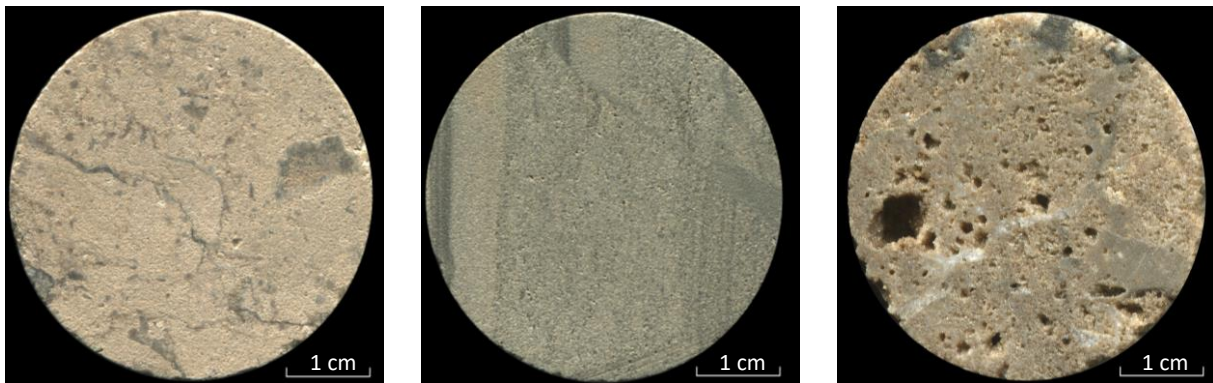


Fig. 52: Left: limestone (peloidal, fossiliferous grainstone (2,526 mTVD)); middle: dolomitic limestone (laminated layer wackestone (2,440 mTVD)); right: medium crystalline dolostone (2,482 mTVD).

A total of 22 UT were performed from the collected samples.

Tab. 16 shows the determined key parameter values of the tests performed.

A summary of all test results of the borehole B-11 is given in the Appendix.

Tab. 16: Characteristic values of the borehole B-11.

Borehole	State	Parameter	Units	min.	mean	med.	max.	n
B-11	dry	$v_{pl}$	[m/s]	2,807.6	<b>5,365.3</b>	5,277.5	7,654.2	22
		$v_{pd}$	[m/s]	3,234.1	<b>5,267.5</b>	5,152.5	6,773.1	
		$v_s$	[m/s]	1,656.0	<b>2,646.2</b>	2,739.5	4,018.0	
		$E_{dyn}$	[GPa]	16.10	<b>51.82</b>	50.50	113.18	
		$G_{dyn}$	[GPa]	6.73	<b>19.58</b>	19.22	43.22	
		$K_{dyn}$	[GPa]	8.85	<b>54.67</b>	57.65	99.20	
		$\nu_{dyn}$	[-]	0.20	<b>0.33</b>	0.35	0.41	
		Z	[10 <sup>6</sup> kg/m <sup>2</sup> s]	6.35	<b>13.88</b>	14.20	20.50	
	dry	$\Phi_{eff}^{He}$	[%]	1.46	<b>9.11</b>	6.70	20.44	
	sat.	$\Phi_{eff}^W$	[%]	0.57	<b>6.04</b>	5.03	17.41	
	dry	$\rho_b$	[g/cm <sup>3</sup> ]	2.25	<b>2.52</b>	2.56	2.70	
		$\rho_g$	[g/cm <sup>3</sup> ]	2.70	<b>2.77</b>	2.76	2.89	



### 2.2.5 Discussion

Due to the fact that information about the Upper Jurassic aquifer is limited to the areas immediately surrounding existing wells/borehole, only statements about those areas can currently be made. This information was summarised in such a way as to allow a more regional analysis. This should help to better describe and understand the entire Upper Jurassic aquifer. First, the specific parameters were plotted against each other and general relationships of geomechanics in the Upper Jurassic aquifer are shown. This should provide information about dependencies in the overall context of the Upper Jurassic aquifer system.

Afterwards, the measured data are subdivided into three different groups according to the publication of BOHNSACK et al. (2020). The results are classified according to their stratigraphy, lithology and facies and the distribution of the respective groups could also be shown.

In the first subdivision, the determined data were related to the location of the examined samples within the well/borehole according to the stratigraphy after QUENSTEDT (1858). This enables the results of each well/borehole to be viewed together and correlated regardless of depth.

In the second subdivision, the core samples were classified according to lithology into three categories (limestone, dolomitic limestone and dolostone).

The third and last subdivision was that the three lithologies were divided into different facies and rock fabric types. The limestone as well as the dolomitic limestone were classified according to their grain and component size (DUNHAM 1978; FLÜGEL & MUNNECKE 2010; LUCIA 1995; LUCIA 2007; LUCIA & CONTI 1987). The dolostone was divided into fine, medium and coarse crystalline according to their dolomite crystal size (BEICHEL et al. 2014; FOLK 1974; LUCIA 2007; SIBLEY & GREGG 1987). Additionally, the morphology of the dolomite crystals (xenomorphic, hypidiomorphic, idiomorphic) was determined (SIBLEY 1982; SIBLEY & GREGG 1987; TUCKER & WRIGHT 1990).

It was considered whether each well should be discussed separately but as can be seen from the results section, the measured parameters are very scattered over the depths and correlations can not be seen. A small number of samples makes up the entire range of values per stratigraphic unit. This limited set of data does not allow reliable statements and might lead to incorrect conclusions. To increase the data set all values determined per well/borehole were considered together in the respective classifications.

An overview of the Upper Jurassic aquifer parameters subdivided into stratigraphy, lithology and facies can be found in the Appendix.

### 2.2.5.1 General geomechanical tests

To investigate the influence of saturation and to obtain reproducible results, the laboratory experiments were done under two conditions. Either the core samples were measured dry after being oven dried or they were measured in the desiccator after being completely saturated.

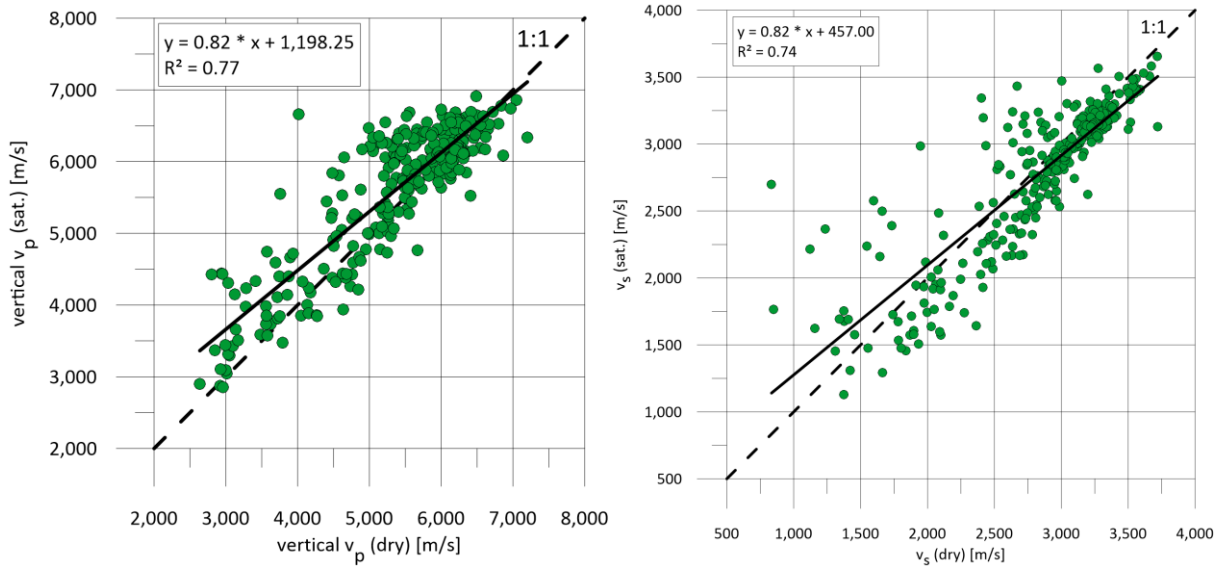


Fig. 53: Vertical  $v_p(\text{dry})$ -velocities plotted against vertical  $v_p(\text{sat.})$ -velocities (left) and  $v_s(\text{dry})$ -velocities plotted against  $v_s(\text{sat.})$ -velocities (right) to consider the influence of saturation of the carbonates from the Upper Jurassic aquifer.

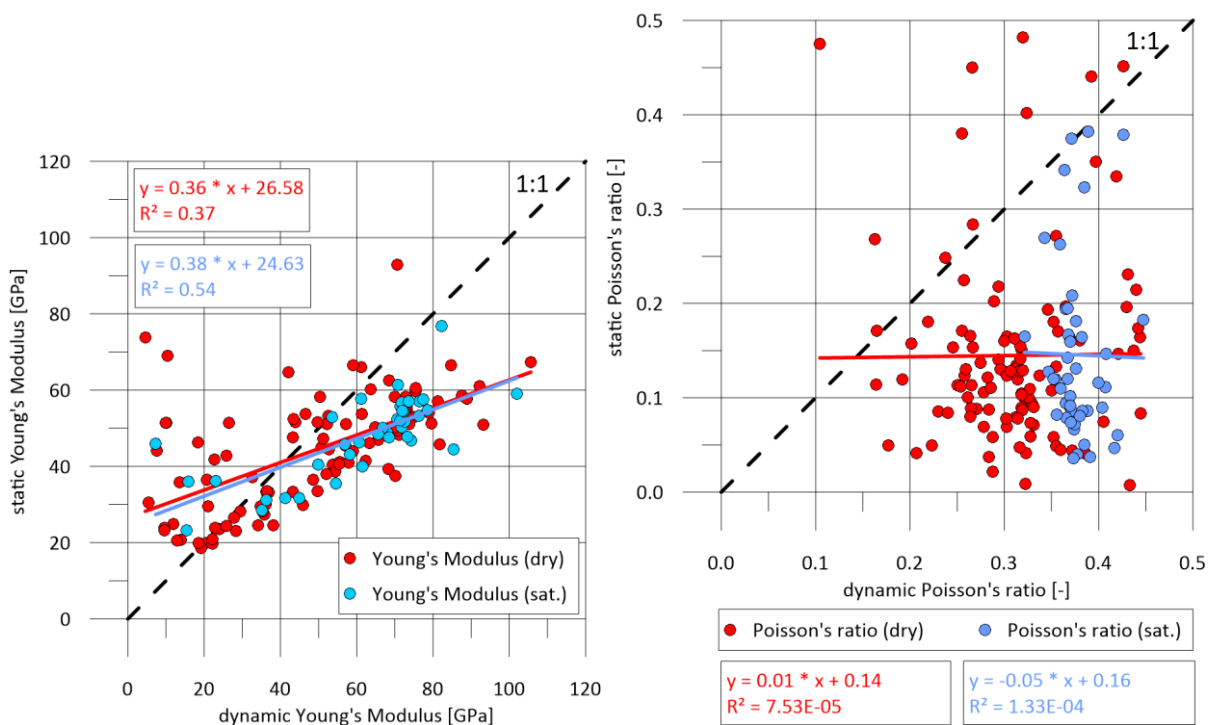


Fig. 54: Dynamic Young's Modulus plotted against static Young's Modulus (left) and dynamic Poisson's ratio plotted against static Poisson's ratio (right) to consider the difference between dynamic and static parameters.

In the non-destructive tests the saturated core samples have higher  $v_{p1}$ -velocities (left) and lower  $v_s$ -velocities (right) than the dried specimens (Fig. 53). This is consistent with the theory of GASSMANN (1951), that the increase in the  $v_{p1}$ -velocities and the decrease in the  $v_s$ -velocities correlate with increasing saturation (KASSAB & WELLER 2015). At full saturation the Gassmann effect causes a higher  $v_{p1}$ -velocity than in a gas, since the pores filled with water have a higher bulk modulus. As the shear modulus of water and gas is close to zero, the  $v_s$ -velocities are not affected (MAYR & BURKHARDT 2006).

For the destructive tests, this direct correlation could not be established. The core samples were measured either dry or saturated and it was therefore not possible to perform both tests on one test sample.

In the field of geothermal energy, the dynamic moduli are calculated from the velocities as well as the densities determined by seismic or borehole measurements (FJÆR et al. 2008). The static moduli are not determined in geothermal energy because no drill cores exist.

In this thesis the dynamic moduli are calculated from the velocities ( $v_p$ - and  $v_s$ -velocities) of the ultrasonic tests and the density (ZOBACK 2010). The static moduli are derived from the slope of a stress-strain curve measured using the core samples.

Fig. 54 (left), shows the correlation between dynamic and static Young's Modulus. At low dynamic Young's Moduli, the static Young's Moduli are higher and at higher dynamic Young's Moduli the static Young's Moduli are lower. The overall correlation of the values is low. There seems to be an opposite trend for low and high values. This may result from the completely different moduli triggered by the different effects of the energy in the different tests (non-destructive vs. destructive) on the test samples. Thus it can be seen that the dynamically determined moduli cannot be used to draw conclusions about the statically determined moduli from the ultrasonic tests because the deviations are too large.

Fig. 54 (right) shows the correlation between the dynamic and static Poisson's ratio. The dynamic Poisson's ratio is concentrated and lies mainly between 0.2 and 0.4 whereas the static Poisson's ratio varies greatly. For the dynamic Poisson's ratio (dry) a mean value of 0.31 was determined and for the saturated dynamic Poisson ratio a mean value of 0.38 was determined. For the static Poisson's ratio (dry) the mean value is 0.15 and for the static Poisson (sat.) the mean value is 0.18. There is no correlation between the dynamic and static Poisson's ratio values. As such, it can be seen that the dynamic Poisson's ratio values do not allow conclusion about the static Poisson's ratio values because the deviations are too large. A further explanation for the deviation of the values may be due to fractures and vugs in rocks. This leads to errors in the determination of the static Poisson's ratio and thus the dynamic Poisson's ratio is more reliable.

These discontinuities may have a different influence on the ultrasonic velocities and uniaxial compression tests (MARTÍNEZ-MARTÍNEZ et al. 2012). MARTÍNEZ-MARTÍNEZ et al. (2012) conclude that compared to the static Young's Modulus, the dynamic Young's Modulus may be over- or underrated.

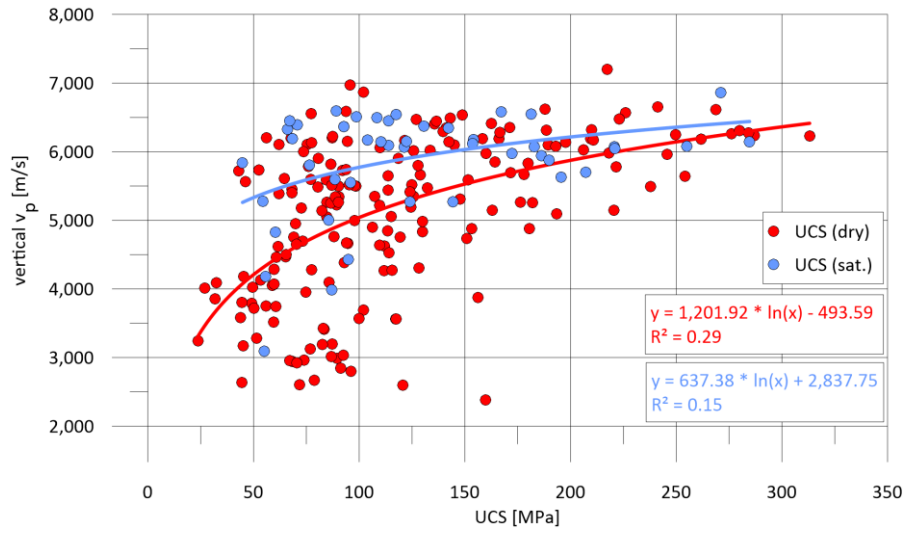


Fig. 55: UCS plotted against  $v_p$ -velocities of the carbonates from the Upper Jurassic aquifer.

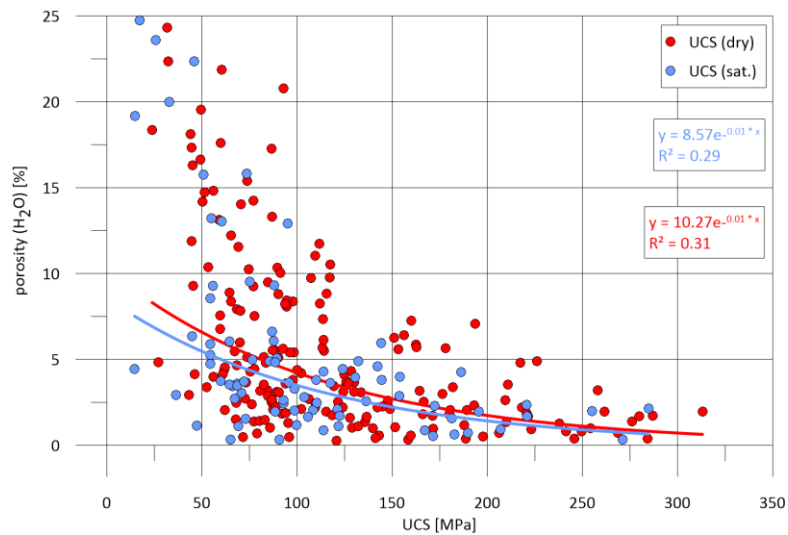


Fig. 56: UCS plotted against the porosity(H<sub>2</sub>O) of the carbonates from the Upper Jurassic aquifer.

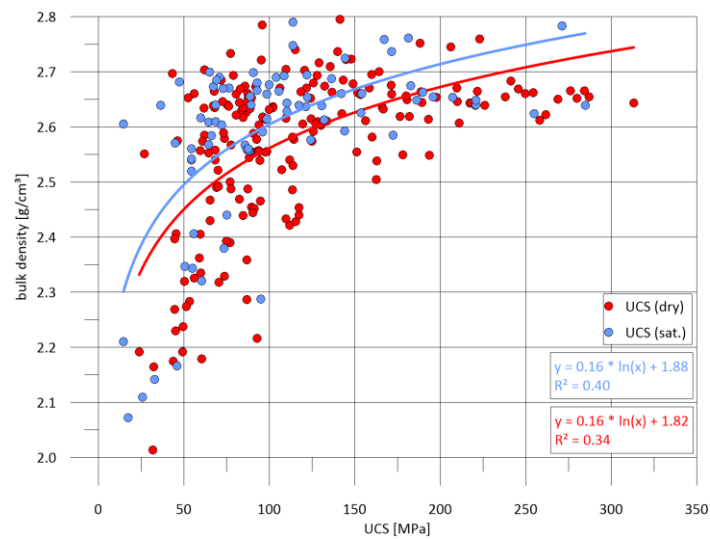


Fig. 57: UCS plotted against the bulk density of the carbonates from the Upper Jurassic aquifer.

Fig. 55 shows the correlation between the uniaxial compressive strength and the  $v_p$ -measurement results. The comparison of UCS and  $v_p$ -velocities displays a widespread variation. In general, the UCS values show a higher strength for core samples with higher  $v_p$ -velocities and vice versa.

With low uniaxial compressive strength, very heterogeneous  $v_p$ -measurement results are obtained. The low  $v_p$ -velocity values with the low UCS values show that there are inhomogeneities in the rock. These values correspond to the UCS range of 50–100 MPa and a  $v_p$ -velocity of approximately 3,000 m/s. The high  $v_p$ -measurements with the low UCS values show that no inhomogeneities can be detected in the rock by using the  $v_p$ -measurements. Therefore, it can be concluded that in the ultrasonic tests the discontinuities do not affect the velocities, but small discontinuities have a strong effect on the UCS values and reduce them. The limit of ultrasonic velocities is about 6,500–6,700 m/s. This velocity corresponds to the ultrasonic velocity in calcite 6,540 m/s (GEBRANDE et al. 1982) and 6,640 m/s (MAVKO et al. 2009).

Fig. 56 shows the correlation of UCS vs. porosity( $H_2O$ ). The porosity varies between 5 % to 25 % porosity mainly at UCS values up to 100 MPa. This can be attributed to the formation of the pores. At 75 MPa a strong scattering is observed. This can be attributed either to finely homogeneously distributed pores which have a distribution of pores similar to 20 % porosity or there are small number of large pores which are not homogeneously distributed and therefore have uniaxial compressive strengths of 50 MPa. The specimens with unconfined compressive strengths greater than 150 MPa are homogeneous specimens with low porosity. With these specimens a fast failure occurs. This figure shows that it is not possible to draw concise conclusions from one parameter or the other. The same result is found for the analogue samples in HEDTMANN & ALBER (2018). The porosity decreases with increasing uniaxial compressive strength. Several authors suggested empirical relations for carbonate rocks (e.g. FARQUHAR et al. (1994), CHANG et al. (2006)). These studies show a progressive weakening of the rocks with increasing porosity.

Fig. 57 shows that the compressive strengths also increase, if the bulk density is higher. The bulk density shows the same tendency as the porosity only in reverse. There are many measurements between 50 and 100 MPa which show a wide range in bulk density. The values which have a high density of around 2.6 to 2.7 g/cm<sup>3</sup> but low UCS values have wide inhomogeneities. These values should normally be at a lower density. This figure shows that it is not possible to draw conclusions from one parameter or the other but for UCS values above 200 MPa bulk density values lie above 2.6 g/cm<sup>3</sup>.

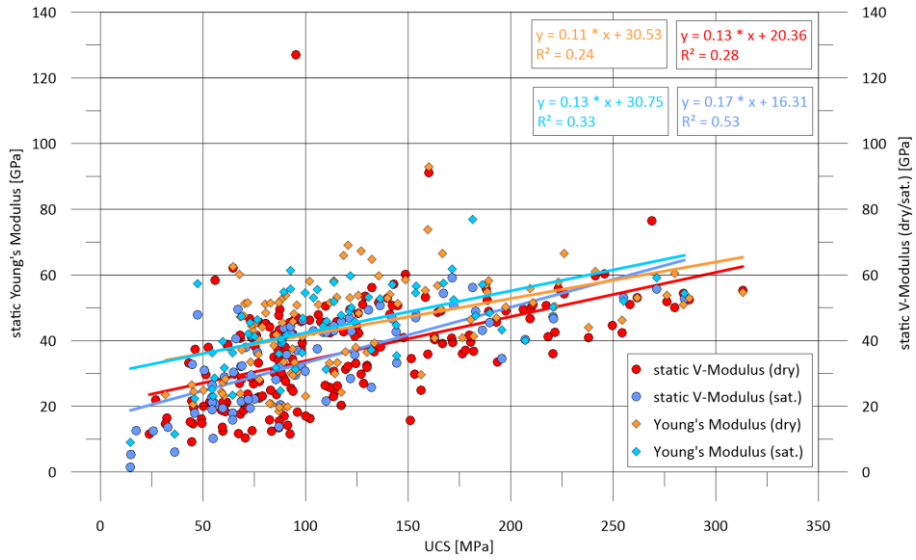


Fig. 58: UCS plotted against the Young's Modulus and the V-Modulus of the carbonates from the Upper Jurassic aquifer.

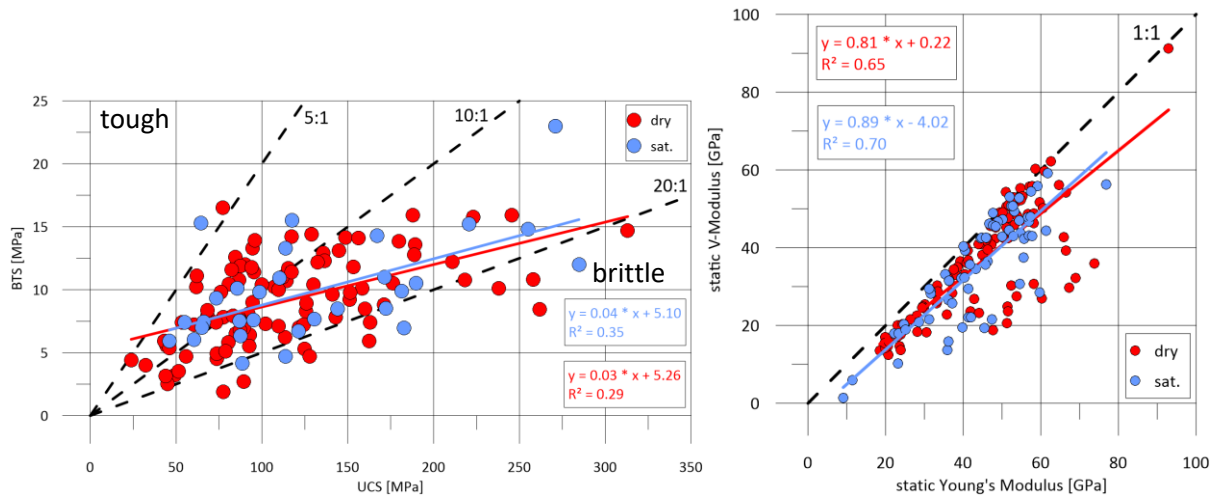


Fig. 59: UCS plotted against the BTS (left) and static Young's Modulus plotted against the V-Modulus (right) and of the carbonates from the Upper Jurassic aquifer.

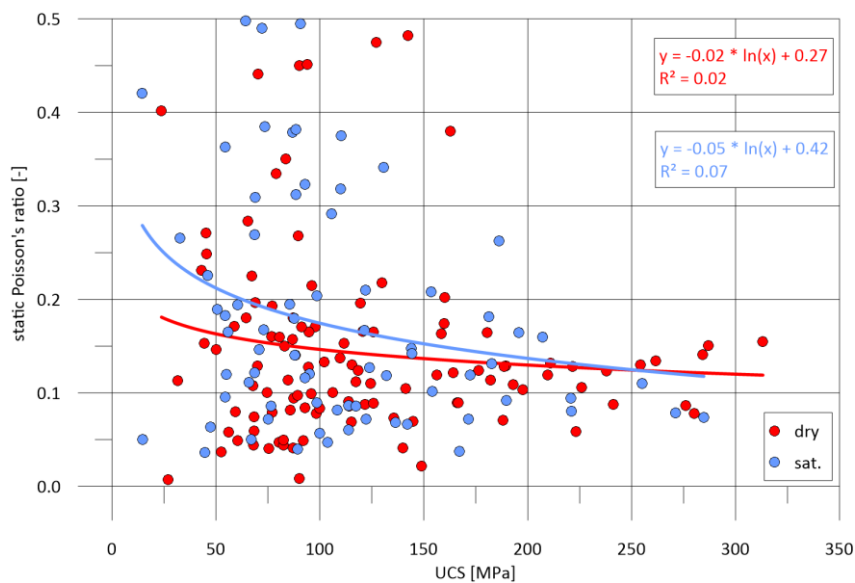


Fig. 60: UCS plotted against the static Poisson's ratio (right) of the carbonates from the Upper Jurassic aquifer.

Fig. 58 shows the correlation of the UCS vs. Young's Modulus and V-Modulus. Overall the values scatter between 50 and 150 MPa and a low correlation of the values can be seen. At UCS values above 150 MPa the dispersion decreases considerably. A tendency of UCS to higher stability of the rock with increasing Young's Modulus was described by CHANG et al. (2006). According to WILFING (2016), this classification can give a first indication of how rocks react to stress. This classification only represents the average modulus ratio of the samples, despite the observed different failure behaviour of the samples (WILFING 2016).

Fig. 59 (left) shows the correlation between UCS and BTS. The high uniaxial compressive strengths have a maximum Brazilian tensile strength of about 15 MPa. Samples with uniaxial compressive strengths of 250 MPa to 300 MPa and Brazilian tensile strengths of more than 10 MPa are homogeneous core samples without inhomogeneities like large pores which are brittle and prone to failure. With the help of the ratio of uniaxial compressive strength to Brazilian tensile strength the toughness coefficient of the rocks can be determined. According to SCHIMAZEK & KNATZ (1976) and THURO (1996) the examined core samples range by single outliers from very tough to very brittle (Fig. 59). However, most values plot in the typical brittle range of carbonates.

The V-Modulus is determined in the curve of the linear section of the stress-strain curve and the E-Modulus in the reloading curve of the linear section of the stress-strain curve.

At an ideal elastic behaviour, the V-Modulus complies with the E-Modulus. With a few exceptions, the Young's Moduli have higher values than the V-Moduli (Fig. 59, right). Most values have nearly a 1:1 correlation. These values can be found mainly in three wells: RW-1, RW-2 and W-3. These samples are from every lithology with different inhomogeneities except stylolites. Then the ratio spreads out to a 2:1 correlation. At these values, the V-Modulus is only half as large as the Young's Modulus. These values can be found in three wells: W-7, W-8 and W-9. These samples are limestones with a mean bulk density of  $2.71 \text{ g/cm}^3$ , stylolites, and healed fissures. The degree of correlation between the two moduli is high and lies between 1:1 and 2:1.

Fig. 60 shows no correlation between UCS and Poisson's ratio. A comparison between these parameters is difficult because the Poisson's ratio is determined in the elastic range of the stress-strain curve whereas the uniaxial compressive strengths only become apparent in the plastic range of the stress-strain curve. The highest UCS values are in the range between about 0.05 and 0.15 of the Poisson's ratio. At a high strength there is a low Poisson's ratio if the strength is not strongly lateral. These samples store the energy and then fail explosively. Samples with a Poisson ratio of 0.1 at 75 MPa show inhomogeneities. At low UCS values and higher Poisson's ratios, the samples increase laterally and then fail immediately.

### 2.2.5.2 Stratigraphy

A section of the drill cores examined in this thesis was investigated for porosity and permeability in BOHNSACK et al. (2020). The porosity of the Upper Jurassic aquifer can be divided into three stratigraphic subgroups: Malm Alpha to Gamma, Malm Delta to Epsilon, and Malm Zeta. This subdivision corresponds to BÖHM et al. (2013). The Upper Jurassic aquifer is surrounded by the overlying Purbeck and Dogger below.

The following porosity ranges were found in the investigated samples. Dogger consists of dolomitic limestones and dolostone and the porosity values range from 4.09 % to 16.32 % with a mean value of 9.20 %. Malm Alpha to Gamma consists mainly of limestone with a mudstone and wackestone facies with a mean porosity of 1.18 % and a dolomitic limestone layer with a porosity of 11.98 %. Malm Gamma has a small dolomitic area in the transition to Malm Delta. The mean porosity is 1.36 %. Malm Delta to Epsilon in this dataset consists solely of dolostones with a relatively low porosity (5.05 %). Malm Zeta 1 to Malm Zeta 5 has a very heterogeneous lithofacies and therefore contains both the lowest (0.15 %) and also the highest porosity (29.35 %). Purbeck consist of all types of lithologies and the porosity values range from 0.17 % to 25.31 % with a mean value of 8.62 %.

A few tendencies can be seen in the  $v_p$ -measurements (Fig. 61, left). Dogger has low mean  $v_p$  values and from Malm Alpha to Malm Zeta 2 a plateau appears. From Malm Zeta 2 to Zeta 4–5 a decrease in  $v_p$ -velocities is observed. The velocities for Purbeck are higher than the velocities for Malm Zeta 4–5.

In Malm Alpha to Gamma it was not possible to examine many core samples. For Malm Alpha 18 core samples were examined, for Malm Beta 14 core samples were examined and for Malm Gamma 15 core samples were examined. This small number of samples compared to Zeta 1 (38 samples) and Zeta 4–5 (85 samples) is probably a reason for the low scattering of results for Malm Alpha, Malm Beta and Malm Gamma.

The extreme outlier in Malm Alpha is the dolomitic lag emitting high porosity. The cores examined, however, show the high  $v_p$ -velocities as they have low porosity and can be taken from the micritic facies. The high  $v_p$ -velocities in Malm Delta and Malm Epsilon can be explained by the mostly fine grained dolomite. The range of variation results from the different dolomite sizes. The  $v_p$ -velocities decrease from Malm Zeta 1 to Malm Zeta 4–5. This can be explained by the heterogeneous lithology. Malm Zeta 3 has a small range of variation compared to the other drillings, because there is only limestone with a Mudstone facies.

The lowest  $v_p$ -velocities in Zeta 1 are found in the shallowest investigated well: RW-1. The cores of this well show open fissures. This material property of the core samples may be the reason for the low  $v_p$ -velocities. The lowest  $v_p$ -velocities in the Zeta 4–5 are found in the deepest well: W-9. These core samples have already experienced the greatest stress of all examined samples. Many healed fractures as well as stylolites were found in the cores of this well. This may be the reason for the low  $v_p$ -velocities despite the low mean porosity of 0.53 %.

The highest  $v_p$ -velocities of all samples are similar. For the samples with the highest  $v_p$ -velocities Malm Epsilon, Zeta 1 and Zeta 2 neither closed or healed fissures are visible. This also speaks for an influence

of this inhomogeneity on the  $v_p$ -velocity. All in all, it can be stated that the  $v_p$ -velocities against stratigraphy show a large dispersion and it is not possible to identify which stratigraphy is characterized by the  $v_p$ -velocities from the laboratory investigations.

The  $v_s$ -measurements in Fig. 61 (right) show a similar tendency. Dogger has low mean  $v_p$ -values and from Malm Alpha to Malm Zeta 2 a plateau appears. From Zeta 2 to 4–5 there is a tendency for the  $v_p$ -velocities to decrease. The velocities for Purbeck are higher than the velocities from Zeta 4–5, but overall, the differences between the minima and maxima of the  $v_s$ -velocities are smaller (3,868 m/s) than for the  $v_p$ -velocities (6,257 m/s). This does not apply to the stratigraphy with the low sample numbers. The same conclusions as described for  $v_p$ -measurement also apply here. All in all, it can be stated that the  $v_s$ -velocities against stratigraphy show a large dispersion and it is not possible to identify which stratigraphy is based on the  $v_s$ -velocities from the laboratory investigations.

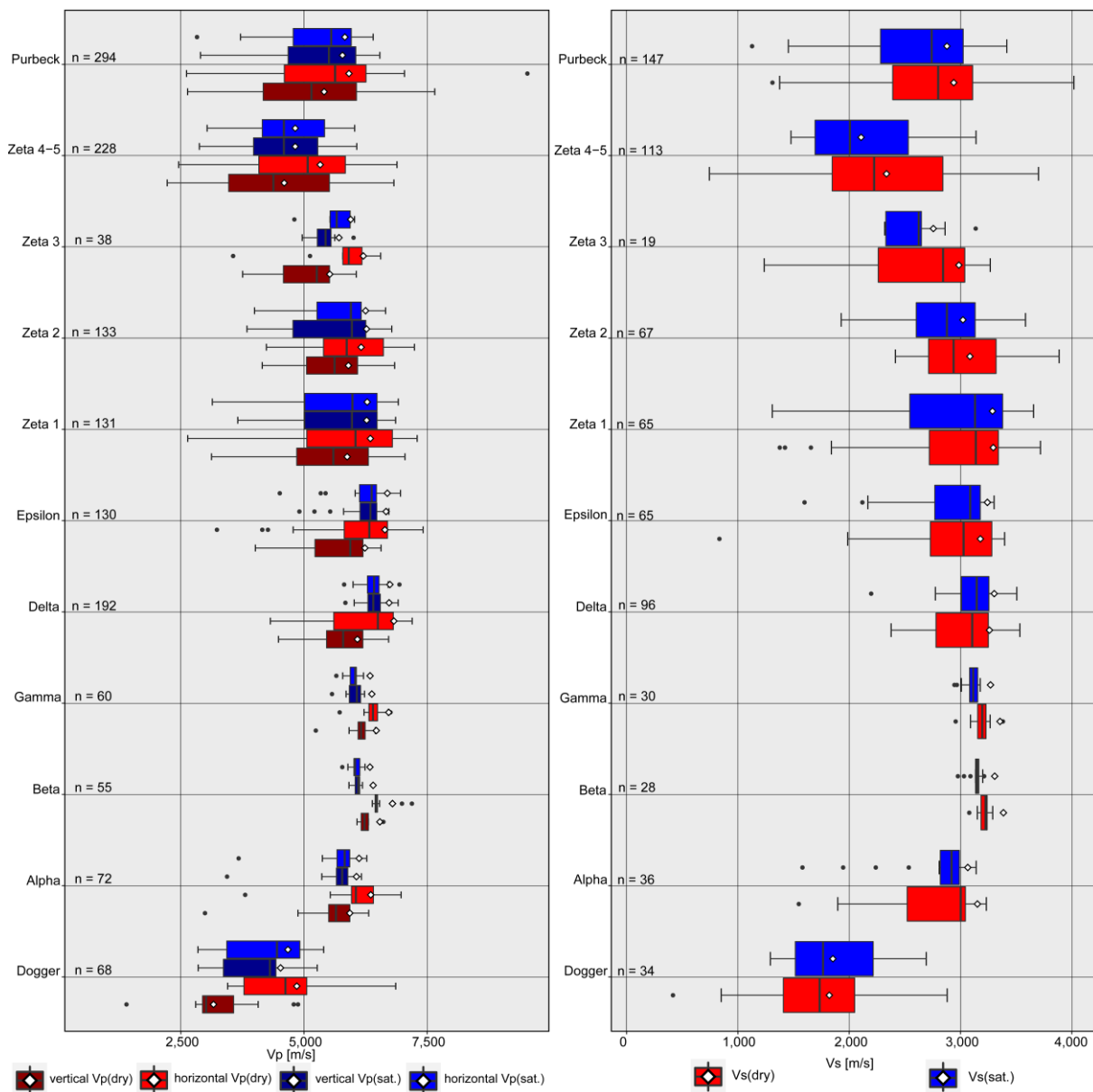


Fig. 61:  $v_p$ - (left) and  $v_s$ -velocity (right) of differently saturated core samples versus stratigraphy.

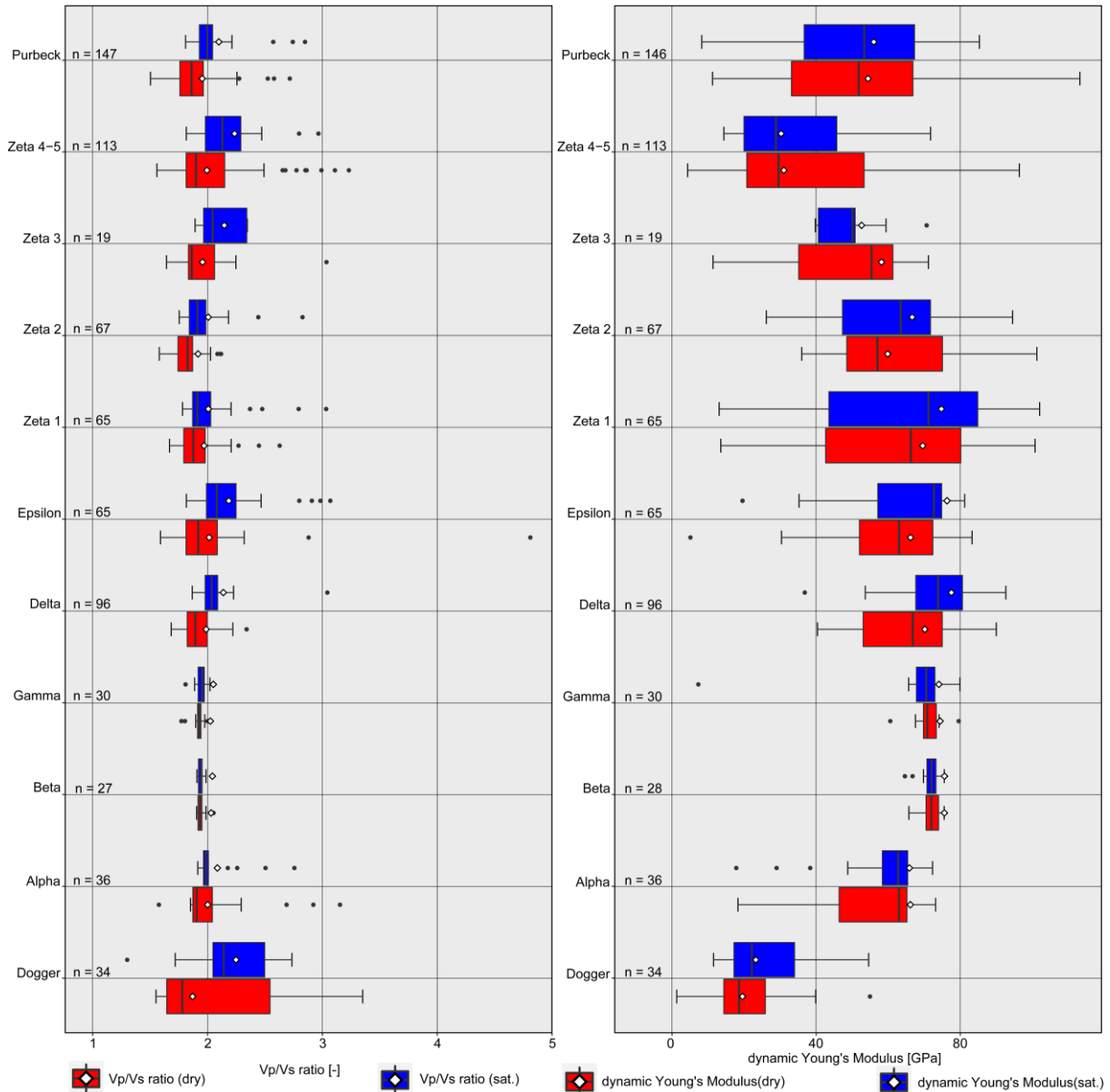


Fig. 62:  $v_p/v_s$  ratio (left) and dynamic Young's Modulus (right) of differently saturated core samples versus stratigraphy.

In Fig. 62 (left) the  $v_p/v_s$  ratio scatters to different extents in the different stratigraphies. Dogger consist of two lithologies (dolomitic limestones and dolostone) which may explain the broad value spread. The  $v_p/v_s$  ratio values for Malm Alpha to Gamma scatter significantly less than for Dogger. This can be attributed to the fact that these stratigraphic units consist of only one lithology (limestone). Malm Delta to Epsilon consist of a different lithology (dolostone) and show about the same range as Malm Alpha but a wider spread of values than Malm Beta and Gamma. The values scatter significantly less than for Dogger. Malm Zeta 1 to 5 have a very heterogeneous Lithology. The  $v_p/v_s$  ratio values of these lithologies show numerous outliers and scatter to varying degrees. Especially the  $v_p/v_s$  ratio of Malm Zeta 4–5 scatters to a similar extent as that of Dogger. All in all, it can be stated that the  $v_p/v_s$  ratio against stratigraphy does not allow the identification of the stratigraphy.

The same trends as described for Fig. 61 are also evident for the Young's Modulus (Fig. 62, right). This can be expected, since the Young's Modulus is calculated from the ultrasonic velocities. Larger differences in the dynamic Young's Modulus would have to be based on a difference in sample density. The density of the samples is relatively uniform between 2.6 g/cm<sup>3</sup> and 2.8 g/cm<sup>3</sup> (Fig. 57). Moreover, the ultrasonic velocity squared is included in the calculation of dynamic Young's Modulus (Eqn. 7) and thus plays a much greater role than the sample density. This explains why Young's Modulus is also unsuitable for characterizing stratigraphy.

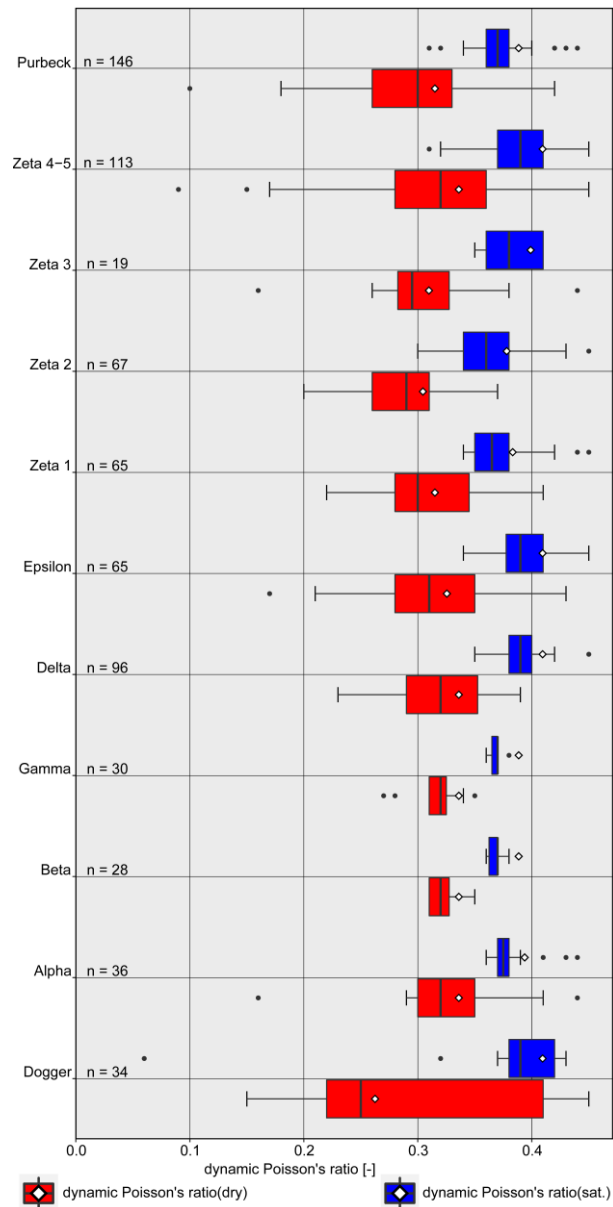


Fig. 63: Dynamic Poisson's ratio of differently saturated core samples versus stratigraphy.

According to literature, the Poisson's ratio increases with well depth (PENG & ZHANG 2007). This trend cannot be seen for the samples from the Upper Jurassic aquifer. This may be due to the fact that the literature calculates values from borehole measurement values (logs). The rocks examined there at depth are under a higher stress and therefore cannot be deformed as much as those samples examined in the laboratory that were not under that high amount of stress.

The number of samples (250) used in the destructive tests is significantly lower than the number of samples (404) used in the non-destructive tests. Here, the number of samples examined (Malm Alpha (18), Beta (14) to Gamma (9)) does not differ so significantly from the number of samples examined from Malm Zeta 1 (17) and Zeta 4–5 (50). The differences in the scattering width of the samples are also significantly smaller.

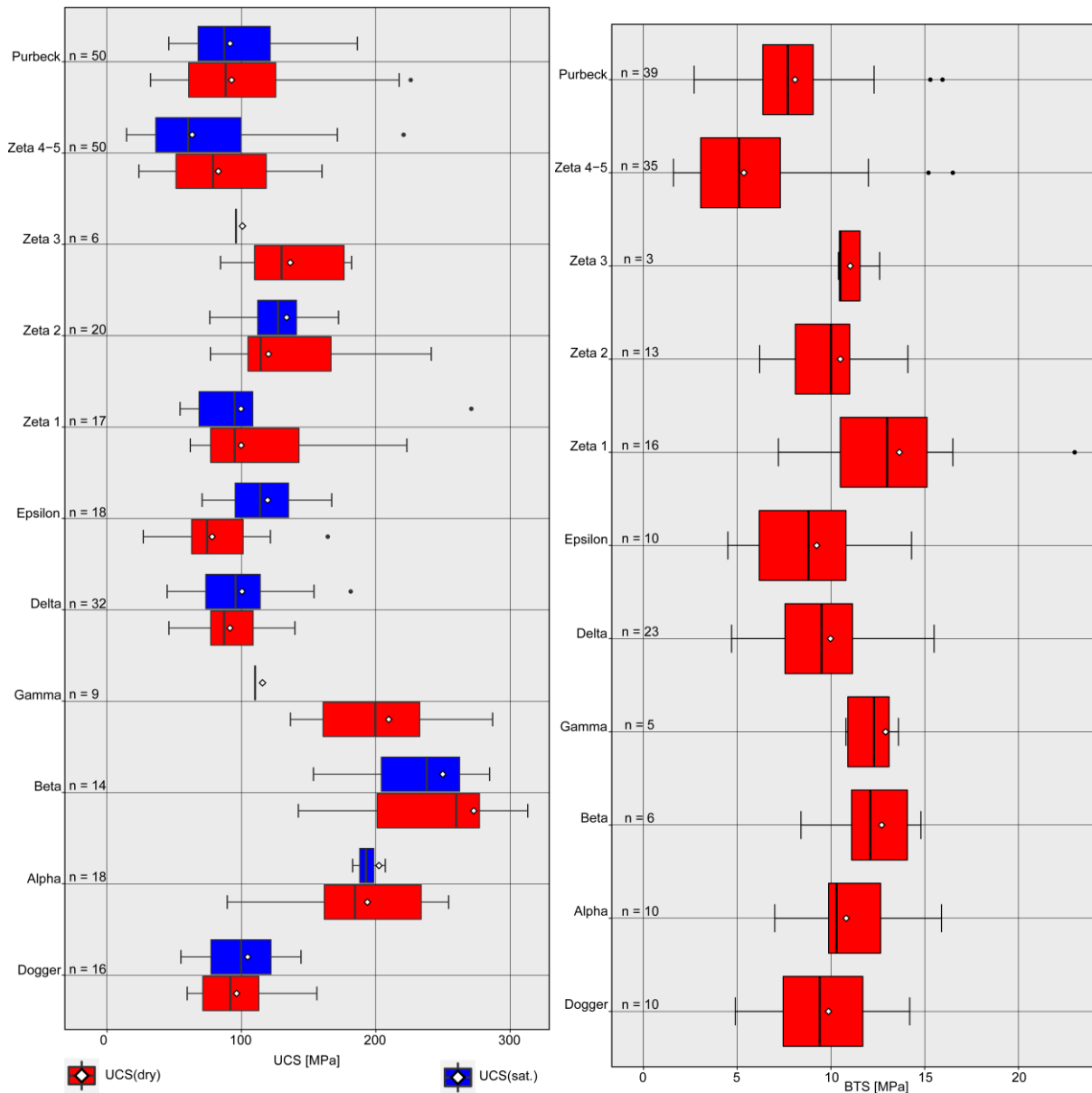


Fig. 64: UCS (left) and BTS (right) of differently saturated core samples versus stratigraphy.

Dogger has low UCS values in the destructive tests (Fig. 64, left). In Malm Alpha to Gamma the highest values are found. This in turn can be explained by the low porosity and the high density of the core samples. These stratigraphies consist of limestone. The high strength of limestone with a fine particle size is generally known. This is confirmed for the observed stratigraphy as it consists of a mudstone facies. In Malm Delta and Epsilon the examined mean values are low. This is unexpected because higher dolomite rocks should have higher values. This finding may be explained by small and large vugs found in the samples. The interquartile range (IQR) increases by trend from Malm Delta to Malm Zeta 3. Malm Zeta 4–5 has the lowest IQR. The saturated UCS values for Zeta 1 show the widest dispersion. Here the samples range from fine crystalline dolostones with low porosity from research well RW-2 (1,333 mTVD) to medium crystalline dolostones with medium porosity from the research well RW-1 (397 mTVD). In Malm Gamma and Malm Zeta 3, only one sample each could be determined for the saturated measurements. The IQR of Purbeck corresponds to Dogger. A comparison of the UCS values with analogue samples described in HOMUTH (2014) shows similar tendencies when comparing the individual stratigraphies, although lithologies and facies are different between the core samples and the analogue samples.

Fig. 64 (right) shows the correlation of BTS to stratigraphy. No trend can be observed but the BTS values of nearly all samples are below 15 MPa. From Malm Alpha to Gamma, the mean value of the Brazilian tensile strength increases (Fig. 64, right). Malm Delta and Epsilon values correspond to Purbeck and Dogger values. From Zeta 1 to Zeta 5, with the exception of Malm Zeta 3, there is a decrease in the Brazilian tensile strength. The BTS values for Zeta 1 show the widest dispersion. In all cases, these are fine crystalline dolostones from well RW-2. There are also no differences in the material properties (cracks, vugs). These are fine dolostones, which have a low porosity. The cracks and vugs are evenly distributed over the samples of Zeta 1. Very few Brazilian tensile tests could be performed in Malm Zeta 3(3) and Malm Gamma (5). The differences in the distribution can be traced back to the number of samples.

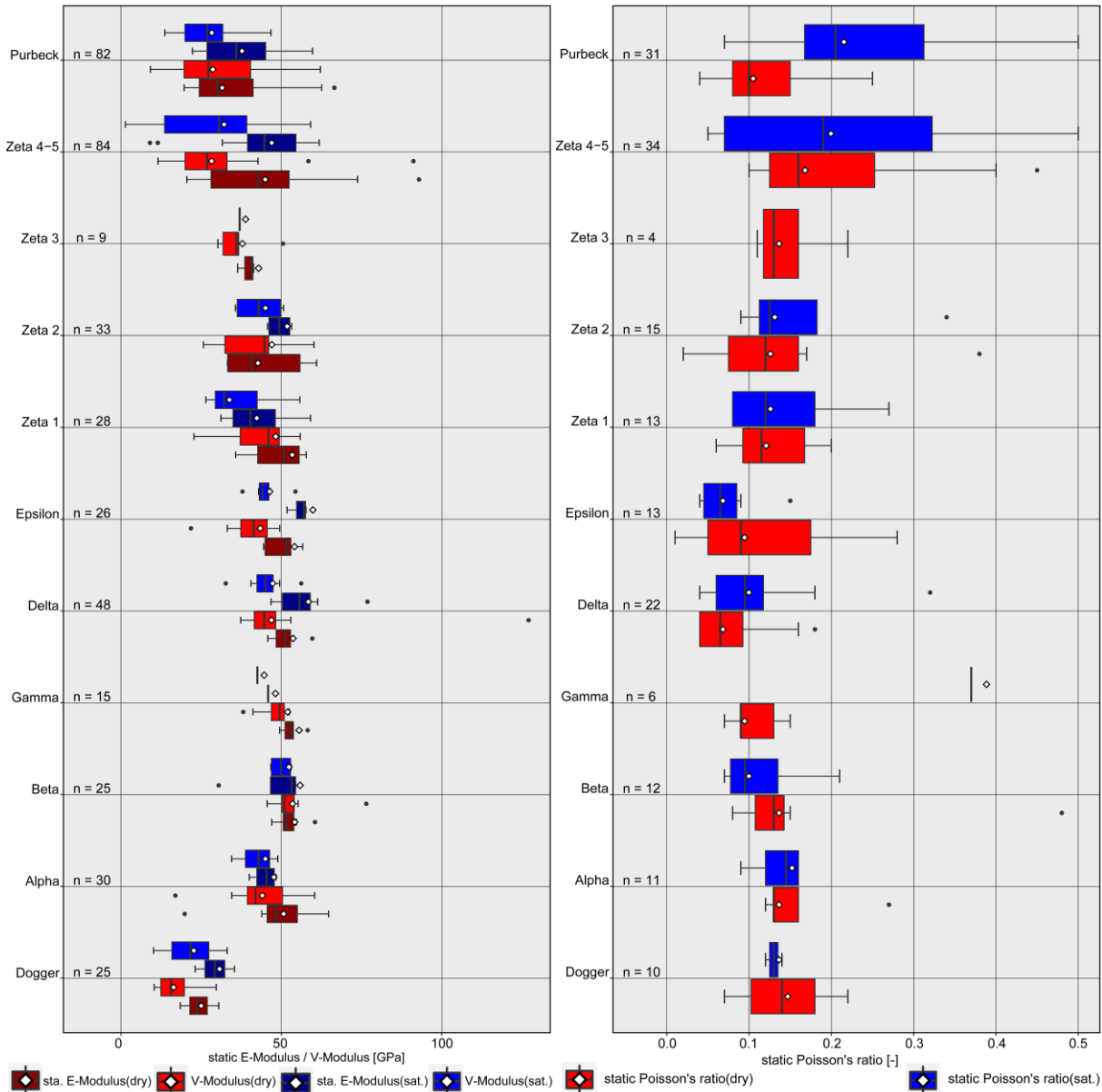


Fig. 65: Static Young's Modulus and V-Modulus (left) and static Poisson's ratio (right) of differently saturated core samples versus stratigraphy.

Fig. 65 (left) shows the correlation of static Young's Modulus and the V-Modulus against the stratigraphy. The values for the static Young's Modulus and the V-Modulus scatter in all stratigraphic units. The measured values for Dogger are low compared to the other stratigraphies. For Malm Alpha to Gamma, the largest mean values are achieved for the moduli around 50 GPa. The high moduli can be attributed to the highest uniaxial compressive strengths in this stratigraphy. From Malm Alpha to Gamma a slight increase in the Young's Modulus and V-Modulus mean values can be observed. From Malm Delta and Epsilon the values remain almost unchanged. From Zeta 1 to Zeta 3 a decrease of the Young's Modulus and V-Modulus values can be identified. No distinction can be drawn between Zeta 4–5 and Purbeck. The tendency of the saturated Young's Modulus and V-Modulus values does not differ from the unsaturated values. The correlation of Vstat(dry) and Estat(dry) is low for Malm Zeta 4–5.

There is no clear trend between the spread of dry and saturated static Poisson's ratio values and stratigraphy (Fig. 65, right). The variance of the values for the static Poisson's ratio decreases with increasing depth. For Malm Alpha to Gamma, low values are found. For Malm Zeta 3 and Malm Gamma only one sample could be measured. This can be attributed to the high strength of the samples. An overall comparison of Fig. 65 (right) shows that the dispersion of the static Poisson's ratio values decreases with increasing depth. The great variation of the static Poisson's ratio may be due to the inhomogeneities of the carbonates.

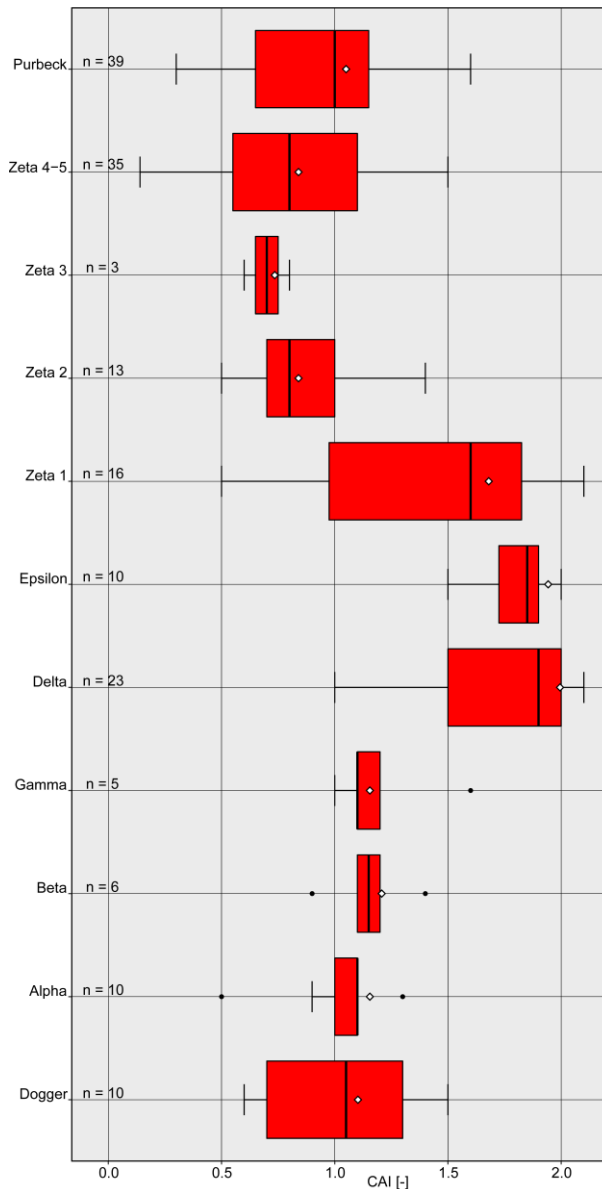


Fig. 66: CAI versus stratigraphy.

increased roughness, because if CAI is determined via a sheared pore, the porosity triggers the surface roughness. Overall, clear differences can be seen in the stratigraphy but a correlation of CAI values to stratigraphy is not found.

The abrasivity of all rocks investigated (Fig. 66) falls into the medium to abrasive category (Cerchar 1986). The CAI values increase from Malm Alpha (value of 1.1) to Malm Delta (value of 1.9). Malm Delta and Malm Epsilon form a plateau. From Malm Epsilon (value of 1.9) to Malm Zeta 3 (value of 0.7) the mean values decrease, with Malm Zeta 1 values spread over a range of 0.5 to 2.0. For Malm Zeta 4–5 there is a mean value of 0.7. Dogger and Purbeck spread over a wide range from a minimum value of 0.3 to maximum value of 1.6. Over all, abrasivity values are low within the tested range of carbonate rocks.

For Malm Alpha to Gamma, the core samples have low porosities and are fine-grained so they have a smooth surface after the BTS test and CAI values of 1 are determined.

As expected, the highest CAI values are found in Malm Delta and Epsilon, where the dolomite crystals are found. These samples show a porosity between 1.3 and 8.5 %. All samples are fine crystalline dolostones from well RW-2. Due to the high porosity there are vugs of different sizes in the samples which leads to a different inhomogeneity in the rock. In the case of fine-grained dolomite samples with a high uniaxial compressive strength and 20 % porosity, uneven surfaces and strong spreading occur. This leads to an increased roughness, because if CAI is determined via a sheared pore, the porosity triggers the surface roughness.

### 2.2.5.3 Lithology

Heterogeneous lithological characters can exist in the same stratigraphy (BOHNSACK et al. 2020). E.g. core samples from Malm  $\zeta$  4–5 have all the same primary lithology and facies but are dolomitized to varying degrees (Fig. 67). The dolomitization has an affect on the rock density (limestone: 2.73 g/cm<sup>3</sup>; dolomitic limestone: 2.77 g/cm<sup>3</sup>; dolostone: 2.85 g/cm<sup>3</sup>) as well as porosity (limestone: 2.4 %; dolomitic limestone: 15.0 %; dolostone: 16.4 %) (BOHNSACK et al. 2020). This variance also affects the geomechanical values.

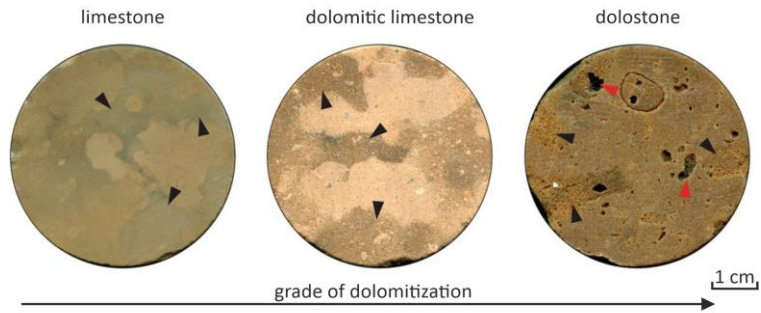


Fig. 67: Bioturbated wackestones from well RW-1 (left) and well RW-2 (middle and right) demonstrate the varying grade of dolomitization which leads to an increasing porosity mod. after BOHNSACK et al. (2020).

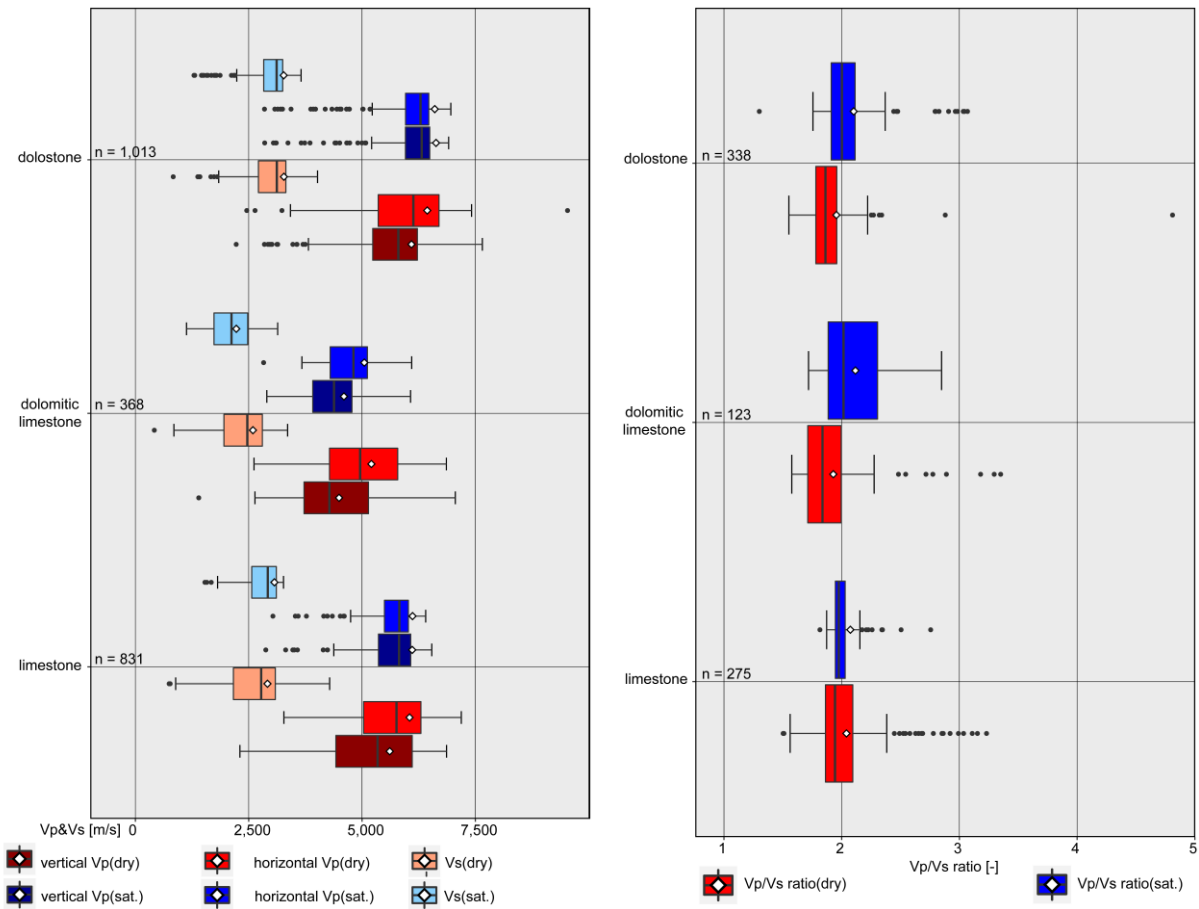


Fig. 68:  $v_p$ - and  $v_s$ -velocities (left) and  $v_p/v_s$  ratio (right) of differently saturated core samples versus lithology.

Fig. 68 (left) shows the correlation between  $v_p$ - and  $v_s$ -velocities and lithologies. The mean values of the three respective lithologies differ around 500 m/s. The  $v_p$ -velocities increase from dolomitic limestone via limestone to dolostone. The  $v_s$ -velocities of the different lithologies display the same trend as the  $v_p$ -velocities. For saturated limestone and dolostone samples, the ultrasonic velocities are higher than for dry samples. This tendency cannot be observed for dolomitic limestones. In all lithologies the dry horizontal measurements have higher mean values than the dry vertical measurements. Core samples which contain stylolites show a higher horizontal than vertical  $v_p$ -velocity.

Numerous outliers can be found in the saturated limestone. In the dolostone, outliers are found in both the dry samples and the saturated samples. All outliers are found below the lower quartile. These outliers are found in Dogger, Malm Zeta 1, Malm Zeta 4–5 and Purbeck as shown in Fig. 61.

Altogether certain trends in the lithology can be seen, but they cannot be assigned to a certain lithology because the values are widely scattered. For the analogue samples in HEDTMANN & ALBER (2018) compared dry and saturated limestone and dolostone. The  $v_p$ -velocities for dry and saturated limestone range around 6,000 m/s and the  $v_s$ -velocities are significantly lower. In contrast to the present findings the dolostone shows lower  $v_p$ - and  $v_s$ -velocities than the limestone.

It is not possible to automatically deduce the lithology from a  $v_p$ -velocity measured in the laboratory. In comparison to stratigraphy it is shown that a more precise description of the samples leads to a better recognition of trends.

Fig. 68 (right) shows the correlation of the  $v_p/v_s$  ratio to the lithology. The water saturated mean value for limestone is 1.98 and for dolostone is 2. According to PICKETT (1963) the  $v_p/v_s$  ratio for water saturated limestones is 1.9 and the  $v_p/v_s$  ratio for water saturated dolostones is 1.8. These values cannot be confirmed by the laboratory tests. These correlate better to the dry mean values (limestone: 1.94 and dolostone: 1.86) shown in Fig. 68 (right). Through dolomitization, a limestone can be completely altered into a dolostone. If the rock is only partially altered, it is called dolomitic limestone. This explains the wide dispersion of  $v_p/v_s$  ratio values found.

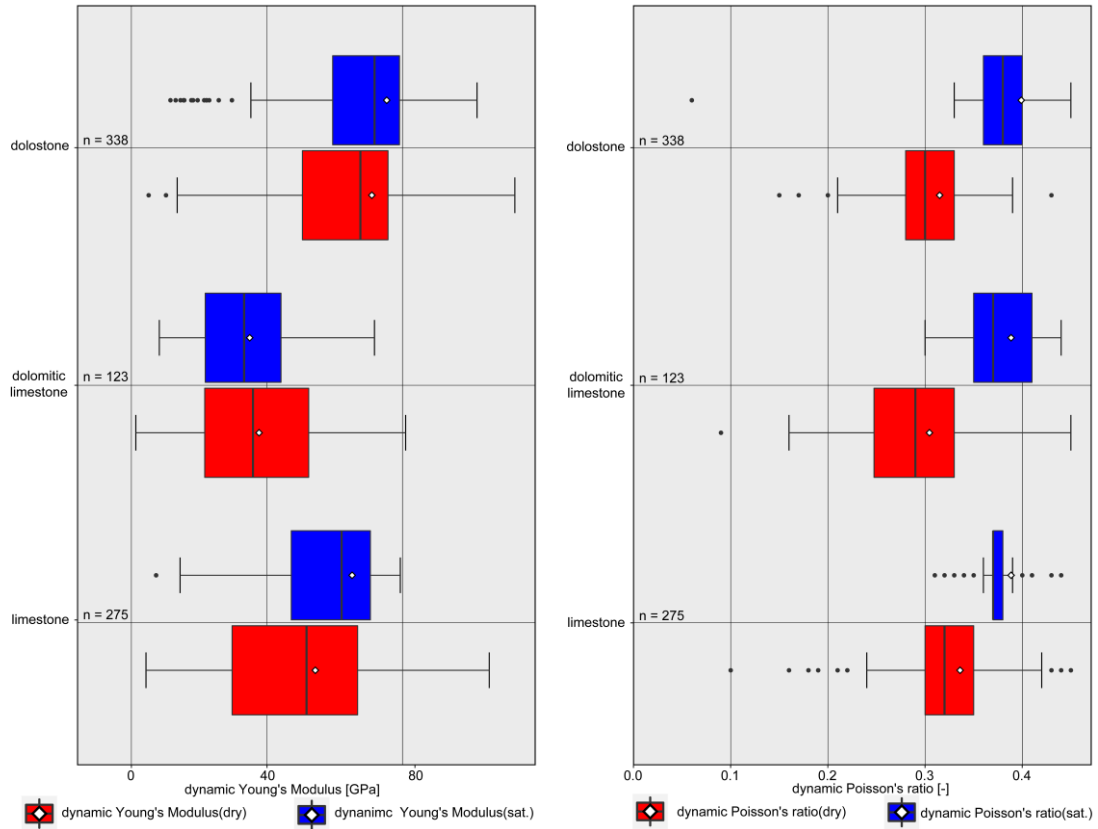


Fig. 69: Dynamic Young's Modulus (left) and dynamic Poisson's ratio (right) of differently saturated core samples versus lithology.

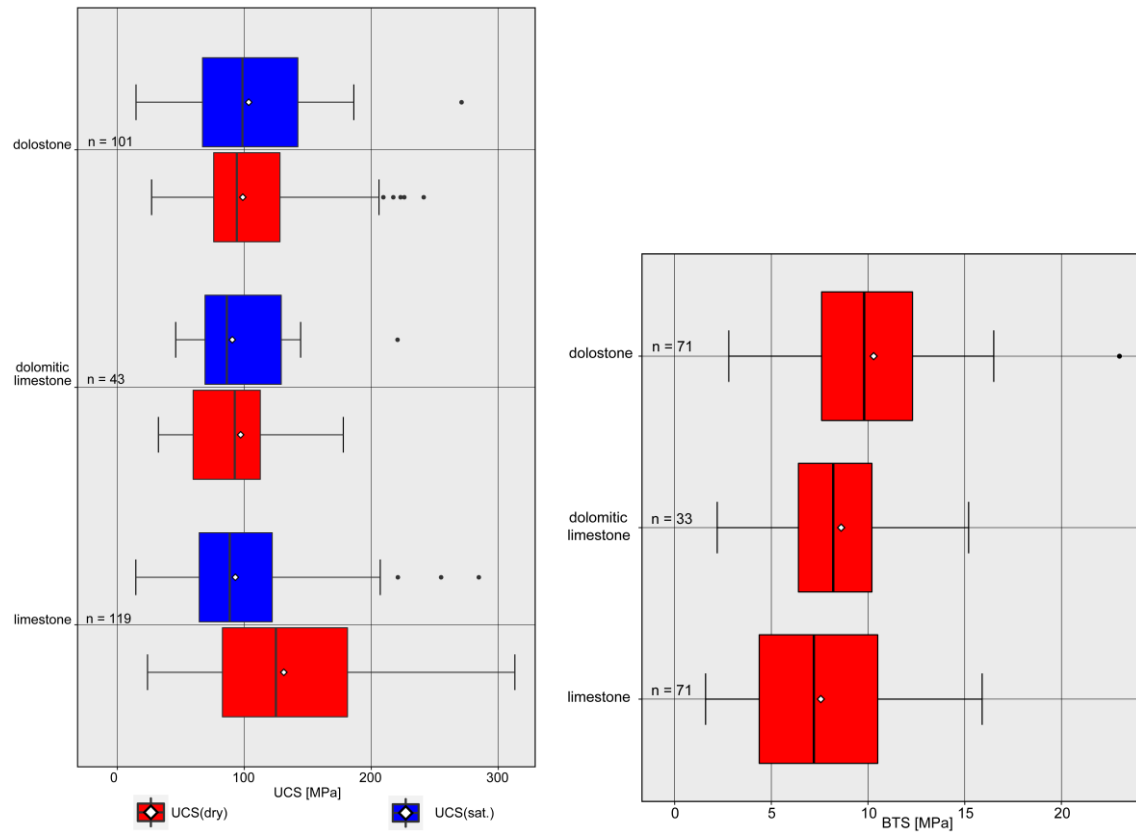


Fig. 70: UCS of differently saturated core samples (left) and BTS (right) versus lithology.

The same trends as described for  $v_p$ - and  $v_s$ -velocities (Fig. 68, left) are also evident for the dynamic Young's Modulus (Fig. 69, left). This can be expected, since the dynamic Young's Modulus is calculated from the ultrasonic velocities. The values scatter over a wide range, independent of the lithology. The outliers for the dolostone do not show irregularities with regard to inhomogeneities with regard to the other dolostone samples.

The general trend that the saturated dynamic Poisson's ratio is higher than the dry dynamic Poisson's ratio is also found in Fig. 69 (right). Therefore, there is no difference in the dynamic Poisson's ratio between the different lithologies.

The mean values found for both parameters correspond very well to the mean values from analogue samples of MRAZ et al. (2018).

The mean UCS values of all three lithologies are similar (Fig. 70, left). A differentiation of the lithologies on the basis of the values is not possible. The examined core samples can be classified as hard to very hard according to ISRM (1978). The mean values for all lithologies range from 90 MPa to 130 MPa. This range is smaller than the range 80 MPa to 250 MPa found by THURO et al. (2019).

Limestone values above 250 MPa are mudstone facies with a very low porosity. These values are higher than the values (maximum 143 MPa) known from analogue samples of TONDERA et al. (2013). HOMUTH (2014) finds an broadest range from 60 MPa to 310 MPa for analogue limestone samples. These ranges, as in this thesis, are the broadest ranges of all lithologies. The UCS values in each lithology do not correlate to inhomogeneities in the core samples.

The Brazilian tensile strength values of the three lithologies are very similar (Fig. 70, right). The mean BTS values increase from limestone via dolomitic limestone to dolostone. The maximum BTS values in all lithologies are about 15 MPa. This corresponds very well to the data from analogue samples in TONDERA et al. (2013) and THURO et al. (2019). On the basis of the BTS, the lithologies cannot be distinguished.

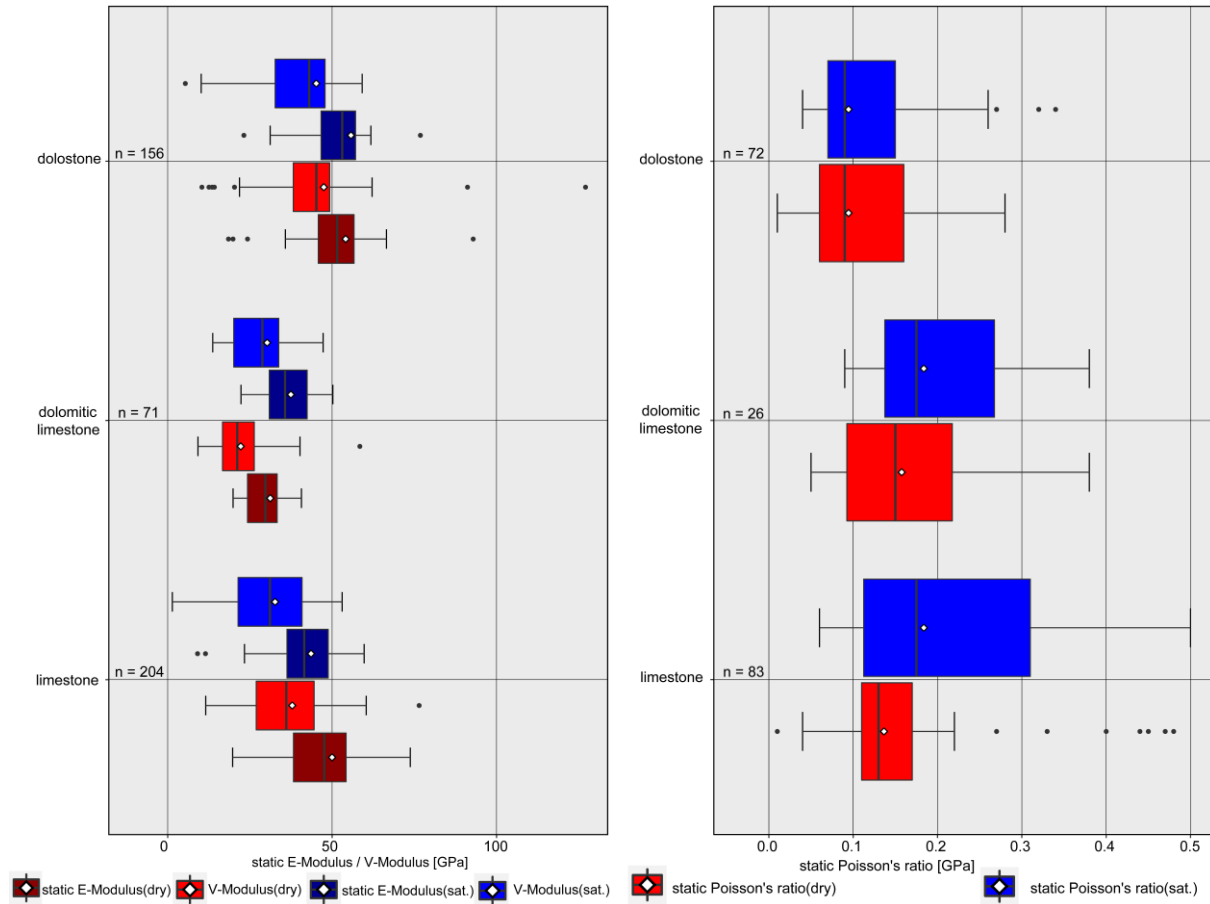


Fig. 71: Static Young's Modulus and V-Modulus (left) and static Poisson's ratio (right) of differently saturated core samples versus lithology.

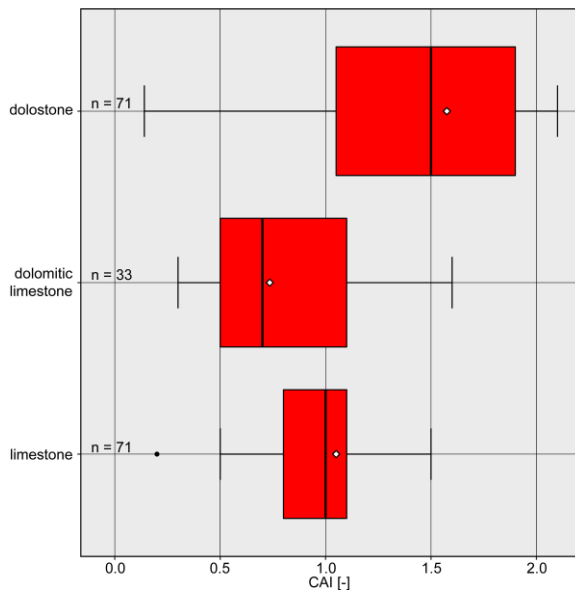


Fig. 72: CAI versus lithology.

The mean values of the static Young's Modulus and V-Modulus increase from dolomitic limestone, to limestone and then on to the dolostone (Fig. 71 left ). As expected, the measured Young's Moduli are higher than the V-Moduli. The measured static Young's Moduli (Fig. 71 left) match the dynamic Young's Moduli (Fig. 69 left).

The static Poisson's ratio is constant for saturated and dry dolostone. This also applies to the mean Poisson's ratio for saturated limestone, which is higher than the mean of the Poisson's ratio for un-saturated limestone.

Fig. 72 shows that the dolostone has the highest abrasivity values of all lithologies. To draw conclusions from the CAI values to a special lithology is hardly possible.

### 2.2.5.4 Facies

For further specification, the lithology was divided into its facies types.

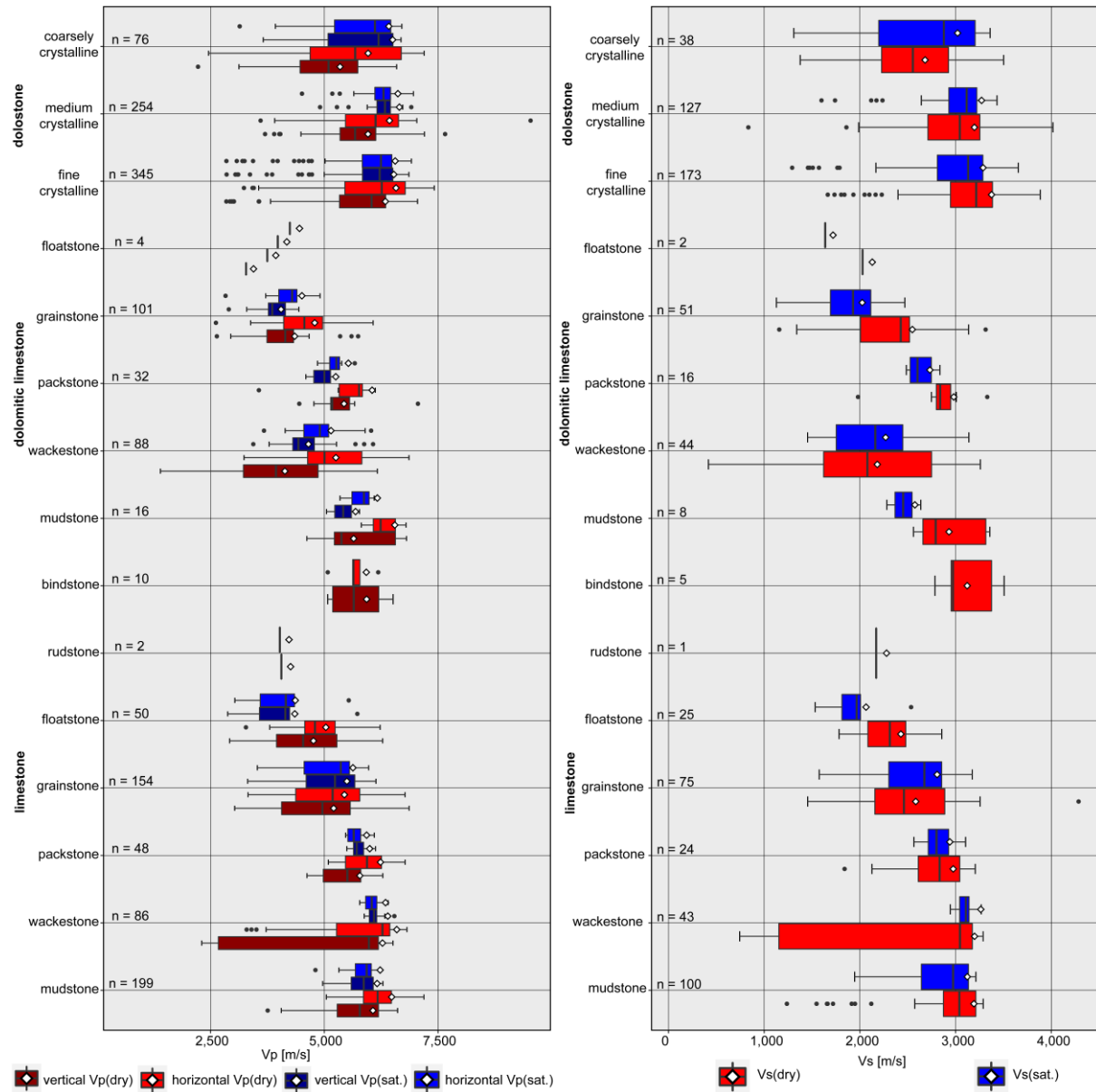


Fig. 73:  $v_p$ -velocities (left) and  $v_s$ -velocities (right) of differently saturated core samples versus facies.

Fig. 73 (left) shows a correlation of the  $v_p$ -velocity to facies of the different lithologies. The  $v_p$ -velocities in each lithology decrease with the increasing particle size. This is clearly evident for the dolomitic limestone (Fig. 73, left). The same applies to the limestone, although the unexpectedly high value for the bindstone is out of the range (Fig. 73, left). This result may be explained by the unexpectedly low porosity values and the high bulk density values. The lowest  $v_p$ -velocities in wackestone are from core samples from the deepest well: W-9. These core samples have already experienced the greatest stress of all examined samples. Many healed fractures as well as stylolites were found in the cores of this well. This may be the reason for the low  $v_p$ -velocities despite the low mean porosity of 0.53 % and the fine particle size of these samples. For the dolostone, only a lower tendency in the above-mentioned direction can be observed. With the exception of the mentioned bindstone, the decreasing  $v_p$ -velocity value correlates with a decreasing bulk density of the samples or the increasing porosity of the samples. However, the  $v_p$ -velocities increase with increasing fineness of the material. Only one sample each of the rudstone (limestone) and the floatstone (dolomitic limestone) could be measured.

The same tendencies as observed for the  $v_p$ -velocities (Fig. 73, left) can also be noticed for the  $v_s$ -velocities Fig. 73 (right). The wackestone has an exceptionally wide  $v_s$ -velocity spread in both the limestone and dolomitic limestone. Half of the readings for the wackestone (limestone) came from the well W-9. These values are also the lowest measured values for this facies. These core samples have already experienced the greatest stress of all examined samples. Many healed fractures as well as stylolites were found in the cores of this well. This may be the reason for the low  $v_p$ -velocities despite the low mean porosity of 0.53 % and the fine particle size of these samples. There are no such inhomogeneities for the wackestone (dolomitic limestone).

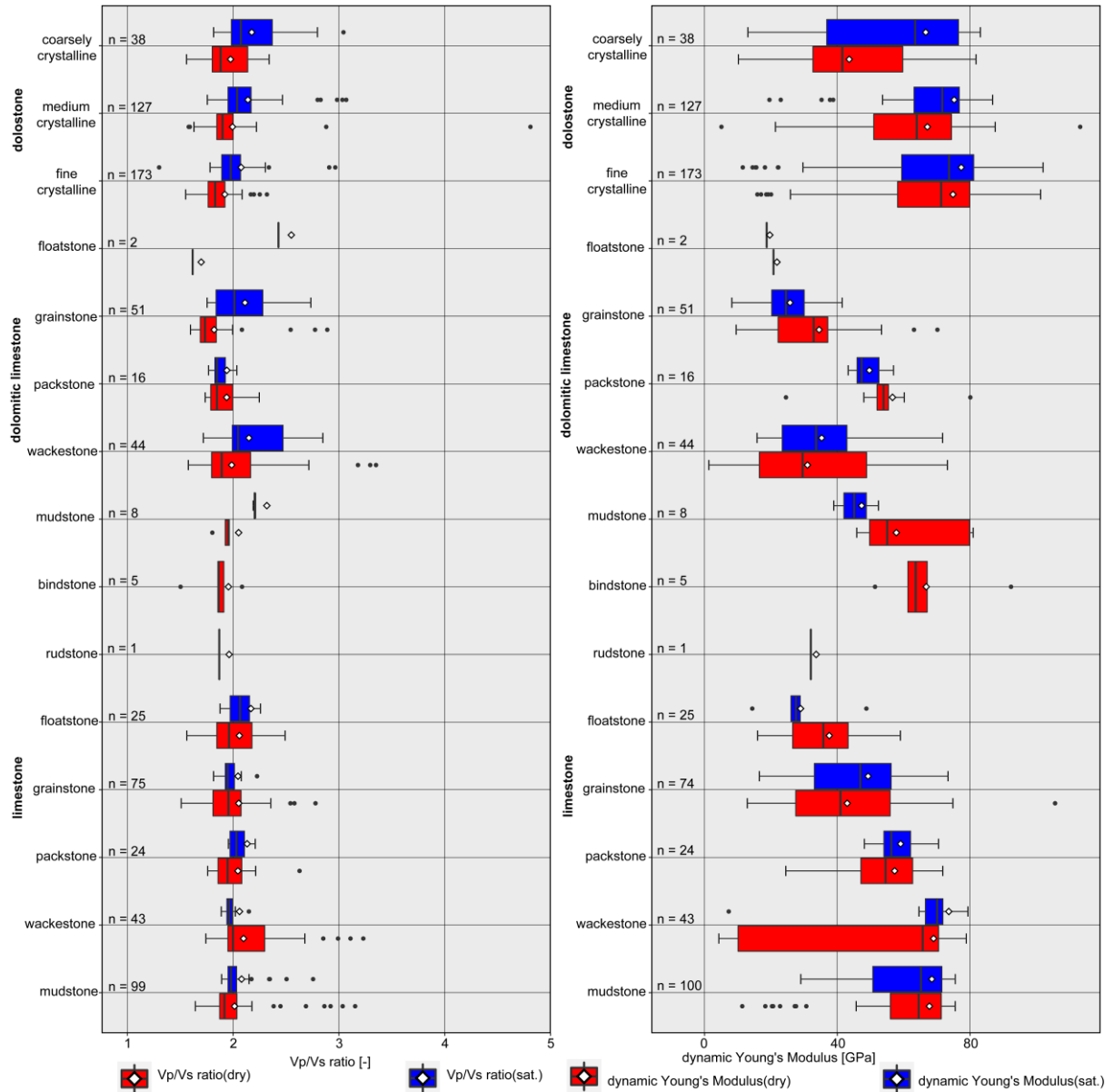


Fig. 74:  $v_p/v_s$  ratio (left) and dynamic Young's Modulus (right) of differently saturated core samples versus facies.

Fig. 74 (left) shows the correlation of the  $v_p/v_s$  ratio versus facies and the associated lithology. There is no correlation of  $v_p/v_s$  ratio to facies/lithology. A correlation of facies/lithology to  $v_p/v_s$  ratio is not possible.

The same trends as described for Fig. 73 are also evident for the dynamic Young's Modulus (Fig. 74, right). This is to be expected, since the dynamic Young's Modulus is calculated from the ultrasonic velocities. If there is little homogeneity and a small particle size, higher strengths are achieved and the material fails as brittle failure and has higher dynamic Young's Modulus values.

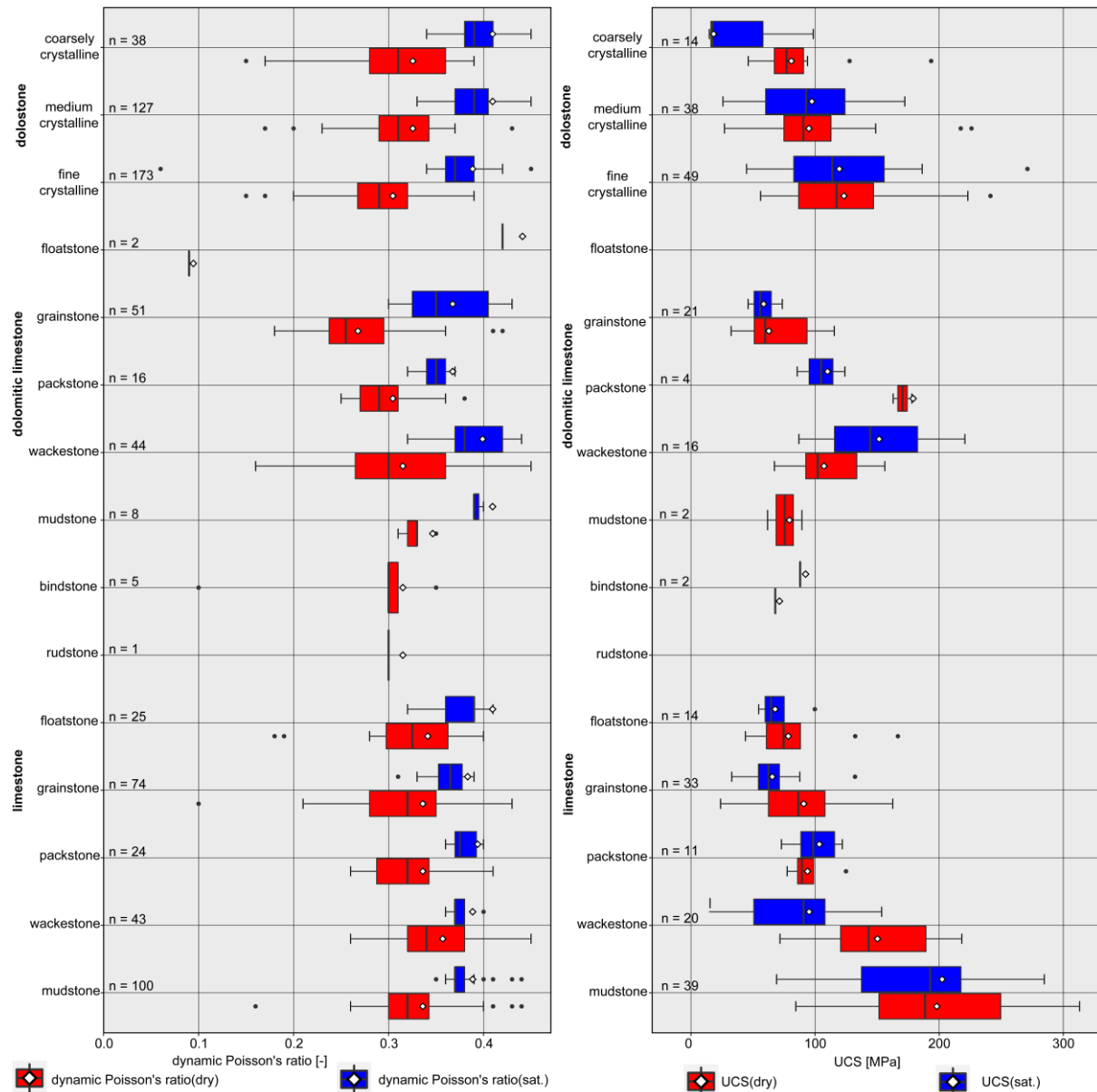


Fig. 75: Dynamic Poisson's ratio (left) and UCS (right) of differently saturated core samples versus facies.

The trend that the saturated dynamic Poisson's ratio is higher than the dry dynamic Poisson's ratio is also present in Fig. 75 (left). There is no tendency between the different facies types. The dynamic Poisson's ratio does not correlate with the different facies types of the different lithologies. For some facies types no dynamic Poisson's ratio could be determined.

The UCS values decrease with increasing particle size (Fig. 75, right). This trend is evident in both lithologies, limestone and dolostone. For dolomitic limestone the trend is uncertain. This may result from a different dolomitization depending on the facies type or from the low number of samples investigated. Only dry experiments could be carried out on the mudstone of the dolomitic limestone. The different degrees of saturation of the samples do not lead to different results in the uniaxial compression tests.

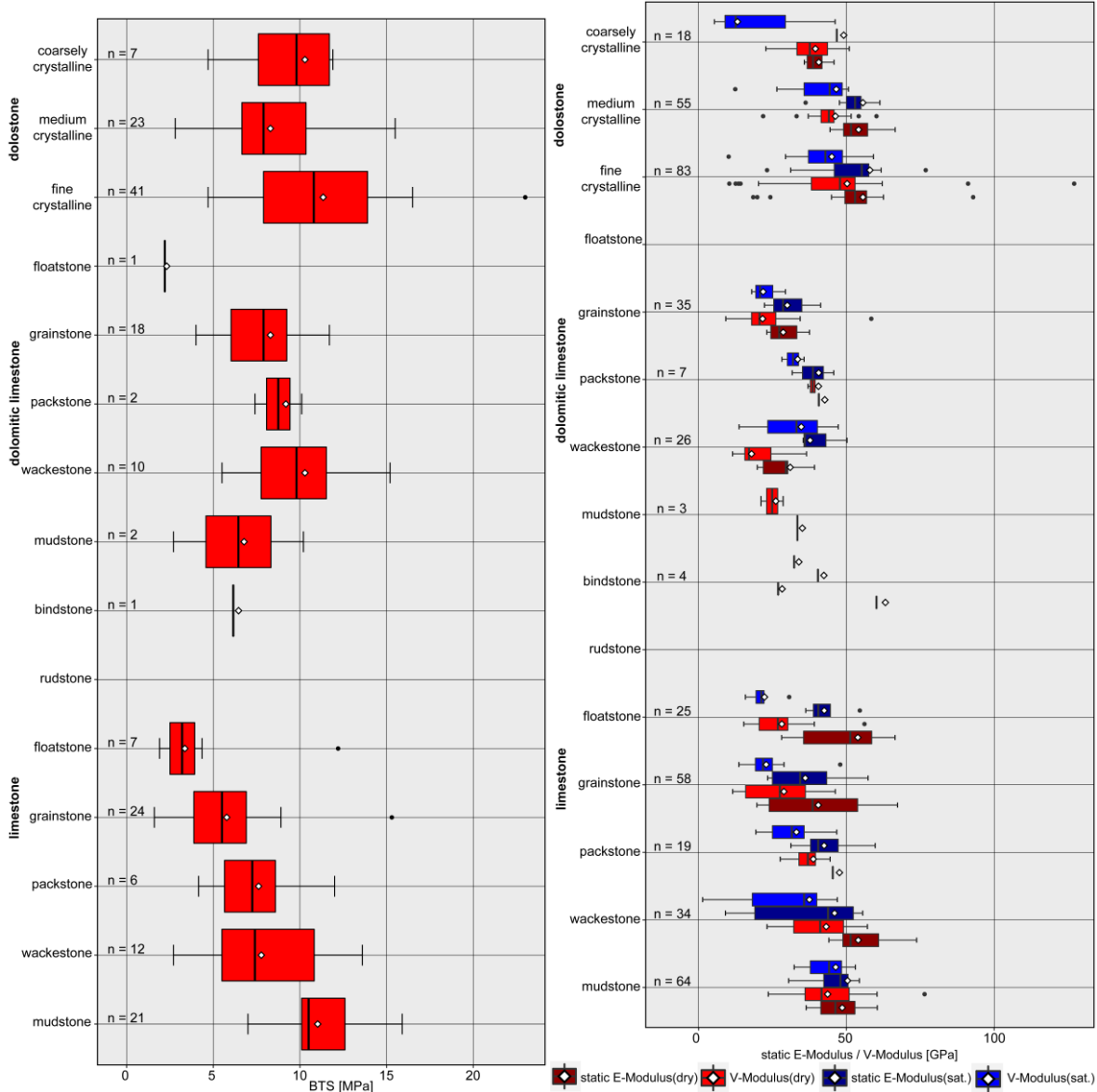


Fig. 76: BTS (left) and static Young’s Modulus and V-Modulus (right) versus facies.

Fig. 76 (left) shows, that the BTS values decrease among limestone types as particle size decreases, with no measurement values for rudstone and only one measurement value for bindstone. The BTS values of the dolomitic limestone are not clear. The reason may be the same as explained for (Fig. 75). Wackestone to grainstone show a slight tendency like limestone, but the mudstone does not fit the tendency. As the most fine-grained sample of dolomitic limestone, mudstone is expected to have the highest value, but it shows the lowest mean value if the floatstone, for which only one measured value is available, is not considered. In the case of dolostone, no tendency can be detected on the basis of the mean values. For some facies types no BTS could be determined.

Fig. 76 (right) shows Static Young’s Modulus and V-Modulus of differently saturated core samples versus facies. The different fine graininess of the core samples does not show a clear increasing or decreasing tendency among the different moduli Fig. 76 (right). The only visible tendency which can be seen for limestone and dolostone, is that the mean value of the dry V-Modulus decreases with increas-

ing particle fineness. For some facies types no static Young's Modulus/V-Modulus could be determined. There is no noticeable difference between the measured mean values of the static Young's Modulus and the V-Modulus.

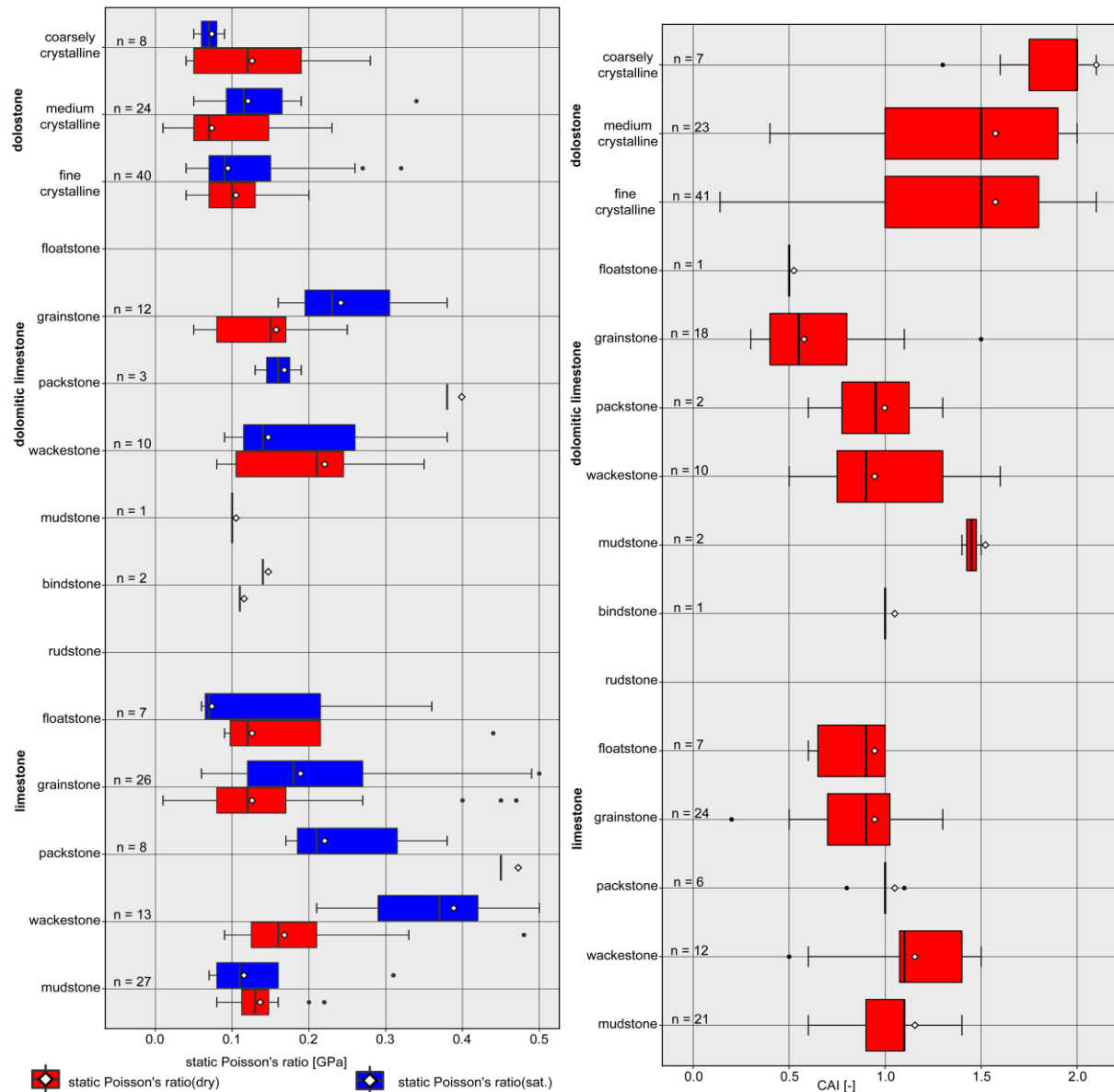


Fig. 77: Static Poisson's ratio (left) and CAI (right) of differently saturated core samples versus facies.

Fig. 77 (left) shows the static Poisson's ratio of differently saturated core samples versus facies. Overall, the measurement results are widely scattered. The dolostones with different crystal sizes have a similar static Poisson's ratio (Fig. 77, left). No trend in the static Poisson's ratio can be identified for the different types of facies of dolomitic limestone and limestone. Only one sample (limestone: packstone, bindstone; dolomitic limestone: mudstone, packstone) or no samples (limestone: rudstone; dolomitic limestone: floatstone) were available. This is due to the measurement procedure. In the case of brittle samples, the measuring instrument (measuring chain) may fail.

Fig. 77 (right) shows the CAI versus facies. The abrasivity of the different facies types of the limestone does not show a tendency. The dolomitic limestone shows a decrease of the CAI value with decreasing

fineness of the facies types (Fig. 77, right). The highest CAI values are found in the dolostones. The sampled dolostones show a tendency of increasing CAI values with increasing crystal size.

### 2.2.6 Conclusions

The carbonates of the Upper Jurassic are already successfully used as a reservoir for hydrothermal geothermal energy in the North Alpine Foreland Basin, SE Germany. So far, the Upper Jurassic aquifer has been analysed and characterized using analogue samples. This work uses for the first time core samples from existing hydrocarbon wells. A total of 449 core samples from different depths were examined. Each well/borehole was characterized individually by specification of the most important parameters.

The core samples were characterized with non-destructive as well as destructive testing methods. The non-destructive laboratory investigations were ultrasonic tests. The destructive laboratory tests included Uniaxial Compression Tests, Brazilian Tensile Tests, Point Load Tests, Cerchar Abrasivity Tests and LCPC Abrasivity Tests. The testing results were summarised. The summarised results were plotted against each other.

A correlation was found when comparing the results of dry and saturated samples for the  $v_{pI}$ -velocity and the  $v_s$ -velocity. When comparing the measurement results of dynamic and static tests, no or low correlations were found. The low correlations cannot be used to draw conclusions about the respective measurement results. A comparison of the various parameters with the uniaxial compressive strength show several tendencies. In general the UCS values show a higher strength for core samples with higher  $v_p$ -velocities. The porosity decreases with increasing uniaxial compressive strength. The bulk density shows the same tendency as the porosity only in reverse. For UCS values in the range between 50 MPa and 100 MPa the measured values of the correlated parameters fluctuate over an extremely wide range from the respective minimum to the maximum values. The brittleness of the examined core samples ranges in the typical brittle range of carbonates.

In addition, the summarised results were correlated with stratigraphy, lithology and facies of the core samples.

In the chapter stratigraphy a few tendencies can be seen for most non-destructive laboratory tests. Dogger has low mean values and from Malm Alpha to Malm Zeta 2 a plateau appears. From Malm Zeta 2 to Malm Zeta 4–5 a decrease in the values is observed. The values for Purbeck are higher than the values for Malm Zeta 4–5. For the  $v_p/v_s$  ratio and for the dynamic Poisson's ratio no tendencies can be seen. In Malm Alpha to Malm Gamma the highest UCS values are found. No trend can be observed but the BTS values of nearly all samples are below 15 MPa. The values for the static Young's Modulus and the V-Modulus scatter in all stratigraphic units. The dispersion of the static Poisson's ratio values decreases with increasing depth. The abrasivity of all rocks investigated falls into the medium to abrasive category. The CAI values increase from Malm Alpha to Malm Delta. Malm Delta and Malm Epsilon form a plateau. From Malm Epsilon to Malm Zeta 3 the mean values decrease, with Malm Zeta 1 values spreading over a wide range. With the measured values it is not possible to characterize

the stratigraphic units. As the aquifer is known to be heterogeneous, the subdivision into stratigraphic units seems too rough for characterization.

In the chapter lithology some tendencies can be seen for most non-destructive laboratory tests. The dynamic values increase from dolomitic limestone via limestone to dolostone. In the dynamic Poisson's ratio no differences between the different lithologies can be seen. Based on the uniaxial compressive strength the core samples can be classified as hard to very hard. From limestone via dolomitic limestone to dolostone the mean BTS values increase. The mean values of the static Young's Modulus and V-Modulus increase from dolomitic limestone, to limestone and then to dolostone. The dolostone has the highest abrasivity values of all lithologies. With the measured values it is not possible to characterize the three lithologies. The same reason as stated for the stratigraphy section above also applies here.

In the chapter facies a few tendencies can be seen for most non-destructive laboratory tests. For the facies in each lithology, the values decrease with the increasing particle size. For the  $v_p/v_s$  ratio and for the dynamic Poisson's ratio no tendencies can be seen. The UCS values decrease with increasing particle size. This trend is evident in both, limestone and dolostone lithologies. The BTS values decrease among limestone facies types as particle size decreases. This tendency is not visible for the facies types in the other lithologies. There is no noticeable difference between the measured mean values of the static Young's Modulus and the V-Modulus. The dolostones with different crystal sizes have a similar static Poisson's ratio. The IQR ranges from 0.05 to 0.22. These values may be used as characteristic values for the dolostones. No trend in the static Poisson's ratio can be identified for the different types of facies of dolomitic limestone and limestone. The abrasivity of the different facies types of the limestone does not show a tendency. The dolomitic limestone shows a decrease of the CAI value with decreasing fineness of the facies types. The highest CAI values are found in the dolostones.

The different stratigraphic units do not show different results and it is not possible to identify the stratigraphy of a sample based on the results of the laboratory investigations. No directional dependence of the parameter examined over the different lithologies is found. For the facies in each lithology, most of the values decrease with the increasing particle size. The results from analogue samples of the state of the art with the drill cores examined in this work show clear agreement. This confirms that analogue samples can be used for an initial analysis of the suitability of a drill site.

The geomechanical results from the core samples show a wide variation and characterize the aquifer as very heterogeneous. Nevertheless the specific parameter ranges presented in this thesis can be used as important input parameters for geomechanical modelling.

## 2.3 NE Bavaria

In Bavaria, new areas are to be developed for petrothermal geothermal energy in the future (DREWS et al. 2019a). The far largest part from geothermal energy in Germany hat could be used for energy production is attributed to the petrothermal geothermal energy (PASCHEN et al. 2003). Studies show that 95 % of the German deep geothermal potential is found in crystalline rocks (PASCHEN et al. 2003). These rocks have an excellent temperature level for the use of petrothermal geothermal energy. A petrothermal geothermal energy project can be implemented at locations with suitable tectonic situations and increased temperature gradients (STOBER & BUCHER 2014).

One of these locations with an elevated temperature anomaly is in NE Bavaria (GUDDEN 1973; 1977; 1981; 1983). The northern part of the Franconian Basin is the center of the geothermal anomaly (BAUER 2000), covering a size of  $\sim 100 \times 65 \text{ km}^2$  with a maximum geothermal gradient of  $48.9 \text{ K/km}$  across a 1,200 m depth interval (BAUER 2000; GUDDEN 1981; KÄMMLEIN et al. 2017). The distribution of the above mean geothermal gradient in this area is illustrated in the Fig. 78.

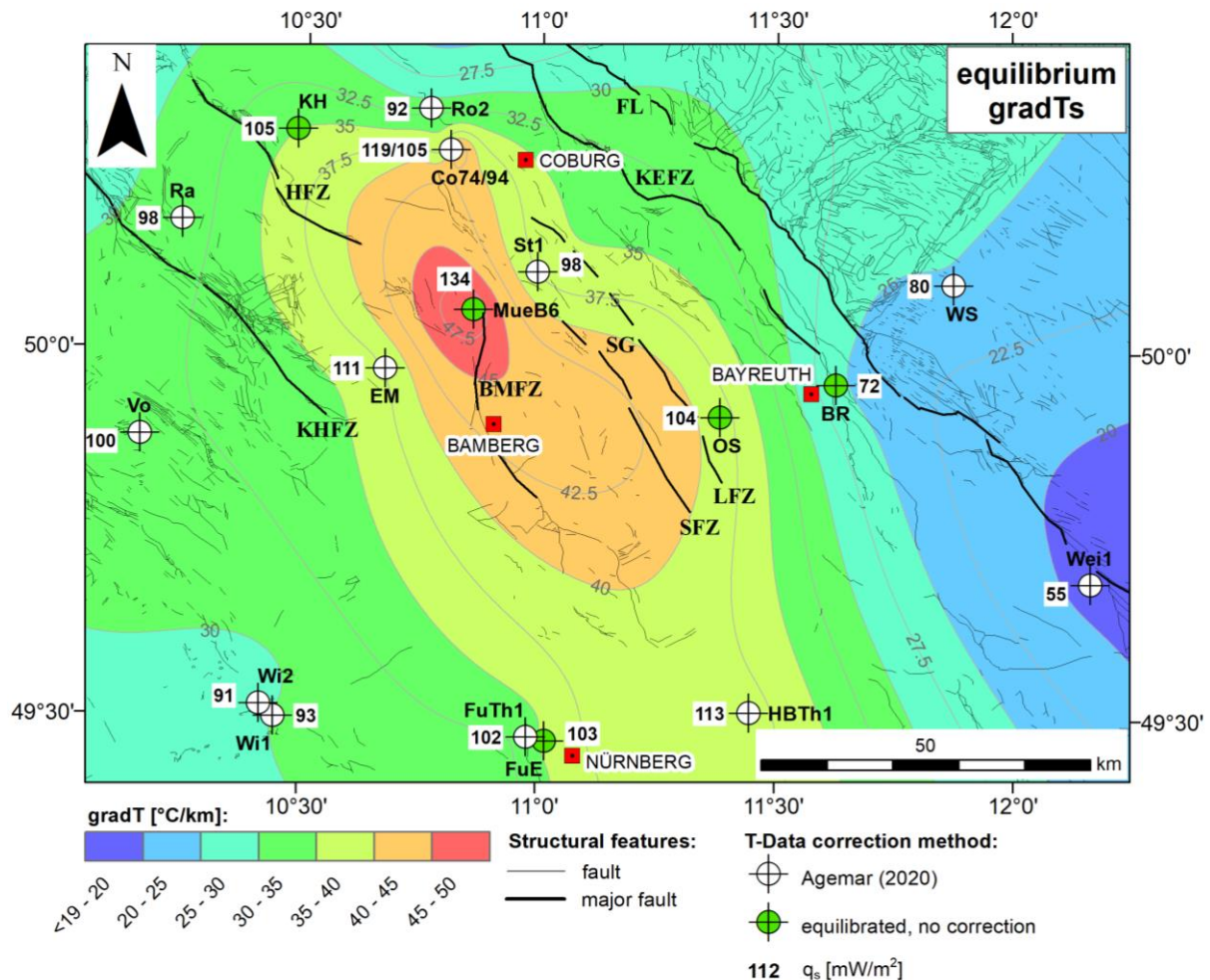


Fig. 78: Expansion and temperature distribution (interpolated gradT map) of the Franconian Basin temperature anomaly in NE Bavaria, based on the analysis of temperature data from 18 wells after KÄMMLEIN et al. (2020).

### 2.3.1 State of the art

As there were no exploration activities in NE Bavaria for the economic use of petrothermal geothermal energy, very few studies on the general characterisation of NE Bavaria have been carried out in the past (BAUER 2000). However, to develop this future technology in this area of Bavaria, the basic research in this area has slowly increased in recent years (DREWS et al. 2019b).

Between the 1960s and 1980s during the exploration activities for hydrocarbons and thermal water, a positive temperature anomaly was detected in the Franconian Basin (GUDDEN 1973; GUDDEN 1977). The first regional study carried out by BAUER (2000), who introduced the term “Mürsbach anomaly”. Near the village of Mürsbach increased temperatures were detected in the subsurface down to a depth of 1,500 m. At the centre of this anomaly, the Mürsbach B6 well at a depth of about 1,200 m (KÄMMLEIN et al. 2020) shows a very high temperature gradient of 48.9 °C/km (BAUER 2000). The anomaly is only used for balneological purposes (GUDDEN 1983; HECHT 1993).

To change this purpose and to evaluate the potential for geothermal energy as well as to reestablish geological exploration in NE Bavaria, a project was carried out by the FAU. The aim was to collect existing and new data for an evaluation of the geothermal potential in NE Bavaria. In addition, relevant data gaps and further research objectives were determined (KÄMMLEIN 2020).

Thereby it can be recognized, that there is a lack of knowledge about the geological structure and the associated properties of the interesting surface.

According to DE WALL et al. (2019) the subsurface structure of the Franconian Basin is not studied in detail yet. The information about the sediment-basement boundary are only known locally from boreholes Obernsees (1,341 m depth) (STETTNER & SALGER 1985) or Bad Staffelstein (> 1,600 m depth) (GUDDEN 1981) (DE WALL et al. 2019).

Therefore, a large data gap exists regarding future geothermal exploration in the Franconian Basin. Neither the geological cause(s) of the anomaly in the Franconian Basin are clarified (KÄMMLEIN et al. 2019). According to KÄMMLEIN (2020) and DE WALL et al. (2019) there are two possible geological causes for the increased temperatures: heat producing granites in the basement or the presence of deep, hydraulically active fault zones in the Franconian Basin.

Within the framework of the GAB, a comprehensive seismic campaign was carried out. The seismic campaign followed the old seismic lines to obtain more detailed information about the basement (DREWS et al. 2019b; STOLLHOFEN et al. 2018). The suspected position of the granites and the distribution of the fault zones in the basement should be examined. The thermo-hydraulic properties of the Permo–Triassic in the Franconian Basin have been investigated in KÄMMLEIN (2020). The acquired data may be helpful as input parameters for the evaluation of seismic data (KÄMMLEIN 2020).

The heat conductivity and natural gamma radiation were measured at the Fichtelgebirge granites exposed east of the Franconian Basin and the resulting heat production was calculated (SCHARFENBERG & DE WALL 2016; SCHARFENBERG et al. 2016). This serves for the future modelling of the geothermal potential of the Franconian basins.

As the Fichtelgebirge is the nearest granite outcrop, these granites were taken as analogue material for the present thesis. These granites were previously investigated and subdivided in different granite types in several studies (HECHT et al. 1997; HECHT & VIGNERESSE 1999; RICHTER & STETTNER 1979).

In addition, the granite samples taken were examined under triaxial conditions (DREWS et al. 2019a).

### 2.3.2 Geological setting

The outcrops investigated in this study, such as geotopes and quarries, are all located in the Fichtelgebirge. The rocks there are regarded as analogue material for the rocks below the Franconian Basin, which are supposed to be important for petrothermal geothermal energy. In 1983 the last deep scientific well (Obersees 1) in the Franconian Basin was drilled (KÄMMLEIN 2020). The deep borehole Obersees 1 encountered a reworked basement (DE WALL et al. 2019). However, these are not granites but shale–sandstone alternating sequences (STETTNER & SALGER 1985). The reservoir rocks, probably granites below the Franconian Basin, which are the origin of the geothermal anomaly, have unfortunately not been investigated up to now.

The dominant fault system in NE Bavaria is NW–SE striking. The elongated NW–SE shape of the anomaly under investigation runs parallel to this striking (KÄMMLEIN 2020). In the centre of this anomaly this fault system coincides with the Itztal–Regnitztal fault system (Gudden 1981). At the moment, the area of geothermal interest in the Franconian Basin is in a “NE–SW to ENE–WSW transtensional strike-slip regime with maximum principal stress axis oriented NW–SE [...] (REITER et al. 2016; NAVABPOUR et al. 2017)” (KÄMMLEIN 2020). This regime thus corresponds to the specific kinematics for the basement east of the Franconian Line (SEHT et al. 2006).

### Franconian Basin

The investigation area with an elevated geothermal anomaly is located in the Franconian Basin. This basin in NE Bavaria is part of the South German platform (FREUDENBERGER & SCHWERD 1996) and a sub-basin of the Central European Basin System (LITKE et al. 2008). The Franconian Basin is located between two gravity highs on the gravity map of Germany (SKIBA et al. 2010). These gravity highs are on the one hand the Kraichgau Terrane in the West and on the other hand the Bohemian Massif in the East. Due to the Permo–Mesozoic basin sediments, the Franconian Basin appears as a gravity low (DE WALL et al. 2019). The southern boundary of the investigated area can be seen as the boundary between the Saxothuringian and Moldanubian zone of the Hercynian basement. According to tectonic and paleogeographical zones proposed by KOSSMAT (1927), the Franconian Basin is situated within the Saxothuringian zone. Fig. 79 shows a schematic SW–NE cross section of the geology of the underground in NE Bavaria with all available information.

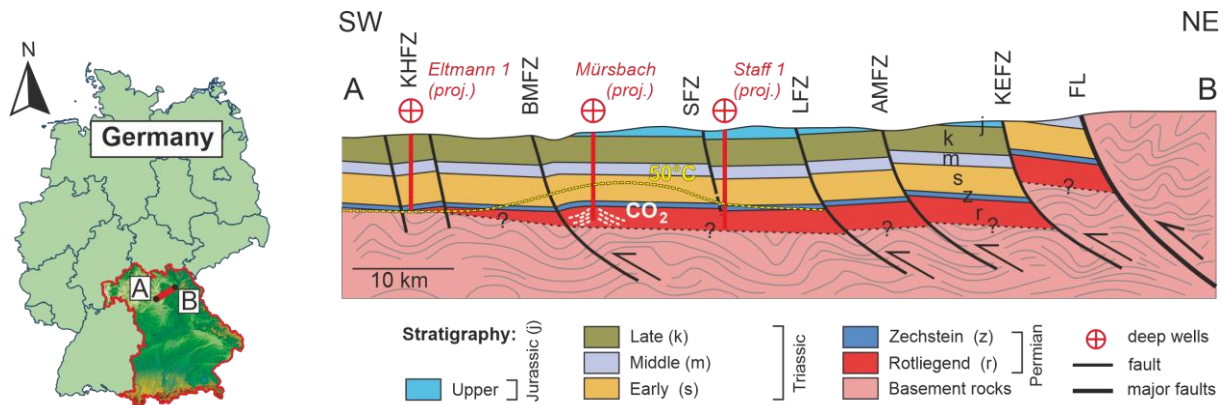


Fig. 79: Schematic SW–NE cross-section through the Franconian Basin from www-23; www-24 (left) and mod. after KÄMMLEIN et al. (2020) (right).

In the centre of the anomaly the sediment cover reaches a thickness of more than 1,600 m (GUDDEN 1977) but in the Franconian Basin the sediment thickness varies and can reach a maximum thickness up to about 3,500 m (SCHRÖDER 1987; SCHRÖDER et al. 1997). The basement of the Franconian Basin was formed during the Hercynian basement. During this time voluminous granites intruded into the basin (FINGER et al. 1997; SCHÄFER et al. 2000). Since the Lower Carboniferous the Hercynian basement was raised and eroded (WELZEL 1991). In the Upper Carboniferous, troughs were formed which were caused by a crustal collapse and an expansion of the lithosphere (FREUDENBERGER & SCHWERD 1996). These formed basins were filled with more than 2,500 m thick Molasse sediments of the eroded Hercynian basement (BAUER 2000; WALTER & DORN 2007; ZIEGLER 1982). The sedimentary rocks that form the Franconian Basin date from the Permian, Mesozoic and Cenozoic (KÄMMLEIN & STOLLHOFEN 2019).

In the Upper Permian a transgression from the North into the Franconian Basin took place. In the Lower Triassic, the sedimentation pattern extended further South (BAUER 2000). In the Lower Triassic the sediments are characterized by continental environments (FREUDENBERGER & SCHWERD 1996). These are interbedded sand-, clay- and siltstones (KÄMMLEIN & STOLLHOFEN 2019). In the Middle Triassic another transgression took place in the Franconian Basin and a shallow marine sedimentation area developed (BAUER 2000). In the Lower Middle Triassic marine fossiliferous limestone, claystone and marlstone were deposited. These deposits were temporarily stored by marine evaporitic lithologies (KÄMMLEIN & STOLLHOFEN 2019). Towards the end of the Middle Triassic, the Franconian Basin first experienced fully marine conditions until a new regression occurred. This led to increased flattening of the deposition area. From the end of the Middle Triassic the area is partly marine with some sandy layers at the edge of the basin (FREUDENBERGER & SCHWERD 1996). From the Upper Triassic onwards, an ingress from the North took place (BAUER 2000). In the Upper Triassic mainly non-marine clayey sandstones were deposited in the Franconian Basin, but also claystones, siltstones, dolomitic rocks and gypsum rocks were deposited (KÄMMLEIN & STOLLHOFEN 2019).

In the Lower Jurassic the condition of formation continued, pelitic and carbonatic sediments were deposited in the Franconian Basin. In the Middle Jurassic the Central German threshold raised. However, the lowering of the Vindelician ridge in the South increased the marine influence in the Franconian Basin. The Middle Jurassic consists of grown claystones and the sandstones near the coast (BAUER 2000).

In the Upper Jurassic (Malm), the Franconian Basin was completely flooded. Fully marine conditions characterize Malm of the Franconian Basin. The deposited rocks correspond to those described in the chapter 2.2.2. At the end of the Jurassic, the Franconian Basin was lifted and was subject to deep karstification during the Lower Cretaceous period (FREUDENBERGER & SCHWERD 1996). The karst relief was filled with sand and clay deposits after the transgression from the South–East during the Upper Cretaceous (BAUER 2000).

From the Cretaceous onwards, the Alpine orogeny formed in the Franconian Basin as a horst and graben system. Then a regression and afterwards an erosion occurred. The Franconian Basin was inverted  $\sim 3\text{--}5^\circ$  to the SE due to the Alpine collision (BAUER 2000). These tectonic movements also led to volcanic activity in the Franconian Basin (FREUDENBERGER & SCHWERD 1996).

## Granites

Large parts of the northern Bavarian Hercynian crust are made up of late orogenic granites. These show different age and therefore compositions (FÖRSTER et al. 2008; HECHT et al. 1997; RICHTER & STETTNER 1979; SIEBEL et al. 1997; SIEBEL et al. 2003). As there are no granitic rock samples from deep underground, the exposed rock units East of the Franconian Lineament were sampled to get an insight into what can be found deep underground below the Franconian Basin. From a geological point of view, the granitic terrain must go further under a cover of Permo–Mesozoic sediments and build the basement of the Franconian Basin (DE WALL et al. 2019). Geophysical experiments have proven this hypothesis (HEINRICHS et al. 1994; SCHÄFER et al. 2000).

The existence of granite bodies at depths between 2–18 km in the subsurface of the Franconian Basin is indicated by gravity modelling (EDEL & WEBER 1995; SCHAARSCHMIDT et al. 2017). The distinct negative Bouguer anomalies were detected and modeled as granitic intrusions in the basement of the Franconian Basin (DE WALL et al. 2019). This conclusion is drawn because the Bohemian Massif contains distinct gravitational lows, which were mapped as Hercynian granites (HECHT et al. 1997; TRZEBSKI et al. 1997).

DE WALL et al. (2019) verified the presence of granite bodies (2–9.5 km) below the Franconian Basin. For this purpose, forward gravity modelling was performed to verify the current idea of the subsurface structure in NE Bavaria. The existing Bouguer anomaly was compared with the calculated gravity anomaly of the model. DE WALL et al. (2019) found out that the heat-producing granites covered by insulating sedimentary rocks (1.35 km) may be responsible for the increased geothermal gradient.

## Fichtelgebirge

Buried granite bodies are set as targets for geothermal prospecting, because they are heat-producing bodies in the Earth's crust (SCHARFENBERG et al. 2016). The nearest basement exposure of the Franconian Basin is the Fichtelgebirge area. It belongs to the Saxothuringian zone of the central European Hercynian basement (KOSSMAT 1927). The Fichtelgebirge granites from different outcrops were taken as analogue material. The Fichtelgebirge, as a part of the Bohemian Massif, is characterized by an intensive granitoid magmatism. Over 40 % of the total area is occupied by Hercynian granitoids (RICHTER & STETTNER 1979).

Investigations on granites of the Fichtelgebirge have shown that there were at least three different main phases of intrusive activity (SIEBEL et al. 1997) with the highest magnetism at the end of the Hercynian basement (SIEBEL et al. 2003). High volumes of I-type to S-type granites intruded into low to medium metamorphic metasediments of the Fichtelgebirge (HECHT et al. 1997; HECHT 1998; SIEBEL et al. 2010).

The classification of the Fichtelgebirge granites is based on the work of STETTNER (1958), RICHTER & STETTNER (1979) and HECHT et al. (1997). Based on geological findings, STETTNER (1958) divided the granites into an older (OIC) and a younger (YIC) group. The magmatic activity of the Older Intrusive Complex (OIC) was between 326 and 324 Ma and has a root zone in its eastern part (HECHT et al. 1997). The magmatic activity of the Younger Intrusive Complex (YIC) was between 298 and 286 Ma and has the root zone near the Franconian Lineament (HECHT & VIGNERESSE 1999). Both granite groups consist of different granite types (RICHTER & STETTNER 1979). Four different main types can be identified and were investigated in this thesis. There are also further variations of these different main types, which were also explained.

Due to mafic/magmatic inclusions as well as isotope signatures (Sr and Nd) of the OIC group, the participation of a mafic lower crust or mantle magma in the formation of the “central granite” is required (HECHT 1998). The YIC group are of purely crustal origin, probably Precambrian rocks of the Saxothuringian or the Moldanubian zone (SIEBEL et al. 1997). Today, due to the significant differences in the isotope signatures (SIEBEL et al. 1995) it can be excluded, that the two groups (OIC & YIC) have developed from a primary magma. Even within one group the different granite types differ in their magma formation (HECHT et al. 1997). Within the YIC group, the G2K and G3K granite types, are special because they show different foreign rock inclusions which can be attributed to an independent intrusion (HECHT et al. 1997; SCHÖDLBAUER et al. 1996; SCHÖDLBAUER et al. 1997) from a deeper crustal level (HECHT 1998).

The “Weißenstadt–Marktleuthener Massif” is a coherent intrusion body. The W–E extension of the massif is 50 km long and was formed by OIC group granites. The massif has a depth extension of max. 3 km in the western and central section and otherwise has a predominantly flat habitus (HECHT 1998). In the East, the massif has a higher thickness which is the root zone of the OIC group granites (HECHT et al. 1997). The OIC group is divided into five granite types G1 (central granite (DILL 2015)) according to HECHT (1998). The exact petrographic description of the selected rocks is given in the chapter 2.3.4 at the respective outcrop.

During the Permian, the tectonic plates rearranged due to strike-slip movements, and the YIC group is supposed to have intruded (FRANKE 2006). This group is distributed over several massifs. The largest of them is situated in the South of the “Weißensstadt–Marktleuthener Massif”. The partial massif of the Kösseine is on the eastern border of this central massif. The central massif has a root zone that is at least 8 km deep (RICHTER & STETTNER 1979).

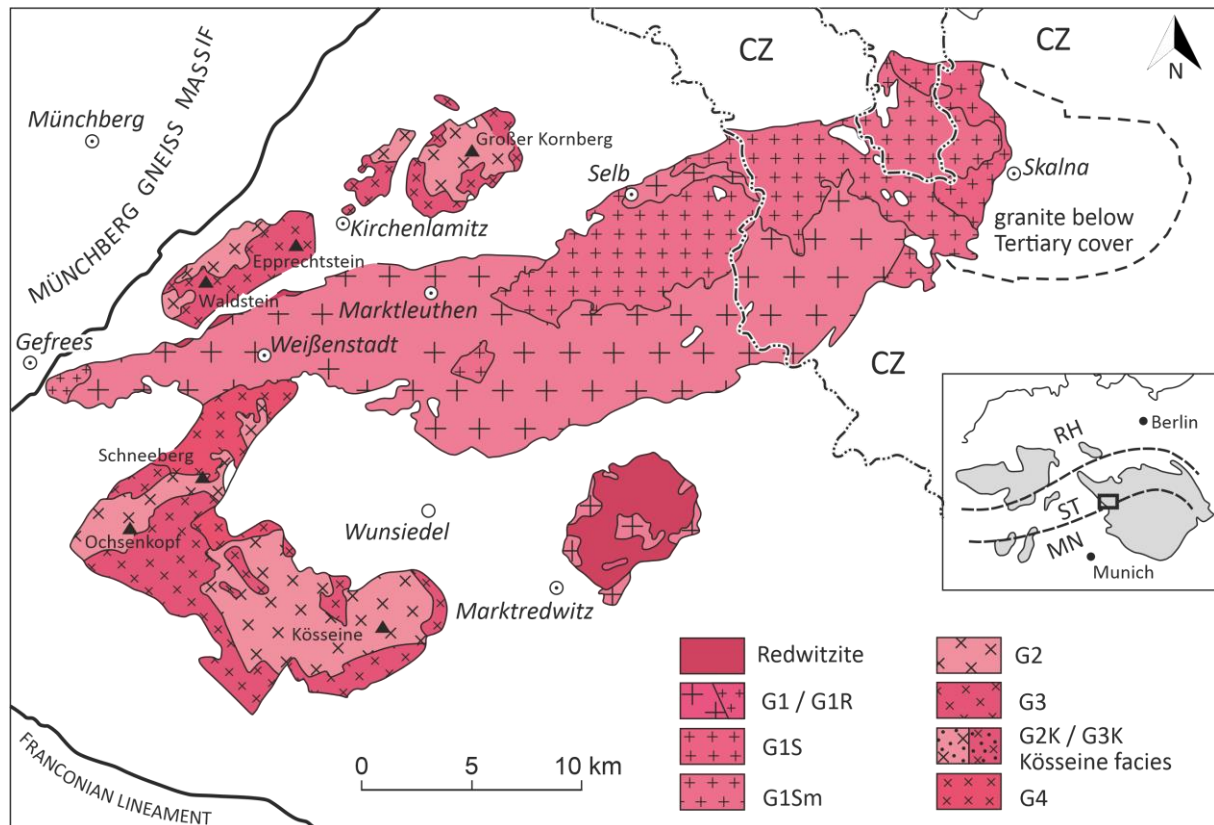


Fig. 80: Map sketch of the late Hercynian granitoids of the Fichtelgebirge mod. after HECHT (1998).

The “Weißensstadt–Marktleuthener Massif” has a greater depth (~3 km) in the area between the central stock in the South and Waldstein Massif in the North than it does in the West and East of it (~1 km). Therefore it can be assumed that the southern central massif and the northern “Waldstein Massif” could be linked (HECHT 1998).

The G2 and G3 granite types have the largest distribution within the YIC group and largely correspond in age and composition. They differ only in their structural fabric and their location within the massifs (HECHT 1998). The G2 granite (marginal granite (DILL 2015)) occupies a position close to the edge of a massif while the G3 granite (core granite (DILL 2015)) occupies a central position within the massif. The SE extension of the YIC group’s central massif forms a partial massif: the Kösseine. These granites are structured in the same way as the G2 and G3 granites on the basis of the structural fabric (HECHT 1998). The G4 granite is only represented in the central stock and has experienced a stronger autometamorphic overprinting than the G3 granite. The higher tin contents gave the G4 granite the designation “tin granite” (DILL 2015; STETTNER 1958). The exact petrographic description of the selected rocks of the YIC are given in the chapter 2.3.4 at the respective outcrop.

## Tectonic stress field

In NE Bavaria there is almost no geomechanical data available. Since only a few deep boreholes have been drilled in the Franconian Basin, the amount of data in the underground is also very small. Only two boreholes were drilled through the Franconian Basin and reached the metasediments of the pre-Permian basement. In the World Stress Map the few accessible stress data for this region can be found (DREWS et al. 2019a; HEIDBACH et al. 2016).

DREWS et al. (2019a) determined a vertical stress gradient by means of geophysical borehole measurements. In the Mürsbach wells, the density logs were approximated with VSP data and a modified GARDNER et al. (1974). At the Obernsee well, the vertical stress could be approached with the density range in the top of the well where as, in the bottom of the well, the density variations had no significant impact on the vertical stress gradient (DREWS et al. 2019a). The determined values vary between 24.7 MPa and 25.7 MPa/km (DREWS et al. 2019a).

Drilling data of additional wells (Eltmann, Mürsbach, Obernsees & Staffelstein) in NE Bavaria indicate generally hydrostatic pore pressure conditions are present yielding a mean pore pressure gradient of  $\sim 10$  MPa/km (DREWS et al. 2019a). DREWS et al. (2019a) recognized, that there can be local overpressure due to artesian head.

In the Franconian Basin, only one measurement to determine the stress field has been carried out so far. These are hydraulic formation tests which were carried out in the research well Lindau 1. The direction of the maximum horizontal principal stress was derived from the hydraulic fracs in the borehole wall. This is on mean  $\sim 135^\circ$  and is in good agreement with the direction derived from the breakouts investigated (RÖCKEL & WONIK 2006). However, since it has so far only been carried out on one borehole and no comparative measurements have been made, this direction has a high uncertainty.

The determination of the minimum horizontal principal stress was carried out at two depths within the borehole (Lindau 1). RUMMEL et al. (2002) performed a series of frac tests at a depth of  $\sim 431$  m. During these frac pressure tests a minimum horizontal principal stress of  $\sim 12.9$  MPa was determined. This would result in a minimum horizontal principal stress of 30 MPa/km and a reverse faulting stress regime, but this measurement does not take into account the cohesion and tensile strength.

In the Rotliegend interval of 441–530 m an initial injection test was carried out to measure the hydraulic permeability. The observed pressure curve is typical for the generation and subsequent reopening of a new fracture. After a stimulation test, the pressure drop was recorded completely and undisturbed. This provides information on the closure pressure of a fracture which corresponds to the mean minimum principal stress. In this depth range it is 9.7–10.6 MPa. This would result in a minimum horizontal principal stress of 20–22 MPa/km.

Two multistage triaxial tests were performed on cores from the metasediments of the Obernsee well (DIETL et al. 2017). The coefficients of friction and cohesion were used to reinterpret the hydrofracs. A strike-slip stress regime was determined under the assumption of a critically stressed condition (DREWS et al. 2019a).

An overview of the available data from the World Stress Map is shown in Fig. 81. The created World Stress Map (www-22) shows, the current data in this area from the WSM database edition (HEIDBACH et al. 2016). The selected data quality of the map is A to C.

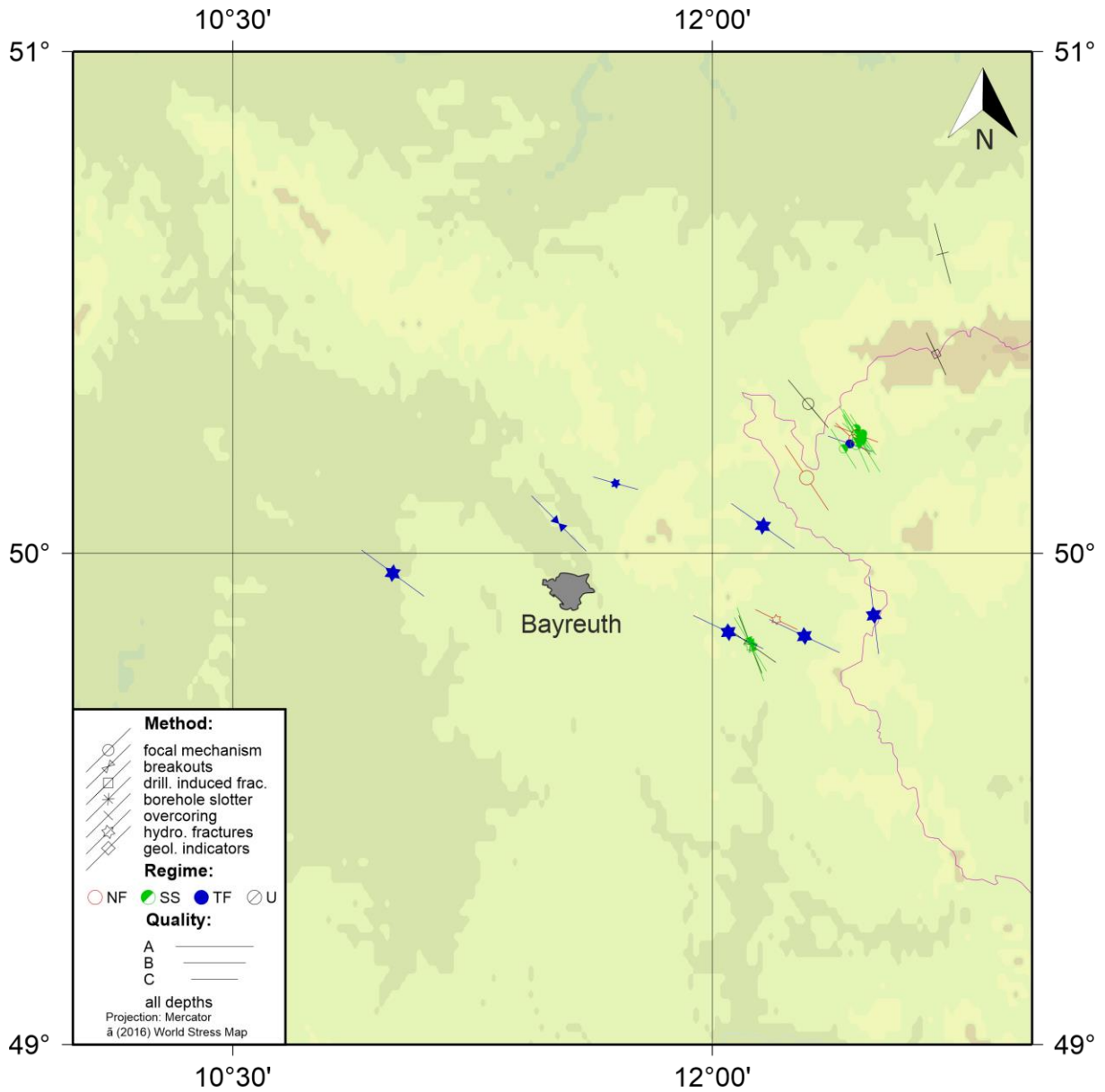


Fig. 81: An overview of existing data from the World Stress Map in NE Bavaria, created with CASMO (www-22) and modified.

### 2.3.3 Data, study area and sampling

Core samples from boreholes in the anomaly situated in NE Bavaria were not accessible. Instead, analogue material similar to the reservoir rock was prospected from nearby outcrops. This was done with the online map service “UmweltAtlas Bayern” of the LfU. For this purpose, the subject area “applied geology” with the content “experience geology” was used (LfU 2018); (www-12). A survey was carried out among quarry owners from the Fichtelgebirge as well as of the Competence centre for natural Stone in Wunsiedel. All accessible outcrops were examined (Fig. 82). These are active and former quarries and geotopes.

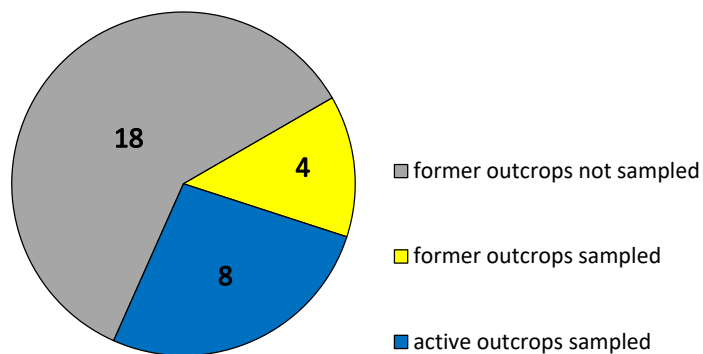


Fig. 82: Overview of the outcrops in the Fichtelgebirge and the finally accessible outcrops for sampling for this work.

Three sampling campaigns (12.07./13.07.2017, 25.07./26.07.2017 & 18.07./19.07./20.07.2018) were conducted. Analogue material was taken from outcrops in the Fichtelgebirge. General information and the geological descriptions of the different outcrops can be found for an easier overview in the results chapter.

In NE Bavaria three geotopes and nine quarries were investigated. At the moment six quarries are operating successfully and three more shall be reactivated. These outcrops were selected because they intruded in different geological ages and are distributed over the whole Fichtelgebirge (Fig. 83). These are the geotopes at the Bibersberg (TUM-008), at the Mühlbach forest (TUM-010) and at the Thüring (TUM-011). The investigated quarries are two quarries at the Kösseine (TUM-001 & TUM-005), a quarry in the Tröstau (TUM-002), two quarries at Epprechtstein (TUM-003 & TUM-006), and the quarries at Waldstein (TUM-004), Reinersreuth (TUM-007), Kornberg (TUM-009) and Gefrees (TUM-012).

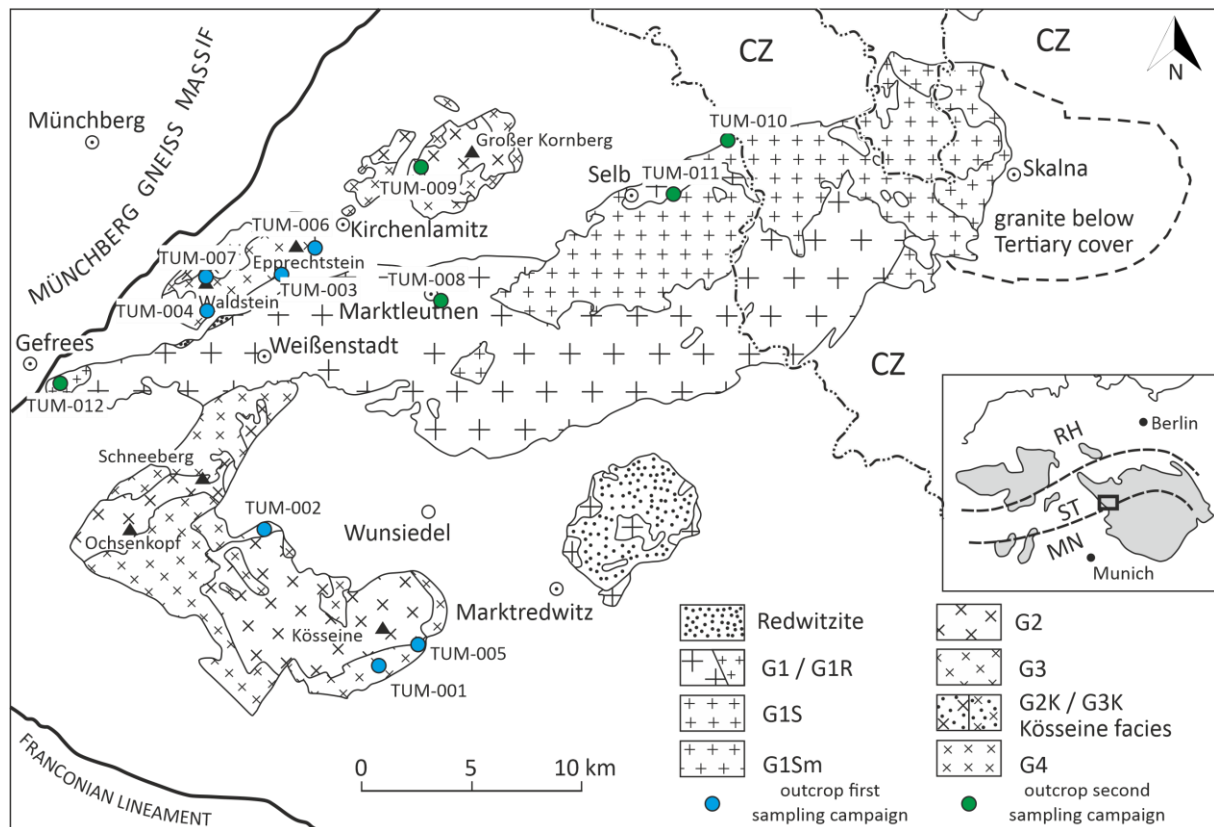


Fig. 83: Overview of the investigated analogue samples of the outcrops in NE Bavaria mod. after HECHT (1998).

After the site identification of the quarries and geotopes, the respective quarry owners sold or donated partly oriented rock blocks. These blocks are only oriented partially, because the owners were not able to calibrate them during mining operation. Nevertheless, it was always possible to determine the acclinic surface of all samples taken. In the geotopes as well as in some quarries, it was not possible to take any rocks with us. In these cases, test samples were drilled in the field during the field campaign.

The WEKA KS 13 diamond core drill rigs (WEKA 2013a) were attached to the walls to be examined in the outcrop and the WEKA DK17 diamond core drill was installed (WEKA 2013b). Samples were extracted in the field with a 50 mm diameter core bit. All investigated drill cores, were orientated and marked with an arrow pointing to the bottom. All collected rock material was then transported to TUM for further sample processing.

Outcrop analogues have been identified as a key feature of the exploration approach to understand the underground reservoirs and to minimize the significant uncertainties associated with many reservoir projects. By using analogue samples, it is possible to have almost unlimited access to the investigated rocks and the possibility of characterizing it in all three dimensions (MRAZ 2019).

### 2.3.4 Results

Due to the fact analogue material is used in NE Bavaria, almost all experiments could be performed in every outcrop. Only in the outcrops TUM-006, TUM-010 and TUM-012 no PLT could be performed due to insufficient sample material. Since the porosity and density determinations for NE Bavaria were not included, a selection of these tests was also carried out over the course of this work.

For the determination of the V-Moduli of NE Bavaria analogue samples, the complete linear range of the pre-loaded stress-strain curve was selected. This was also applied to the E-Moduli in the linear reloaded range of the curve. The entire determined range completely covers the linear-elastic range of the stress-strain curve to determine the respective moduli. This could be done in the analogue samples, since this range per test could be well determined by preliminary tests.

The number of performed measurements for NE Bavaria in each outcrop is listed in the Tab. 17.

Tab. 17: Overview of the tests performed in NE Bavaria.

Quarry/geotope	Number n (samples)	UT ( $v_p$ )	UT ( $v_s$ )	UCT	BTT	PLT	CAIT	LCPC
TUM-001	47	258	86	24	48	12	29	6
TUM-002	25	276	86	14	40	41	36	6
TUM-003	61	366	74	40	37	68	30	14
TUM-004	14	168	48	6	39	13	19	2
TUM-005	49	282	90	28	35	12	26	6
TUM-006	68	426	142	46	58	-	35	6
TUM-007	39	306	98	23	50	48	26	4
TUM-008	11	120	40	7	20	12	14	2
TUM-009	23	276	92	15	27	11	22	8
TUM-010	4	48	16	2	2	-	2	2
TUM-011	7	84	28	4	16	23	10	2
TUM-012	10	120	40	7	5	-	5	2
Number n (total)	358	2,730	840	216	377	240	254	60

At the beginning, each quarry/geotope is characterized individually. A short overview about the outcrop locations as well as a description of the examined analogue samples can then be found. Furthermore, there is a figure of a stress-strain curve of a characteristic sample of the outcrop and a short description of it. For each quarry/geotope, the key parameters (min., mean, med. & max.) per quarry/geotope are listed in a table.

### Quarry TUM-001

The active quarry TUM-001 is located 7 km west–southwest of the town of Marktredwitz. Three blocks were bought from the Kösseine massif and nine samples were drilled directly in the field from the southwest hillside of the Kösseine.

A total of 47 samples were drilled from the three blocks. The quarry under investigation is the westernmost quarry of the three active quarries at the Kösseine. There, the “Kösseine Kern granite” is exposed, which is a variety (G3K) of the Variscan G3 granite.

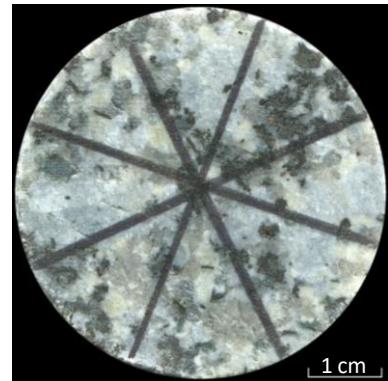


Fig. 84: Scan of a sample of TUM-001.

The rock appears a dark blue gray colour with nodule shaped accumulation of biotite (RICHTER & STETTNER 1979). The blue coloration is caused by cordierite (MÜLLER 1997). Due to the occurrence of varying grain sizes of alkali feldspar next to the biotite, there is an uneven structural fabric (HECHT 1998). The maximum grain size determined is 5 mm. According to HECHT (1998) the mineral content is: quartz 32.3 %, alkali feldspar 34.9 %, plagioclase 18.8 %, biotite 8.3 %, muscovite 4.6 % and ~1 % of garnet, cordierite and accessory minerals. It is classified as coarse grained, garnet and cordierite-bearing biotite granite (Fig. 84) (HECHT 1998; SCHARFENBERG et al. 2016).

Fig. 85 shows a typical stress-strain curve of the Kösseine granite. Clearly visible is the long path of the axial strain and the low lateral strain. At the beginning of the curve the shape is nonlinear and the elastic deformation takes place. Then the shape of the curve is linear and the elasto–plastic deformation takes place. The last part of the curve with unstable crack growth and plastic deformation begins at 95 %. In this quarry the failure mode builds mostly conjugate pairs of shear failure surfaces.

A total of 31 UT, 24 UCT (8 preliminary tests and 16 main tests), 48 BTT, 12 PLT as well as 29 CAIT and 6 LCPCT were performed from the collected samples.

Tab. 18 shows the determined key parameter values of the tests performed.

A summary of all test results of the quarry TUM-001 is given in the Appendix.

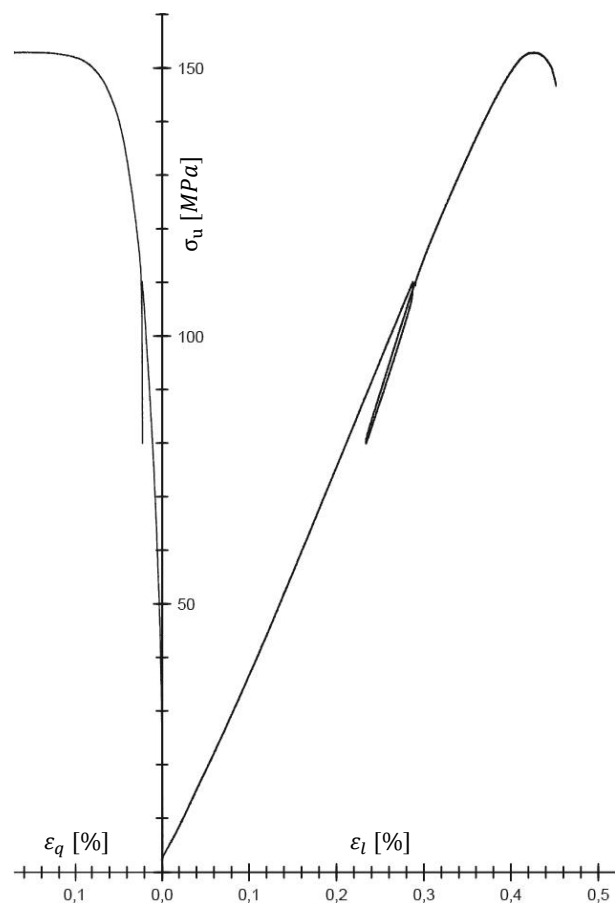


Fig. 85: Example of a typical stress-strain curve (TUM-001-01A-03).

Tab. 18: Characteristic values of the quarry TUM-001.

Quarry	State	Parameter	Units	min.	mean	med.	max.	n
TUM-001	dry	$v_{pl}$	[m/s]	4,733.5	<b>5,270.9</b>	5,301.8	5,884.9	31
		$v_{pd}$	[m/s]	4,645.3	<b>5,290.0</b>	5,212.5	6,075.0	
		$v_s$	[m/s]	2,744.0	<b>2,951.1</b>	2,897.0	3,296.0	
		$E_{dyn}$	[GPa]	51.54	<b>59.28</b>	57.43	69.88	
		$G_{dyn}$	[GPa]	20.05	<b>23.19</b>	22.28	28.55	
		$K_{dyn}$	[GPa]	32.80	<b>45.16</b>	45.15	56.40	
		$\nu_{dyn}$	[-]	0.20	<b>0.28</b>	0.29	0.32	
		Z	[ $10^6$ kg/m <sup>2</sup> s]	12.70	<b>14.32</b>	14.33	15.25	
	sat.	$v_{pl}$	[m/s]	5,503.2	<b>5,623.7</b>	5,654.3	5,714.5	12
		$v_{pd}$	[m/s]	5,274.9	<b>5,487.3</b>	5,443.8	5,724.6	
		$v_s$	[m/s]	2,849.0	<b>2,982.1</b>	2,970.3	3,120.5	
		$E_{dyn}$	[GPa]	59.51	<b>64.20</b>	64.00	69.15	
		$G_{dyn}$	[GPa]	21.57	<b>23.66</b>	23.48	25.96	
		$K_{dyn}$	[GPa]	47.95	<b>73.60</b>	75.93	82.65	
		$\nu_{dyn}$	[-]	0.33	<b>0.36</b>	0.36	0.38	
		Z	[ $10^6$ kg/m <sup>2</sup> s]	16.50	<b>16.86</b>	16.88	17.20	
	dry	$\sigma_u$	[MPa]	167.0	<b>151.5</b>	153.1	134.5	24
		V	[GPa]	39.47	<b>44.36</b>	42.11	63.77	16
		E	[GPa]	51.06	<b>56.65</b>	53.93	78.90	
		$\nu$	[-]	0.03	<b>0.13</b>	0.11	0.33	48
		$\sigma_t$	[MPa]	7.8	<b>10.5</b>	10.5	12.7	12
		$I_s$	[MPa]	8.4	<b>10.5</b>	10.3	13.1	
		$I_{s(50)}$	[MPa]	8.4	<b>10.6</b>	10.4	13.2	
		$\sigma_m$	[MPa]	168.4	<b>212.1</b>	206.8	264.1	29
		CAI	[-]	3.7	<b>4.6</b>	4.5	5.6	6
		LAC	[g/t]	1180	<b>1338</b>	1290	1660	
	LBC	[%]	43	<b>45</b>	45	46		
dry	$\Phi_{eff}^{He}$	[%]	0.60	<b>0.79</b>	0.79	0.96	4	
sat.	$\Phi_{eff}^W$	[%]	0.66	<b>0.79</b>	0.80	0.90	12	
dry	$\rho_b$	[g/cm <sup>3</sup> ]	2.63	<b>2.67</b>	2.66	2.70	39	
	$\rho_g$	[g/cm <sup>3</sup> ]	2.67	<b>2.68</b>	2.68	2.69	4	

### Quarry TUM-002

The active quarry TUM-002 is located 7 km west–northwest of the town of Wunsiedel and north of the federal highway 303. Six Blocks were donated and seven samples were drilled directly in the field.

A total of 18 samples were drilled from the six blocks. In the largest quarry of the Fichtelgebirge, the “Zufurt Granite” is exposed which is a Varsican G4 granite. This granite has a relatively “high” tin content which has given the G4 granite the name “Zinn Granite”. The rock has a very homogeneous structural fabric (STETTNER 1958).

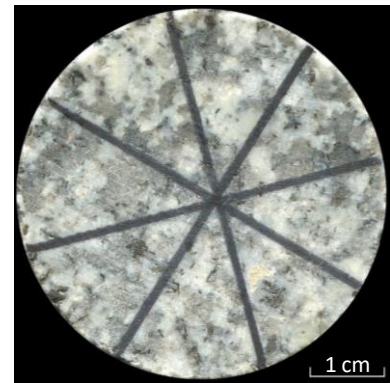


Fig. 86: Scan of a sample of TUM-002.

The G4 granite rock appears as a white to light gray colour with a maximum determined grain size of 4 mm. The content of the mineral components varies from sample to sample. Overall, however, it can be said that the quartz content is sometimes above and sometimes below that of alkali feldspar. In all cases the alkali feldspar content is above the content of the plagioclase (RICHTER & STETTNER 1979).

The mean determined mineral content is: quartz 30 %, alkali feldspar 35 %, plagioclase 25 %, biotite 5 %, muscovite 3 % and ~2 % accessory minerals. Of the accessory minerals, tin is the most important (MÜLLER 1997). It is classified as medium- to coarse-grained two-mica granite (Fig. 86) (HECHT 1998; SCHARFENBERG et al. 2016).

Fig. 87 shows a typical stress-strain curve of the Zufurt granite. Clearly visible is the long path of the longitudinal deformation and a very low transverse deformation. At the beginning of the curve the shape is nonlinear and the elastic deformation takes place. Then the shape of the curve is linear and the elasto–plastic deformation takes place. The last part of the curve with unstable crack growth and plastic deformation begins at 95 %.

In this quarry the failure mode builds mostly a conjugate pairs of shear failure surfaces.

A total of 23 UT, 14 UCT (2 preliminary tests and 12 main tests), 40 BTT, 36 CAIT, 6 LCPCT as well as 41 PLT were performed from the collected samples.

Tab. 19 shows the determined mean values of the tests performed.

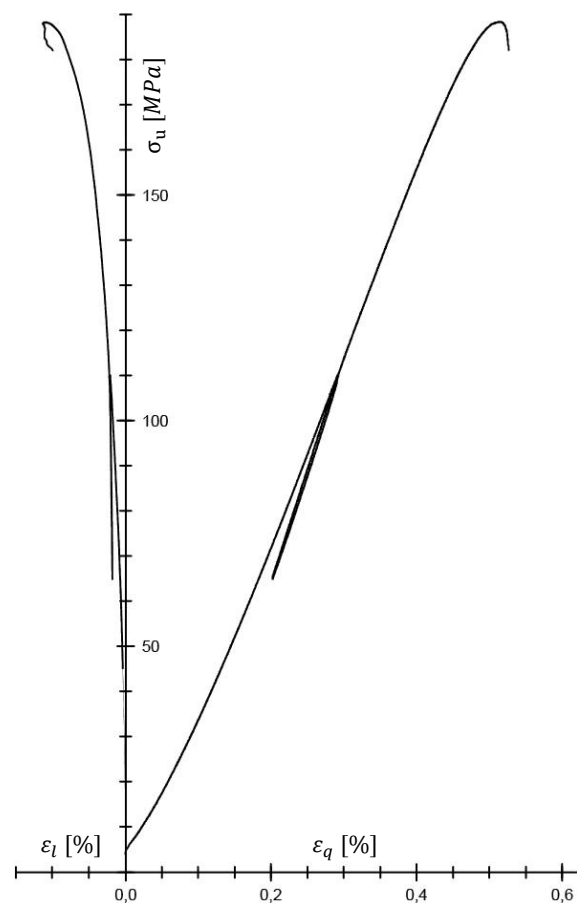


Fig. 87: Example of a typical stress-strain curve (TUM-001-04A-01).

Tab. 19: Characteristic values of the quarry TUM-002.

Quarry	State	Parameter	Units	min.	mean	med.	max.	n
TUM-002	dry	$v_{pl}$	[m/s]	3,643.8	<b>4,207.1</b>	4,237.7	4,570.0	23
		$v_{pd}$	[m/s]	3,544.7	<b>4,379.4</b>	4,356.7	5,028.7	
		$v_s$	[m/s]	2,190.0	<b>2,501.9</b>	2,542.5	2,790.0	
		$E_{dyn}$	[GPa]	32.19	<b>39.69</b>	39.27	48.39	
		$G_{dyn}$	[GPa]	12.57	<b>16.28</b>	16.77	20.55	
		$K_{dyn}$	[GPa]	19.10	<b>23.97</b>	24.10	30.30	
		$\nu_{dyn}$	[-]	0.18	<b>0.22</b>	0.22	0.29	
		Z	[ $10^6$ kg/m <sup>2</sup> s]	10.0	<b>11.08</b>	11.25	12.0	
	sat.	$v_{pl}$	[m/s]	4,854.0	<b>5,376.3</b>	5,381.0	5,672.9	22
		$v_{pd}$	[m/s]	4,703.9	<b>5,368.8</b>	5,418.4	5,930.8	
		$v_s$	[m/s]	2,160.0	<b>2,510.1</b>	2,526.3	2,764.5	
		$E_{dyn}$	[GPa]	35.94	<b>46.52</b>	47.29	53.43	
		$G_{dyn}$	[GPa]	12.86	<b>17.09</b>	17.18	20.21	
		$K_{dyn}$	[GPa]	48.60	<b>57.52</b>	57.78	72.80	
		$\nu_{dyn}$	[-]	0.32	<b>0.36</b>	0.36	0.40	
		Z	[ $10^6$ kg/m <sup>2</sup> s]	13.70	<b>14.48</b>	14.48	15.90	
	dry	$\sigma_u$	[MPa]	100.7	<b>153.0</b>	149.0	193.4	14
		V	[GPa]	27.16	<b>36.27</b>	38.37	42.38	12
		E	[GPa]	35.32	<b>47.0</b>	49.17	52.44	
		$\nu$	[-]	0.08	<b>0.15</b>	0.13	0.26	40
		$\sigma_t$	[MPa]	5.3	<b>8.7</b>	8.9	11.8	
		$I_s$	[MPa]	2.0	<b>7.8</b>	8.0	13.10	41
		$I_{s(50)}$	[MPa]	2.0	<b>7.7</b>	7.40	13.20	
$\sigma_m$		[MPa]	39.10	<b>154.7</b>	148.0	264.10	36	
CAI		[-]	4.3	<b>5.3</b>	5.4	5.8		
LAC		[g/t]	1100	<b>1290</b>	1330	1340	6	
LBC		[%]	53	<b>59</b>	58	71		
dry	$\Phi_{eff}^{He}$	[%]	1.20	<b>2.35</b>	2.50	3.84	1	
sat.	$\Phi_{eff}^W$	[%]	0.59	<b>1.17</b>	1.17	1.89	23	
dry	$\rho_b$	[g/cm <sup>3</sup> ]	2.52	<b>2.62</b>	2.63	2.67	23	
	$\rho_g$	[g/cm <sup>3</sup> ]	2.65	<b>2.65</b>	2.65	2.65	1	

A summary of all test results of the quarry TUM-002 is given in the Appendix.

### Quarry TUM-003

The active quarry TUM-003 is located 2 km west–southwest of the town of Kirchenlamitz. Three blocks were bought from the Waldstein massif and no samples were drilled directly in the field from the Epprechtstein hill. A total of 61 samples were drilled from these three blocks. These granite blocks show different stages of weathering. The quarry under investigation is the western quarry of the two examined quarries at the Epprechtstein hill. There, at the NE end of the Waldstein massif, the “Epprechtstein granite” is exposed. This granite is a Variscan G3 “Kern granite” and has a homogeneous structural fabric (RICHTER & STETTNER 1979) The rock appears as a bright gray to pastel yellow colour with biotite shed and shiny muscovite (MÜLLER 1997). The maximum grain size determined is 3 mm. According to HECHT (1998) the mineral content is: quartz 39.7 %, alkali feldspar 31.5 %, plagioclase 18.5 %, biotite 4.5 %, muscovite 5.6 % and the rest is made up of accessory minerals like chlorite. It is classified as medium-grained two-mica granite (Fig. 88) (HECHT 1998; SCHARFENBERG et al. 2016).

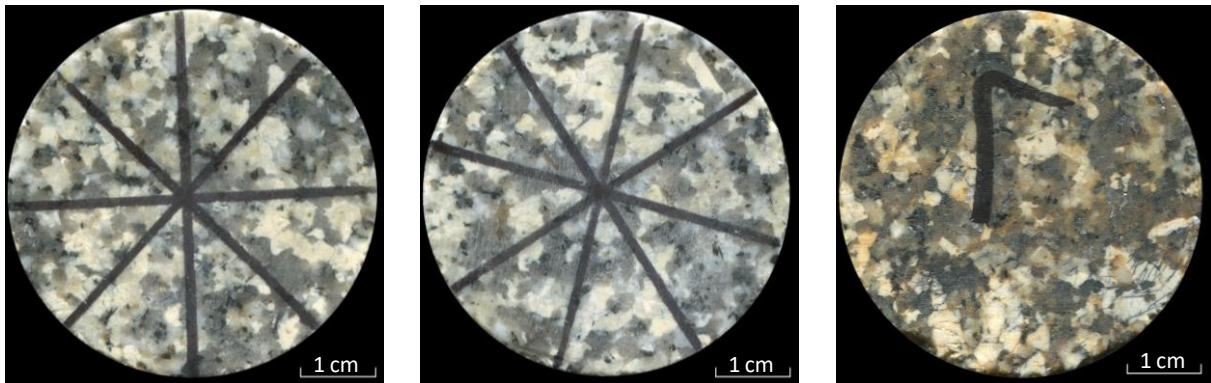


Fig. 88: Scans of samples of TUM-003 which were exposed to different weathering conditions.

Fig. 89 shows a typical stress-strain curve of the Epprechtstein granite. Clearly visible is the long path of the axial and also lateral strain. At the beginning of the curve there is nearly no nonlinear shape to the curve. Then the shape of the curve becomes linear and the elasto–plastic deformation takes place. The last part of the curve with unstable crack growth and plastic deformation begins at 90 %. In this quarry the failure mode builds mostly conjugate pairs of shear failure surfaces.

A total of 46 UT, 40 UCT (12 preliminary tests and 28 main tests), 37 BTT, 30 CAIT, 14 LCPCT as well as 68 PLT were performed from the collected samples.

The Tab. 20 shows the determined key parameter values of the tests performed.

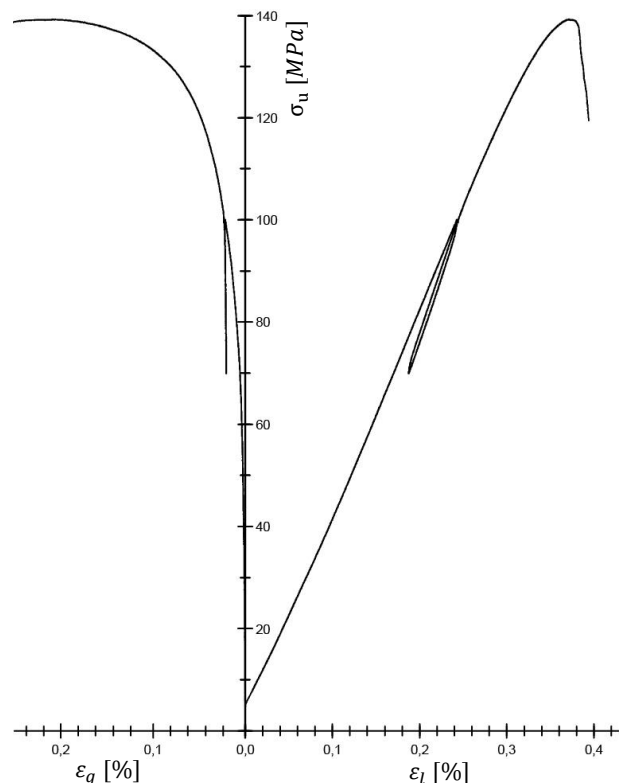


Fig. 89: Example of a typical stress-strain curve (TUM-003-011-05).

Tab. 20: Characteristic values of the quarry TUM-003.

Quarry	State	Parameter	Units	min.	mean	med.	max.	n
TUM-003	dry	$v_{pl}$	[m/s]	3,660.0	<b>5,045.5</b>	5,120.6	6,394.1	46
		$v_{pd}$	[m/s]	3,682.1	<b>5,197.7</b>	5,207.7	6,321.7	
		$v_s$	[m/s]	2,041.0	<b>2,769.9</b>	2,795.3	3,261.0	
		$E_{dyn}$	[GPa]	28.77	<b>51.74</b>	52.90	69.14	
		$G_{dyn}$	[GPa]	10.87	<b>20.42</b>	20.58	27.80	
		$K_{dyn}$	[GPa]	16.20	<b>37.13</b>	40.08	58.50	
		$\nu_{dyn}$	[-]	0.17	<b>0.27</b>	0.28	0.32	
		Z	[10 <sup>6</sup> kg/m <sup>2</sup> s]	10.40	<b>13.09</b>	13.35	15.25	
	sat.	$v_{pl}$	[m/s]	4,830.8	<b>5,298.5</b>	5,398.4	5,567.6	15
		$v_{pd}$	[m/s]	4,784.7	<b>5,130.1</b>	5,135.3	5,421.8	
		$v_s$	[m/s]	2,347.0	<b>2,726.7</b>	2,731.0	3,001.0	
		$E_{dyn}$	[GPa]	39.67	<b>53.74</b>	53.97	64.01	
		$G_{dyn}$	[GPa]	14.52	<b>19.77</b>	19.62	23.79	
		$K_{dyn}$	[GPa]	49.65	<b>64.45</b>	64.40	74.45	
		$\nu_{dyn}$	[-]	0.34	<b>0.36</b>	0.36	0.39	
		Z	[10 <sup>6</sup> kg/m <sup>2</sup> s]	13.45	<b>15.44</b>	15.70	16.30	
	dry	$\sigma_u$	[MPa]	113.0	<b>136.4</b>	137.6	149.4	40
		V	[GPa]	32.99	<b>40.79</b>	39.72	60.22	28
		E	[GPa]	47.39	<b>51.76</b>	50.66	74.01	
		$\nu$	[-]	0.09	<b>0.22</b>	0.22	0.31	37
		$\sigma_t$	[MPa]	6.3	<b>8.5</b>	8.4	11.4	68
		$I_s$	[MPa]	3.0	<b>6.59</b>	7.0	9.30	
		$I_{s(50)}$	[MPa]	3.0	<b>6.61</b>	7.0	9.50	
		$\sigma_m$	[MPa]	60.70	<b>132.2</b>	139.2	189.3	30
		CAI	[-]	4.3	<b>5.1</b>	5.2	5.6	14
		LAC	[g/t]	1160	<b>1260</b>	1260	1360	
		LBC	[%]	65	<b>70</b>	69	75	
	dry	$\Phi_{eff}^{He}$	[%]	3.53	<b>5.0</b>	5.67	5.79	3
	sat.	$\Phi_{eff}^W$	[%]	0.66	<b>1.07</b>	0.81	4.63	15
	dry	$\rho_b$	[g/cm <sup>3</sup> ]	2.59	<b>2.63</b>	2.63	2.66	46
$\rho_g$		[g/cm <sup>3</sup> ]	2.64	<b>2.64</b>	2.64	2.64	3	

A summary of all test results of the quarry TUM-003 is given in the Appendix.

### Quarry TUM-004

The active quarry TUM-004 is located 3 km north–westnorth of the town of Weißenstadt. One block was obtained from the Waldstein massif and three samples were drilled directly in the field from the east hillside of the Waldstein.

A total of 11 samples were drilled from the one block. In the quarry the “Waldstein granite” is exposed, revealing a Variscan G3 “Kern granite” with a homogeneous structural fabric (RICHTER & STETTNER 1979). The rock appears as a bright grey to beige colour (MÜLLER 1997). The maximum grain size determined is 4 mm.

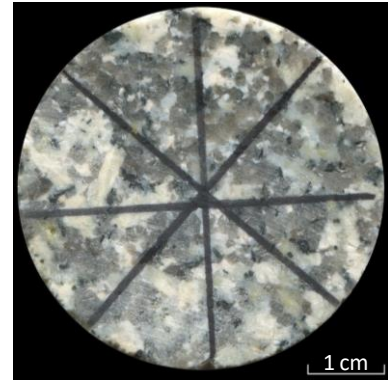


Fig. 90: Scan of a sample of TUM-004.

According to www-14, the mineral content is: quartz max. 43.3 %, max. 62 % alkali feldspar+plagioclase, max. 13.4 % biotite+muscovite and the rest accessory minerals. It is classified as medium- to coarse-grained two-mica granite (Fig. 90) (HECHT 1998; SCHARFENBERG et al. 2016).

Fig. 91 shows a typical stress-strain curve of Waldstein granite. Clearly visible is the long path of the axial strain and the very low lateral strain. At the beginning of the curve the shape is nonlinear and the elastic deformation takes place. Then the shape of the curve becomes linear and the elasto–plastic deformation takes place. Afterwards the curve shows one small step where a fracture was probably reactivated and then closed. The lateral strain is recorded undisturbed up to this step. The last part of the curve with unstable crack growth and plastic deformation is nearly not visible. In this quarry, the failure is spontaneous and the failure mode builds mostly conjugate pairs of shear failure surfaces.

A total of 14 UT, 8 UCT (3 preliminary tests and 5 main tests), 39 BTT, 19 CAIT, 2 LCPCT as well as 13 PLT were performed from the collected samples.

Tab. 21 shows the determined key parameter values of the tests performed.

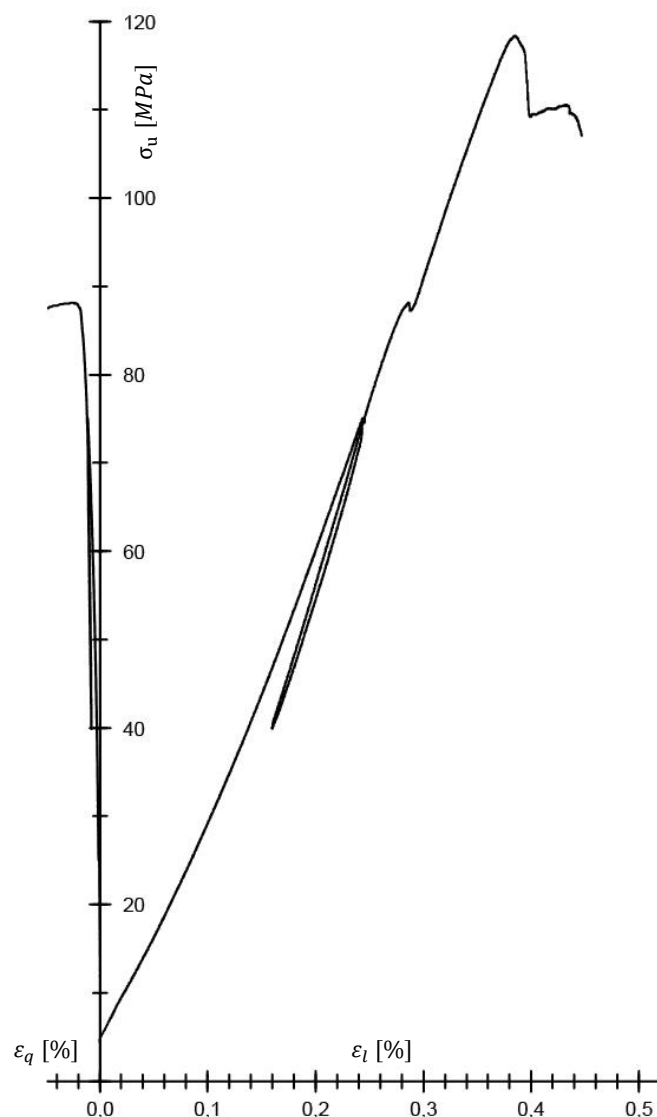


Fig. 91: Example of a typical stress-strain curve (TUM-004-01C-03).

Tab. 21: Characteristic values of the quarry TUM-004.

Quarry	State	Parameter	Units	min.	mean	med.	max.	n
TUM-004	dry	$v_{pl}$	[m/s]	4,637.6	<b>4,885.0</b>	4,787.0	5,492.6	14
		$v_{pd}$	[m/s]	4,629.4	<b>4,899.3</b>	4,899.3	5,411.1	
		$v_s$	[m/s]	2,784.5	<b>2,858.0</b>	2,832.5	3,023.0	
		$E_{dyn}$	[GPa]	49.72	<b>53.30</b>	51.35	61.08	
		$G_{dyn}$	[GPa]	20.30	<b>21.43</b>	21.07	24.05	
		$K_{dyn}$	[GPa]	29.30	<b>35.21</b>	32.35	47.25	
		$\nu_{dyn}$	[-]	0.22	<b>0.24</b>	0.23	0.30	
		Z	[10 <sup>6</sup> kg/m <sup>2</sup> s]	12.20	<b>12.89</b>	12.55	14.15	
	sat.	$v_{pl}$	[m/s]	5,270.6	<b>5,541.6</b>	5,542.8	5,793.3	12
		$v_{pd}$	[m/s]	5,368.2	<b>5,628.9</b>	5,621.2	6,096.0	
		$v_s$	[m/s]	2,873.5	<b>2,904.9</b>	2,905.0	2,944.5	
		$E_{dyn}$	[GPa]	56.44	<b>58.53</b>	58.37	60.36	
		$G_{dyn}$	[GPa]	21.49	<b>22.14</b>	22.17	22.83	
		$K_{dyn}$	[GPa]	43.50	<b>56.16</b>	54.60	72.30	
		$\nu_{dyn}$	[-]	0.28	<b>0.32</b>	0.32	0.36	
		Z	[10 <sup>6</sup> kg/m <sup>2</sup> s]	13.90	<b>14.98</b>	14.88	16.30	
	dry	$\sigma_u$	[MPa]	82.8	<b>108.4</b>	112.5	127.6	8
		V	[GPa]	29.63	<b>33.55</b>	33.67	36.18	5
		E	[GPa]	36.64	<b>40.61</b>	40.79	45.71	
		$\nu$	[-]	0.06	<b>0.07</b>	0.07	0.09	39
		$\sigma_t$	[MPa]	7.8	<b>9.2</b>	9.2	10.8	13
		$I_s$	[MPa]	6.5	<b>7.7</b>	7.9	8.6	
		$I_{s(50)}$	[MPa]	6.5	<b>7.7</b>	7.9	8.6	
		$\sigma_m$	[MPa]	129.8	<b>153.7</b>	157.2	172.8	19
CAI		[-]	4.6	<b>5.1</b>	5.1	5.4	2	
LAC		[g/t]	1380	<b>1410</b>	1410	1440		
LBC	[%]	57	<b>60</b>	60	63			
dry	$\Phi_{eff}^{He}$	[%]	0.81	<b>0.91</b>	0.91	1.0	2	
sat.	$\Phi_{eff}^W$	[%]	0.34	<b>0.51</b>	0.41	0.95	14	
dry	$\rho_b$	[g/cm <sup>3</sup> ]	2.60	<b>2.62</b>	2.63	2.67	14	
	$\rho_g$	[g/cm <sup>3</sup> ]	2.64	<b>2.64</b>	2.64	2.64	2	

A summary of all test results of the quarry TUM-004 is given in the Appendix.

### Quarry TUM-005

The active quarry TUM-005 is located 7 km west–southwest of the town of Marktredwitz. Three blocks were donated from the Kösseine massif and nine samples were drilled directly in the field from the southwest hillside of the Kösseine.

A total of 49 samples were drilled from the three blocks. The quarry under investigation is the easternmost quarry of the three quarries at the Kösseine. There, two different “Kösseine granites” are exposed. One is, as in TUM-001, the variety (G3K) of the Variscan G3 “Kern granite” and additionally accessible is the variety (G2K) of the Variscan G2 “Rand granite” (RICHTER & STETTNER 1979).

The G2K granite rock appears as a bright blue gray colour and is relatively homogeneous (SCHÖDLBAUER et al. 1996; SCHÖDLBAUER et al. 1997). The blue coloration is caused by cordierite (MÜLLER 1997). The rock has a variable, slightly porphyritically irregular structural fabric (MIELKE 1982) (www-15). According to www-15, the mineral content is: quartz 36 %, alkali feldspar 41 %, plagioclase 13 %, biotite 6 %, muscovite and chlorite 2 % and ~2 % accessory minerals. It is classified as medium-grained, weak porphyritic biotite granite (Fig. 92) (HECHT 1998; SCHARFENBERG et al. 2016).

Fig. 93 shows a typical stress-strain curve of the Kösseine granite. Clearly visible is the long path of the axial strain and the low lateral strain. At the beginning of the curve the shape is nonlinear and the elastic deformation takes place. Then the shape of the curve becomes linear and the elasto–plastic deformation takes place. The last part of the curve with unstable crack growth and plastic deformation begins at 90 %. In this quarry the failure mode builds mostly conjugate pairs of shear failure surfaces.

A total of 34 UT, 28 UCT (8 preliminary tests and 20 main tests), 35 BTT, 12 PLT as well as 26 CAIT and 8 LCPCT were performed from the collected samples.

Tab. 22 shows the determined key parameter values of the tests performed.

A summary of all test results of the quarry TUM-005 is given in the Appendix.

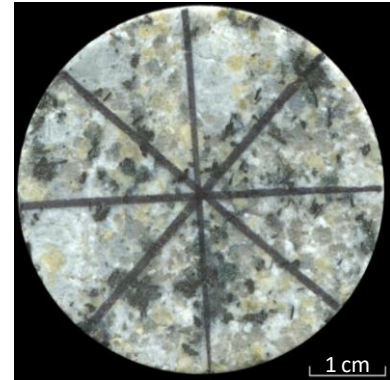


Fig. 92: Scan of a sample of TUM-005.

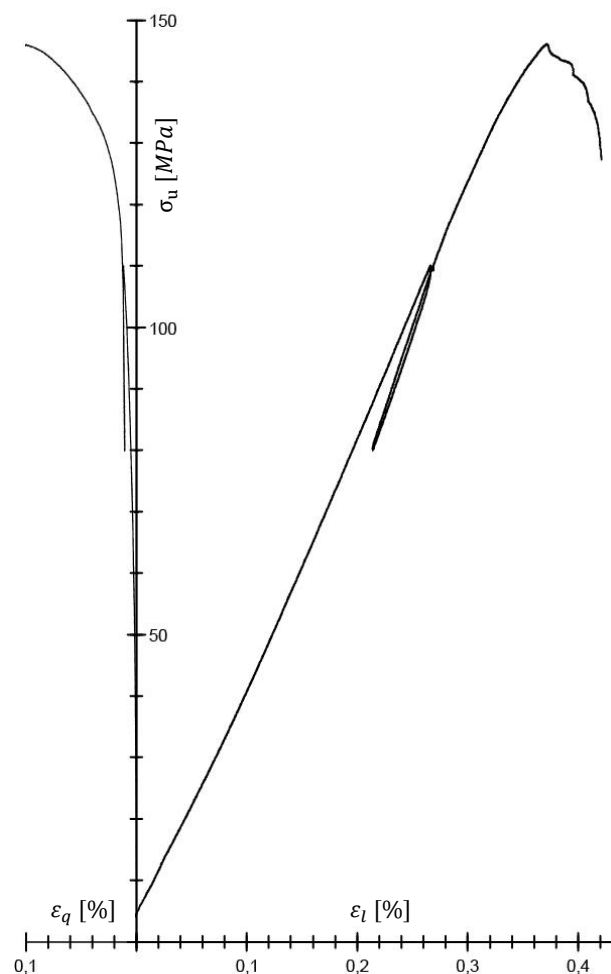


Fig. 93: Example of a typical stress-strain curve (TUM-005-01A-04).

Tab. 22: Characteristic values of the quarry TUM-005.

Quarry	State	Parameter	Units	min.	mean	med.	max.	n
TUM-005	dry	$v_{pl}$	[m/s]	3,633.4	<b>5,101.9</b>	5,206.4	6,318.7	34
		$v_{pd}$	[m/s]	3,622.6	<b>5,120.6</b>	5,244.7	6,357.8	
		$v_s$	[m/s]	1,439.0	<b>2,697.1</b>	2,789.5	3,152.0	
		$E_{dyn}$	[GPa]	15.61	<b>50.39</b>	53.23	64.95	
		$G_{dyn}$	[GPa]	5.48	<b>19.72</b>	20.59	26.19	
		$K_{dyn}$	[GPa]	25.30	<b>40.77</b>	40.80	54.55	
		$\nu_{dyn}$	[-]	0.14	<b>0.29</b>	0.29	0.44	
		Z	[10 <sup>6</sup> kg/m <sup>2</sup> s]	9.78	<b>13.39</b>	13.53	16.61	
	sat.	$v_{pl}$	[m/s]	4,653.7	<b>5,440.9</b>	5,527.3	5,734.6	13
		$v_{pd}$	[m/s]	5,218.1	<b>5,384.4</b>	5,332.3	5,771.3	
		$v_s$	[m/s]	1,757.5	<b>2,750.0</b>	2,879.0	3,191.0	
		$E_{dyn}$	[GPa]	23.69	<b>56.08</b>	59.73	72.85	
		$G_{dyn}$	[GPa]	8.23	<b>20.56</b>	22.02	27.03	
		$K_{dyn}$	[GPa]	61.80	<b>71.88</b>	71.90	81.35	
		$\nu_{dyn}$	[-]	0.35	<b>0.37</b>	0.36	0.44	
		Z	[10 <sup>6</sup> kg/m <sup>2</sup> s]	13.90	<b>16.19</b>	16.55	17.50	
	dry	$\sigma_u$	[MPa]	85.5	<b>149.5</b>	152.8	170.4	28
		V	[GPa]	26.71	<b>42.52</b>	42.39	58.21	20
		E	[GPa]	46.81	<b>54.66</b>	53.28	78.38	
		$\nu$	[-]	0.04	<b>0.17</b>	0.13	0.49	35
		$\sigma_t$	[MPa]	7.0	<b>10.0</b>	10.2	12.6	12
		$I_s$	[MPa]	6.3	<b>7.7</b>	7.6	9.2	
		$I_{s(50)}$	[MPa]	6.4	<b>7.7</b>	7.6	9.3	
		$\sigma_m$	[MPa]	128.1	<b>154.2</b>	154.2	185.6	26
		CAI	[-]	3.6	<b>4.6</b>	4.6	5.5	8
		LAC	[g/t]	1120	<b>1213</b>	1200	1340	
		LBC	[%]	46	<b>47</b>	47	49	
	dry	$\Phi_{eff}^{He}$	[%]	0.67	<b>0.86</b>	0.90	1.01	3
sat.	$\Phi_{eff}^W$	[%]	0.61	<b>0.97</b>	1.0	1.33	13	
dry	$\rho_b$	[g/cm <sup>3</sup> ]	2.63	<b>2.65</b>	2.65	2.69	41	
	$\rho_g$	[g/cm <sup>3</sup> ]	2.66	<b>2.67</b>	2.67	2.68	3	

### Quarry TUM-006

The active quarry TUM-006 is located ~1.8 km west–southwest of the town of Kirchenlamitz. Three blocks were donated from the Waldstein massif and seven samples were drilled directly in the field from the Epprechtstein hill. A total of 61 samples were drilled from three blocks. The quarry under investigation is the easternmost of the two quarries at the Epprechtstein hill. There, at the NE end of the Waldstein massif, the “Epprechtstein granite” is exposed. This granite is a Variscan G3 “Kern granite” and has a homogeneous structural fabric (RICHTER & STETTNER 1979) The rock appears as a bright grey to pastel yellow colour with biotite shed and shiny muscovite (MÜLLER 1997). The maximum grain size determined is 4 mm. According to GOEMAN (1972) the mineral content is: quartz 36.9 %, alkali feldspar 33.4 %, plagioclase 19.8 %, biotite 4.5 %, muscovite 5 % and the rest is made up of accessory minerals like chlorite. It is classified as medium- to coarse-grained two-mica granite (Fig. 94) (HECHT 1998; SCHARFENBERG et al. 2016).

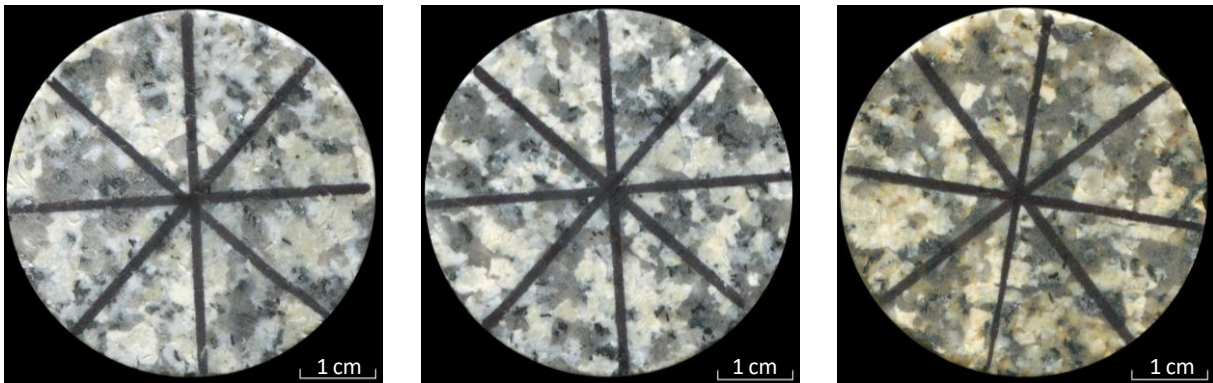


Fig. 94: Scan of samples of TUM-006. From left to right the colour changes from grey to pastel yellow.

Fig. 95 shows a typical stress-strain curve of Epprechtstein granite. Clearly visible is the long path of the axial strain and the low transversal strain. At the beginning of the curve the shape is nonlinear and the elastic deformation takes place. Then the shape of the curve becomes linear and the elasto-plastic deformation takes place. The last part of the curve with unstable crack growth and plastic deformation begins at 95 %. In this quarry the failure mode builds mostly conjugate pairs of shear failure surfaces.

A total of 51 UT, 46 UCT (17 preliminary tests and 29 main tests), 58 BTT, 35 CAIT as well as 6 LCPCT were performed from the collected samples.

Tab. 23 shows the determined key parameter values of the tests performed.

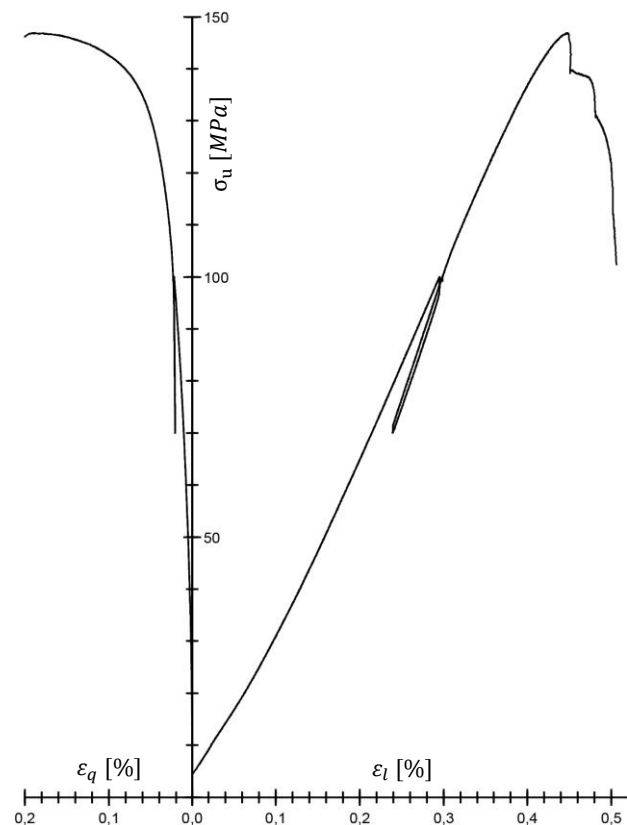


Fig. 95: Example of a typical stress-strain curve (TUM-006-03A-10).

Tab. 23: Characteristic values of the quarry TUM-006.

Quarry	State	Parameter	Units	min.	mean	med.	max.	n
TUM-006	dry	$v_{pl}$	[m/s]	3,499.5	<b>4,719.4</b>	4,811.1	5,452.1	51
		$v_{pd}$	[m/s]	3,938.4	<b>4,848.3</b>	4,921.1	5,591.1	
		$v_s$	[m/s]	2,151.0	<b>2,693.8</b>	2,760.0	3,082.0	
		$E_{dyn}$	[GPa]	31.06	<b>48.27</b>	51.02	61.64	
		$G_{dyn}$	[GPa]	12.02	<b>19.42</b>	20.01	43.26	
		$K_{dyn}$	[GPa]	18.40	<b>35.04</b>	36.70	47.60	
		$\nu_{dyn}$	[-]	0.21	<b>0.27</b>	0.28	0.32	
		Z	[ $10^6$ kg/m <sup>2</sup> s]	9.80	<b>12.62</b>	12.68	15.65	
	sat.	$v_{pl}$	[m/s]	4,767.1	<b>5,090.2</b>	5,062.2	5,436.4	20
		$v_{pd}$	[m/s]	4,452.0	<b>5,017.6</b>	5,017.6	5,446.7	
		$v_s$	[m/s]	2,225.5	<b>2,570.1</b>	2,512.3	2,836.0	
		$E_{dyn}$	[GPa]	35.80	<b>47.80</b>	45.48	57.29	
		$G_{dyn}$	[GPa]	12.94	<b>17.41</b>	16.53	21.08	
		$K_{dyn}$	[GPa]	51.05	<b>62.98</b>	61.55	71.0	
		$\nu_{dyn}$	[-]	0.36	<b>0.37</b>	0.37	0.39	
		Z	[ $10^6$ kg/m <sup>2</sup> s]	13.30	<b>15.01</b>	14.93	16.10	
	dry	$\sigma_u$	[MPa]	101.0	<b>141.4</b>	142.2	176.3	29
		V	[GPa]	32.09	<b>40.11</b>	38.28	64.03	17
		E	[GPa]	46.95	<b>53.56</b>	51.20	81.40	
		$\nu$	[-]	0.01	<b>0.15</b>	0.13	0.43	58
		$\sigma_t$	[MPa]	5.6	<b>9.1</b>	9.1	11.9	35
		CAI	[-]	5.1	<b>5.4</b>	5.4	5.8	6
		LAC	[g/t]	1220	<b>1263</b>	1260	1320	
		LBC	[%]	61	<b>64</b>	63	69	
	dry	$\phi_{eff}^{He}$	[%]	0.95	<b>1.06</b>	1.05	1.22	6
	sat.	$\phi_{eff}^W$	[%]	0.94	<b>1.04</b>	1.01	1.44	20
	dry	$\rho_b$	[g/cm <sup>3</sup> ]	2.60	<b>2.63</b>	2.62	2.69	65
$\rho_g$		[g/cm <sup>3</sup> ]	2.63	<b>2.64</b>	2.64	2.65	6	

A summary of all test results of the quarry TUM-006 is given in the Appendix.

## Quarry TUM-007

The currently inactive TUM-007 is located ~1.5 km south–east of the town of Reinersreuth and east of the through road 18. Two blocks were donated from the Waldstein massif and 17 samples were drilled directly in the field from the north hillside of the Waldstein. A total of 22 samples were drilled from the two blocks. There, the “Reinersreuth granite” is exposed. This granite is a Variscan G3 “Kern granite” and has a homogeneous structural fabric (RICHTER & STETTNER 1979). The rock appears as a bright grey to pastel yellow colour with biotite shed and shiny muscovite (MÜLLER 1997). The maximum grain size determined is 3 mm. According to GOEMAN (1972) the mineral content is: quartz max. 33.3 %, 35.5 % alkali feldspar, 23.3 % plagioclase, 3.7 % biotite, 4.4 % muscovite and the rest is composed of accessory minerals. It is classified as medium-grained two-mica granite (Fig. 97: left) (HECHT 1998; SCHARFENBERG et al. 2016). In addition, samples were taken from the “Reinersreuth Granitporphyr”. This rock has a dark microcrystalline, structurally irregular variable fabric with millimetre to centimetre sized granite inclusions (Fig. 96) (www-16).

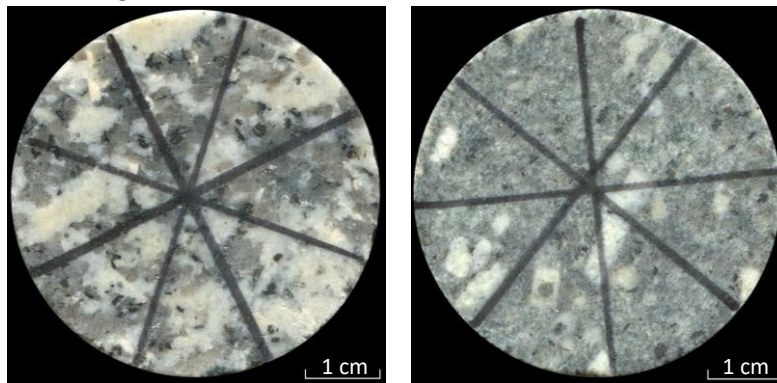


Fig. 96: Scan of a samples of TUM-007. Left: Reinersreuth granite; right: Reinersreuth Granitporphyr.

Fig. 97 shows a typical stress-strain curve of Reinersreuth granite. Clearly visible is the long path of the axial strain and the very low lateral strain. At the beginning of the curve the shape is nonlinear and the elastic deformation takes place. Then the shape of the curve becomes linear and the elasto–plastic deformation takes place. The last part of the curve with unstable crack growth and plastic deformation begins at 95 %. In this quarry the failure mode builds mostly conjugate pairs of shear failure surfaces.

In total 30 UT, 23 UCT (8 preliminary tests and 15 main tests), 50 BTT, 26 CAIT, 4 LCPCT as well as 48 PLT were performed from the collected samples.

Tab. 24 shows the determined key parameters values of the tests performed.

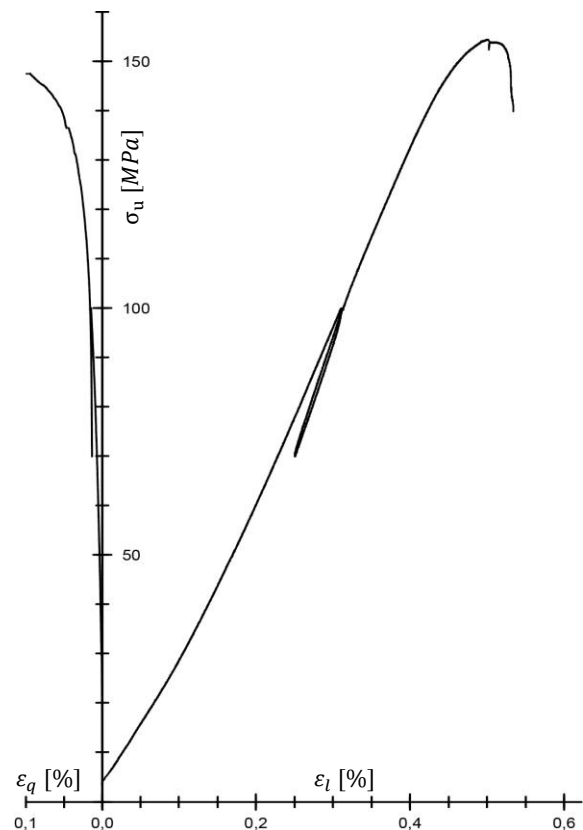


Fig. 97: Example of a typical stress-strain curve (TUM-007-01C-04).

Tab. 24: Characteristic values of the quarry TUM-007.

Quarry	State	Parameter	Units	min.	mean	med.	max.	n
TUM-007	dry	$v_{pl}$	[m/s]	3,847.5	<b>5,011.3</b>	5,139.9	6,458.5	30
		$v_{pd}$	[m/s]	3,680.8	<b>5,044.6</b>	5,039.0	6,049.6	
		$v_s$	[m/s]	2,220.0	<b>2,841.1</b>	2,824.0	3,366.0	
		$E_{dyn}$	[GPa]	31.33	<b>54.0</b>	52.47	75.26	
		$G_{dyn}$	[GPa]	12.87	<b>21.49</b>	20.95	29.86	
		$K_{dyn}$	[GPa]	18.0	<b>37.46</b>	36.50	62.80	
		$\nu_{dyn}$	[-]	0.19	<b>0.25</b>	0.25	0.31	
		Z	[ $10^6$ kg/m <sup>2</sup> s]	10.10	<b>13.16</b>	13.35	16.30	
	sat.	$v_{pl}$	[m/s]	4,715.3	<b>5,432.5</b>	5,497.9	5,785.3	21
		$v_{pd}$	[m/s]	4,538.1	<b>5,329.7</b>	5,467.2	5,640.5	
		$v_s$	[m/s]	2,220.0	<b>2,867.5</b>	2,885.5	3,269.5	
		$E_{dyn}$	[GPa]	31.33	<b>59.26</b>	59.56	74.97	
		$G_{dyn}$	[GPa]	12.87	<b>22.0</b>	21.92	28.41	
		$K_{dyn}$	[GPa]	18.40	<b>66.77</b>	69.80	85.15	
		$\nu_{dyn}$	[-]	0.22	<b>0.35</b>	0.35	0.39	
		Z	[ $10^6$ kg/m <sup>2</sup> s]	10.10	<b>15.84</b>	16.55	17.60	
	dry	$\sigma_u$	[MPa]	80.3	<b>145.4</b>	142.2	226.6	23
		V	[GPa]	24.10	<b>35.48</b>	37.04	46.22	15
		E	[GPa]	30.33	<b>47.28</b>	47.74	53.39	
		$\nu$	[-]	0.03	<b>0.12</b>	0.12	0.21	50
		$\sigma_t$	[MPa]	5.0	<b>9.6</b>	9.5	16.3	
$I_s$		[MPa]	5.2	<b>8.9</b>	8.7	13.7	48	
$I_{s(50)}$		[MPa]	5.2	<b>8.9</b>	8.7	13.4		
$\sigma_m$		[MPa]	103.3	<b>177.4</b>	172.7	268.9	26	
CAI		[-]	4.5	<b>5.0</b>	5.0	5.6		
LAC		[g/t]	1280	<b>1355</b>	1350	1440	4	
LBC	[%]	65	<b>66</b>	66	67			
dry	$\Phi_{eff}^{He}$	[%]	0.70	<b>1.20</b>	1.20	1.71	2	
sat.	$\Phi_{eff}^W$	[%]	0.41	<b>0.79</b>	0.81	1.54	22	
dry	$\rho_b$	[g/cm <sup>3</sup> ]	2.59	<b>2.63</b>	2.63	2.68	35	
	$\rho_g$	[g/cm <sup>3</sup> ]	2.64	<b>2.65</b>	2.65	2.65	2	

A summary of all test results of the quarry TUM-007 is given in the Appendix.

### Geotope TUM-008

The geotope TUM-008 is located ~0.5 km east-southeast of the town of Markt-leuthen. One block was taken from the Weissenstadt–Markt-leuthen massif and eight samples were drilled directly in the field.

In total three samples were drilled from the block. The quarry under investigation is the easternmost quarries of the two quarries at the Bibersberg hill. There the “Bibersberg granite” is exposed (www-17). This granite is a Variscan G1 “porphyric granite” and has an irregular structural fabric (MIELKE & STETTNER 1984).

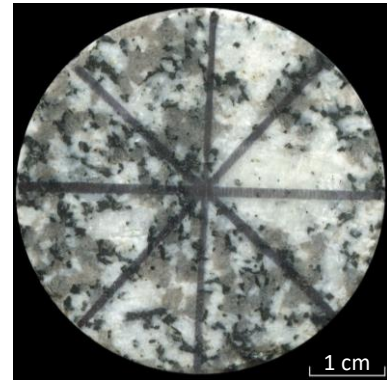


Fig. 98: Scan of a sample of TUM-008.

The rock appears as a bright grey colour with large alkali feldspars (RICHTER & STETTNER 1979) (www-18). The maximum grain size determined is 10 mm. The mean determined mineral content is: quartz 30 %, alkali feldspar 40 %, plagioclase 15 %, biotite 10 %, muscovite 3 % and 2 % accessory minerals. It is classified as porphyritic, coarse-grained biotite granite (Fig. 98) (HECHT 1998; SCHARFENBERG et al. 2016).

Fig. 99 shows a typical stress-strain curve of Bibersberg granite. Clearly visible is the long path of the axial strain and the low lateral strain. At the beginning of the curve the shape is nonlinear and the elastic deformation takes place. Then the shape of the curve becomes linear and the elasto-plastic deformation takes place.

The last part of the curve with unstable crack growth and plastic deformation begins at 85 %. In this quarry the failure mode builds mostly conjugate pairs of shear failure surfaces.

A total of 10 UT, 7 UCT (2 preliminary tests and 5 main tests), 20 BTT, 14 CAIT, 2 LCPCT as well as 12 PLT were performed from the collected sample material.

Tab. 25 shows the determined key parameter values of the tests performed.

A summary of all test results of the quarry TUM-008 is given in the Appendix.

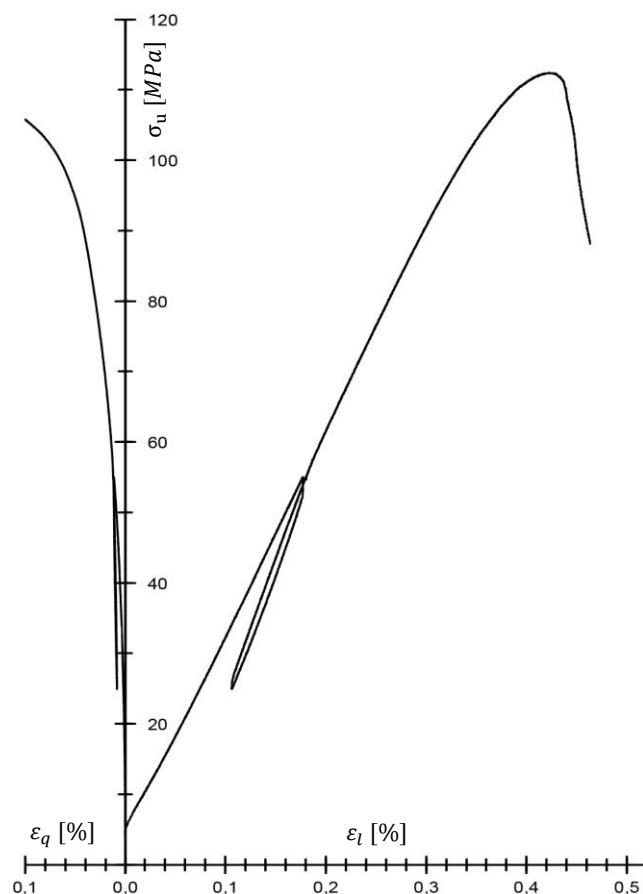


Fig. 99: Example of a typical stress-strain curve (TUM-008-01A-02).

Tab. 25: Characteristic values of the geotope TUM-008.

Geotope	State	Parameter	Units	min.	mean	med.	max.	n
TUM-008	dry	$v_{pl}$	[m/s]	4,021.4	<b>4,264.9</b>	4,204.3	4,503.1	10
		$v_{pd}$	[m/s]	3,783.6	<b>4,288.0</b>	4,168.3	4,790.4	
		$v_s$	[m/s]	2,328.0	<b>2,489.4</b>	2,501.5	2,673.0	
		$E_{dyn}$	[GPa]	35.73	<b>41.05</b>	41.09	46.78	
		$G_{dyn}$	[GPa]	14.31	<b>16.50</b>	16.62	19.06	
		$K_{dyn}$	[GPa]	20.52	<b>26.25</b>	26.55	29.90	
		$\nu_{dyn}$	[-]	0.23	<b>0.24</b>	0.25	0.27	
		Z	[ $10^6$ kg/m <sup>2</sup> s]	10.60	<b>11.37</b>	11.25	12.0	
	sat.	$v_{pl}$	[m/s]	5,001.8	<b>5,182.7</b>	5,115.5	5,516.2	10
		$v_{pd}$	[m/s]	4,745.5	<b>5,200.8</b>	5,155.6	5,603.3	
		$v_s$	[m/s]	2,317.0	<b>2,506.4</b>	2,473.8	2,697.0	
		$E_{dyn}$	[GPa]	39.07	<b>45.60</b>	44.38	52.11	
		$G_{dyn}$	[GPa]	14.28	<b>16.79</b>	16.26	19.46	
		$K_{dyn}$	[GPa]	46.30	<b>54.96</b>	51.03	67.70	
		$\nu_{dyn}$	[-]	0.33	<b>0.36</b>	0.36	0.39	
		Z	[ $10^6$ kg/m <sup>2</sup> s]	13.30	<b>14.34</b>	14.28	15.80	
	dry	$\sigma_u$	[MPa]	73.5	<b>98.6</b>	89.2	121.9	7
		V	[GPa]	20.72	<b>27.24</b>	26.57	33.88	5
		E	[GPa]	34.31	<b>38.57</b>	40.08	42.16	
		$\nu$	[-]	0.04	<b>0.10</b>	0.11	0.14	20
		$\sigma_t$	[MPa]	5.4	<b>6.3</b>	6.4	7.3	12
		$I_s$	[MPa]	6.6	<b>7.1</b>	6.9	7.8	
		$I_{s(50)}$	[MPa]	6.6	<b>7.1</b>	6.9	7.8	
		$\sigma_m$	[MPa]	131.2	<b>141.0</b>	137.8	156.0	14
		CAI	[-]	3.5	<b>4.2</b>	3.9	5.2	
		LAC	[g/t]	1180	<b>1200</b>	1200	1220	2
		LBC	[%]	69	<b>71</b>	71	72	
	dry	$\Phi_{eff}^{He}$	[%]	1.25	<b>1.32</b>	1.32	1.39	2
sat.	$\Phi_{eff}^W$	[%]	0.68	<b>0.89</b>	0.95	1.02	10	
dry	$\rho_b$	[g/cm <sup>3</sup> ]	2.64	<b>2.66</b>	2.65	2.68	10	
	$\rho_g$	[g/cm <sup>3</sup> ]	2.68	<b>2.68</b>	2.68	2.69	2	

### Quarry TUM-009

The currently inactive quarry TUM-009 is located 4.5 km north–east of the town of Kirchenlamitz. On the large Kornberg massif, four blocks were taken and six samples were directly in the field. The quarry under investigation is on the northwest hillside of the Großer Kornberg hill. A total of 17 samples were drilled from the four blocks. There the “Kornberg granite” is exposed, which is a Variscan G2 “Rand granite” (RICHTER & STETTNER 1979). In the quarry the granite exhibits different colours. The G2 granite rock appears either as a beige colour or a yellow colour. Due to limonite the alkali feldspars are more or less strongly yellow in colour (MÜLLER 1997). The granite has a homogenous ground mass and medium grained porphyric structural fabric (GOEMAN 1972). According to GOEMAN (1972) the mineral content is: quartz 31.6 %, alkali feldspar 44.5 %, plagioclase 14 %, biotite 7.3 %, muscovite 1.6 % and the rest accessory minerals. It is classified as porphyritic, medium-grained two-mica granite (Fig. 101) (HECHT 1998; SCHARFENBERG et al. 2016).

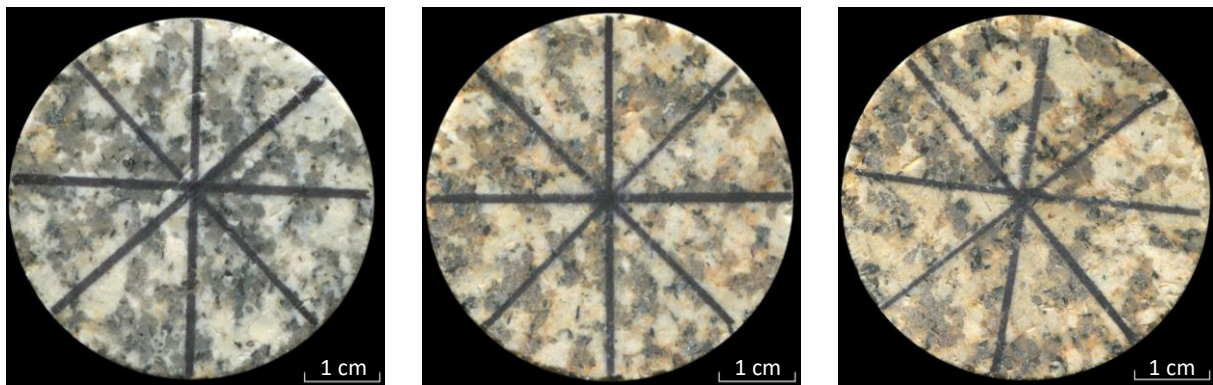


Fig. 101: Scan of samples of TUM-009 which were exposed to different weatherings (the degree of weathering increases from left to right).

Fig. 100 shows a typical stress-strain curve of Kornberg granite. Clearly visible is the long path of the axial strain and the low lateral strain. At the beginning of the curve the shape is nonlinear and the elastic deformation takes place. In this quarry this part is ~40 % of the curve. Then the shape of the curve becomes linear and the elasto–plastic deformation takes place. The last part of the curve with unstable crack growth and plastic deformation begins at 95 %. In this quarry the failure mode builds mostly conjugate pairs of shear failure surfaces.

A total of 23 UT, 15 UCT (5 preliminary tests and 10 main tests), 27 BTT, 22 CAIT, 8 LCPCT as well as 11 PLT were performed from the collected samples.

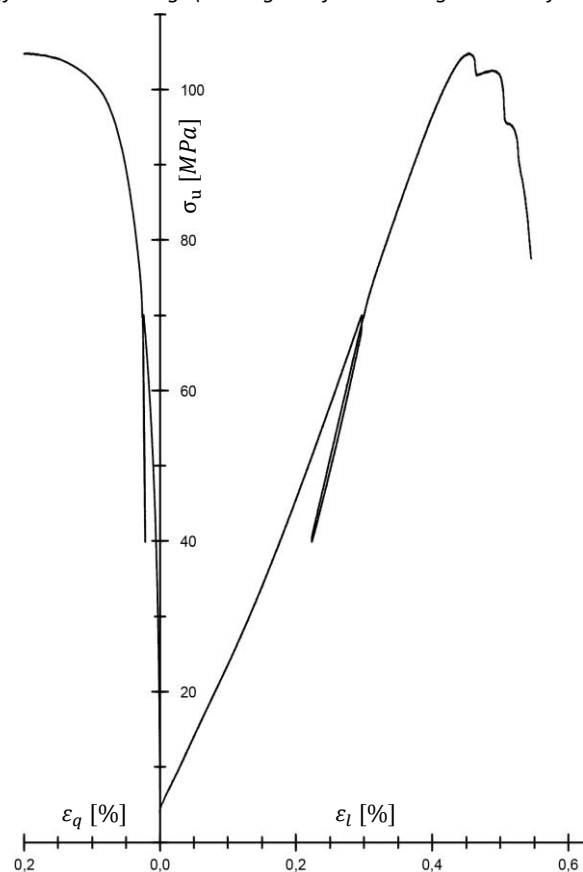


Fig. 100: Example of a typical stress-strain curve (TUM-009-04A-05).

Tab. 26 shows the determined key parameter values of the tests performed.

Tab. 26: Characteristic values of the quarry TUM-009.

Quarry	State	Parameter	Units	min.	mean	med.	max.	n
TUM-009	dry	$v_{pl}$	[m/s]	2,915.3	<b>3,709.1</b>	3,793.7	4,535.3	23
		$v_{pd}$	[m/s]	3,043.9	<b>4,128.4</b>	3,965.0	5,202.8	
		$v_s$	[m/s]	1,587.0	<b>2,067.1</b>	2,182.0	2,559.0	
		$E_{dyn}$	[GPa]	16.34	<b>29.93</b>	31.48	42.48	
		$G_{dyn}$	[GPa]	6.51	<b>11.58</b>	12.40	17.21	
		$K_{dyn}$	[GPa]	11.10	<b>19.78</b>	19.35	27.40	
		$v_{dyn}$	[-]	0.20	<b>0.26</b>	0.26	0.31	
		Z	[ $10^6$ kg/m <sup>2</sup> s]	7.50	<b>9.73</b>	9.80	11.95	
	sat.	$v_{pl}$	[m/s]	3,749.2	<b>4,780.7</b>	4,804.3	5,441.9	23
		$v_{pd}$	[m/s]	4,213.3	<b>4,890.0</b>	4,916.2	5,459.1	
		$v_s$	[m/s]	1,755.5	<b>2,272.5</b>	2,258.0	2,790.5	
		$E_{dyn}$	[GPa]	22.25	<b>38.20</b>	37.08	54.46	
		$G_{dyn}$	[GPa]	8.04	<b>13.96</b>	13.42	20.63	
		$K_{dyn}$	[GPa]	25.70	<b>52.33</b>	50.40	80.40	
		$v_{dyn}$	[-]	0.31	<b>0.37</b>	0.39	0.42	
		Z	[ $10^6$ kg/m <sup>2</sup> s]	9.80	<b>13.57</b>	13.40	16.70	
	dry	$\sigma_u$	[MPa]	87.9	<b>105.2</b>	104.9	119.5	15
		V	[GPa]	23.34	<b>27.19</b>	27.05	33.24	10
		E	[GPa]	33.16	<b>38.32</b>	38.92	41.69	
		$\nu$	[-]	0.06	<b>0.12</b>	0.10	0.18	27
		$\sigma_t$	[MPa]	4.6	<b>6.6</b>	6.0	9.9	
		$I_s$	[MPa]	5.9	<b>7.3</b>	7.3	8.4	
		$I_{s(50)}$	[MPa]	5.9	<b>7.3</b>	7.3	8.4	11
		$\sigma_m$	[MPa]	117.6	<b>145.1</b>	145.1	167.2	
		CAI	[-]	3.6	<b>4.6</b>	4.7	5.1	22
		LAC	[g/t]	1120	<b>1260</b>	1250	1400	8
	LBC	[%]	63	<b>69</b>	70	72		
dry	$\phi_{eff}^{He}$	[%]	1.09	<b>1.58</b>	1.76	1.89	3	
sat.	$\phi_{eff}^W$	[%]	0.47	<b>1.17</b>	1.19	1.96	23	
dry	$\rho_b$	[g/cm <sup>3</sup> ]	2.59	<b>2.63</b>	2.62	2.96	23	
	$\rho_g$	[g/cm <sup>3</sup> ]	2.65	<b>2.65</b>	2.65	2.65	3	

A summary of all test results of the quarry TUM-009 is given in the Appendix.

### Geotope TUM-010

The geotope TUM-010 is located 5 km east–northeast of the town of Selb on the Czech border. On the eastern part of the Weissenstadt–Marktleuthen massif, one block was taken and no samples were drilled directly in the field.

A total of 4 samples were drilled from the block. There, the “Holzmühl granite” is exposed, which is a variety (G1HS) of the Variscan G1 granite. The geotope under investigation is the north-eastern field of the G1HS (www-19). The rock is partly streaky relics of porphyritic granite (HECHT 1998) and partly streaky relics of biotite due to an irregularly variable structural fabric (RICHTER & STETTNER 1979).

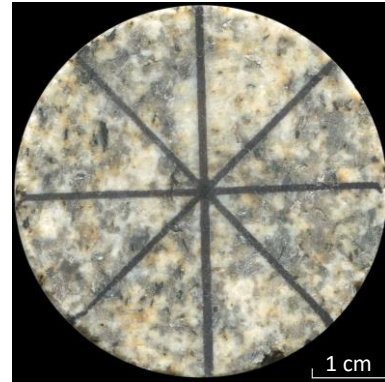


Fig. 102: Scan of a sample of TUM-010.

The Holzmühl granite rock appears as a beige colour with accumulation of biotite. The maximum grain size determined is 3 mm. According to RICHTER & STETTNER (1979) and the mean self determined mineral content is: quartz 36 %, alkali feldspar 28 %, plagioclase ~23 %, biotite 6.6 %, muscovite 3.1 % and chlorite ~2 % and the rest is composed of accessory minerals. It is classified as medium- to coarse-grained two-mica granite (Fig. 102) (HECHT 1998; SCHARFENBERG et al. 2016).

Fig. 103 shows a typical stress-strain curve of Holzmühl granite. Clearly visible is the long path of the axial strain and the low lateral strain. At the beginning of the curve the shape is nonlinear and the elastic deformation takes place. In this quarry this part is ~30 % of the curve. Then the shape of the curve becomes linear and the elasto–plastic deformation takes place. The last part of the curve with unstable crack growth and plastic deformation begins at 95 %. In this quarry the failure mode builds mostly conjugate pairs of shear failure surfaces.

A total of 4 UT, 2 UCT (1 preliminary tests and 1 main tests), 2 BTT, 2 CAIT as well as 2 LCPCT were performed from the collected samples.

Tab. 27 shows the determined key parameter values of the tests performed.

A summary of all test results of the quarry TUM-010 is given in the Appendix.

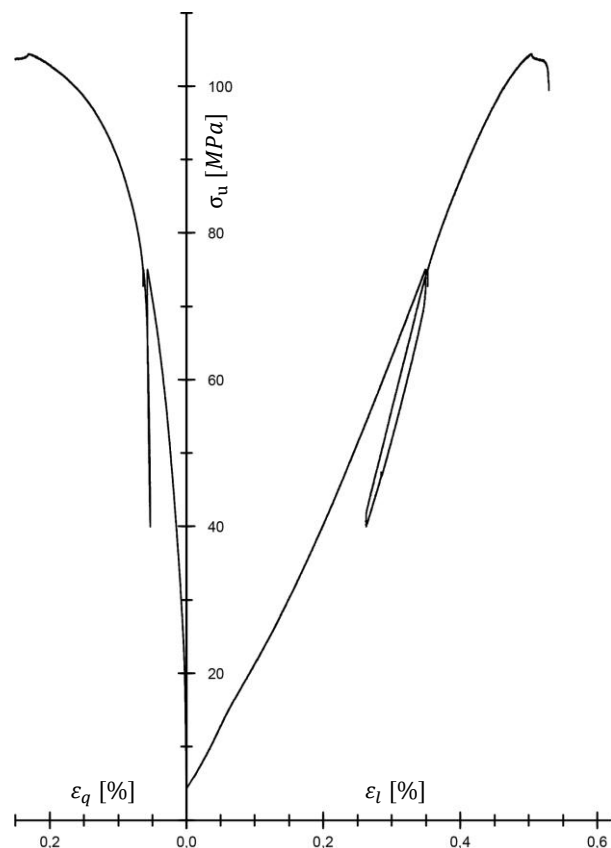


Fig. 103: Example of a typical stress-strain curve (TUM-010-G-02).

Tab. 27: Characteristic values of the geotope TUM-010.

Geotope	State	Parameter	Units	min.	mean	med.	max.	n
TUM-010	dry	$v_{pl}$	[m/s]	3,490.4	<b>3,581.6</b>	3,502.2	3,831.8	4
		$v_{pd}$	[m/s]	3,479.6	<b>3,521.1</b>	3,495.6	3,613.7	
		$v_s$	[m/s]	2,022.0	<b>2,105.1</b>	2,096.8	2,205.0	
		$E_{dyn}$	[GPa]	26.56	<b>28.74</b>	28.01	32.41	
		$G_{dyn}$	[GPa]	10.65	<b>11.57</b>	11.48	12.67	
		$K_{dyn}$	[GPa]	16.25	<b>18.81</b>	17.30	24.40	
		$v_{dyn}$	[-]	0.21	<b>0.24</b>	0.24	0.28	
		Z	[ $10^6$ kg/m <sup>2</sup> s]	9.10	<b>9.45</b>	9.15	10.4	
	sat.	$v_{pl}$	[m/s]	4,429.8	<b>4,494.6</b>	4,511.0	4,526.5	4
		$v_{pd}$	[m/s]	4,505.2	<b>4,620.8</b>	4,649.4	4,679.4	
		$v_s$	[m/s]	2,108.0	<b>2,133.1</b>	2,125.3	2,174.0	
		$E_{dyn}$	[GPa]	32.25	<b>33.10</b>	32.98	34.19	
		$G_{dyn}$	[GPa]	11.64	<b>11.93</b>	11.87	12.36	
		$K_{dyn}$	[GPa]	46.75	<b>48.71</b>	48.90	50.30	
		$v_{dyn}$	[-]	0.38	<b>0.39</b>	0.39	0.39	
		Z	[ $10^6$ kg/m <sup>2</sup> s]	12.80	<b>13.03</b>	13.10	13.10	
	dry	$\sigma_u$	[MPa]	104.4	<b>104.7</b>	104.7	105.0	2
		V	[GPa]	23.32	<b>23.42</b>	23.42	23.52	1
		E	[GPa]	36.87	<b>36.87</b>	36.87	36.87	
		$\nu$	[-]	0.28	<b>0.28</b>	0.28	0.28	2
		$\sigma_t$	[MPa]	5.6	<b>6.3</b>	6.3	7.0	2
		CAI	[-]	3.2	<b>3.4</b>	3.4	3.5	2
		LAC	[g/t]	1100	<b>1130</b>	1130	1160	2
		LBC	[%]	84	<b>85</b>	85	86	
dry	$\phi_{eff}^{He}$	[%]	1.54	<b>1.57</b>	1.57	1.59	2	
sat.	$\phi_{eff}^W$	[%]	2.66	<b>2.82</b>	2.76	3.10	4	
dry	$\rho_b$	[g/cm <sup>3</sup> ]	2.61	<b>2.64</b>	2.64	2.67	4	
	$\rho_g$	[g/cm <sup>3</sup> ]	2.65	<b>2.65</b>	2.65	2.65	2	

### Geotope TUM-011

The geotope TUM-011 is located 3 km south–east of the town of Selb. On the eastern part of the Weissenstadt–Marktleuthen massif, two blocks were taken and no samples were drilled directly in the field.

A total of 7 samples were drilled from one block. There, the “Selber granite” is exposed (www-20), which is a variety (G1S) of the Variscan G1 granite. The geotope under investigation is the north–eastern field of the G1S. The rock is has a low biotite and rich muscovite composition and an homogenous structural fabric (RICHTER & STETTNER 1979). The Selber granite rock appears as a bright gray colour with accumulation of muscovite.

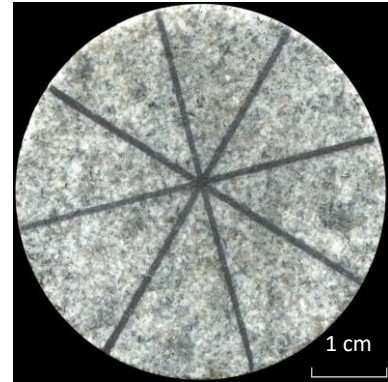


Fig. 104: Scan of a sample of TUM-011.

The maximum grain size determined is 1 mm. According to RICHTER & STETTNER (1979) and the mean self determined mineral content is: quartz 38 %, alkali feldspar 24 %, plagioclase 23 %, biotite 3 %, muscovite 9.4 % and  $\sim 2$  % accessory minerals. It is classified as fine- to medium-grained two-mica granite (Fig. 104) (HECHT 1998; SCHARFENBERG et al. 2016).

Fig. 105 shows a typical stress-strain curve of the Selber granite. Clearly visible is the long path of the axial strain and the low lateral strain. At the beginning of the curve the shape is nonlinear and the elastic deformation takes place. In this quarry this part is  $\sim 25$  % of the curve. Then the shape of the curve becomes linear and the elasto–plastic deformation takes place. The last part of the curve with unstable crack growth and plastic deformation begins at 90 %. In this quarry the failure mode builds mostly a conjugate pairs of shear failure surfaces.

A total of 7 UT, 4 UCT (1 preliminary tests and 3 main tests), 16 BTT, 10 CAIT, 2 LCPCT as well as 23 PLT were performed from the collected samples.

Tab. 28 show the determined key parameter values of the tests performed.

A summary of all test results of the quarry TUM-011 is given in the Appendix.

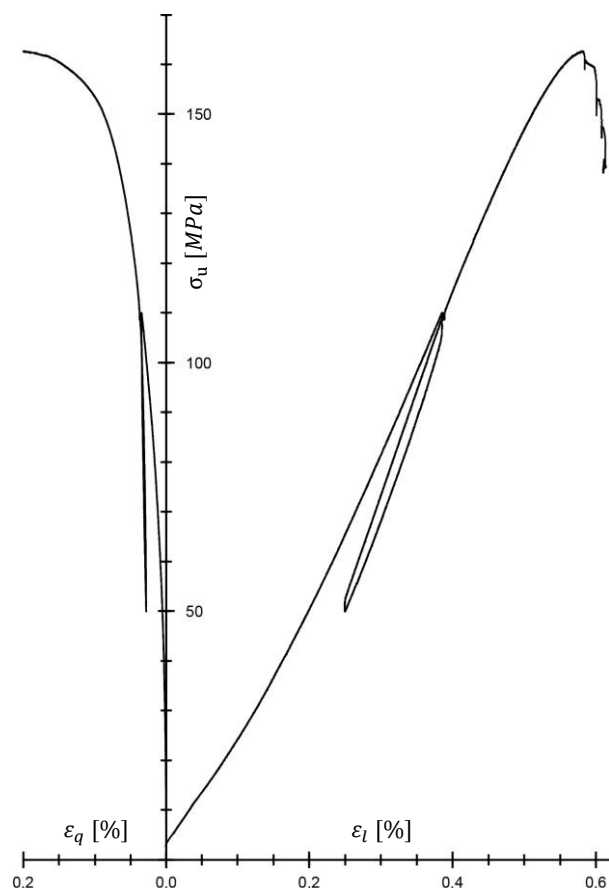


Fig. 105: Example of a typical stress-strain curve (TUM-011-02C-02).

Tab. 28: Characteristic values of the geotope TUM-011.

Geotope	State	Parameter	Units	min.	mean	med.	max.	n
TUM-011	dry	$v_{pl}$	[m/s]	4,451.5	<b>4,526.6</b>	4,467.6	4,703.5	7
		$v_{pd}$	[m/s]	4,614.3	<b>4,652.7</b>	4,659.3	4,680.9	
		$v_s$	[m/s]	2,535.0	<b>2,677.9</b>	2,633.5	2,844.0	
		$E_{dyn}$	[GPa]	42.36	<b>46.42</b>	44.54	53.21	
		$G_{dyn}$	[GPa]	16.79	<b>18.66</b>	18.09	21.06	
		$K_{dyn}$	[GPa]	26.70	<b>30.39</b>	28.55	37.40	
		$\nu_{dyn}$	[-]	0.21	<b>0.24</b>	0.25	0.26	
	Z	[ $10^6$ kg/m <sup>2</sup> s]	11.60	<b>11.96</b>	11.60	13.10		
	sat.	$v_{pl}$	[m/s]	5,054.2	<b>5,108.7</b>	5,099.5	5,194.5	7
		$v_{pd}$	[m/s]	4,913.0	<b>5,171.8</b>	5,168.9	5,528.3	
		$v_s$	[m/s]	2,583.5	<b>2,640.9</b>	2,629.0	2,746.0	
		$E_{dyn}$	[GPa]	46.09	<b>48.85</b>	48.08	53.20	
		$G_{dyn}$	[GPa]	17.48	<b>18.24</b>	18.06	19.72	
		$K_{dyn}$	[GPa]	42.20	<b>51.99</b>	48.40	66.20	
		$\nu_{dyn}$	[-]	0.32	<b>0.34</b>	0.34	0.37	
	Z	[ $10^6$ kg/m <sup>2</sup> s]	13.20	<b>14.12</b>	13.65	15.45		
	dry	$\sigma_u$	[MPa]	136.8	<b>146.6</b>	143.6	162.4	4
		V	[GPa]	29.21	<b>30.42</b>	30.14	32.17	19
		E	[GPa]	41.41	<b>41.89</b>	41.89	42.38	
		$\nu$	[-]	0.10	<b>0.18</b>	0.15	0.29	7
		$\sigma_t$	[MPa]	8.5	<b>9.1</b>	8.8	10.5	
		$I_s$	[MPa]	8.1	<b>8.8</b>	8.8	9.5	23
		$I_{s(50)}$	[MPa]	8.1	<b>8.8</b>	8.8	9.5	
		$\sigma_m$	[MPa]	161.3	<b>175.6</b>	176.9	190.9	7
		CAI	[-]	4.2	<b>4.5</b>	4.5	5.1	
		LAC	[g/t]	1240	<b>1250</b>	1250	1260	2
		LBC	[%]	59	<b>59</b>	59	59	
	dry	$\Phi_{eff}^{He}$	[%]	1.42	<b>1.42</b>	1.42	1.42	2
sat.	$\Phi_{eff}^W$	[%]	0.60	<b>0.87</b>	0.91	1.06	7	
dry	$\rho_b$	[g/cm <sup>3</sup> ]	2.56	<b>2.63</b>	2.64	2.69	7	
	$\rho_g$	[g/cm <sup>3</sup> ]	2.64	<b>2.64</b>	2.64	2.65	2	

### Quarry TUM-012

The currently inactive quarry TUM-012 is located 1 km south-east of the town of Gefrees and south of state road 2180. On this lift (“Hohe Reuth”), ten samples were taken directly in the field at one of the four former quarries. The valuable quarries were mentioned for the first time in 1758 (HEIM 1932).

There, the “Reut-/Gefreeser granite” is exposed, which is a variety (G1R) of the Variscan G1 granite (www-21). Due to the grain size, the rock appears very bright overall and has a bluish-grey colour

with a high content of biotite (STETTNER 1977). It possesses larger irregularly distributed nearly idiomorphic feldspars. The rock has a slightly porphyritic structural fabric (MÜLLER 1997). According to GRIMM (1990) the mineral content is: quartz 30 %, alkali feldspar 30 %, plagioclase 25 %, biotite 11 %, muscovite 2 % and 2 % of hornblende, chlorite and accessory minerals. It is classified as medium grained weakly porphyritic biotite granite (Fig. 106) (HECHT 1998; RICHTER & STETTNER 1979).

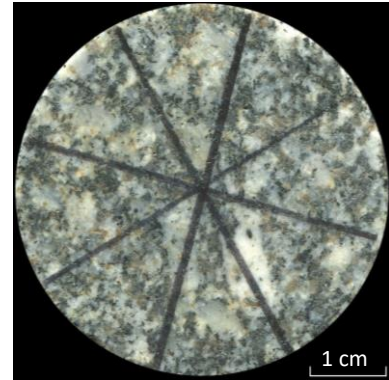


Fig. 106: Scan of a sample of TUM-012.

Fig. 107 shows a typical stress-strain curve of Gefreeser granite. Clearly visible is the long path of the axial strain and the very low lateral strain. At the beginning of the curve the shape is nonlinear and the elastic deformation takes place. In this quarry this part is not easy to see. Then the shape of the curve becomes linear and the elasto-plastic deformation takes place. The last part of the curve is unstable crack growth and plastic deformation. In this quarry the failure mode builds mostly conjugate pairs of shear failure surfaces.

A total of 10 UT, 7 UCT (2 preliminary tests and 5 main tests), 5 BTT and 5 CAIT and 2 LCPCT were performed from the collected samples.

Tab. 29 shows the determined key parameter values of the tests performed.

A summary of all test results of the quarry TUM-012 is given in the Appendix.

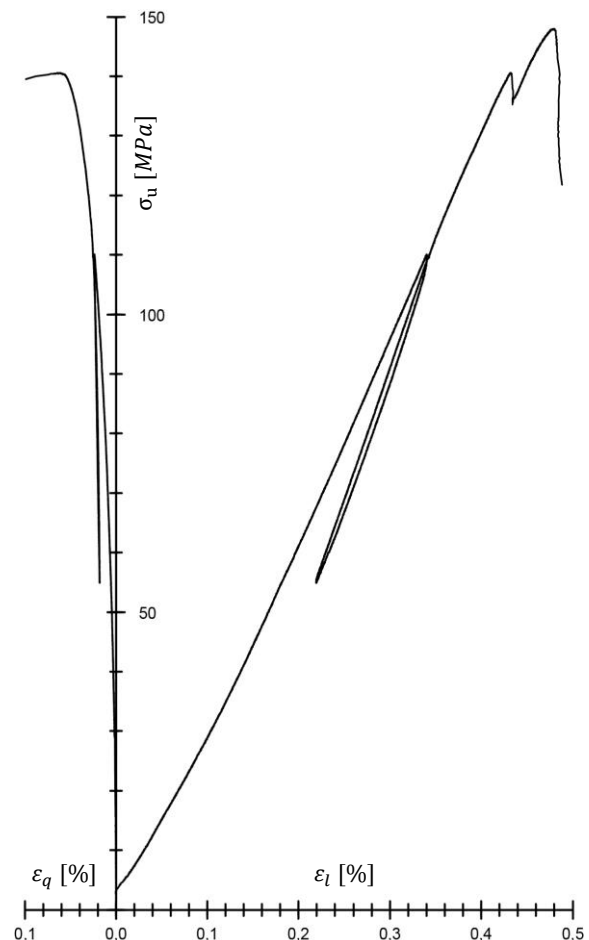


Fig. 107: Example of a typical stress-strain curve (TUM-012-G-03).

Tab. 29: Characteristic values of the quarry TUM-012.

Quarry	State	Parameter	Units	min.	mean	med.	max.	n
TUM -012	dry	$v_{pl}$	[m/s]	5,067.9	<b>5,191.8</b>	5,177.2	5,368.5	10
		$v_{pd}$	[m/s]	5,177.8	<b>5,488.9</b>	5,533.5	5,552.4	
		$v_s$	[m/s]	2,914.0	<b>2,983.4</b>	2,960.8	3,148.5	
		$E_{dyn}$	[GPa]	56.86	<b>59.61</b>	58.60	66.55	
		$G_{dyn}$	[GPa]	22.53	<b>23.70</b>	23.30	26.47	
		$K_{dyn}$	[GPa]	37.75	<b>41.05</b>	40.70	45.65	
		$\nu_{dyn}$	[-]	0.25	<b>0.26</b>	0.26	0.26	
		Z	[ $10^6$ kg/m <sup>2</sup> s]	13.45	<b>13.91</b>	13.80	14.70	
	sat.	$v_{pl}$	[m/s]	5,494.8	<b>5,598.8</b>	5,598.5	5,740.6	10
		$v_{pd}$	[m/s]	5,476.5	<b>5,624.0</b>	5,635.1	5,714.4	
		$v_s$	[m/s]	2,898.0	<b>2,994.2</b>	2,988.8	3,094.5	
		$E_{dyn}$	[GPa]	60.79	<b>65.0</b>	64.65	69.18	
		$G_{dyn}$	[GPa]	22.37	<b>23.92</b>	23.81	25.52	
		$K_{dyn}$	[GPa]	70.45	<b>76.78</b>	76.45	83.80	
		$\nu_{dyn}$	[-]	0.35	<b>0.36</b>	0.36	0.37	
		Z	[ $10^6$ kg/m <sup>2</sup> s]	16.40	<b>17.01</b>	17.00	17.70	
	dry	$\sigma_u$	[MPa]	141.1	<b>154.2</b>	149.3	170.7	7
		V	[GPa]	34.77	<b>37.37</b>	36.83	40.36	5
		E	[GPa]	44.27	<b>47.68</b>	45.70	56.13	
		$\nu$	[-]	0.10	<b>0.11</b>	0.11	0.12	
		$\sigma_t$	[MPa]	10.3	<b>11.9</b>	12.4	13.2	5
CAI		[-]	4.1	<b>4.6</b>	4.5	5.2	5	
LAC		[g/t]	1240	<b>1250</b>	1250	1260	2	
LBC	[%]	50	<b>51</b>	51	51	2		
dry	$\phi_{eff}^{He}$	[%]	0.63	<b>0.69</b>	0.69	0.74	2	
sat.	$\phi_{eff}^W$	[%]	0.33	<b>0.43</b>	0.42	0.53	10	
dry	$\rho_b$	[g/cm <sup>3</sup> ]	2.66	<b>2.66</b>	2.66	2.67	10	
	$\rho_g$	[g/cm <sup>3</sup> ]	2.68	<b>2.68</b>	2.68	2.68	2	

### 2.3.5 Discussion

In order to get a characterization of the possibly granitic reservoir, the outcrops distributed over the Fichtelgebirge were summarised. This should help to better describe and understand the possible reservoir in the Franconian Basin.

First, the specific parameters were plotted against each other and general geomechanical relationships within the possible granitic reservoir are shown. This should provide information about dependencies in the overall context of this reservoir.

Afterwards, the measured data are subdivided into two different groups. The results are classified according to their different phases of granite intrusion (G type) as well as to their orientation in the different phases of granite intrusion (G type). The distribution of the respective group could also be shown.

In the first subdivision, the determined data were related to the different phases of granite intrusion (G type) by the different granite type according to RICHTER & STETTNER (1979).

In the second subdivision, the analogue samples were classified by their orientation in the different phases of granite intrusion (G type) into four categories (vertical, horizontal, outcrop and for G3 type: 90° horizontal).

An overview of the possible granitic reservoir's parameters subdivided into granite types and orientation of drilling can be found in the Appendix.

### 2.3.5.1 General geomechanical tests

To investigate the influence of saturation and to obtain reproducible results, the non-destructive laboratory experiments were done under two conditions the same way as described in chapter 2.2.5.

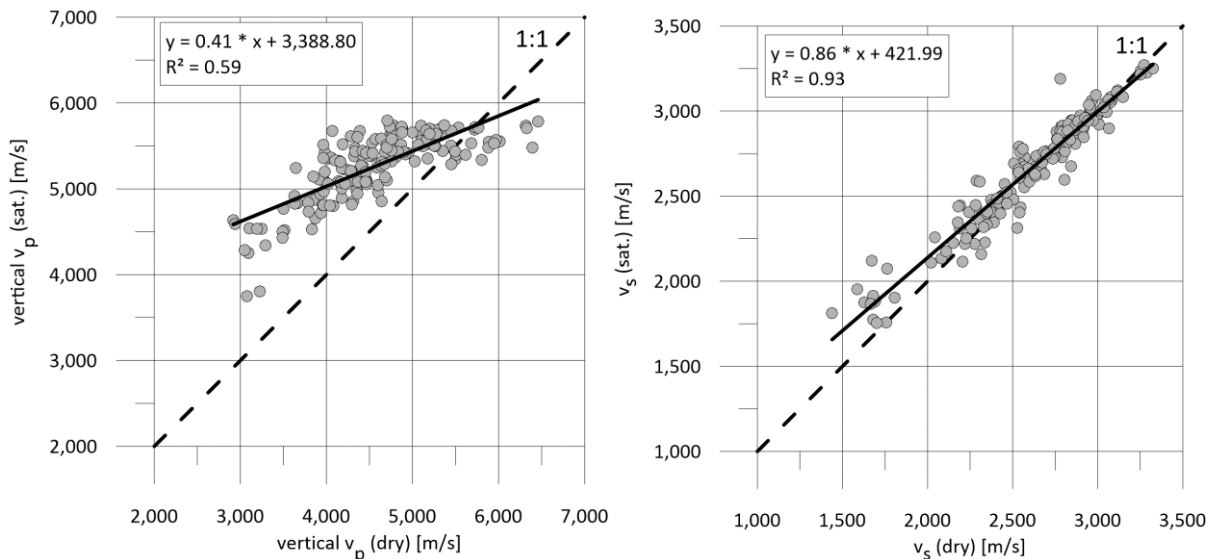


Fig. 108: Vertical  $v_p$ (dry)-velocities plotted against vertical  $v_p$  (sat.)-velocities (left) and  $v_s$ (dry)-velocities plotted against  $v_s$ (sat.)-velocities (right) to consider the influence of saturation.

Fig. 108 (left) shows that the saturated  $v_p$ -velocity values are mostly higher than the dry  $v_p$ -velocity values. This could be because the water surrounding the sample during the measurement process possesses a distinctly higher compressional velocity than air (water = 1,402 m/s, air = 335 m/s, CARMICHAEL (1982)). Therefore, a bigger part of the ultrasonic wave may travel over the water saturated sample surface than over the dry sample surface. This may lead to higher  $v_p$ (sat.) values. The samples with higher dry  $v_p$ -velocities than saturated  $v_p$ -velocities are all G3 type samples. The ultrasonic tests do not trigger the complete rock but rather minerals with high ultrasonic velocities. Minerals with low ultrasonic velocities are triggered later and are therefore not recorded in the ultrasonic measurement. These minerals are therefore lost and only the ultrasonic velocities of the fastest minerals are determined.

The  $v_s$ -velocities do not vary between dry and saturated samples (Fig. 108 right) as  $v_s$ -measurement is not effected by the wetness of the sample.

For the destructive tests, this direct correlation could not be established. The analogue samples were measured either dry or saturated and it was therefore not possible to perform both tests on one test sample.

The examined granite samples show a low porosity. Therefore, the difference between dry and saturated samples was expected to be small. Due to this fact and the limited number of samples the destructive laboratory tests were only measured under dry conditions.

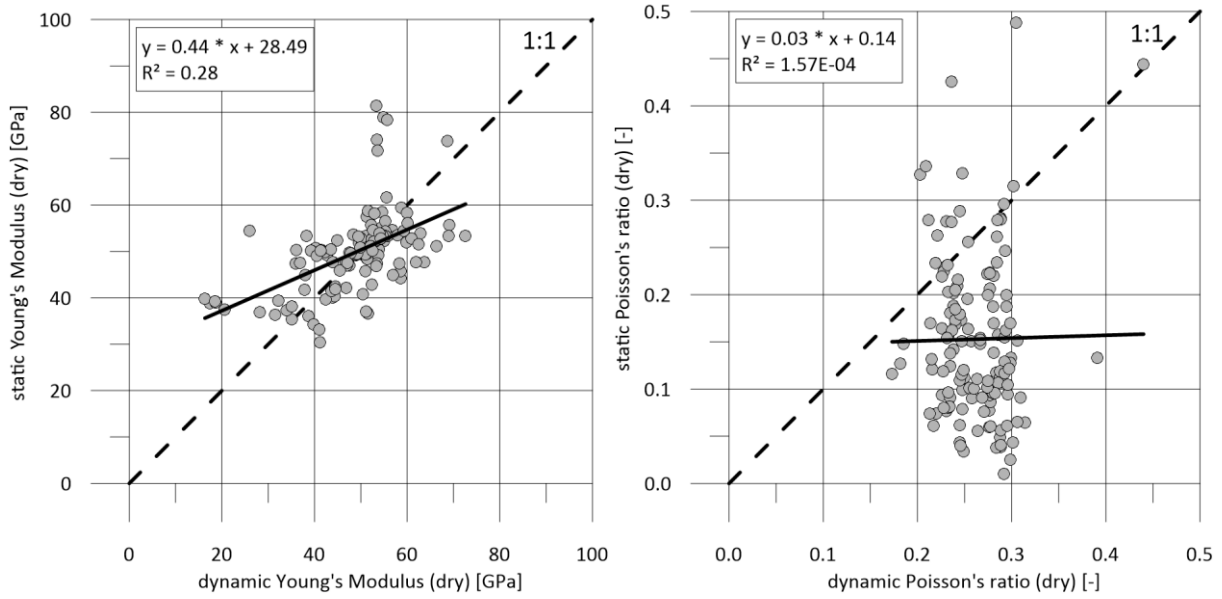


Fig. 109: Dynamic Young's Modulus(dry) plotted against static Young's Modulus(dry.) (left) and dynamic Poisson's ratio(dry) plotted against static Poisson's ratio(dry.) (right) to consider the difference between dynamic and static parameters.

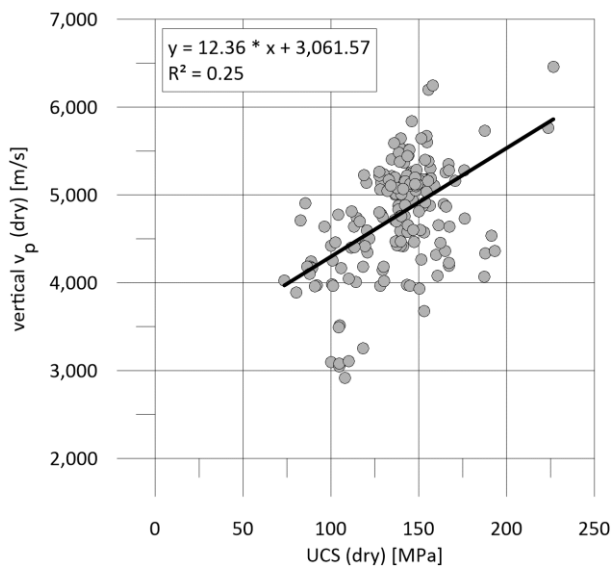


Fig. 110: UCS(dry) plotted against  $v_p$ (dry)-velocities of the granites from the Fichtelgebirge.

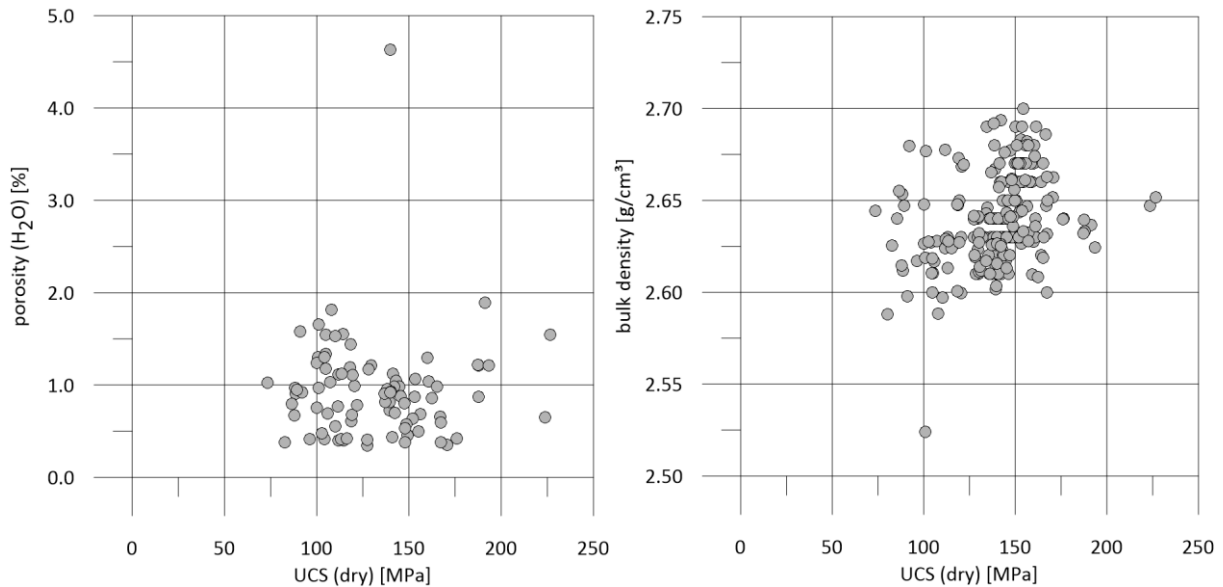


Fig. 111: UCS(dry) plotted against the porosity(H<sub>2</sub>O) (left) and against the bulk density (right) of the granites from the Fichtelgebirge.

Fig. 109 (left) shows the dynamic Young's Modulus(dry) plotted against static Young's Modulus(dry). The values for the dynamic Young's Modulus and the static Young's Modulus are predominantly between 25 and 75 GPa. There is no correlation between the values of the two moduli.

Fig. 109 (right) shows dynamic Poisson's ratio(dry) plotted against static Poisson's ratio(dry). The values for the dynamic Poisson's ratio of the dry samples show a narrow range between 0.2 and 0.3 and there is no correlation between the values of the two ratios. The static values of the Poisson's ratio are extremely scattered. This shows that the rocks are very heterogeneous from fine to coarse grained. The mean values from literature are about 0.20 (ZHANG 2016).

Fig. 110 shows the tendency that with increasing uniaxial compressive strength the  $v_p$ -velocity also increases.

The low porosity of the granites seems to have no influence on the uniaxial compressive strength of the samples (Fig. 111, left). The single value with a porosity greater than 4.5 % is a highly weathered granite sample. Highly weathered samples are known to have high porosity.

The mean density of the examined granites is between 2.6 and 2.7 g/cm<sup>3</sup> (Fig. 111, right). There is no influence of the bulk density on the uniaxial compressive strength.

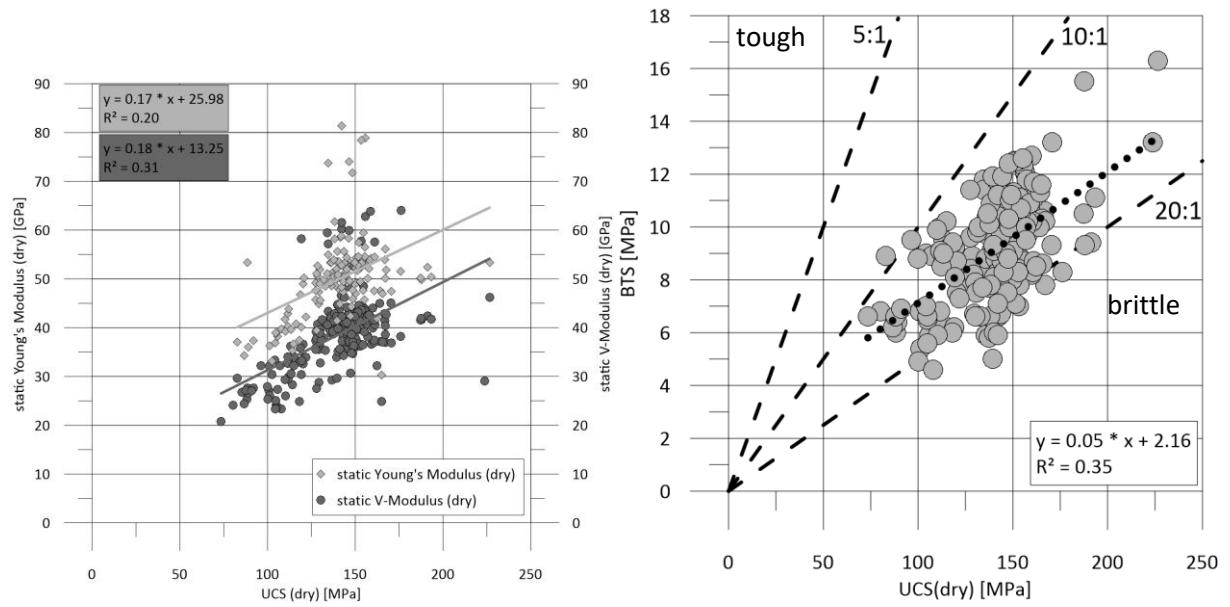


Fig. 112: UCS(dry) plotted against the Young's Modulus and the V-Modulus (left) and against the Brazilian tensile strength of the granites from the Fichtelgebirge.

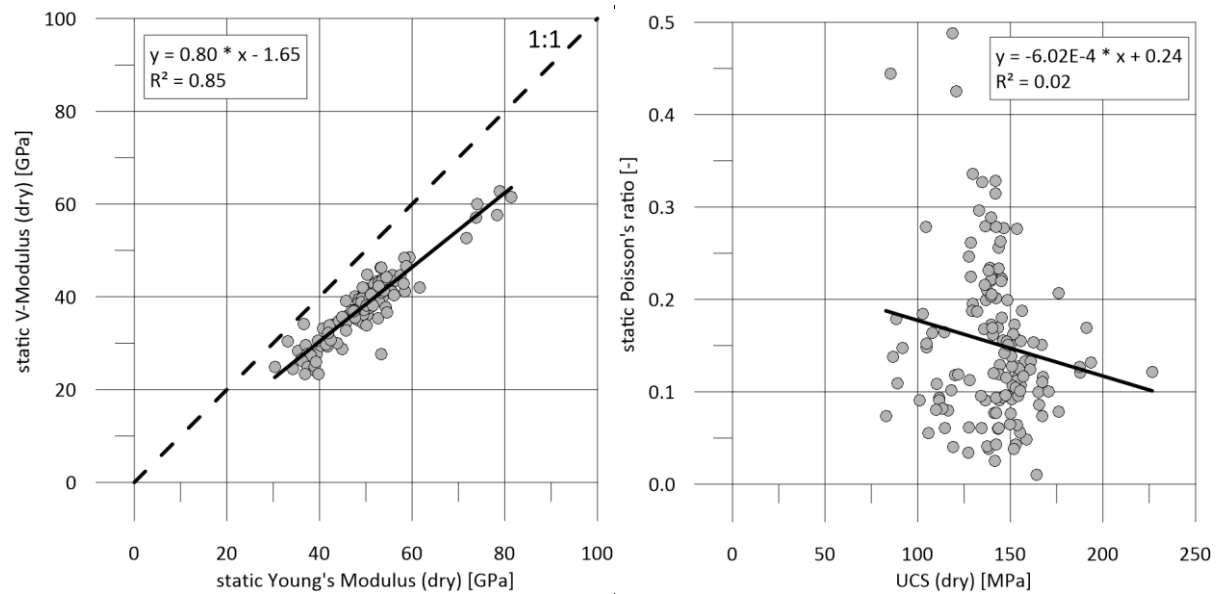


Fig. 113: Static Young's Modulus(dry) plotted against the V-Modulus (left) and on the right UCS(dry) plotted against the static Poisson's ratio of the granites from the Fichtelgebirge.

At an ideal elastic behaviour, the V-Modulus complies with the E-Modulus. With a few exceptions, the Young's Moduli have higher values than the V-Moduli. Both moduli show the tendency that with increasing UCS value the moduli values increase (Fig. 112, left). The degree of correlation between the two moduli is low.

Fig. 112 (right) shows the UCS plotted against the BTS. With the help of the ratio of uniaxial compressive strength to Brazilian tensile strength the toughness coefficient of the rocks can be determined. The examined outcrop samples range from tough to very tough (SCHIMAZEK & KNATZ 1976; THURO 1996). Nearly all values, however, plot in the typical brittle range of granites.

Fig. 113 (left) shows the tendency that the static Young's Moduli have higher values than the V-Moduli. The degree of correlation between the two moduli is high.

The comparison of UCS against Poisson's ratio shows no correlation (Fig. 113, right). Most of the UCS values are in the range between 100 MPa and 170 MPa independent of the static Poisson's ratio.

### 2.3.5.2 Granite types

The measured geomechanical values were correlated with the different rock properties. The granites were subdivided according to their different phases of granite intrusion (G type).

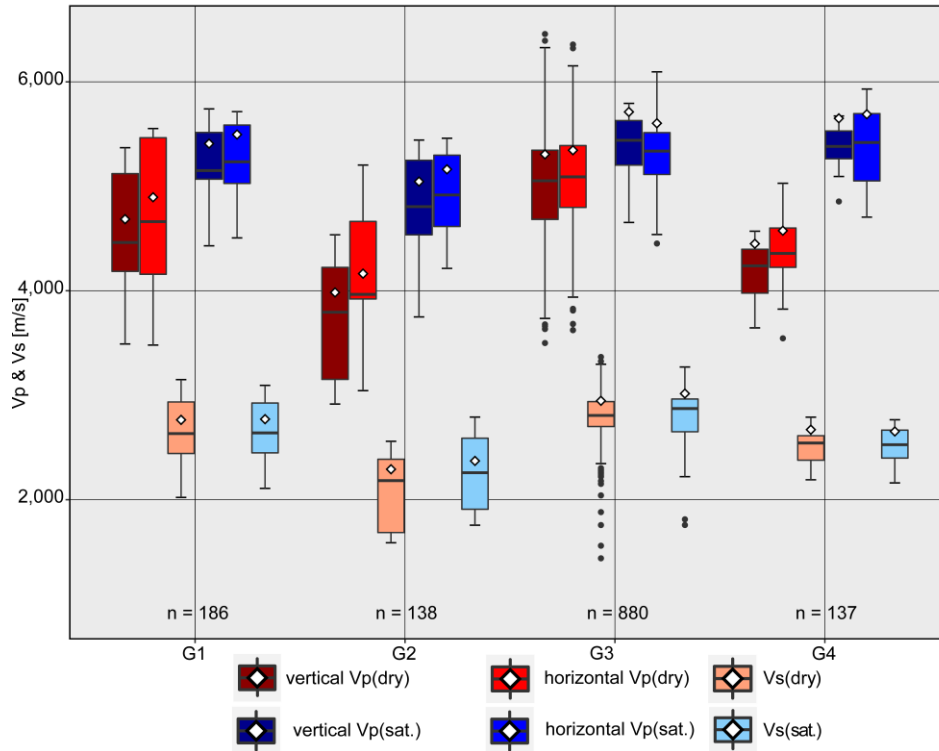


Fig. 114:  $v_p$ - and  $v_s$ -velocities of differently saturated samples versus type of granite.

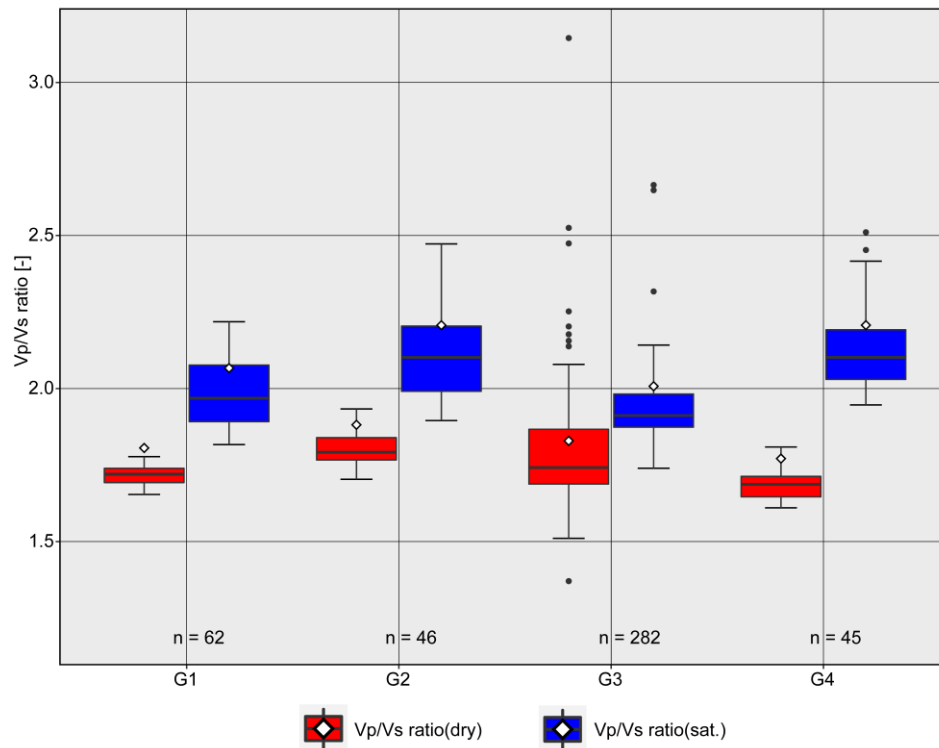


Fig. 115:  $v_p/v_s$  ratio of differently saturated samples versus type of granite.

Fig. 114 shows the  $v_p$ - and  $v_s$ -velocities of differently saturated samples versus type of granite. The  $v_p$  mean values of the granite types are between 4,000 m/s and 5,300 m/s. The mean  $v_p$  values for G1 and G3 are higher than the  $v_p$  values for G2 and G4. The  $v_s$  mean values are between 2,000 m/s and 3,000 m/s. The  $v_s$  values for G1 and G3 are higher than the  $v_s$  values for G2 and G4 (Fig. 114). The different phases of granite intrusion do not show different results and it is not possible to identify the G type based on the  $v_p$ -velocities from the laboratory investigations.

Fig. 115 shows the  $v_p/v_s$  ratio of differently saturated samples versus type of granite. The mean value of the saturated samples for all granite types is higher than the  $v_p/v_s$  ratio of the dry samples. The mean values of the dry samples of the individual granite types hardly differ. The mean values of the wet samples differ more than the mean values of the dry samples, but none of the mean values allows an assignment of the  $v_p/v_s$  ratio to individual granite types.

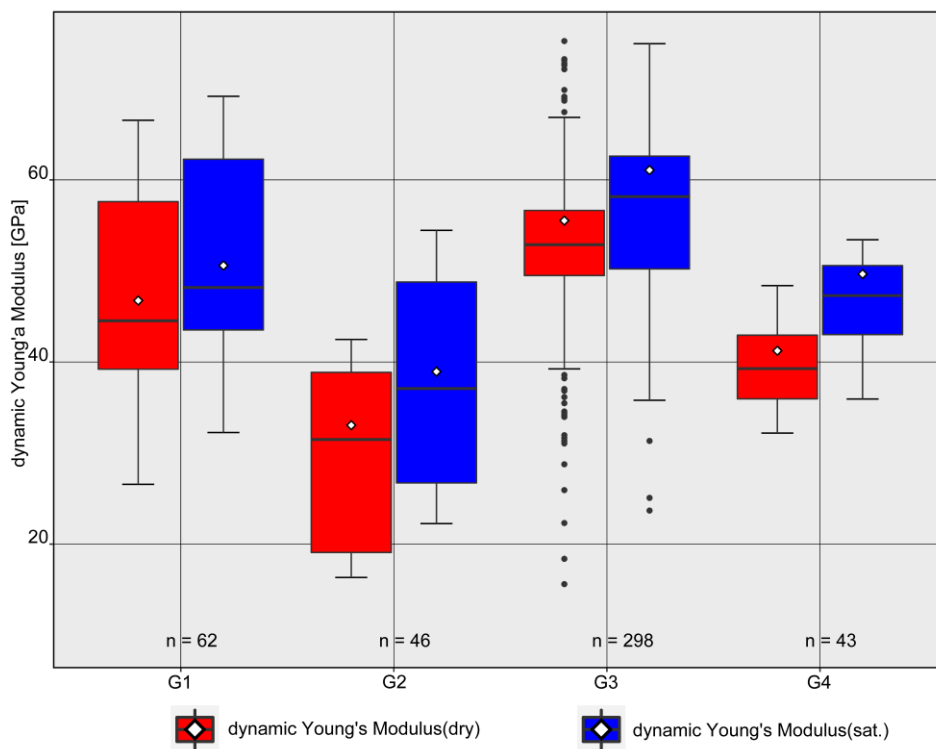


Fig. 116: Dynamic Young's Modulus of differently saturated samples versus type of granite.

The values of dynamic Young's Modulus (Fig. 116) show the same trend as the  $v_p$ - and  $v_s$ -velocities (Fig. 114).

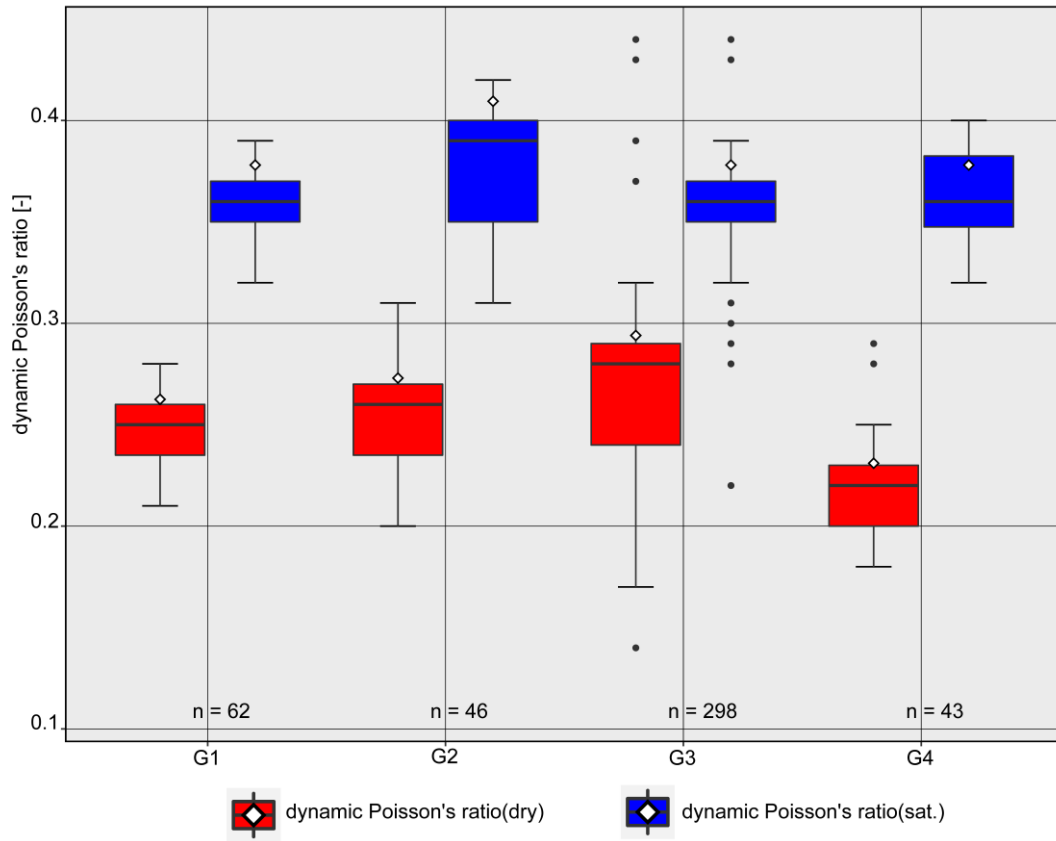


Fig. 117: Dynamic Poisson's ratio of differently saturated samples versus type of granite

The values for the dry dynamic Poisson's ratio are essentially between 0.2 and 0.3. The values for the saturated dynamic Poisson's ratio are mostly between 0.34 and 0.4 (Fig. 117). These ranges seem characteristic for the analogue samples.

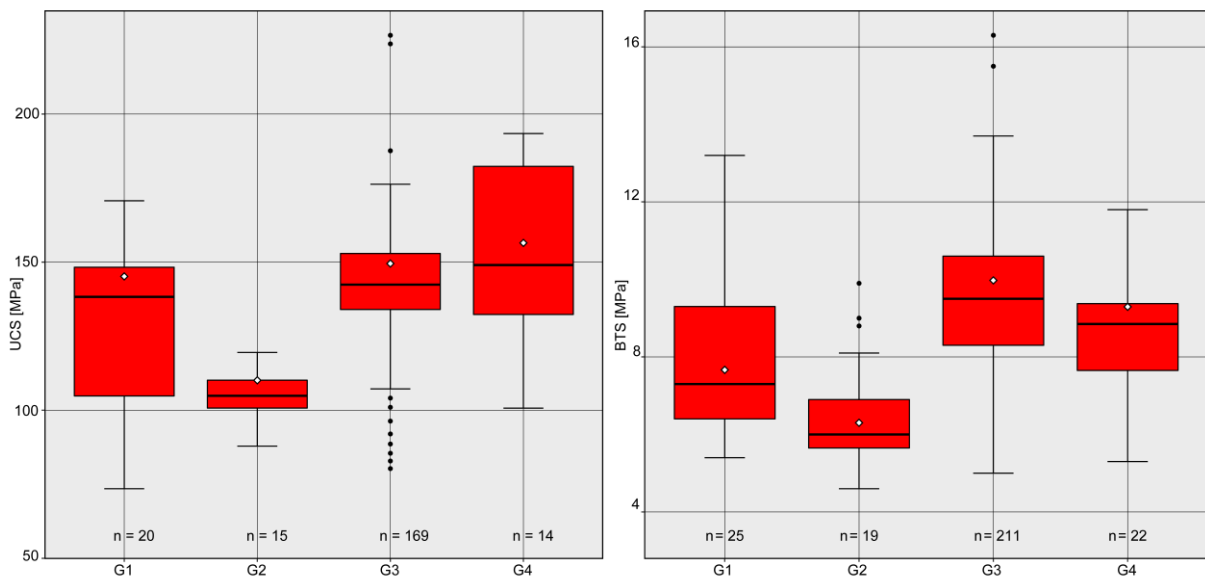


Fig. 118: UCS(dry) (left) and BTS(dry) (right) versus type of granite.

The values of uniaxial compressive strength for all age groups are between 75 MPa and 195 MPa (Fig. 118 left). The rock type can therefore be classified as high to very high strength granites (ISRM 1978). The different phases of granite intrusion do not show different results but in general the G2 types have the lowest UCS values. It is not possible to identify the G type based on the UCS value from the laboratory investigations.

The values of the Brazilian tensile test are between 4.5 and 13.5 MPa (Fig. 118, right). It turns out that the G2 types have the lowest BTS values. The different granite intrusion phases do not affect the Brazilian tensile strength values.

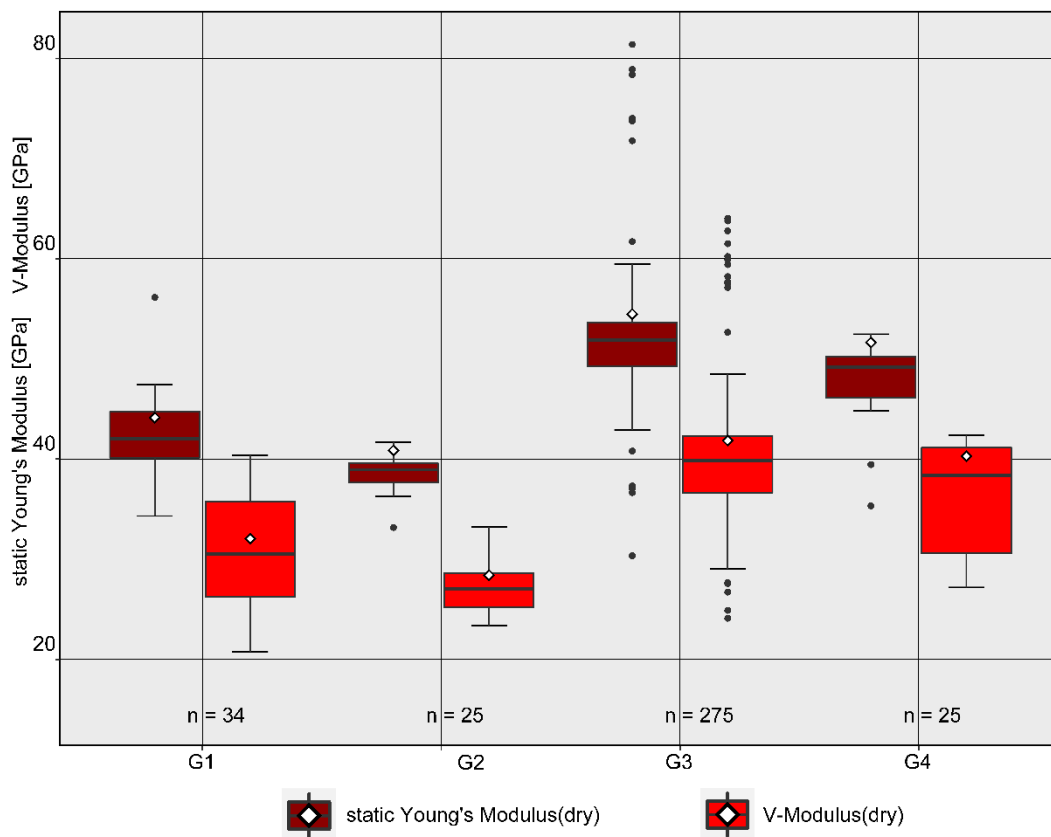


Fig. 119: Static Young's Modulus and V-Modulus versus type of granite.

The static Young's Modulus values for G1 and G3 are higher than the static Young's Modulus values for G2 and G4 (Fig. 119). The Young's Moduli have higher values than the V-Moduli. The different granite intrusion phases have no influence on Young's Modulus or V-Modulus. It is noticeable that the G3 has a wide scattering for the static Young's Moduli as well as the V-Moduli. The upper outliers of the static Young's Modulus come from two areas (Epprechtstein, Kösseine) which are geographically quite distant. The lower outliers come from one area. One of the higher outliers is also located in that same area. It is therefore not even possible to differentiate between the areas on the basis of the upper and lower outliers. The IQR of the static Young's Modulus spans from 38 MPa to 55 MPa. The IQR of the V-Modulus ranges from 25 MPa to 41 MPa. The different phases of granite intrusion do not show different results and it is not possible to identify the G type based on the static Young's Modulus and V-Modulus from the laboratory investigations.

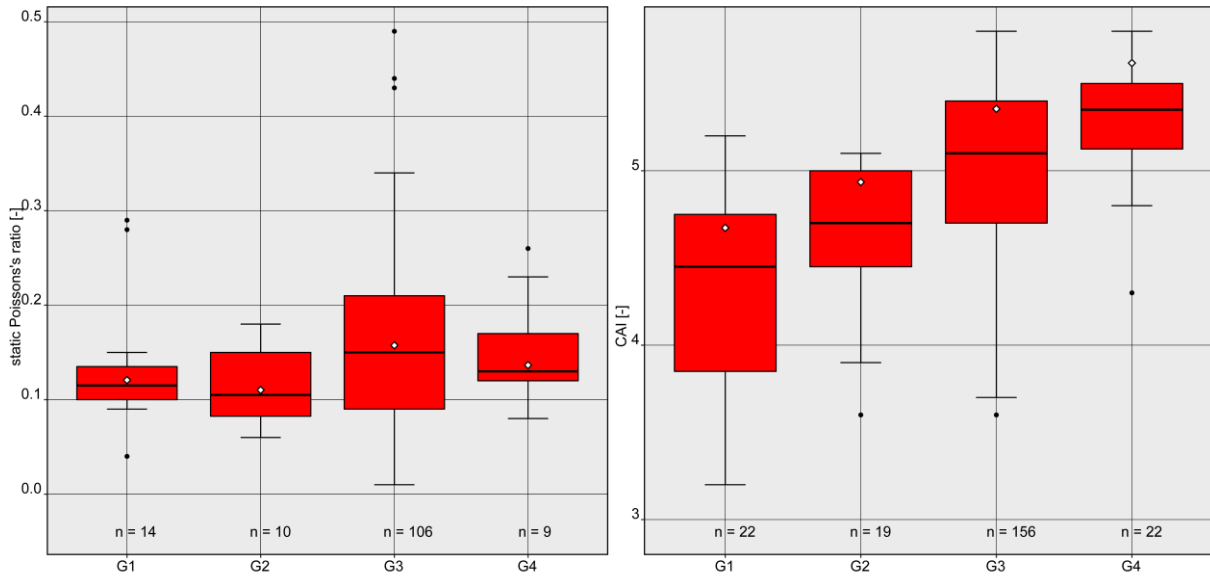


Fig. 120: Static Poisson's ratio (dry) (left) and CAI (dry) (right) versus type of granite.

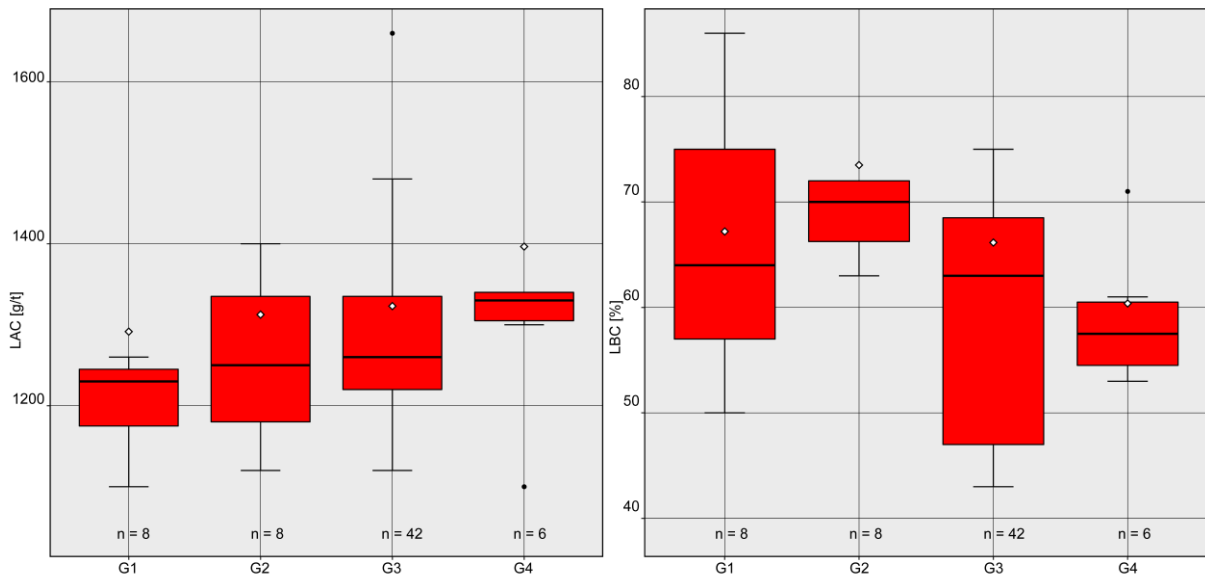


Fig. 121: LAC (left) and LBC (right) versus type of granite.

The mean static Poisson's ratio is between 0.1 and 0.15 and an interquartile range (IQR) from 0.09 to 0.21 (Fig. 120, left). The different granite intrusion phases do not lead to different results. A differentiation of the granite types by the static Poisson's ratio is therefore not possible.

The CAI values range between 3.2 and 5.8 (Fig. 120, right). The granites are therefore classified as highly abrasive (2–4) or predominantly extremely abrasive (4–6) (Cerchar 1986). The abrasiveness increases with decreasing age of the granites. A correlation of the CAI values to the mineralogy or the grain size can not be found.

The LAC values range between about 1,100 g/t and 1,470 g/t (Fig. 121, left). The granites are therefore classified as highly abrasive (500–1,250 g/t) or predominantly extremely abrasive (1,250–2,000 g/t) (THURO et al. 2006). The abrasiveness increases with decreasing age of the granites.

Fig. 121 (right) shows that the breakability varies over a broad range within and between the G types. The LBC values of the granites can be classified as medium poor to medium high (BÜCHI et al. 1995).

### 2.3.5.3 Orientation

The measured geomechanical values were correlated with the different rock properties. The granites were subdivided according to their orientation (vertical, horizontal, outcrop and for G3 type: 90° horizontal) in the different phases of granite intrusion (G type). Outcrop samples are analogue samples with unclear orientation.

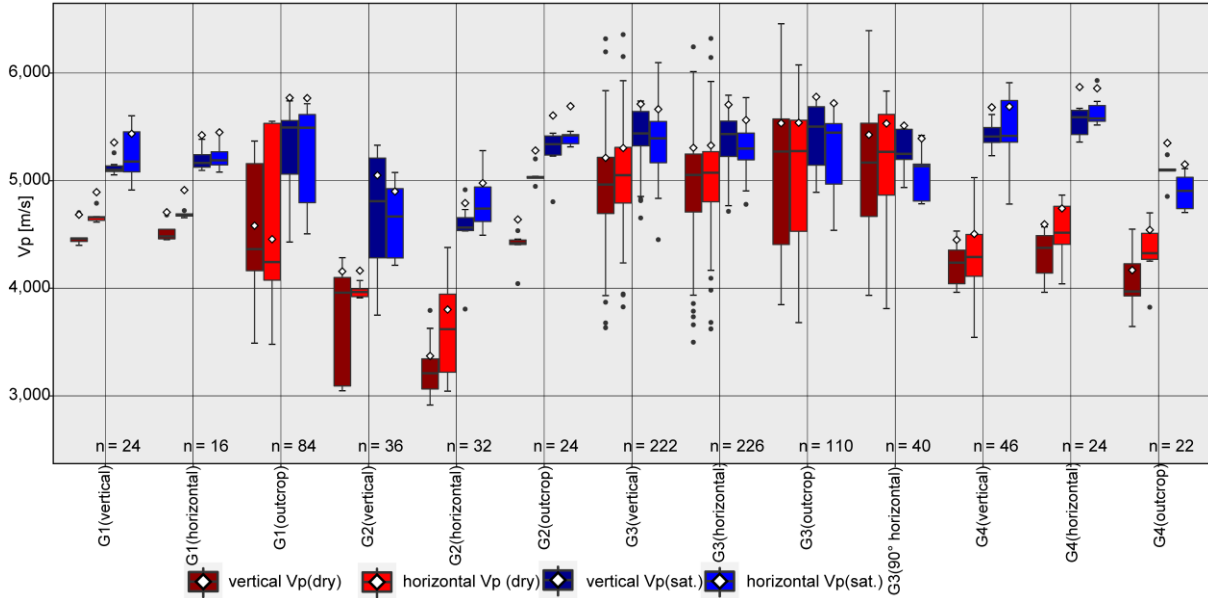


Fig. 122:  $v_p$ -velocities of differently saturated samples versus orientation.

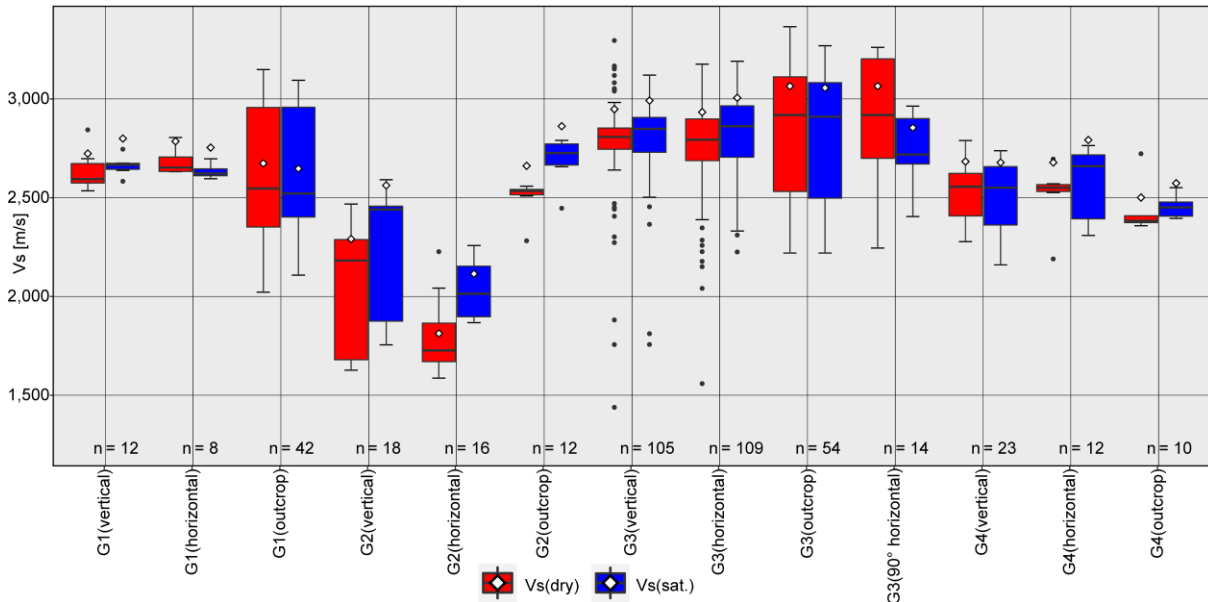


Fig. 123:  $v_s$ -velocities of differently saturated samples versus orientation.

Fig. 122 shows the  $v_p$ -velocities of differently saturated samples versus drilling direction of the type of granite. G1 and G3 show no direction dependence of the  $v_p$ -velocities. Direction dependencies can be seen in G2 and G4 (differences between vertical  $v_p$  and horizontal  $v_p$ ). There is no difference between the drilling directions (vertical and horizontal) of the different granite types for  $v_p$ (dry) and  $v_p$ (sat.). The mean values of the outcrop samples for G1 correspond to the G1 vertical and G1 horizontal  $v_p$  mean values. The broad IQR of the outcrop samples probably results from the unclear orientation of these samples. For G3, the same situation is observed (Fig. 122).

Here, the third dimensional direction is also examined. There is no difference to the previously considered dimensional directions. The mean values of the outcrop samples for G2 are higher than the G2 vertical and G2 horizontal  $v_p$  mean values. The mean values of the dry outcrop samples for G4 correspond to the dry G4 vertical and G4 horizontal  $v_p$  mean values. The mean values of the saturated outcrop samples for G4 are significantly lower than the saturated G4 vertical and G4 horizontal  $v_p$  means. The  $v_p$ -velocities are directionally independent of the different drill orientations of the granite intrusive phases.

There is no difference between the drilling directions (vertical, horizontal, outcrop) of each of the G1, G3 and G4 granite types for  $v_s$ (dry) and  $v_s$ (sat.). The mean value of G3 (90° horizontal, saturated) is lower than the mean value of G3 (90° horizontal, dry) (Fig. 123). For G2 the saturated  $v_s$  mean values are higher than the dry  $v_s$  mean values. The G2 outcrop means are higher than the G2 vertical and G2 horizontal means. The  $v_p$ -velocities are directionally independent of the different drill orientations of the granite intrusive phases.

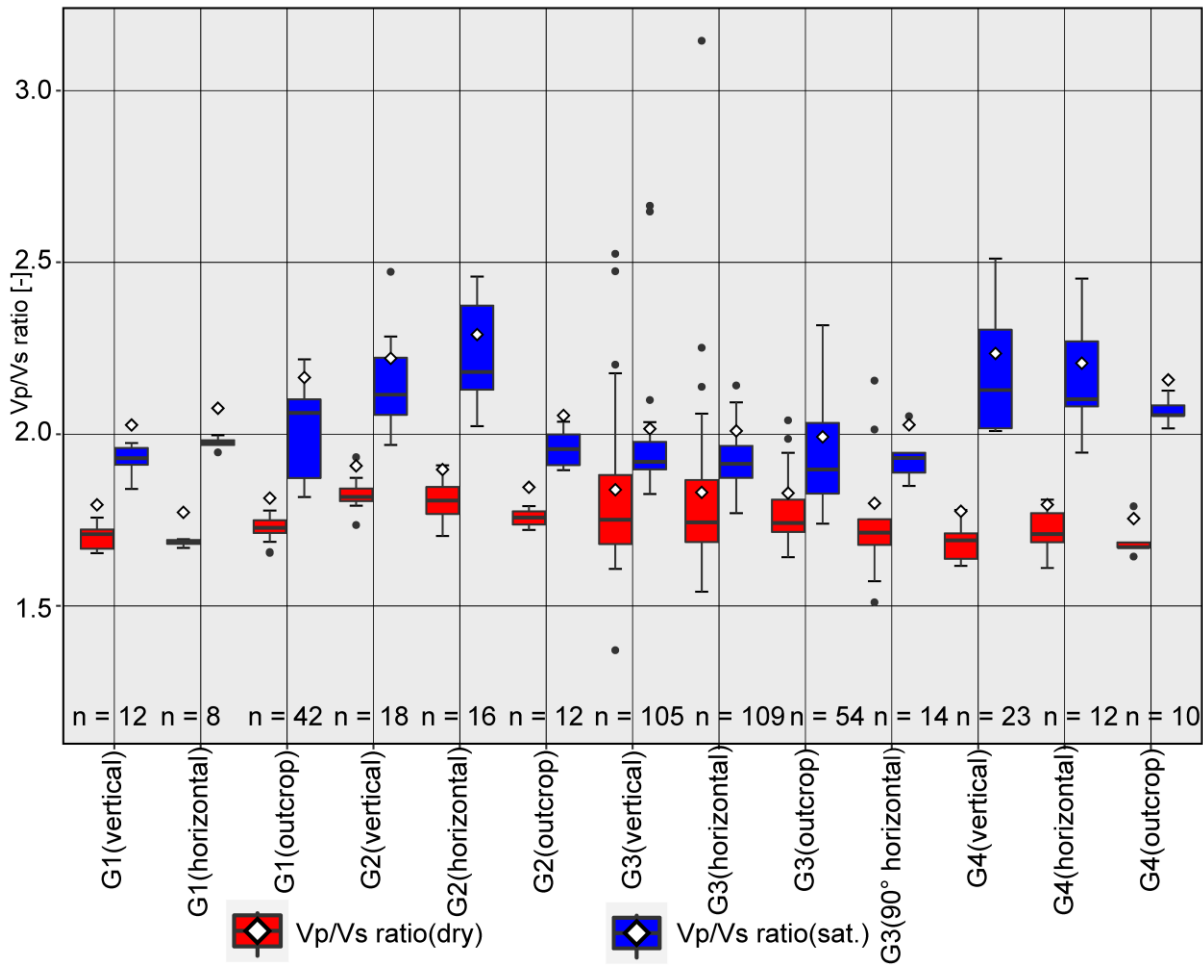


Fig. 124:  $v_p/v_s$  ratio of differently saturated samples versus orientation.

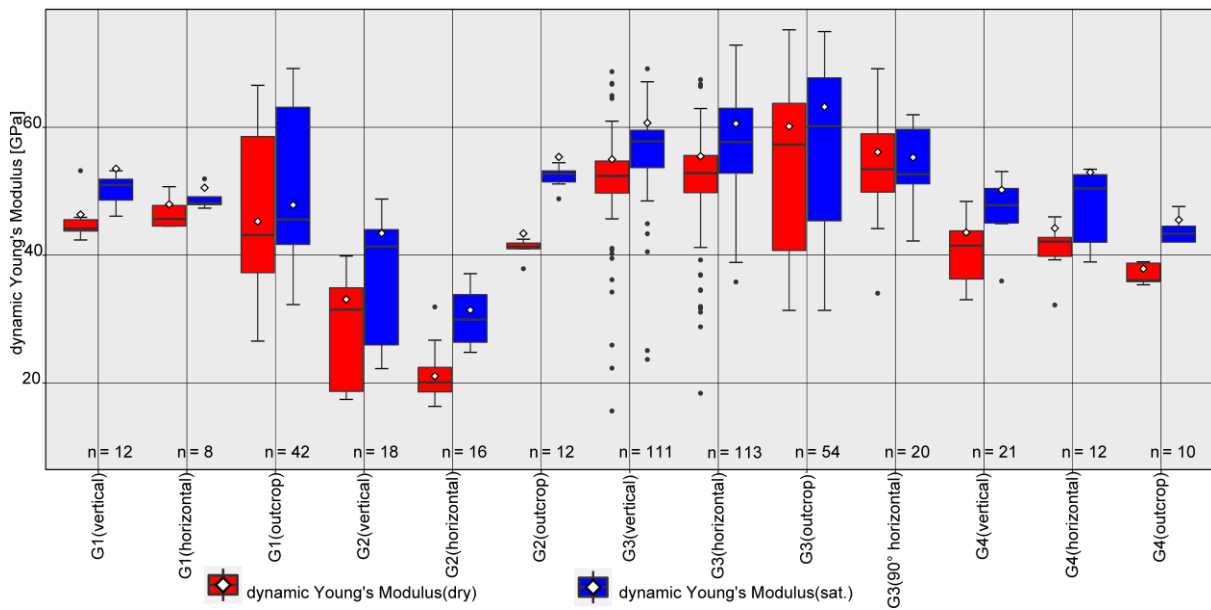


Fig. 125: Dynamic Young's Modulus of differently saturated samples versus orientation.

Fig. 124 shows the  $v_p/v_s$  ratio of differently saturated samples versus drilling direction of the granite types. The mean value of the saturated samples for all granite types is higher than the  $v_p/v_s$  ratio of the dry samples. The mean values of the dry samples of the individual granite types hardly differ. The mean values of the wet samples differ more than the mean values of the dry samples, but none of the mean values allow the  $v_p/v_s$  ratio to be assigned to individual granite types.

G1 and G3 show no directional dependence of the  $v_p/v_s$  ratio. Directional dependencies can be seen in G2 and G4 (differences between  $v_{p1}$  and  $v_{pd}$ ). There is no difference in  $v_p/v_s$  ratio dry and  $v_p/v_s$  ratio sat. between the drilling directions (vertical and horizontal) of the different granite types. The mean values of the outcrop samples for G1 correspond to the G1 vertical and G1 horizontal  $v_p/v_s$  ratio mean values. For G3, the same situation is observed (Fig. 124). Here, the third dimensional direction is also examined. There is no difference to the previously considered dimensional directions. The mean values of the outcrop samples for G2 are higher than the G2 vertical and G2 horizontal  $v_p/v_s$  ratio mean values. The mean values of the dry outcrop samples for G4 correspond to the dry G4 vertical and G4 horizontal  $v_p/v_s$  ratio mean values. The mean values of the saturated outcrop samples for G4 are significantly lower than the saturated G4 vertical and G4 horizontal  $v_p/v_s$  ratio means. The  $v_p/v_s$  ratios are directionally independent of the different drill orientations of the granite intrusive phases.

Fig. 125 shows dynamic Young's Modulus of differently saturated samples versus drilling direction of the type of granite. The values of dynamic Young's Modulus (Fig. 125) show the same trend as the  $v_p$ - and  $v_s$ -velocities (Fig. 122 & Fig. 123). There is no trend of Young's Modulus change over the different drill orientations of the granite intrusive phases.

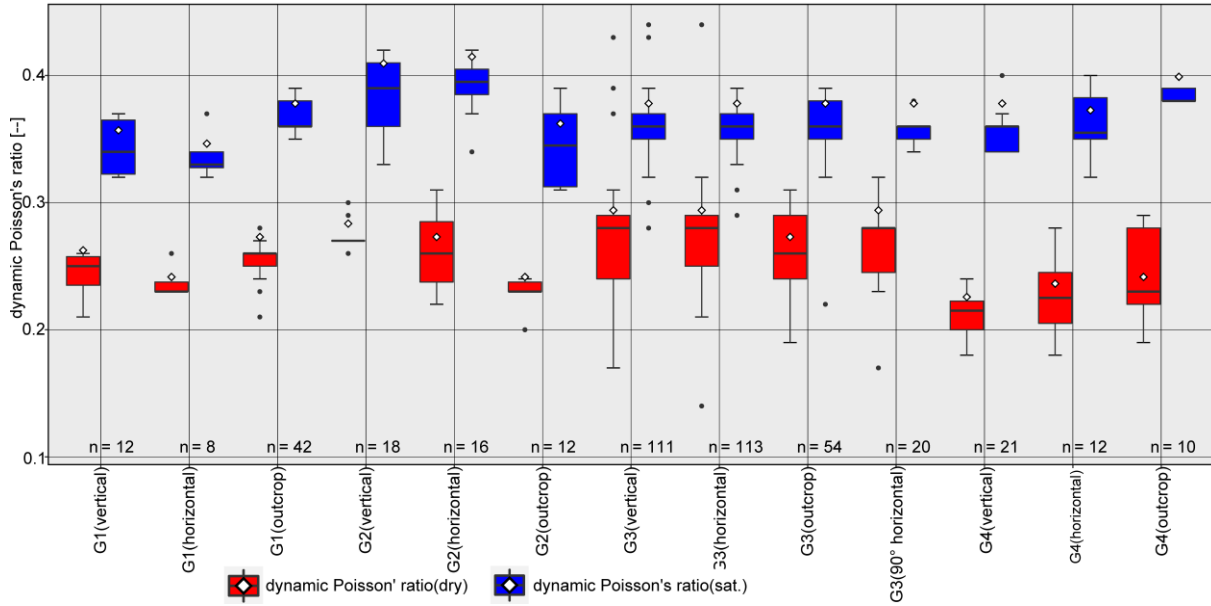


Fig. 126: Dynamic Poisson's ratio of differently saturated samples versus orientation.

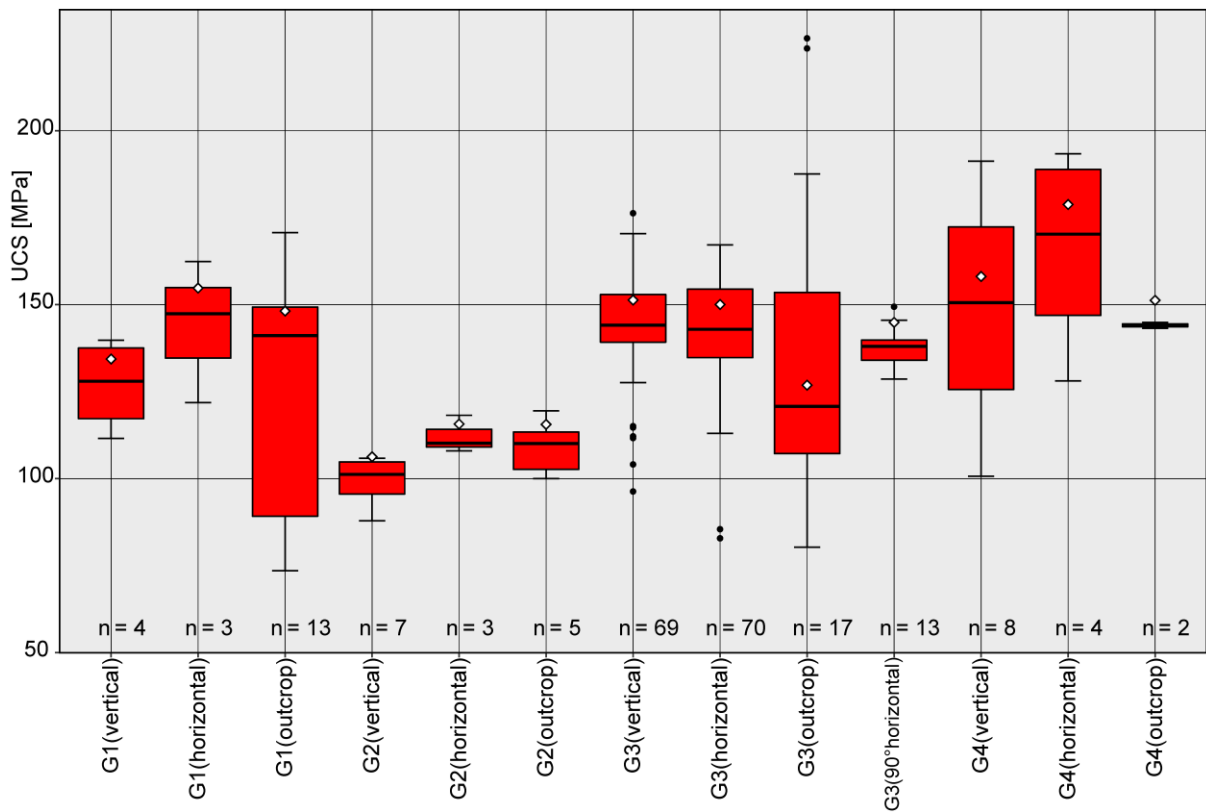


Fig. 127: UCS (dry) versus orientation.

Fig. 126 shows dynamic Poisson’s ratio of differently saturated samples versus drilling direction of the type of granite. There is no difference in the dry and saturated dynamic Poisson's ratios between the drilling directions (vertical, horizontal and outcrop) of the G1 and G3 granite types (Fig. 126). This also applies to the mean values of G3 (90° horizontal) dry and saturated. Between the drilling directions (vertical, horizontal) of the G2 granite type there is no difference for the dry and saturated dynamic Poisson's ratio. The outcrop samples show a lower mean value. For G4, an increase in the mean dynamic Poisson’s ratio from G4 vertical to horizontal to outcrop is observed. There is no trend of changing dynamic Poisson’s ratio over the different drill orientations of the granite intrusive phases.

For G1, G2 and G4, the UCS mean of the horizontal samples is higher than the mean of the vertical samples (Fig. 127). For G3, there is no difference in the UCS means of the different drilling directions of the samples. The UCS values of the G1 and G3 outcrop samples scatter over a wide range. For the UCS there is no trend over the different drill orientations of the granite intrusive phases.

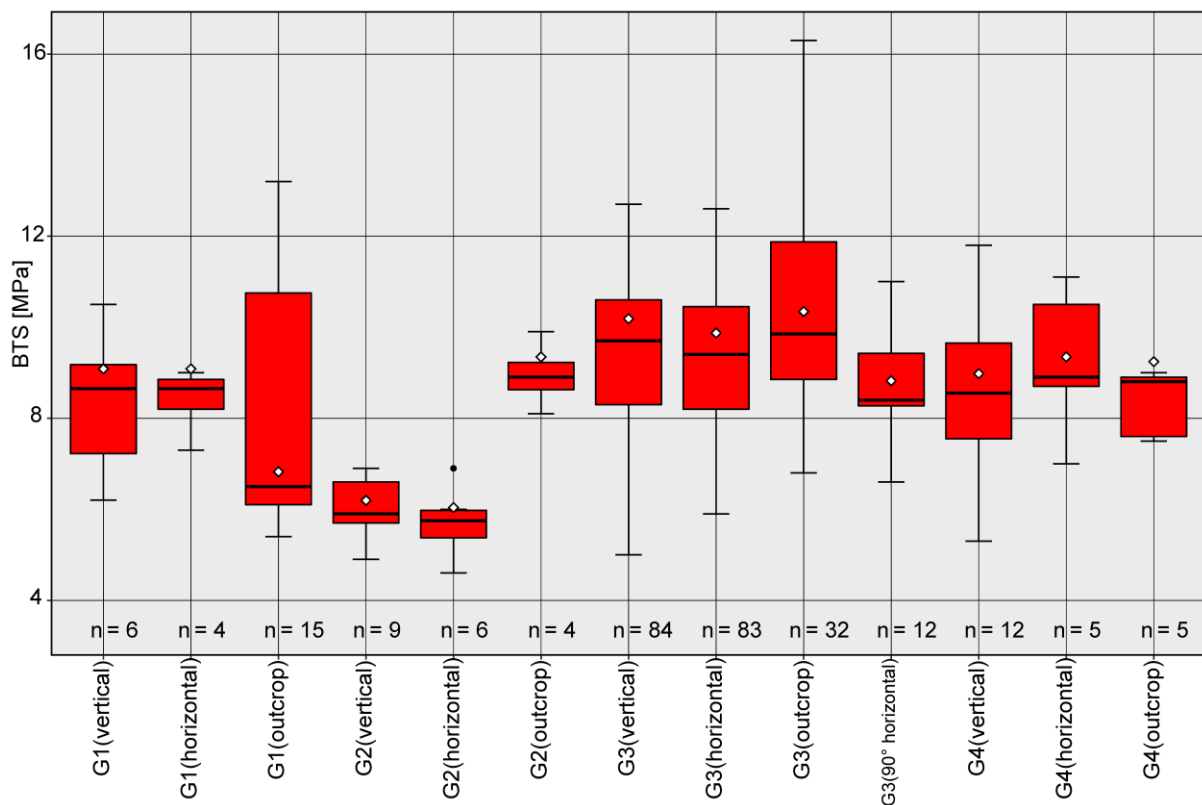


Fig. 128: BTS versus orientation.

The drilling direction (vertical or horizontal) of the samples has no influence on the BTS mean values. The outcrop samples for G1 and G3 scatter over a wide range (Fig. 128). For the BTS there is no trend over the different drill orientations of the granite intrusive phases.

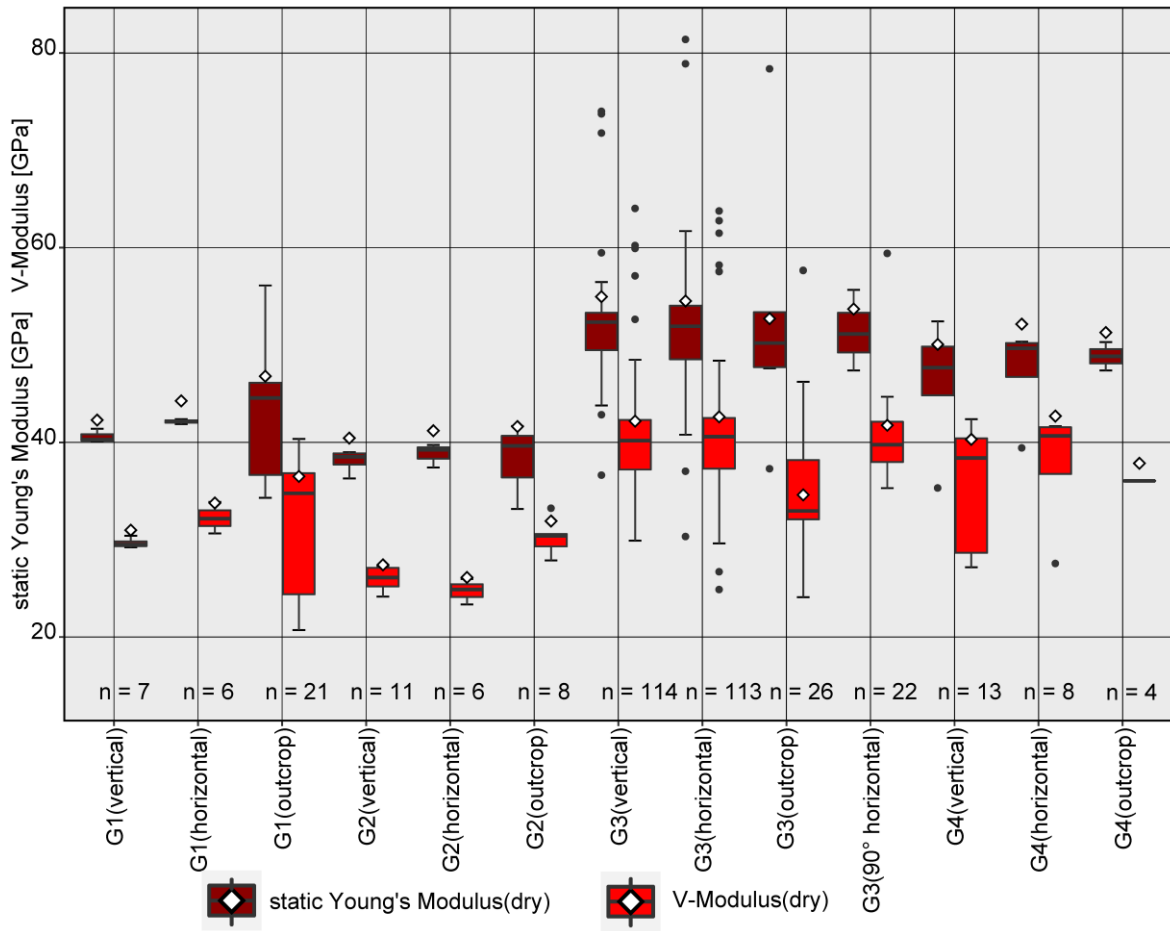


Fig. 129: Static Young's Modulus and V-Modulus versus orientation.

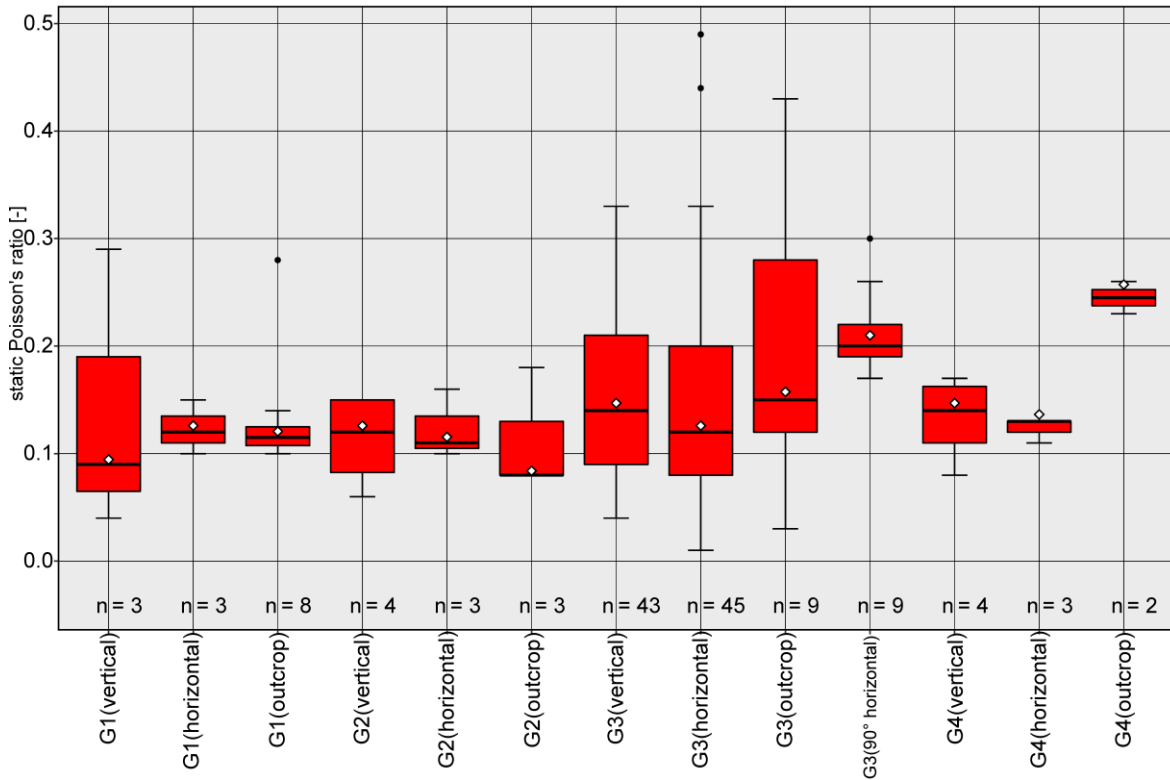


Fig. 130: Static Poisson's ratio(dry) versus orientation.

The drilling direction (vertical or horizontal) of the samples has no influence on the mean values of the different moduli. The outcrop samples for G1 and G3 scatter over wide ranges (Fig. 129). There is no trend of static Young's Modulus and V-Modulus change over the different drill orientations of the granite intrusive phases.

For G1(vertical) the mean value of the static Poisson's ratio is less than for G1(horizontal). For all other G types, the mean static Poisson's ratio for the vertical samples is higher than the mean static Poisson's ratio for the horizontal samples. The outcrop values do not show a clear pattern (Fig. 130). There is no trend of static Poisson's ratio change over the different drill orientations of the granite intrusive phases.

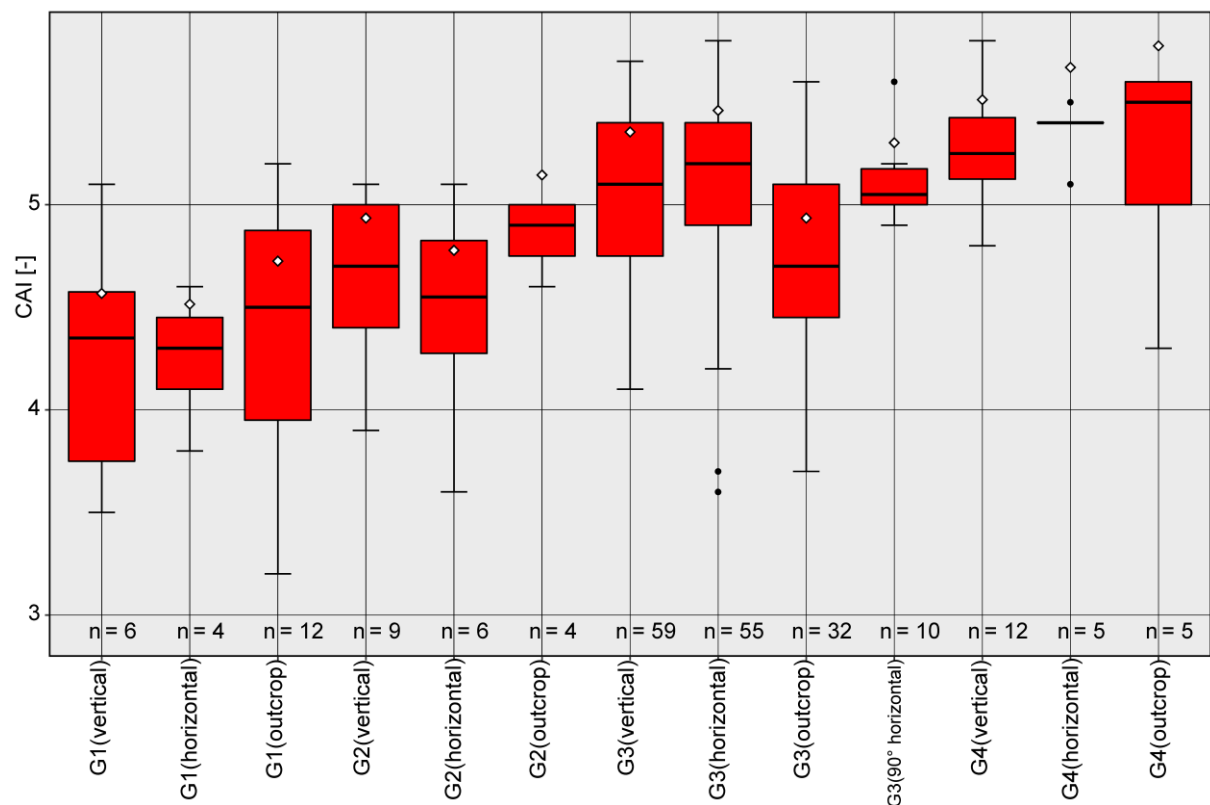


Fig. 131: CAI versus orientation.

The drilling direction of the samples has no influence on the abrasivity of the samples (Fig. 131).

### 2.3.6 Conclusions

In the Franconian basin is a demonstrable geothermal anomaly. This anomaly is suspected to correlate with granites but there are no geomechanical data for that area yet. In order to obtain initial data, 358 analogue samples from the next outcrop, the Fichtelgebirge, were examined in the course of this work. Each outcrop was characterized individually by specification of the most important parameters.

The samples were characterized with non-destructive as well as destructive testing methods. The non-destructive laboratory investigations were ultrasonic tests. The destructive laboratory tests included Uniaxial Compression Tests, Brazilian Tensile Tests, Point Load Tests, Cerchar Abrasivity Tests and LCPC Abrasivity Tests. The testing results were summarised. The summarised results were plotted against each other.

A correlation was found when comparing the results of dry and saturated samples for the vertical  $v_p$ -velocity and the  $v_s$ -velocity. When comparing the measurement results of dynamic and static tests, no correlations were found. A comparison of the various parameters with the uniaxial compressive strength also did not lead to any correlations. The brittleness of the examined samples ranges from tough to very tough. They lie in the typical brittle range of granites.

In addition, the summarised results were correlated with granite intrusion phase (G types) and the orientation of the analogue samples. The  $v_p$ - &  $v_s$ -values for G1 and G3 are higher than the  $v_p$ - &  $v_s$ -values for G2 and G4. The values of dynamic Young's Modulus show the same trend as the  $v_p$ - and  $v_s$ -velocities. The values for the dry dynamic Poisson's ratio don't differ between the G types. The same results were found for the saturated dynamic Poisson's ratio. The values for the dry dynamic Poisson's ratio are essentially between 0.2 and 0.3. The values for the saturated dynamic Poisson's ratio are mostly between 0.34 and 0.4. These ranges seem characteristic for the analogue samples.

The values of uniaxial compressive strength for all analogue samples range between 75 MPa and 195 MPa. The granites can therefore be classified as having high to very high strength. The values of the Brazilian tensile test are between 4.5 and 13.5 MPa. These ranges seem characteristic for the granites.

The static Young's Modulus values for G1 and G3 are higher than the static Young's Modulus values for G2 and G4. The IQR of the static Young's Modulus spans from 38 MPa to 55 MPa. The IQR of the V-Modulus ranges from 25 MPa to 41 MPa. These ranges seem characteristic for the analogue samples.

The static Poisson's ratio is on average between 0.1 and 0.15 and has an interquartile range (IQR) from 0.09 to 0.21. This range seems characteristic for these granites.

The CAI values range between 3.2 and 5.8 are therefore classified as highly abrasive or predominantly extremely abrasive. The abrasiveness increases with the decreasing age of the granites. The LAC values show the same result. They range from about 1,100 g/t and 1,470 g/t. The granites are therefore classified as highly abrasive or predominantly extremely abrasive. These values show that high drilling costs are to be expected due to high abrasion. The LBC values shows no trend and can be classified as

medium poor to medium high. The breakability varies over a broad range within and between the G types.

The different phases of granite intrusion do not show different results and it is not possible to identify which G type is based on the results of the laboratory investigations. No directional dependence of the parameter examined over the different drill orientations of the granite intrusive phases are found. But the wide range of the outcrop samples shows that it is important to take the orientation of the analogue samples into account for the measurements. The geomechanical results of the analogue samples show that any granites present below the Franconian Basin in NE Bavaria are homogeneous. This conclusion assumes that granites form the reservoir in the Franconian Basin in NE Bavaria.

Should a petrothermal well in this area one day be drilled, these specific parameter ranges will serve as first important input parameters for geomechanical modelling. The rock properties of the analogue samples must then be correlated with the geomechanical parameters of drill cores from the possible reservoir with information from geophysical borehole measurements.

## 2.4 Numerical simulations

As an application of the obtained geomechanical properties, seven different scenarios were considered to determine the borehole stability and the depth of failure around the borehole. For the Upper Jurassic aquifer, the three different lithologies were considered and for NE Bavaria the four different G types. The determined laboratory parameters served as input parameters for the model. The mean values were used for the calculations. In addition to the mean UCS values, the minimum and maximum UCS values were also taken into account for the observation of the borehole stability and depth of failure. An overview of the different parameters is shown in Tab. 30.

Tab. 30: Overview of the parameters used for modelling the respective rocks.

Parameter	Units	Limestone	Dolomitic Limestone	Dolostone	G1 type	G2 type	G3 type	G4 type
Unit Weight	[MN/m <sup>3</sup> ]	0.0252117	0.0242307	0.0256041	0.0259965	0.0258003	0.0258984	0.0257022
v	[-]	0.22	0.21	0.12	0.13	0.12	0.16	0.15
E	[MPa]	40.79	36.39	51.62	42.41	38.32	52.28	36.72
$\sigma_u$ (min.)	[MPa]	14.6	46.0	14.7	73.5	87.9	80.3	100.7
$\sigma_u$ (mean)	[MPa]	105.4	104.6	105.9	128.3	105.2	142.0	153.0
$\sigma_u$ (max.)	[MPa]	284.7	220.7	271.1	170.7	119.5	226.6	193.4
mb	[-]	10	9.5	9	32	32	32	32
s	[-]	1						
a	[-]	0.5						

The parameters discussed in the respective section were used for the applied stress field. Since not all parameters were known for the stress field in NE Bavaria, the granites of the Fichtelgebirge were investigated in triaxial experiments in a seedfunding project. Thereby a friction coefficient  $\mu$  of 1.2 was calculated. This value is the highest value determined. With the help of the coefficient of friction and the assumption that the granites have no porosity, the two missing values  $\sigma_H$  and  $\sigma_h$  were calculated.

Eqn. 26: Calculation of the maximal horizontal stress  $\sigma_H$  and the minimum horizontal stress  $\sigma_h$  for NE Bavaria.

$$\frac{\sigma_h}{\sigma_H} = [\sqrt{(\mu^2 + 1)} + \mu]^2 \quad (\text{Eqn. 26})$$

with:	$\sigma_h$	minimum horizontal stress	[MPa]
	$\sigma_H$	maximum horizontal stress	[MPa]
	$\mu$	coefficient of friction	[-]

This results in the following relationship:  $\sigma_h = 0.13 \cdot \sigma_H$ . Since a strike-slip regime prevails in NE Bavaria, the following states of stress are present:  $\sigma_H > \sigma_v > \sigma_h$ . With the help of the relationship  $\sigma_v = 0.5 \cdot (\sigma_H + \sigma_h)$  and the information that  $\sigma_v = 25.7$  MPa/km the values  $\sigma_H = 45.5$  MPa/km and  $\sigma_h = 5.9$  MPa/km were calculated. An overview of the stress field parameters is given in Tab. 31.

Tab. 31: Overview of the stress field parameters and stress regime used for modelling in the respective area.

Stress gradient	Stress field parameters				Stress regime
	$\sigma_H$	$\sigma_v$	$\sigma_h$	angle	[-]
Units	[MPa/km]	[MPa/km]	[MPa/km]	[°]	[-]
North Alpine Foreland Basin, SE Germany	23	23	14	90	SS-NF
NE Bavaria	45.5	25.7	5.9	135	SS

Each scenario was divided into four stages explicitly described below. Four different depth ranges (2 km, 3 km, 4 km and 5 km) were considered for each scenario. Since the figures are very similar in each area, only one lithology and G type per stage is shown below. If the stability of a borehole does not reach a depth of 1 km, the borehole is considered unstable in this work.

### 2.4.1 North Alpine Foreland Basin, SE Germany

The respective rock parameters from Tab. 30 and the stress field parameters from Tab. 31 were taken as input parameters for the different modelling scenarios.

#### 2.4.1.1 Stage 1 – lithostatic stress

In order to check whether the model with the acting in situ stresses was built up correctly, the area of the borehole before drilling was considered for each depth as stage 1 of the different modelling scenarios. The resulting maximum horizontal stress patterns for the North Alpine Foreland Basin, SE Germany are shown in Fig. 132.

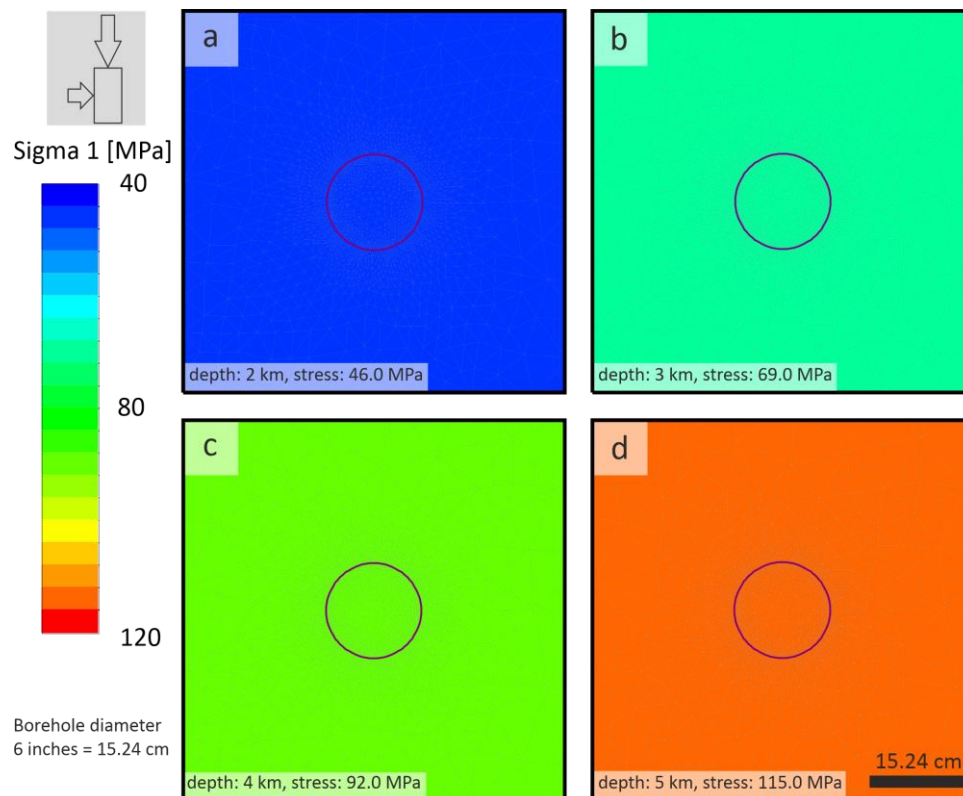


Fig. 132: Stresses before drilling in Upper Jurassic limestone (15.24 cm = 6" borehole diameter). Stress field in depths of 2 km (a), 3 km (b), 4 km (c) and 5 km (d).

In the North Alpine Foreland Basin, SE Germany, the lowest maximum horizontal stress in 1 km depth is 23 MPa and the highest maximum horizontal stress in 5 km depth is 115 MPa. The lowest minimum horizontal stress in 1 km depth is 14 MPa and the highest maximum horizontal stress in 5 km depth is 70 MPa.

### 2.4.1.2 Stage 2 – excavated borehole

A borehole was modelled by excavating the borehole for each depth. Stage 2 does not correspond to practice, since boreholes are always filled with water at those depths. It is just an interstage, which is needed for the further modelling. The maximum horizontal stresses are higher than before the borehole was created at the respective depths. The highest stresses at the borehole wall are concentrated at 90° to the maximum horizontal stresses of the stress field. The stress pattern that forms after the excavation is shown in Fig. 133 for the depth range from 2 km to 5 km.

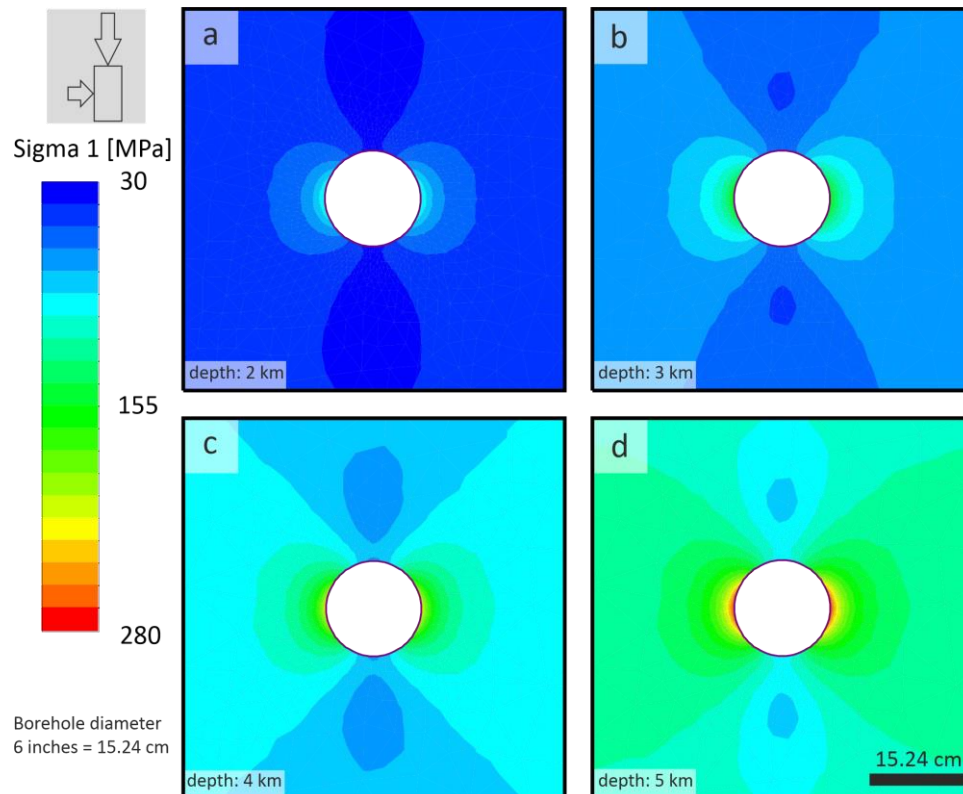


Fig. 133: Stress patterns after drilling in Upper Jurassic limestone without hydrostatic water pressure ("dry"). Borehole diameter 6" = 15.24 cm. Stress field in depths of 2 km (a), 3 km (b), 4 km (c) and 5 km (d).

In all models, a relatively homogeneous stress pattern is formed, depending on the depth considered at a distance from the borehole wall. This corresponds approximately to the stress pattern before drilling at the respective depth. When comparing the maximum horizontal stresses acting at the wall of the borehole, it is noticeable that the calculated stresses correspond to the modelled stresses more or less exactly (Tab. 32). The only advantage of the numerical modelling is the visualization of the stress field.

Tab. 32: Calculated and modelled maximum borehole wall stress after the drilling at the respective depth for the North Alpine Foreland Basin, SE Germany.

Depth	Units	$\sigma_{\max}$									
		1		2		3		4		5	
Calculated or modeled	[-]	cal.	mod.	cal.	mod.	cal.	mod.	cal.	mod.	cal.	mod.
Limestone	[MPa]	55.0	54.9	110.0	109.9	165.0	164.8	220.0	219.8	275.0	274.7
Dolomitic Limestone		55.0	55.0	110.0	110.1	165.0	165.1	220.0	220.1	275.0	275.1
Dolostone		55.0	54.9	110.0	109.9	165.0	164.8	220.0	219.8	275.0	274.7

### 2.4.1.3 Stage 3 – hydrostatic pressure in borehole

In stage 3, the hydrostatic pressure through water, i.e. water pressure as a function of depth, was calculated. This was then applied to the wall of the borehole in the respective depth. This pressure reduces the stresses around the borehole significantly. The stress patterns that form applying hydrostatic pressure are shown in Fig. 134 for the depth range from 2 km to 5 km.

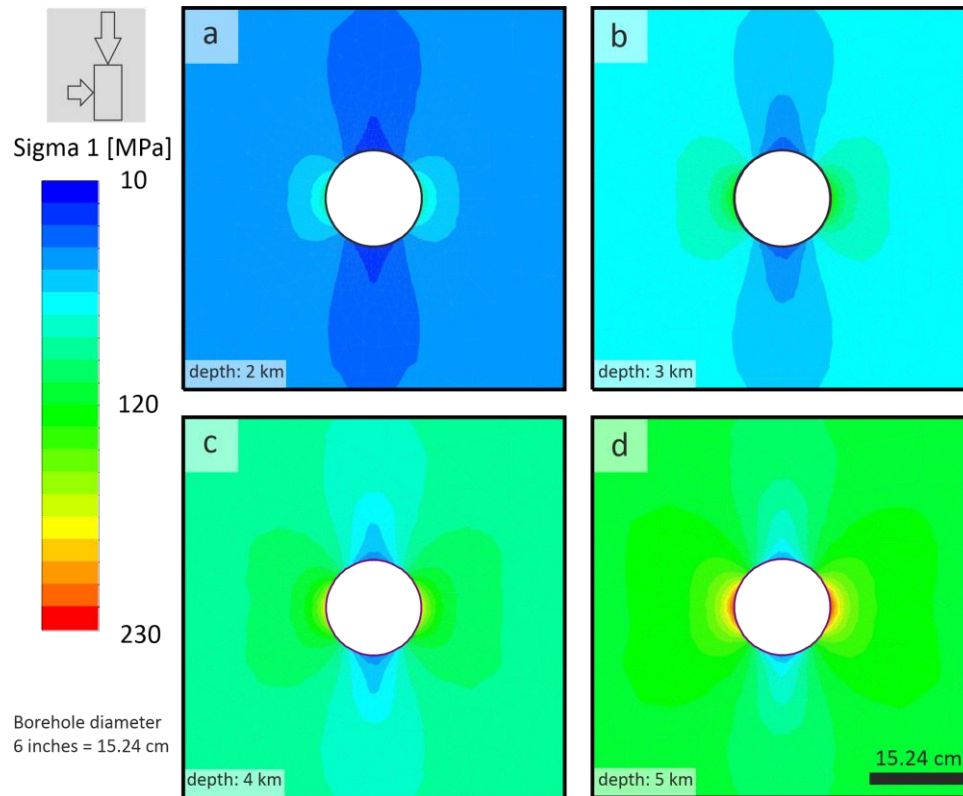


Fig. 134: Stress patterns including hydrostatic pressure in a borehole in Upper Jurassic limestone. Borehole diameter 6" = 15.24 cm. Stress field in depths of 2 km (a), 3 km (b), 4 km (c) and 5 km (d).

When comparing the maximum horizontal stresses acting at the borehole wall, it is noticeable that the calculated stresses correspond to the modelled stresses more or less exactly (Tab. 33). The only advantage of the numerical modelling is the visualization of the stress field pattern.

Tab. 33: Calculated and modelled maximum borehole wall stress with hydrostatic pressure at the respective depth for the North Alpine Foreland Basin, SE Germany.

Depth	Units	$\sigma_{max}$									
		1		2		3		4		5	
Calculated or modeled	[-]	cal.	mod.	cal.	mod.	cal.	mod.	cal.	mod.	cal.	mod.
Limestone	[MPa]	45.2	45.1	90.4	90.1	135.6	135.2	180.8	180.2	226.0	225.3
Dolomitic Limestone		45.2	45.1	90.4	90.2	135.6	135.4	180.8	180.5	226.0	225.6
Dolostone		45.2	45.1	90.4	90.1	135.6	135.2	180.8	180.2	226.0	225.3

### 2.4.1.4 Stage 4 – drilling mud applied

In stage 4 a drilling mud with a density of  $1.9 \text{ g/cm}^3$  was applied to represent the stress distribution in the near-field of a borehole for the respective depth. This mud density is the maximum value taken for drilling, since mud densities typically vary between  $1.1 \text{ g/cm}^3$  and  $1.9 \text{ g/cm}^3$ . This pressure reduces the stresses around the borehole much more than the water pressure. The stress patterns that form after a drilling mud was added to the created hydrostatic pressure is shown in Fig. 135 for the depth range from 2 km to 5 km.

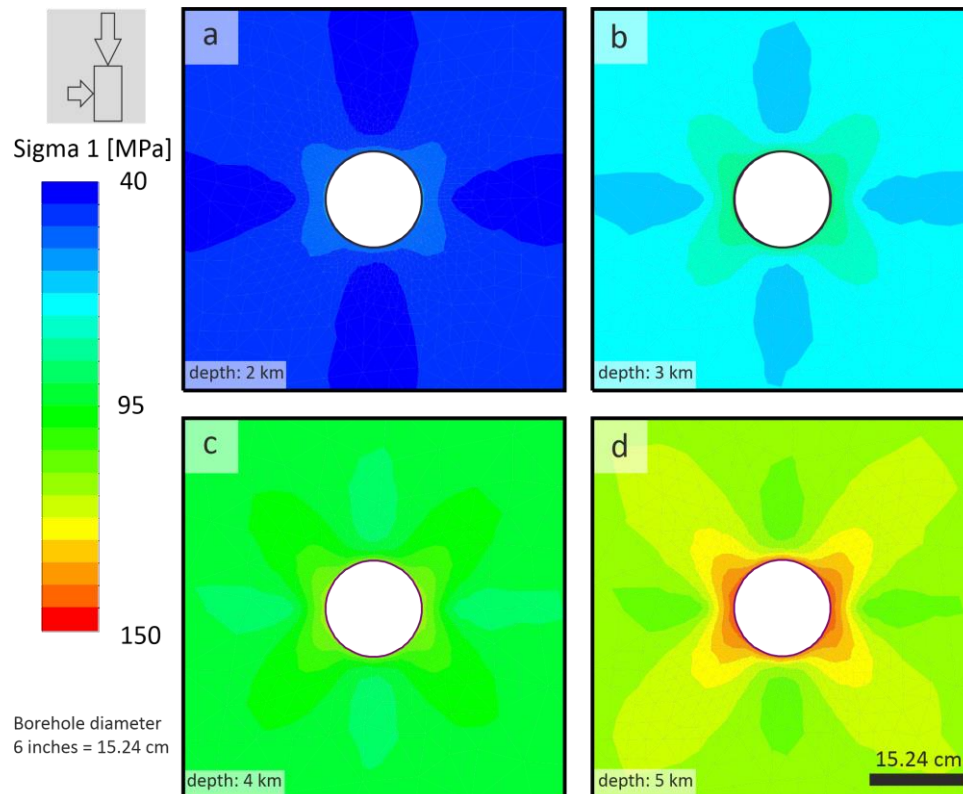


Fig. 135: Stress patterns including drilling mud in a borehole in Upper Jurassic limestone. Borehole diameter  $6'' = 15.24 \text{ cm}$ . Stress field in depths of 2 km (a), 3 km (b), 4 km (c) and 5 km (d).

When comparing the maximum horizontal stresses acting at the borehole wall, it is noticeable that the calculated stresses correspond to the modelled stresses more or less exactly (Tab. 34). The only advantage of the numerical modelling is the visualization of the stress field pattern.

Tab. 34: Calculated and modelled maximum wall stress including drilling mud at the respective depth for the North Alpine Foreland Basin, SE Germany.

Depth	Units	$\sigma_{\max}$									
		1		2		3		4		5	
Calculated or modeled	[-]	cal.	mod.	cal.	mod.	cal.	mod.	cal.	mod.	cal.	mod.
Limestone	[MPa]	26.6	28.8	53.1	57.5	79.7	86.3	106.2	115.0	132.8	143.8
Dolomitic Limestone		26.6	28.8	53.1	57.7	79.7	86.5	106.2	115.4	132.8	144.2
Dolostone		26.6	28.8	53.1	57.5	79.7	86.3	106.2	115.0	132.8	143.8

### 2.4.1.5 Results and Discussion

The following results were determined for the Upper Jurassic limestone. Fig. 136 shows the stress pattern in a borehole under hydrostatic pressure in the selected depth levels with the depth of failure in the borehole after HOEK & MARTIN (2014) using the UCS mean value of Tab. 30.

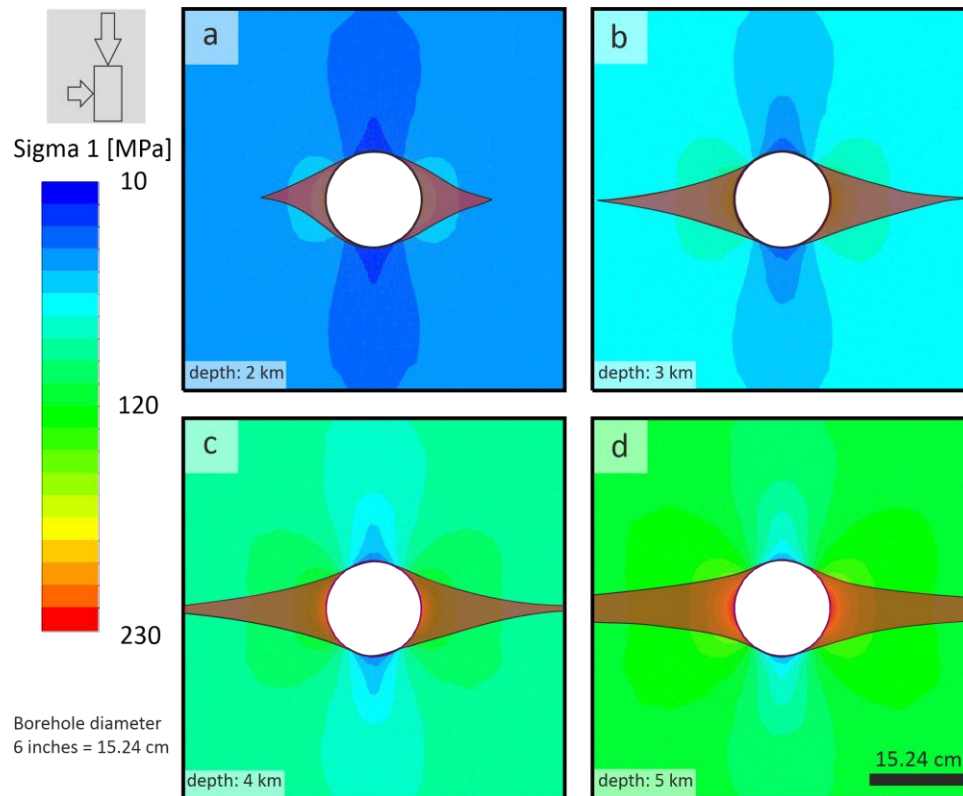


Fig. 136: Stress patterns in a borehole in Upper Jurassic limestone, hydrostatic pressure in depths of 2 km (a), 3 km (b), 4 km (c) and 5 km (d) with depth of failure after HOEK & MARTIN (2014), using the UCS mean value.

For the different stages 2–4 the depths of failure with the formula of HOEK & MARTIN (2014) were calculated in the vertical borehole. Since this concept is derived from tunnel projects mainly using data from crystalline rock, this scenario was assigned the term „pessimistic failure criterion“. It is not clear whether this case also applies to the brittle limestone of the Upper Jurassic.

Tab. 35 shows the calculated depth of failure for maximum borehole stress from the calculation and from the numerical modelling for the different UCS values for a depth range between 1 km and 5 km. For the mean UCS value, the depth of failure with the maximum modelled borehole stress ranges from 2.2 cm to 41.9 cm in the dry borehole, from 0.4 cm to 32.9 cm in the water saturated borehole, and from -2.6 cm to 18.2 cm for the borehole with a drilling mud. The depth of failure increases with increasing depth. This was calculated for the stages 2 to 4 depending on the depth and the different UCS values. In Fig. 137 the depth of failure is plotted against the drilling depth for the different UCS values.

For the „optimistic failure criterion“, the difference between the maximum wall stress and the UCS (stage 2), the difference between the maximum wall stress and the summary of UCS and pore pressure (stage 3) and the difference between the maximum wall stress and the summary of UCS, pore pressure and mud weight (stage 4) was calculated for each depth. Tab. 36 shows the calculated differential stress from the calculation and from the numerical modelling for the different UCS values for a depth range

between 1 km and 5 km. In Fig. 137 (right) the differential stress is plotted against the drilling depth for the different UCS values.

Tab. 35: Calculated and modelled depth of failure at the respective depth for the Upper Jurassic limestone. Negative values indicate, that there are no borehole breakouts. Marked section indicates a reasonable scenario using UCS mean.

Lithology	UCS	Depth	calc.	mod.	calc.	mod.	calc.	mod.
	[MPa]		$d_f$ (dry)	$d_f$ (dry)	$d_f$ (sat.)	$d_f$ (sat.)	$d_f$ (mud)	$d_f$ (mud)
		[km]	[cm]	[cm]	[cm]	[cm]	[cm]	[cm]
Limestone	14.6	1	64.0	63.9	51.2	51.0	26.9	29.8
		2	135.8	135.6	110.2	109.8	61.5	67.3
		3	207.5	207.3	169.1	168.6	96.2	104.8
		4	279.3	279.0	228.1	227.4	130.8	142.3
		5	351.0	350.7	287.0	286.2	165.4	179.9
	105.4	1	2.2	2.2	0.4	0.4	-3.0	-2.6
		2	12.1	12.1	8.6	8.5	1.8	2.6
		3	22.0	22.0	16.7	16.7	6.6	7.8
		4	32.0	31.9	24.9	24.8	11.4	13.0
		5	41.9	41.9	33.1	32.9	16.2	18.2
	284.7	1	-4.1	-4.1	-4.7	-4.8	-6.0	-5.8
		2	-0.4	-0.4	-1.7	-1.7	-4.2	-3.9
		3	3.3	3.3	1.3	1.3	-2.4	-2.0
		4	6.9	6.9	4.3	4.3	-0.7	-0.1
		5	10.6	10.6	7.3	7.3	1.1	1.8

Tab. 36: Calculated and modelled differential stress at the respective depth for the Upper Jurassic limestone. Negative values indicate a stable borehole. Marked section indicates a reasonable scenario using the UCS mean value.

Lithology	UCS	Depth	calc.	mod.	calc.	mod.	calc.	mod.
	[MPa]		$\Delta S$ (dry)	$\Delta S$ (dry)	$\Delta S$ (sat.)	$\Delta S$ (sat.)	$\Delta S$ (mud)	$\Delta S$ (mud)
		[km]	[MPa]	[MPa]	[MPa]	[MPa]	[MPa]	[MPa]
Limestone	14.6	1	40.4	40.3	30.6	30.5	12.0	14.2
		2	95.4	95.3	75.8	75.5	38.5	42.9
		3	150.4	150.2	121.0	120.6	65.1	71.7
		4	205.4	205.2	166.2	165.6	91.6	100.4
		5	260.4	260.1	211.4	210.7	118.2	129.2
	105.4	1	-50.4	-50.5	-60.2	-60.3	-78.8	-76.6
		2	4.6	4.5	-15.0	-15.3	-52.3	-47.9
		3	59.6	59.4	30.2	29.8	-25.7	-19.1
		4	114.6	114.4	75.4	74.8	0.8	9.6
		5	169.6	169.3	120.6	119.9	27.4	38.4
	284.7	1	-229.7	-229.8	-239.5	-239.6	-258.1	-255.9
		2	-174.7	-174.8	-194.3	-194.6	-231.6	-227.2
		3	-119.7	-119.9	-149.1	-149.5	-205.0	-198.4
		4	-64.7	-64.9	-103.9	-104.5	-178.5	-169.7
		5	-9.7	-10.0	-58.8	-59.4	-151.9	-140.9

In Fig. 137 only the modelled values are shown since the calculated and modelled values are more or less the same. In the diagrams, on the left side the depth of failure and on the right side the differential stress is plotted versus the drilling depth for the different UCS values.

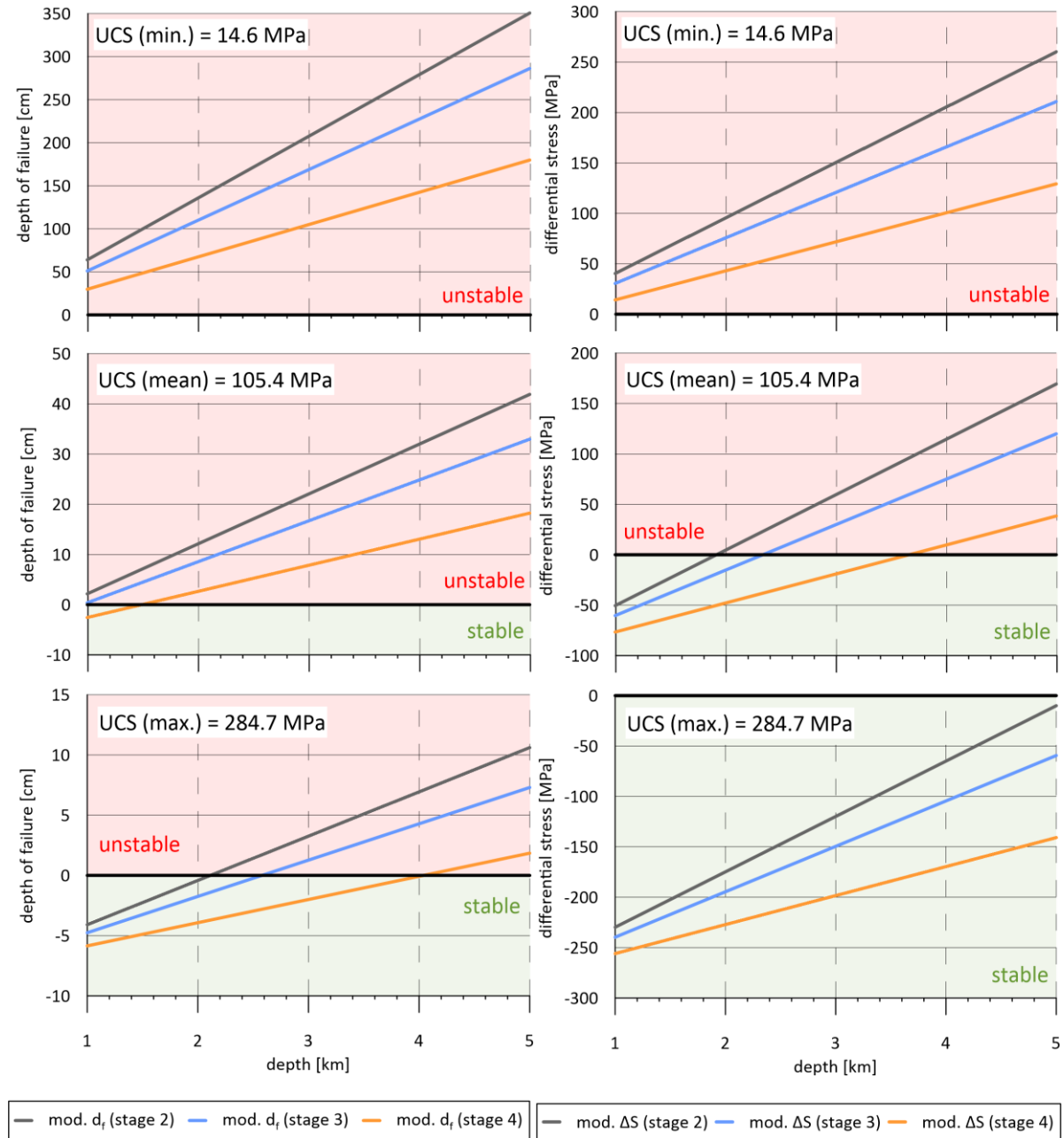


Fig. 137: The depth of failure for the pessimistic failure criterion (left) and the differential stress for the optimistic failure criterion (right) versus depth of the borehole in the Upper Jurassic limestone.

For the „pessimistic failure criterion“ and the minimum UCS value, the borehole is unstable in every of the four stages (Fig. 137, top diagram (left)). With a mean limestone UCS value at stage 4 (including mud), the borehole is stable up to a depth of 1.5 km. The other wells (stage 2 and stage 3) are unstable (Fig. 137, diagram in the middle (left)). At the maximum UCS value, the borehole is stable at stage 4 to a depth of 4.2 km. The water saturated borehole (stage 3) is stable to a depth of 2.5 km, the dry borehole (stage 2) to 2 km (Fig. 137, bottom diagram (left)).

For the „optimistic failure criterion“ and the UCS minimum value, the borehole is unstable in every stage (Fig. 137, top diagram (right)). With a mean UCS limestone's value the well is stable with a mud weight up to a depth of 4 km. The water saturated well is stable to a depth of 2.3 km and the dry well is stable to a depth of 2 km (Fig. 137, diagram in the middle (right)). At the maximum UCS value, all wells are stable down to a depth of 5 km (Fig. 137, bottom (right)).

The same evaluations were carried out for the dolomitic limestone and dolostone. The calculated results are summarised for the dolomitic limestone in Tab. 37 and Tab. 38 as well as for the dolostone in Tab. 39 and Tab. 40.

For all lithologies, borehole stability decreases with increasing depth. The depth of failure around the borehole hardly differs between the individual lithologies when considering the UCS mean values. Considering the pessimistic failure criterion, all minimum UCS values of all lithologies show a large depth of failure around the borehole and all boreholes are unstable at all depths. For all mean UCS values a borehole stability of up to 1.5 km is shown for boreholes with the selected drilling mud. The remaining boreholes are unstable for this UCS value. For the maximum UCS values a borehole stability of 1.5 km to 4.3 km is found. Considering the optimistic failure criterion, the minimum UCS values of limestone and dolostone show that all boreholes are unstable. For dolomitic limestone, there is a borehole stability to a depth of 1.8 km. For the mean UCS values, all lithologies show that the dry boreholes are stable down to a depth of 2 km, the water saturated boreholes are stable down to a depth of 2.3 km and the boreholes with a drilling mud are stable down to a depth of 4 km.

Considering the optimistic fracture criterion, the maximum UCS values of limestone and dolostone show that all boreholes are stable. For dolomitic limestone, the dry borehole shows a stability down to a depth of 4 km. The other two boreholes are stable down to a depth of 5 km.

The average values were used in the calculations, as these represent the strength of the rock best. As the pessimistic fracture criterion for the limestones has not been proven in investigations so far, an optimistic fracture criterion is more likely to be expected. As can be seen from the diagram, in the optimistic failure criterion the boreholes are stable in most of the lithologies which is evident for the limestones in the deep North Alpine Foreland Basin.

Tab. 37: Calculated and modelled depth of failure at the respective depth for the Upper Jurassic dolomitic limestone. Negative values indicate, that there are no borehole breakouts. Marked section indicates a reasonable scenario using UCS mean.

Lithology	UCS	Depth	calc.	mod.	calc.	mod.	calc.	mod.
	[MPa]		$d_f$ (dry)	$d_f$ (dry)	$d_f$ (sat. )	$d_f$ (sat. )	$d_f$ (mud)	$d_f$ (mud)
		[km]	[cm]	[cm]	[cm]	[cm]	[cm]	[cm]
Dolomitic Limestone	46	1	15.0	15.0	10.9	10.9	3.2	4,2
		2	37.8	37.8	29.7	29.6	14.2	16,1
		3	60.6	60.6	48.4	48.3	25.2	28,1
		4	83.3	83.4	67.1	67.0	36.2	40,0
		5	106.1	106.2	85.8	85.7	47.2	51,9
	104.6	1	2.2	2.2	0.5	0.4	-2.9	-2,5
		2	12.3	12.3	8.7	8.7	1.9	2,7
		3	22.3	22.3	16.9	16.9	6.7	8,0
		4	32.3	32.3	25.1	25.1	11.6	13,2
		5	42.3	42.3	33.4	33.3	16.4	18,5
	220.7	1	-3.0	-3.0	-3.9	-3.9	-5.5	-5,3
		2	1.7	1.7	0.0	0.0	-3.2	-2,8
		3	6.5	6.5	3.9	3.9	-0.9	-0,3
		4	11.2	11.2	7.8	7.8	1.4	2,2
		5	16.0	16.0	11.7	11.7	3.7	4,7

Tab. 38: Calculated and modelled differential stress at the respective depth for the Upper Jurassic dolomitic limestone. Negative values indicate a stable borehole. Marked section indicates a reasonable scenario using the UCS mean value.

Lithology	UCS	Depth	calc.	mod.	calc.	mod.	calc.	mod.
	[MPa]		$\Delta S$ (dry)	$\Delta S$ (dry)	$\Delta S$ (sat. )	$\Delta S$ (sat. )	$\Delta S$ (mud)	$\Delta S$ (mud)
		[km]	[MPa]	[MPa]	[MPa]	[MPa]	[MPa]	[MPa]
Dolomitic Limestone	46	1	9.0	9.0	-0.8	-0.9	-19.4	-17.2
		2	64.0	64.1	44.4	44.2	7.1	11.7
		3	119.0	119.1	89.6	89.4	33.7	40.5
		4	174.0	174.1	134.8	134.5	60.2	69.4
		5	229.0	229.1	180.0	179.6	86.8	98.2
	104.6	1	-49.6	-49.6	-59.4	-59.5	-78.0	-75.8
		2	5.4	5.5	-14.2	-14.4	-51.5	-46.9
		3	60.4	60.5	31.0	30.8	-24.9	-18.1
		4	115.4	115.5	76.2	75.9	1.6	10.8
		5	170.4	170.5	121.4	121.0	28.2	39.6
	220.7	1	-165.7	-165.7	-175.5	-175.6	-194.1	-191.9
		2	-110.7	-110.7	-130.3	-130.5	-167.6	-163.0
		3	-55.7	-55.6	-85.1	-85.3	-141.0	-134.2
		4	-0.7	-0.6	-39.9	-40.2	-114.5	-105.3
		5	54.3	54.4	5.3	4.9	-87.9	-76.5

Tab. 39: Calculated and modelled depth of failure at the respective depth for the Upper Jurassic dolostone. Negative values indicate, that there are no borehole breakouts. Marked section indicates a reasonable scenario using UCS mean.

Lithology	UCS	Depth	calc.	mod.	calc.	mod.	calc.	mod.
	[MPa]		$d_f$ (dry)	$d_f$ (dry)	$d_f$ (sat. )	$d_f$ (sat. )	$d_f$ (mud)	$d_f$ (mud)
		[km]	[cm]	[cm]	[cm]	[cm]	[cm]	[cm]
Dolostone	14.7	1	63.5	63.4	50.8	50.6	26.6	29.5
		2	134.8	134.6	109.4	109.0	61.0	66.8
		3	206.1	205.8	167.9	167.4	95.5	104.0
		4	277.3	277.0	226.5	225.8	129.9	141.3
		5	348.6	348.2	285.0	284.2	164.3	178.6
	105.9	1	2.1	2.1	0.4	0.3	-3.0	-2.6
		2	12.0	12.0	8.5	8.4	1.8	2.6
		3	21.9	21.9	16.6	16.5	6.6	7.7
		4	31.8	31.8	24.7	24.6	11.3	12.9
		5	41.7	41.6	32.9	32.8	16.1	18.1
	271.1	1	-3.9	-3.9	-4.6	-4.6	-5.9	-5.8
		2	0.0	-0.1	-1.4	-1.4	-4.0	-3.7
		3	3.8	3.8	1.8	1.7	-2.2	-1.7
		4	7.7	7.7	4.9	4.9	-0.3	0.3
		5	11.6	11.5	8.1	8.1	1.6	2.3

Tab. 40: Calculated and modelled differential stress at the respective depth for the Upper Jurassic dolostone. Negative values indicate a stable borehole. Marked section indicates a reasonable scenario using the UCS mean value.

Lithology	UCS	Depth	calc.	mod.	calc.	mod.	calc.	mod.
	[MPa]		$\Delta S$ (dry)	$\Delta S$ (dry)	$\Delta S$ (sat. )	$\Delta S$ (sat. )	$\Delta S$ (mud)	$\Delta S$ (mud)
		[km]	[MPa]	[MPa]	[MPa]	[MPa]	[MPa]	[MPa]
Dolostone	14.7	1	40.3	40.2	30.5	30.4	11.9	14.1
		2	95.3	95.2	75.7	75.4	38.4	42.8
		3	150.3	150.1	120.9	120.5	65.0	71.6
		4	205.3	205.1	166.1	165.5	91.5	100.3
		5	260.3	260.0	211.3	210.6	118.1	129.1
	105.9	1	-50.9	-51.0	-60.7	-60.8	-79.3	-77.1
		2	4.1	4.0	-15.5	-15.8	-52.8	-48.4
		3	59.1	58.9	29.7	29.3	-26.2	-19.6
		4	114.1	113.9	74.9	74.3	0.3	9.1
		5	169.1	168.8	120.1	119.4	26.9	37.9
	271.1	1	-216.1	-216.2	-225.9	-226.0	-244.5	-242.3
		2	-161.1	-161.2	-180.7	-181.0	-218.0	-213.6
		3	-106.1	-106.3	-135.5	-135.9	-191.4	-184.8
		4	-51.1	-51.3	-90.3	-90.9	-164.9	-156.1
		5	3.9	3.6	-45.2	-45.8	-138.3	-127.3

## 2.4.2 NE Bavaria

The respective rock parameters from Tab. 30 and the stress field parameters from Tab. 31 were taken as input parameters for the different modelling scenarios.

### 2.4.2.1 Stage 1 – lithostatic stress

In order to check whether the model with the acting in situ stresses was built up correctly, the area of the borehole before drilling was considered for each depth as stage 1 of the different modelling scenarios. The resulting maximum horizontal stress patterns for the NE Bavaria are shown in Fig. 138.

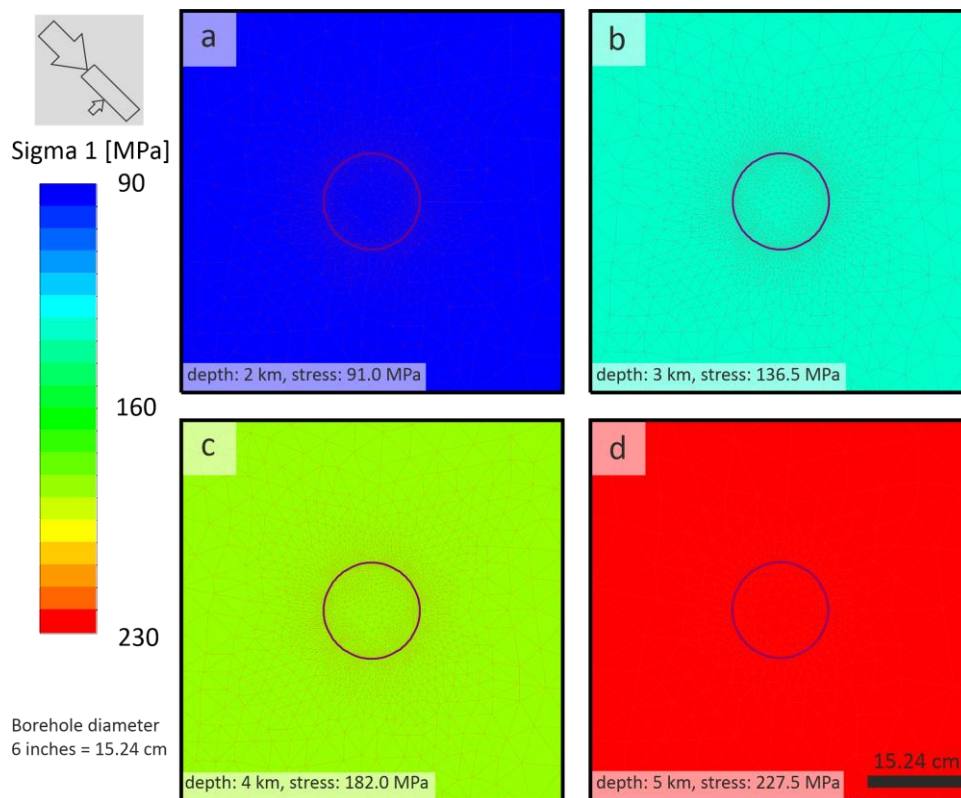


Fig. 138: Stresses before drilling in G1 type (15.24 cm = 6" borehole diameter). Stress field in depths of 2 km (a), 3 km (b), 4 km (c) and 5 km (d).

In NE Bavaria, the lowest maximum horizontal stress at 1 km depth is 45.5 MPa and the highest maximum horizontal stress at 5 km depth is 227.5 MPa. The lowest minimum horizontal stress at 1 km depth is 5.9 MPa and the highest maximum horizontal stress at 5 km depth is 29.5 MPa. It is noticeable that prevail in the two areas, completely different maximum and minimum horizontal stresses exist in the underground. In NE Bavaria, larger differences in the situ stresses are present. The maximum horizontal stresses in the North Alpine Foreland Basin, SE Germany are only half as high as in NE Bavaria. The minimum horizontal stresses in the North Alpine Foreland Basin, SE Germany are two and a half times as large as those in NE Bavaria.

### 2.4.2.2 Stage 2 – excavated borehole

A borehole was modelled by excavating the borehole for each depth. Stage 2 does not correspond to practice, since boreholes are always filled with water at those depths. It is just an interstage, which is needed for the further modelling. The maximum horizontal stresses are higher than before the borehole was created at the respective depths. The highest stresses at the borehole wall are concentrated at 90° to the maximum horizontal stresses of the stress field. The stress pattern that forms after the excavation is shown in Fig. 139 for the depth range from 2 km to 5 km.

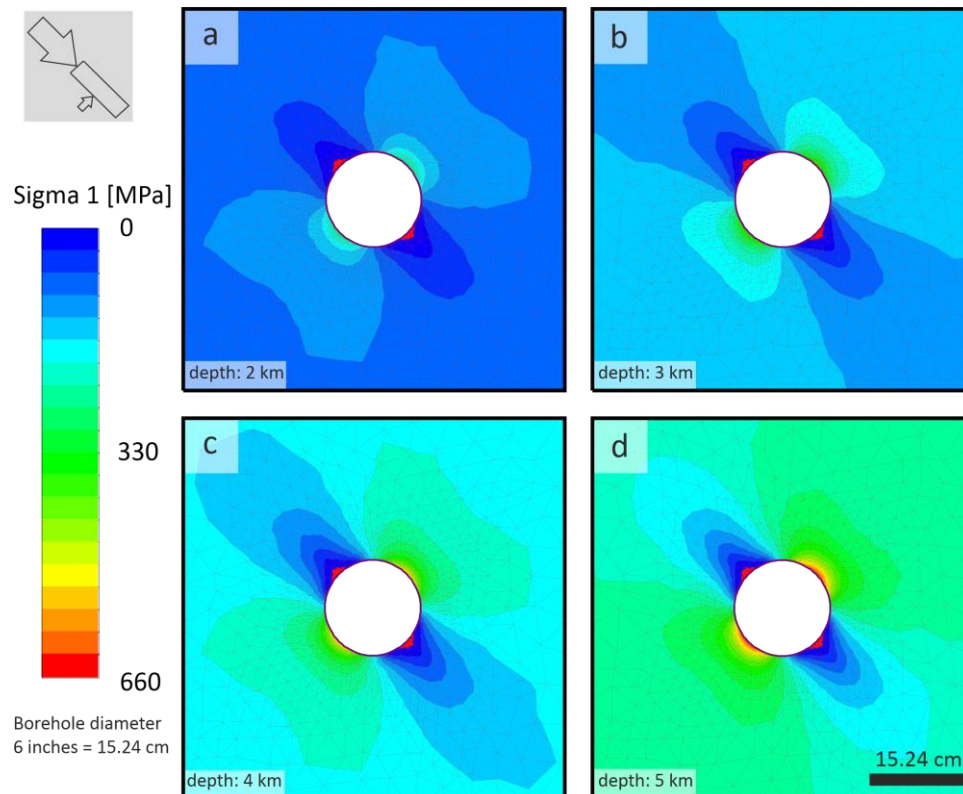


Fig. 139: Stress patterns after drilling in G1 type without hydrostatic water pressure ("dry"). Borehole diameter 6" = 15.24 cm. Stress field in depths of 2 km (a), 3 km (b), 4 km (c) and 5 km (d).

Clearly visible is that tensile cracks occur in the direction of the maximum horizontal stress (red). In all models, a relatively homogeneous stress pattern is formed, depending on the depth considered at a distance from the borehole wall. This corresponds approximately to the stress pattern before drilling at the respective depth. When comparing the maximum horizontal stresses acting at the wall of the borehole, it is noticeable that the calculated stresses correspond to the modelled stresses more or less exactly (Tab. 41). The only advantage of the numerical modelling is the visualization of the stress field.

Tab. 41: Calculated and modelled maximum borehole wall stress after the drilling at the respective depth for NE Bavaria.

Depth		Units	$\sigma_{\max}$									
			1		2		3		4		5	
Calculated or modeled	[-]	[MPa]	cal.	mod.	cal.	mod.	cal.	mod.	cal.	mod.	cal.	mod.
			NE Bavaria	G1		130.6	130.8	261.2	261.5	391.8	392.2	522.4
G2		130.6		130.7	261.2	261.4	391.8	392.2	522.4	483.2	653.0	653.6
G3		130.6		130.7	261.2	261.7	391.8	392.5	522.4	523.3	653.0	654.2
G4		130.6		130.7	261.2	261.6	391.8	392.4	522.4	523.2	653.0	654.0

### 2.4.2.3 Stage 3 – hydrostatic pressure in borehole

In stage 3, the hydrostatic pressure through water, i.e. water pressure as a function of depth, was calculated. This was then applied to the wall of the borehole in the respective depth. This pressure reduces the stresses around the borehole significantly. The stress patterns that form applying hydrostatic pressure are shown in Fig. 140 for the depth range from 2 km to 5 km.

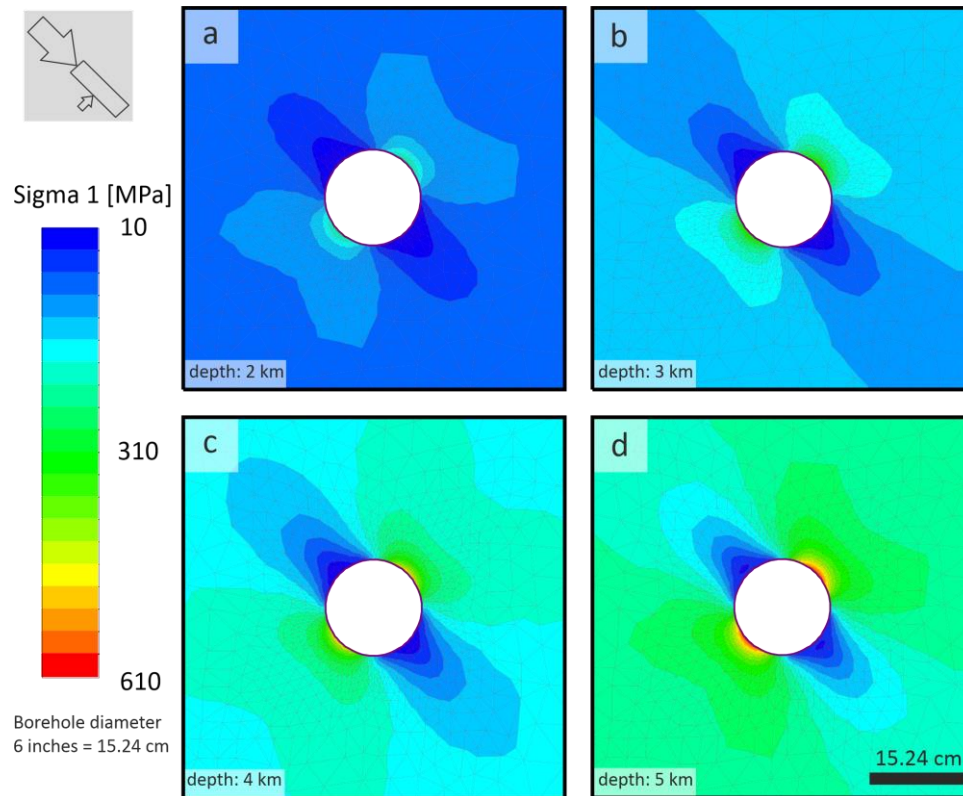


Fig. 140: Stress patterns including hydrostatic pressure in a borehole in G1 type. Borehole diameter 6" = 15.24 cm. Stress field in depths of 2 km (a), 3 km (b), 4 km (c) and 5 km (d).

When comparing the maximum horizontal stresses acting at the borehole wall, it is noticeable that the calculated stresses correspond to the modelled stresses more or less exactly (Tab. 42). The only advantage of the numerical modelling is the visualization of the stress field pattern.

Tab. 42: Calculated and modelled maximum borehole wall stress with hydrostatic pressure at the respective depth for NE Bavaria.

Depth		Units	$\sigma_{max}$									
			1		2		3		4		5	
Calculated or modeled	G1 G2 G3 G4	[MPa]	cal.	mod.	cal.	mod.	cal.	mod.	cal.	mod.	cal.	mod.
						120.8	120.9	241.6	241.8	362.4	362.8	483.2
			120.8	120.9	241.6	241.6	362.4	362.7	483.2	483.6	604.0	604.5
			120.8	121.0	241.6	242.0	362.4	363.0	483.2	484.0	604.0	605.0
			120.8	121.0	241.6	241.9	362.4	362.9	483.2	483.9	604.0	604.9

### 2.4.2.4 Stage 4 – drilling mud applied

In stage 4 a drilling mud with a density of  $1.9 \text{ g/cm}^3$  was applied to represent the stress distribution in the near-field of a borehole for the respective depth. This mud density is the maximum value taken for drilling, since mud densities typically vary between  $1.1 \text{ g/cm}^3$  and  $1.9 \text{ g/cm}^3$ . This pressure reduces the stresses around the borehole much more than the water pressure. The stress patterns that form after a drilling mud was added to the created hydrostatic pressure is shown in Fig. 141 for the depth range from 2 km to 5 km.

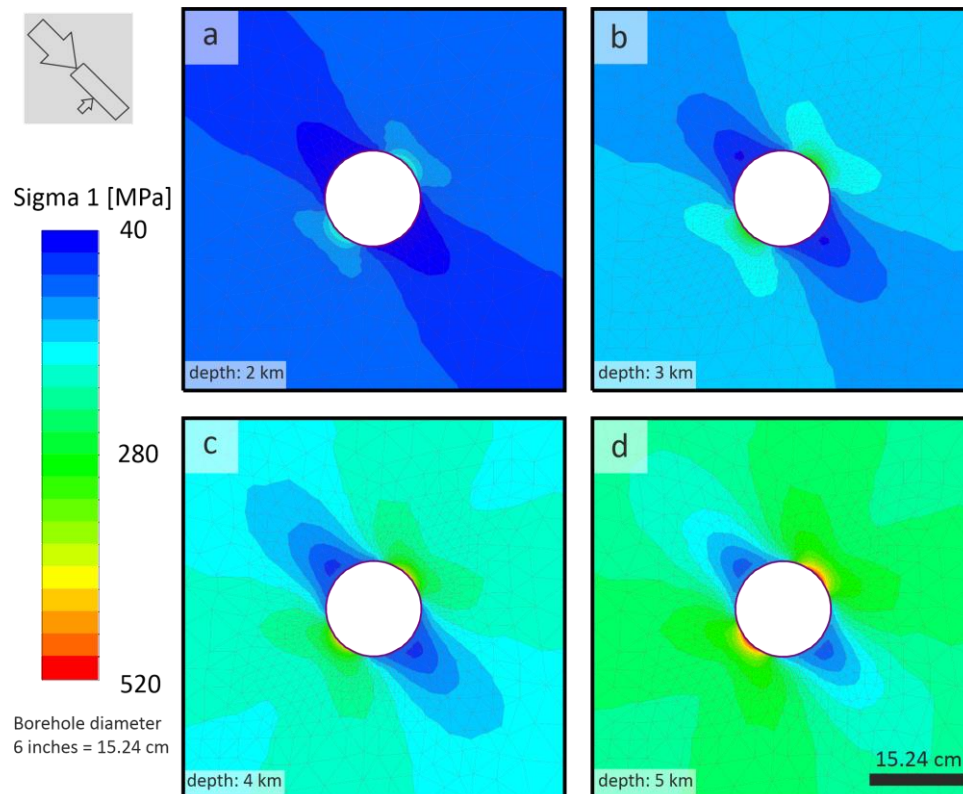


Fig. 141: Stress patterns including drilling mud in a borehole in G1 type. Borehole diameter  $6'' = 15.24 \text{ cm}$ . Stress field in depths of 2 km (a), 3 km (b), 4 km (c) and 5 km (d).

When comparing the maximum horizontal stresses acting at the borehole wall, it is noticeable that the calculated stresses correspond to the modelled stresses more or less exactly (Tab. 43). The only advantage of the numerical modelling is the visualization of the stress field pattern.

Tab. 43: Calculated and modelled maximum wall stress including drilling mud at the respective depth for NE Bavaria.

Depth	Units	$\sigma_{\max}$										
		1		2		3		4		5		
Calculated or modeled	[-]	cal.	mod.	cal.	mod.	cal.	mod.	cal.	mod.	cal.	mod.	
NE Bavaria	G1	[MPa]	102.2	102.2	204.3	204.5	306.5	306.7	408.6	409.0	510.8	511.2
	G2		102.2	102.2	204.3	204.4	306.5	306.7	408.6	408.9	510.8	511.1
	G3		102.2	102.3	204.3	204.6	306.5	306.9	408.6	409.2	510.8	511.6
	G4		102.2	102.3	204.3	204.6	306.5	306.9	408.6	409.1	510.8	511.4

### 2.4.2.5 Results and Discussion

The following results were determined for the G1 type. Fig. 142 shows the stress pattern in a borehole under hydrostatic pressure in the selected depth levels with the depth of failure in the borehole after HOEK & MARTIN (2014) using the UCS mean value of Tab. 30.

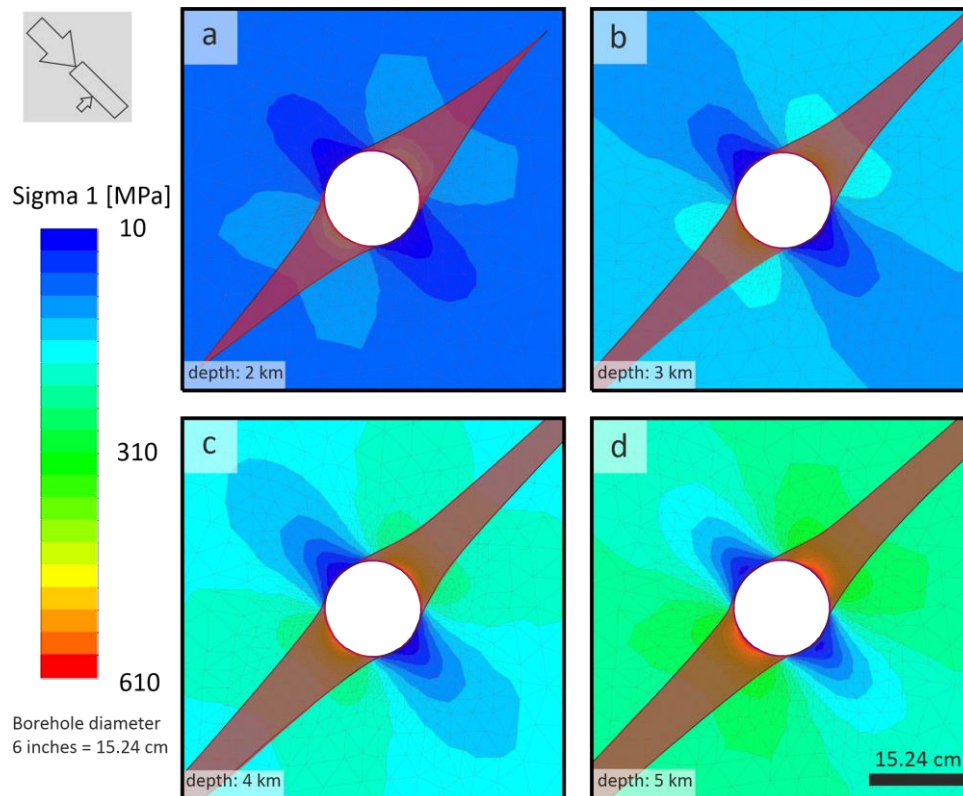


Fig. 142: Stress patterns in a borehole in G1 type, hydrostatic pressure in depths of 2 km (a), 3 km (b), 4 km (c) and 5 km (d) with depth of failure after HOEK & MARTIN (2014), using the UCS mean value.

For the different stages 2–4 the depths of failure with the formula of HOEK & MARTIN (2014) were calculated in the vertical borehole. Since this concept is derived from tunnel projects mainly using data from crystalline rock, this scenario was assigned the term “pessimistic failure criterion”.

Tab. 44 shows the calculated depth of failure for maximum borehole stress from the calculation and from the numerical modelling for the different UCS values for a depth range between 1 km and 5 km. For the mean UCS value, the depth of failure with the maximum modelled borehole stress ranges from 11.6 cm to 89.3 cm in the dry borehole, from 10.2 cm to 82.0 cm in the water saturated borehole, and from 7.4 cm to 68.1 cm for the borehole with a drilling mud. The depth of failure increases with increasing depth. This was calculated for the stages 2 to 4 depending on the depth and the different UCS values. In Fig. 143 (left) the depth of failure is plotted against the drilling depth for the different UCS values.

For the “optimistic failure criterion”, the difference between the maximum wall stress and the UCS (stage 2), the difference between the maximum wall stress and the summary of UCS and pore pressure (stage 3) and the difference between the maximum wall stress and the summary of UCS, pore pressure and mud weight (stage 4) was calculated for each depth. Tab. 45 shows the calculated differential stress from the calculation and from the numerical modelling for the different UCS values for a depth range

between 1 km and 5 km. In Fig. 143 (right) the differential stress is plotted against the drilling depth for the different UCS values.

Tab. 44: Calculated and modelled depth of failure at the respective depth for the G1 type. Marked section indicates a reasonable scenario using the UCS mean value.

G type	UCS	Depth	calc. $d_f$ (dry)	mod. $d_f$ (dry)	calc. $d_f$ (sat.)	mod. $d_f$ (sat.)	calc. $d_f$ (mud)	mod. $d_f$ (mud)
	[MPa]	[km]	[cm]	[cm]	[cm]	[cm]	[cm]	[cm]
G1	73.5	1	26.1	26.1	23.5	23.6	18.7	18.7
		2	59.9	60.0	54.8	54.9	45.2	45.2
		3	93.8	93.9	86.1	86.2	71.7	71.7
		4	127.6	127.8	117.5	117.6	98.1	98.2
		5	161.5	161.7	148.8	148.9	124.6	124.7
	128.3	1	11.6	11.6	10.2	10.2	7.4	7.4
		2	31.0	31.1	28.1	28.1	22.6	22.6
		3	50.4	50.5	46.0	46.1	37.7	37.8
		4	69.8	69.9	64.0	64.0	52.9	53.0
		5	89.2	89.3	81.9	82.0	68.1	68.1
	170.7	1	6.8	6.8	5.7	5.7	3.6	3.6
		2	21.4	21.4	19.2	19.2	15.0	15.0
		3	36.0	36.0	32.7	32.7	26.4	26.5
		4	50.5	50.6	46.1	46.2	37.8	37.9
		5	65.1	65.2	59.6	59.7	49.2	49.3

Tab. 45: Calculated and modelled differential stress at the respective depth for the G1 type. Negative values indicate a stable borehole. Marked section indicates a reasonable scenario using the UCS mean value.

G type	UCS	Depth	calc. $\Delta S$ (dry)	mod. $\Delta S$ (dry)	calc. $\Delta S$ (sat.)	mod. $\Delta S$ (sat.)	calc. $\Delta S$ (mud)	mod. $\Delta S$ (mud)
	[MPa]	[km]	[MPa]	[MPa]	[MPa]	[MPa]	[MPa]	[MPa]
G1	73.5	1	57.1	57.3	47.3	47.4	28.7	28,7
		2	187.7	188.0	168.1	168.3	130.8	131,0
		3	318.3	318.7	288.9	289.3	233.0	233,2
		4	448.9	449.5	409.7	410.2	335.1	335,5
		5	579.5	580.2	530.5	531.1	437.3	437,7
	128.3	1	2.3	2.4	-7.5	-7.4	-26.1	-26,1
		2	132.9	133.2	113.3	113.5	76.0	76,2
		3	263.5	263.9	234.1	234.5	178.2	178,4
		4	394.1	394.7	354.9	355.4	280.3	280,7
		5	524.7	525.4	475.7	476.3	382.5	382,9
	170.7	1	-40.1	-40.0	-49.9	-49.8	-68.5	-68,5
		2	90.5	90.8	70.9	71.1	33.6	33,8
		3	221.1	221.5	191.7	192.1	135.8	136,0
		4	351.7	352.3	312.5	313.0	237.9	238,3
		5	482.3	483.0	433.3	433.9	340.1	340,5

In Fig. 143 only the modelled values are shown since the calculated and modelled values are more or less the same. In the diagrams, on the left side the depth of failure and on the right side the differential stress is plotted versus the drilling depth for the different UCS values.

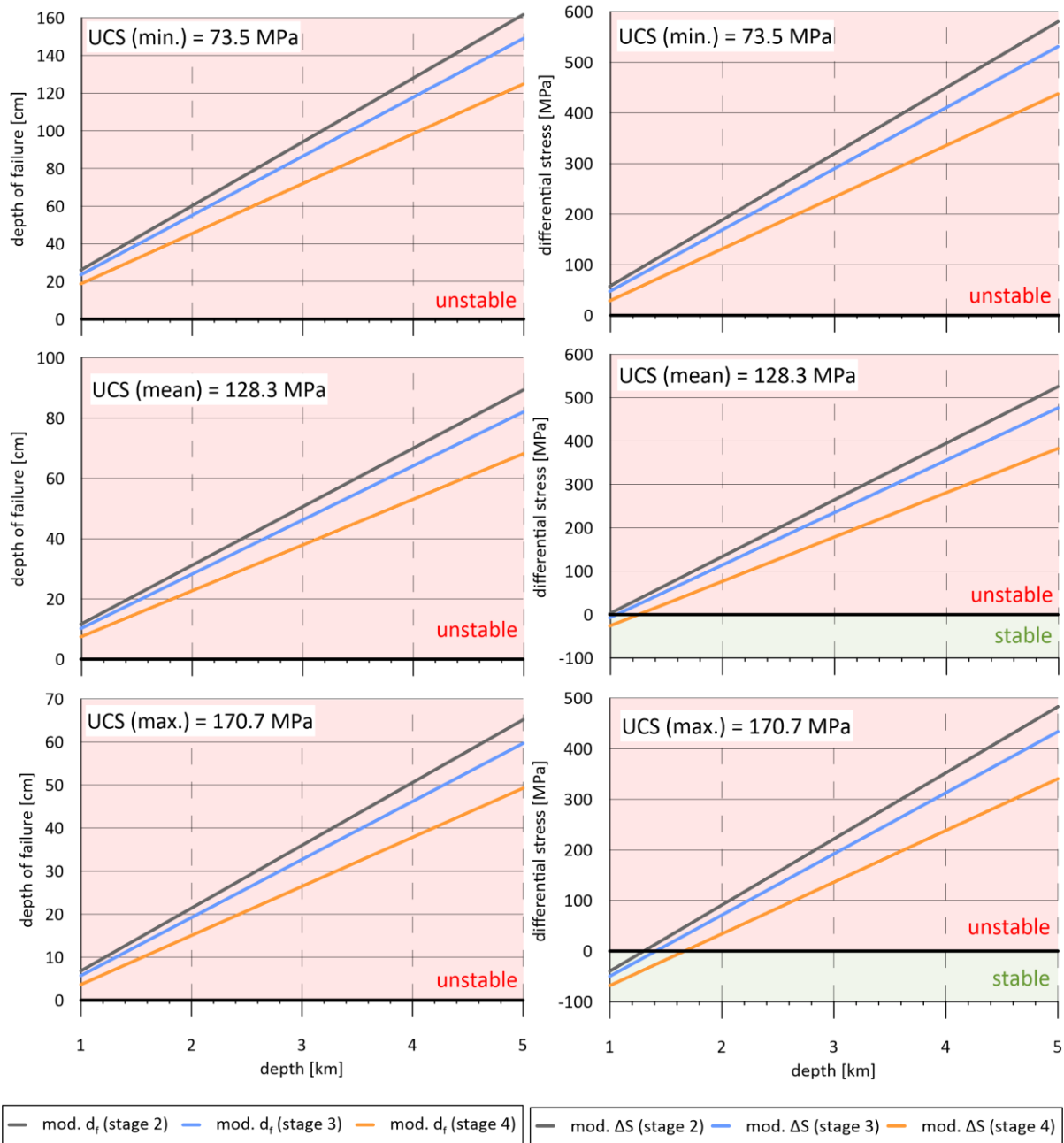


Fig. 143: The depth of failure for the pessimistic failure criterion (left) and the differential stress for the optimistic failure criterion (right) versus depth of the borehole in the G1 type.

For the “pessimistic failure criterion” all UCS values of the G1 type show boreholes which are all unstable (Fig. 143, diagram left). The same results were found for the G2 to G4 types.

For the “optimistic failure criterion” of the UCS min value for all G types, all boreholes are unstable (Fig. 143, top diagram (right)). For the G1 type and mean UCS values the borehole is stable with the selected mud weight up to a depth of 1.3 km. The water saturated borehole is stable to a depth of 1.1 km. The dry borehole is stable to a depth of 1 km (Fig. 143, diagram in the middle). For the G1 type and maximum UCS values the borehole is stable with a mud weight up to a depth of 1.6 km. The water saturated well is stable to a depth of 1.4 km. The dry well is stable to a depth of 1.3 km (Fig. 143, bottom diagram (right)).

The same evaluations were carried out for the G2-, G3- and G4 type. The calculated results are summarised for the G2 type in Tab. 46 and Tab. 47, G3 type in Tab. 48 and Tab. 49 as well as for G4 type in Tab. 50 and Tab. 51.

For the Franconian Basin, the pessimistic failure criterion shows that all boreholes are unstable regardless of the UCS values and the G type. When the optimistic failure criterion is considered, all boreholes are unstable for the minimum UCS values of all G types. For the UCS mean values, G1 type and G2 type show unstable dry and saturated boreholes. The dry wells in G3 type and G4 type are stable down to a depth of 1.2 km and 1.3 km respectively. The saturated boreholes are stable to a depth of 1.3 and 1.4 km respectively. The boreholes with a drilling mud are unstable in G2 type, in G1 type, G3 type and G4 type the borehole stability reaches to a depth of 1.3 km, 1.4 km and 1.5 km respectively. For the UCS max values, the dry and saturated wells are unstable in the G2 type. The borehole with the selected drilling mud weight is stable down to a depth of 1.2 km. With a maximum G1 type UCS value at stage 4, the borehole is stable up to a depth of 1.7 km. The water saturated well is stable up to a depth of 1.5 km. The dry well is stable up to a depth of 1.4 km. At the maximum UCS value for the G3 type, the borehole is stable at stage 4 to a depth of 2.3 km. The water saturated borehole (stage 3) is stable to a depth of 1.8 km, the dry borehole (stage 2) to 1.7 km. For the G4 type and maximum UCS values the borehole is stable with a mud weight up to a depth of 1.8 km. The water saturated well is stable to a depth of 1.6 km. The dry well is stable to a depth of 1.5 km.

The borehole stability is very low for all G types for all UCS values. Therefore a successful drilling in NE Bavaria is hardly possible under the condition that the given values for the stress field are correct. A critical review of the values for the stress field therefore seems reasonable. The depth of failure around the borehole hardly differs between the individual G types when considering the UCS mean values.

Tab. 46: Calculated and modelled depth of failure at the respective depth for the G2 type. Marked section indicates a reasonable scenario using the UCS mean value.

G type	UCS	Depth	calc.	mod.	calc.	mod.	calc.	mod.
	[MPa]		$d_f$ (dry)	$d_f$ (dry)	$d_f$ (sat. )	$d_f$ (sat. )	$d_f$ (mud)	$d_f$ (mud)
		[km]	[cm]	[cm]	[cm]	[cm]	[cm]	[cm]
G2	87.9	1	20.5	20.6	18.4	18.4	14.4	14.4
		2	48.8	48.9	44.6	44.6	36.5	36.5
		3	77.1	77.2	70.8	70.8	58.6	58.7
		4	105.4	105.5	96.9	97.0	80.8	80.8
		5	133.7	133.9	123.1	123.2	102.9	103.0
	105.2	1	15.9	15.9	14.1	14.1	10.7	10.7
		2	39.5	39.6	36.0	36.0	29.2	29.2
		3	63.2	63.2	57.8	57.9	47.7	47.8
		4	86.8	86.9	79.7	79.8	66.2	66.3
		5	110.5	110.6	101.6	101.7	84.7	84.8
	119.5	1	13.0	13.1	11.5	11.5	8.5	8.5
		2	33.9	33.9	30.7	30.8	24.8	24.8
		3	54.7	54.7	50.0	50.0	41.1	41.1
		4	75.5	75.6	69.3	69.3	57.4	57.4
		5	96.3	96.4	88.5	88.6	73.6	73.7

Tab. 47: Calculated and modelled differential stress at the respective depth for the G2 type. Negative values indicate a stable borehole. Marked section indicates a reasonable scenario using the UCS mean value.

G type	UCS	Depth	calc.	mod.	calc.	mod.	calc.	mod.
	[MPa]		$\Delta S$ (dry)	$\Delta S$ (dry)	$\Delta S$ (sat. )	$\Delta S$ (sat. )	$\Delta S$ (mud)	$\Delta S$ (mud)
		[km]	[MPa]	[MPa]	[MPa]	[MPa]	[MPa]	[MPa]
G2	87.9	1	42.7	42.8	32.9	33.0	14.3	14.3
		2	173.3	173.5	153.7	153.9	116.4	116.5
		3	303.9	304.3	274.5	274.8	218.6	218.8
		4	434.5	435.0	395.3	395.7	320.7	321.0
		5	565.1	565.7	516.1	516.6	422.9	423.2
	105.2	1	25.4	25.5	15.6	15.7	-3.0	-3.0
		2	156.0	156.2	136.4	136.6	99.1	99.2
		3	286.6	287.0	257.2	257.5	201.3	201.5
		4	417.2	417.7	378.0	378.4	303.4	303.7
		5	547.8	548.4	498.8	499.3	405.6	405.9
	119.5	1	11.1	11.2	1.3	1.4	-17.3	-17.3
		2	141.7	141.9	122.1	122.3	84.8	84.9
		3	272.3	272.7	242.9	243.2	187.0	187.2
		4	402.9	403.4	363.7	364.1	289.1	289.4
		5	533.5	534.1	484.5	485.0	391.3	391.6

Tab. 48: Calculated and modelled depth of failure at the respective depth for the G3 type. Marked section indicates a reasonable scenario using the UCS mean value.

G type	UCS	Depth	calc. $d_f$ (dry)	mod. $d_f$ (dry)	calc. $d_f$ (sat.)	mod. $d_f$ (sat.)	calc. $d_f$ (mud)	mod. $d_f$ (mud)
	[MPa]	[km]	[cm]	[cm]	[cm]	[cm]	[cm]	[cm]
G3	80.3	1	23.2	23.2	20.9	20.9	16.5	16.5
		2	54.2	54.3	49.5	49.6	40.7	40.8
		3	85.2	85.3	78.2	78.3	64.9	65.0
		4	116.2	116.4	106.9	107.0	89.2	89.3
		5	147.1	147.4	135.5	135.8	113.4	113.6
	142	1	9.7	9.8	8.4	8.5	5.9	6.0
		2	27.3	27.3	24.6	24.7	19.6	19.7
		3	44.8	44.9	40.8	40.9	33.3	33.4
		4	62.3	62.4	57.0	57.2	47.0	47.1
		5	79.8	80.0	73.3	73.4	60.7	60.9
	226.6	1	3.2	3.2	2.4	2.4	0.8	0.8
		2	14.2	14.2	12.5	12.6	9.4	9.4
		3	25.2	25.2	22.7	22.7	18.0	18.0
		4	36.1	36.2	32.8	32.9	26.6	26.6
		5	47.1	47.2	43.0	43.1	35.2	35.2

Tab. 49: Calculated and modelled differential stress at the respective depth for the G3 type. Negative values indicate a stable borehole. Marked section indicates a reasonable scenario using the UCS mean value.

G type	UCS	Depth	calc. $\Delta S$ (dry)	mod. $\Delta S$ (dry)	calc. $\Delta S$ (sat.)	mod. $\Delta S$ (sat.)	calc. $\Delta S$ (mud)	mod. $\Delta S$ (mud)
	[MPa]	[km]	[MPa]	[MPa]	[MPa]	[MPa]	[MPa]	[MPa]
G3	80.3	1	50.3	50.4	40.5	40.7	21.9	22.0
		2	180.9	181.4	161.3	161.7	124.0	124.3
		3	311.5	312.2	282.1	282.7	226.2	226.6
		4	442.1	443.0	402.9	403.7	328.3	328.9
		5	572.7	573.9	523.7	524.7	430.5	431.3
	142	1	-11.4	-11.3	-21.2	-21.0	-39.8	-39.7
		2	119.2	119.7	99.6	100.0	62.3	62.6
		3	249.8	250.5	220.4	221.0	164.5	164.9
		4	380.4	381.3	341.2	342.0	266.6	267.2
		5	511.0	512.2	462.0	463.0	368.8	369.6
	226.6	1	-96.0	-95.9	-105.8	-105.6	-124.4	-124.3
		2	34.6	35.1	15.0	15.4	-22.3	-22.0
		3	165.2	165.9	135.8	136.4	79.9	80.3
		4	295.8	296.7	256.6	257.4	182.0	182.6
		5	426.4	427.6	377.4	378.4	284.2	285.0

Tab. 50: Calculated and modelled depth of failure at the respective depth for the G4 type. Marked section indicates a reasonable scenario using the UCS mean value.

G type	UCS	Depth	calc. d <sub>f</sub> (dry)	mod. d <sub>f</sub> (dry)	calc. d <sub>f</sub> (sat. )	mod. d <sub>f</sub> (sat. )	calc. d <sub>f</sub> (mud)	mod. d <sub>f</sub> (mud)
	[MPa]	[km]	[cm]	[cm]	[cm]	[cm]	[cm]	[cm]
G4	100.7	1	16.9	17.0	15.1	15.1	11.6	11.6
		2	41.6	41.7	37.9	38.0	30.9	30.9
		3	66.3	66.5	60.8	60.9	50.2	50.3
		4	91.1	91.2	83.6	83.8	69.5	69.6
		5	115.8	116.0	106.5	106.7	88.9	89.0
	153	1	8.5	8.5	7.3	7.3	4.9	5.0
		2	24.7	24.8	22.3	22.4	17.7	17.7
		3	41.0	41.1	37.3	37.4	30.4	30.4
		4	57.3	57.4	52.4	52.5	43.1	43.2
		5	73.5	73.7	67.4	67.5	55.8	55.9
	193.4	1	5.1	5.1	4.1	4.1	2.3	2.3
		2	18.0	18.0	16.0	16.1	12.4	12.4
		3	30.8	30.9	27.9	28.0	22.4	22.5
		4	43.7	43.8	39.8	39.9	32.5	32.5
		5	56.5	56.6	51.7	51.8	42.5	42.6

Tab. 51: Calculated and modelled differential stress at the respective depth for the G4 type. Negative values indicate a stable borehole. Marked section indicates a reasonable scenario using the UCS mean value.

G type	UCS	Depth	calc. ΔS (dry)	mod. ΔS (dry)	calc. ΔS (sat. )	mod. ΔS (sat. )	calc. ΔS (mud)	mod. ΔS (mud)
	[MPa]	[km]	[MPa]	[MPa]	[MPa]	[MPa]	[MPa]	[MPa]
G4	100.7	1	29.9	30.0	20.1	20.3	1.5	1.6
		2	160.5	160.9	140.9	141.2	103.6	103.9
		3	291.1	291.7	261.7	262.2	205.8	206.2
		4	421.7	422.5	382.5	383.2	307.9	308.4
		5	552.3	553.3	503.3	504.2	410.1	410.7
	153	1	-22.4	-22.3	-32.2	-32.0	-50.8	-22.4
		2	108.2	108.6	88.6	88.9	51.3	108.2
		3	238.8	239.4	209.4	209.9	153.5	238.8
		4	369.4	370.2	330.2	330.9	255.6	369.4
		5	500.0	501.0	451.0	451.9	357.8	500.0
	193.4	1	-62.8	-62.7	-72.6	-72.4	-91.2	-91,1
		2	67.8	68.2	48.2	48.5	10.9	11,2
		3	198.4	199.0	169.0	169.5	113.1	113,5
		4	329.0	329.8	289.8	290.5	215.2	215,7
		5	459.6	460.6	410.6	411.5	317.4	318,0

### 3 Summary

In this work, the rocks in the two areas that are important for geothermal energy in Bavaria are geo-mechanically characterized and with the obtained data a numerical borehole stability modelling was carried out with RS2 (©Rocsience).

The two selected areas are the North Alpine Foreland Basin, SE Germany in the area around Munich and the Franconian Basin in NE Bavaria. For the North Alpine Foreland Basin, SE Germany, drilled core samples were analysed. In NE Bavaria, analogue samples from the Fichtelgebirge, which are considered the closest analogue material for the rocks below the Franconian Basin, were examined.

The samples were tested non-destructively as well as destructively and the wells/borehole and outcrops were described individually. In addition, the testing results for the respective reservoir are summarised. The testing results of the Upper Jurassic aquifer are classified according to their stratigraphy, lithology and facies. The testing results of the granites from the Fichtelgebirge are classified according to their age of intrusion (G types) and their orientation.

For both the North Alpine Foreland Basin, SE Germany and NE Bavaria, it was demonstrated that a correlation existed between the vertical  $v_p$ -velocity and the  $v_s$ -velocity for the differently saturated samples. Further correlations could not be found for static and dynamic test results. No further conclusions can be drawn from these results.

For the North Alpine Foreland Basin, SE Germany a comparison of the various parameters with the uniaxial compressive strength shows several trends. The UCS values showed a higher strength for core samples with higher  $v_p$ -velocities. The porosity decreases with increasing uniaxial compressive strength. The bulk density showed the same trend as the porosity, only in reverse. For UCS values in the range between 50 MPa and 100 MPa the measured values of the correlated parameters fluctuate over an extremely wide range from the respective minimum to the maximum values. The brittleness of the examined core samples ranges in the typical brittle range of carbonates. The summarised results were correlated with stratigraphy, lithology and facies of the core samples.

In correlation with the stratigraphy the following trends can be seen for most non-destructive laboratory tests. Dogger has low mean values and from Malm Alpha to Malm Zeta 2 a plateau appears. From Malm Zeta 2 to Malm Zeta 4–5 a decrease in the values is observed. The values for Purbeck are higher than the values for Malm Zeta 4–5. For the  $v_p/v_s$  ratio and for the dynamic Poisson's ratio no tendencies can be seen. In Malm Alpha to Gamma the highest UCS values are found. No trend can be observed but the BTS values of nearly all samples are below 15 MPa. The values for the static Young's Modulus and the V-Modulus scatter in all stratigraphic units. The dispersion of the static Poisson's ratio values decreases with increasing depth. The abrasivity of all rocks investigated falls into the medium to abrasive category.

In correlation with the lithology the following trends can be seen for most non-destructive laboratory tests. The dynamic values increase from dolomitic limestone via limestone to dolostone. In the dynamic Poisson's ratio, no differences between the different lithologies were found. Based on the uniaxial compressive strength the core samples can be classified as hard to very hard. From limestone via

dolomitic limestone to dolostone the mean BTS values increase. The mean values of the static Young's Modulus and V-Modulus increase from dolomitic limestone, to limestone to dolostone. The dolostone has the highest abrasivity values of all lithologies. The results from analogue samples of the state of the art with the drill cores examined in this work showed clear agreement. This confirms that analogue samples can be used for an initial analysis of the suitability of a drill site.

In terms of the facies, the following trends can be seen for most non-destructive laboratory tests. For the facies in each lithology, the values decrease with the increasing particle size. For the  $v_p/v_s$  ratio and for the dynamic Poisson's ratio no trends can be seen. The UCS values decrease with increasing particle size. This trend is evident in both, limestone and dolostone lithologies. The BTS values decrease among limestone facies types as particle size decreases. This tendency is not visible for the facies types in the other lithologies. There is no noticeable difference between the measured mean values of the static Young's Modulus and the V-Modulus. The dolostones with different crystal sizes have a similar static Poisson's ratio. The interquartile range (IQR) ranges from 0.05 to 0.22. These values may be used as characteristic values for the dolostones. No trend in the static Poisson's ratio can be identified for the different types of facies of dolomitic limestone and limestone. The abrasivity of the different facies types of the limestone does not show a tendency. The dolomitic limestone shows a decrease of the CAI value with decreasing fineness of the facies types. The highest CAI values are found in the dolostones.

The different stratigraphic units do not show different results and it is not possible to identify the stratigraphy of a sample based on the results of the laboratory investigations. No directional correlation of the parameters examined over the different lithologies is found. For the facies in each lithology, most of the values decrease with the increasing particle size.

For NE Bavaria a comparison of the various parameters with the uniaxial compressive strength did not lead to further correlations. The brittleness of the examined samples ranges from tough to very tough.

The summarised results were correlated with granite intrusion phase (G types) and the orientation of the analogue samples. The  $v_p$ - &  $v_s$  values as well as the dynamic Young's Modulus for G1 and G3 are higher than the  $v_p$ - &  $v_s$  values for G2 and G4. The values for the dry and saturated dynamic Poisson's ratio do not differ between the G types. The values for the dry dynamic Poisson's ratio are essentially between 0.2 and 0.3. The values for the saturated dynamic Poisson's ratio are mostly between 0.34 and 0.4.

The values of uniaxial compressive strength for all analogue samples range between 75 MPa and 195 MPa. The granites can therefore be classified as having high to very high strength. The values of the Brazilian tensile test are between 4.5 and 13.5 MPa. The static Young's Modulus values for G1 and G3 are higher than the static Young's Modulus values for G2 and G4. The interquartile range (IQR) of the static Young's Modulus spans from 38 MPa to 55 MPa. The IQR of the V-Modulus ranges from 25 MPa to 41 MPa. The static Poisson's ratio is on average between 0.1 and 0.15 and has an IQR from 0.09 to 0.21. The above cited values may be used as characteristic values for further investigations.

The CAI values are classified as highly abrasive or predominantly extremely abrasive. The abrasiveness increases with the decreasing age of the granites. The LAC values show that the granites can be classified as highly abrasive or predominantly extremely abrasive. These values show that high drilling costs are to be expected due to high abrasion. The LBC values show no trend and can be classified as medium poor to medium high. The breakability varies over a broad range within and between the G types. The different phases of granite intrusion do not show different results and therefore the granites of the analogue samples are homogeneous.

The determined key parameters from the two areas served as input parameters for an initial numerical modelling with the finite element code RS2 (©Rocsience). For both locations a stress distribution in the near-field of the borehole was determined. The depth of failure around the borehole was also determined with the formula after Martin (HOEK & MARTIN 2014).

The modelling was divided into 4 stages. Stage 1 considers the stress field before drilling begins. In stage 2 the dry borehole was considered after the drilling process. For stage 3 the water saturated borehole and for stage 4 the borehole with a maximum mud weight of  $1.9 \text{ g/cm}^3$  was considered.

For stage 1 it is noticeable that, in addition to the different stress regimes and direction of the maximum horizontal stress that prevail in the two areas, completely different maximum and minimum horizontal stresses exist in the underground. It is noticeable that in NE Bavaria, larger differences in the in situ stresses are present than in the North Alpine Foreland Basin, SE Germany. The maximum horizontal stresses in the North Alpine Foreland Basin, SE Germany, are only half as high as in NE Bavaria. However, the minimum horizontal stresses in the North Alpine Foreland Basin, SE Germany are two and a half times as large as in NE Bavaria.

For the North Alpine Foreland Basin, SE Germany, the pessimistic failure criterion for all minimum UCS values of all lithologies shows a large depth of failure around the borehole and all boreholes are unstable at all depths. For all mean UCS values a borehole stability of up to 1.5 km is shown for boreholes with the selected drilling mud weight. The remaining boreholes are unstable for this UCS value. For the maximum UCS values a borehole stability of 1.5 km to 4.3 km is found.

When considering the optimistic failure criterion, the minimum UCS values of limestone and dolostone show that all boreholes are unstable. For dolomitic limestone, a borehole stability is shown to a depth of 1.8 km. For the mean UCS values it is shown for all lithologies that the dry boreholes are stable down to a depth of 2 km, the water saturated boreholes are stable down to a depth of 2.3 km and the wells with the selected drilling mud weight are stable down to a depth of 4 km. Considering the optimistic fracture criterion, the maximum UCS values of limestone and dolostone show that all boreholes are stable.

For NE Bavaria it was shown that the borehole stability is very low for all G types for all UCS values. Therefore, provided that the values for the stress field are correct, a successful drilling in NE Bavaria is hardly possible. Therefore, a critical review of the values for the stress field seems to be inevitable.

This work was the first to determine geomechanical parameter ranges using drill cores. Such data are of uttermost importance for the reservoir analysis (TAVAKOLI 2018) as can be seen in the section 2.4. of the numerical modelling. The obtained parameter ranges can be used in the future to check existing

geomechanical models and are basic for new geomechanical models concerning borehole stability and fracture propagation around boreholes. Thus, they provide a more precise knowledge of the sedimentary and crystalline reservoirs and a more effective use of geothermal energy in Bavaria.

## 4 Outlook

Future investigations on the geomechanical characterization of reservoirs in Bavaria will be facilitated by the values of the parameter study of this thesis. Likewise, the determined values and the conclusions drawn should be integrated into existing geomechanical models, thereby allowing new conclusions about the reservoir to be drawn.

If further samples from former drilled oil/gas wells should become accessible, they should be investigated in the same way as in this thesis to better characterize the heterogeneous Upper Jurassic aquifer. In order to gain a better geomechanical understanding of the entire basin, the additional earlier cored oil/gas wells distributed over the entire North Alpine Foreland Basin, SE Germany, should be investigated. The main focus of the investigations of earlier oil/gas wells should be at the greater Munich area, if possible, since this region will be the main focus of geothermal energy use in the near future.

The situation is different in the subsurface of NE Bavaria, which has not been a subject of much exploration so far. At the moment there are still large data gaps in the different rock and stress properties of the underground. These form an obstacle to the first geothermal exploration in this area. In order to close the data gap further, a possibility would have to be created to further geomechanically characterize the area. This could be done by releasing the few cores which are available from exploratory wells and by providing the possibility to create an underground laboratory in this area. The drill cores, even if they are not granites from the underground would allow this area to be covered with geomechanical data from the subsurface for the first time.

After the evaluation of the seismic campaign carried out in NE Bavaria, the  $v_p$ - and  $v_s$ -velocity values from the ultrasonic measurements determined in this thesis could be used for the purpose of comparison. The correlations determined between the non-destructive and destructive laboratory tests, may help to better characterize and understand the geothermal anomaly. If the geothermal energy in NE Bavaria is to be further explored, a test borehole would be highly desirable.

To verify the results of known analogue samples, it may be helpful to compare these results with the results obtained from the core samples in this work.

Likewise, the collected core samples as well as analogue samples are to be geomechanically examined in triaxial tests and a 3D fracture model should be created. The already gained abrasivity database determined in this study should be extended and should also cover the overburden rock types.

In summary, it can be said that geothermal energy projects are still associated with risks due to the complexity of the subsurface and the technical/economic uncertainties resulting therefrom. The investigations carried out in the course of this work tried to provide important data for the reduction of those risks.

## References

- AGEMAR, T., ALTEN, J.-A., GANZ, B., KUDER, J., KÜHNE, K., SCHUMACHER, S. & SCHULZ, R. (2014a): The Geothermal Information System for Germany – GeotIS. – *Zeitschrift der Deutschen Gesellschaft für Geowissenschaften*, 165 (2): pp. 129–144.
- AGEMAR, T., SCHELLSCHMIDT, R. & SCHULZ, R. (2012): Subsurface temperature distribution in Germany. – *Geothermics*, 44: pp. 65–77.
- AGEMAR, T., SUCHI, E. & MOECK, I. (2018): Die Rolle der tiefen Geothermie bei der Wärmewende. – 14 p., [https://www.leibniz-liag.de/fileadmin/user\\_upload/s4/downloads/positionspapier\\_waermewende.pdf](https://www.leibniz-liag.de/fileadmin/user_upload/s4/downloads/positionspapier_waermewende.pdf) (last access on July 09, 2020).
- AGEMAR, T., WEBER, J. & SCHULZ, R. (2014b): Deep Geothermal Energy Production in Germany. – *Energies*, 7 (7): pp. 4397–4416.
- ALBER, M., BACKERS, T., HEDTMANN, N., SYMANK, A.-I., GALLAS, J., MATTHES, L. & MEIER, T. (2019): Entwicklung eines Werkzeuges zur Steigerung der Zuverlässigkeit der Vorhersage permeabler Bereiche in geothermischen Systemen: Akronym: PrognosPermae: Abschlussbericht zum Verbundprojekt: Bearbeitungszeitraum: 01.11.2015 bis 31.03.2019. – 93 p., <https://www.tib.eu/de/suchen/id/TIBKAT:1688047344/> (last access on July 09, 2020).
- ALBER, M., YARALI, O., DAHL, F., BRULAND, A., KÄSLING, H., MICHALAKOPOULOS, T. N., CARDU, M., HAGAN, P., AYDIN, H. & ÖZARSLAN, A. (2014): ISRM Suggested Method for Determining the Abrasivity of Rock by the CERCHAR Abrasivity Test. – *Rock Mech Rock Eng*, 47 (1): pp. 261–266.
- American Petroleum Institute (1998): Recommended Practices for Core Analysis: recommended practice 40. – 236 p., <http://w3.energistics.org/RP40/rp40.pdf> (last access on July 09, 2020).
- AMRO, M., ARAB, A., BAISCH, S., BEMS, C., BLASCHEK, P., BLÖCHER, G., HÄFNER, F., HILD, S., JOSWIG, M., KAULISKY, A., KLAPPERICH, H., KREUTER, H., MERKEL, B., MOECK, I., SCHRAGE, C., STEIGER, T. & UHLIG, S. (2014): Forschungsprojekt “Geothermie Allgäu 2.0”. – *bbr - Fachmagazin für Brunnen- und Leitungsbau*, Sonderheft Geothermie: pp. 74–79.
- ANDERSON, E. M. (1951): *The Dynamic of Faulting and Dyke Formation with Application to Britain*. – 2nd ed., 206 p., Edinburgh (Oliver and Boyd).
- ANOVITZ, L. M. & COLE, D. R. (2015): Characterization and Analysis of Porosity and Pore Structures. – *Reviews in Mineralogy and Geochemistry*, 80 (1): pp. 61–164.
- ASTM D4543-19: (2019): *Practices for Preparing Rock Core as Cylindrical Test Specimens and Verifying Conformance to Dimensional and Shape Tolerances*. – West Conshohocken, PA (ASTM International).
- BACHMANN, G. H., KOCH, K., MUELLER, M. & WEGGEN, K. (1981): Ergebnisse und Erfahrungen bei der Exploration in den bayerischen Alpen. – *Erdoel-Erdgas-Zeitschrift*, 97: pp. 127–133.
- BACHMANN, G. H. & MÜLLER, M. (1996): Die Entwicklung des süddeutschen Molassebeckens seit dem Variszikum: Eine Einführung. – *Zeitschrift für Geologische Wissenschaften*, 24: pp. 3–20.

- BACHMANN, G. H., MÜLLER, M. & WEGGEN, K. (1987): Evolution of the Molasse Basin (Germany, Switzerland). – *Tectonophysics*, 137: pp. 77–92.
- BACKERS, T., MEIER, T., GIPPER, P., MUNSCHE, P., BÜCKEN, D. & NOKAR, K. (2017): Abschlussbericht zum Teilprojekt B: Struktur- und Spannungsfeld im Verbundprojekt MAFA: Parametrisierung von Fazies, Diagenese, Struktur- und Spannungsfeld sowie Optimierung der Testabläufe im Malm zur Verringerung des Erfolgsrisikos. – 44 p., <https://www.tib.eu/de/suchen/id/TIBKAT:1010051989/> (last access on July 09, 2020).
- BARTON, C. A., ZOBACK, M. D. & MOOS, D. (1995): Fluid flow along potentially active faults in crystalline rock. – *Geology*, 23 (8): pp. 683–686.
- BAUER, M., FREEDEN, W., JACOBI, H. & NEU, T. (2014): *Handbuch Tiefe Geothermie*. – 867 p., Berlin, Heidelberg (Springer).
- BAUER, W. (2000): Geothermische Verhältnisse des Fränkischen Beckens. – Ph.D.-thesis, Forschungsergebnisse aus dem Bereich Hydrogeologie und Umwelt (22), Universität Würzburg, 186 p., Würzburg.
- BEICHEL, K., KOCH, R. & WOLFGRAMM, M. (2014): Die Analyse von Spülproben zur Lokalisierung von Zuflusszonen in Geothermiebohrungen. Beispiel der Bohrungen Gt Unterhaching 1/1a und 2. (Süddeutschland, Molassebecken, Malm). – *Geologische Blätter für Nordost-Bayern*, 64: pp. 43–65.
- BERTANI, R. (2016): Geothermal power generation in the world 2010–2014 update report. – *Geothermics*, 60: pp. 31–43.
- BIRNER, J. (2013): Hydrogeologisches Modell des Malmaquifers im Süddeutschen Molassebecken. – Ph.D.-thesis, Institute of Geological Sciences, Free University of Berlin, 86 p., Berlin.
- BIRNER, J., FRITZER, T., JODOCY, M., SAVVATIS, A., SCHNEIDER, M. & STOBER, I. (2012): Hydraulische Eigenschaften des Malmaquifers im Süddeutschen Molassebecken und ihre Bedeutung für die geothermische Erschließung. – *Zeitschrift für Geologische Wissenschaften*, 40 (2-3): pp. 133–156.
- BMU (2007): *Tiefe Geothermie in Deutschland*. – 44 p., [https://www.mags-projekt.de/MAGS/DE/Downloads/BMU\\_TiefeGeothermie.pdf%3F\\_\\_blob%3DpublicationFile%26v%3D1](https://www.mags-projekt.de/MAGS/DE/Downloads/BMU_TiefeGeothermie.pdf%3F__blob%3DpublicationFile%26v%3D1) (last access on July 09, 2020).
- BÖHM, F. (2012): Die Lithofazies des Malm im Großraum München und deren Einfluss auf die tiefegeothermische Nutzung. – Ph.D.-thesis, Institute of Geological Sciences, Free University of Berlin, 148 p., Berlin.
- BÖHM, F., BIRNER, J., STEINER, U., KOCH, R., SOBOTT, R., SCHNEIDER, M. & WANG, A. (2011): Tafelbankiger Dolomit in der Kernbohrung Moosburg SC4: Ein Schlüssel zum Verständnis der Zuflussraten in Geothermiebohrungen (Östliches Molassebecken, Malm Delta-Zeta Süddeutschland). – *Zeitschrift für Geologische Wissenschaften*, 39: pp. 117–157.
- BÖHM, F., KOCH, R., HÖFERLE, R. & BAASCH, R. (2010): Der Malm in der Geothermiebohrung Pullach Th2 – Faziesanalyse aus Spülproben (München, S-Deutschland). – *Geologische Blätter für Nordost-Bayern*, 60 (1-4): pp. 17-49.

- BÖHM, F., SAVVATIS, A., STEINER, U., SCHNEIDER, M. & KOCH, R. (2013): Lithofazielle Reservoircharakterisierung zur geothermischen Nutzung des Malm im Großraum München. – *Grundwasser*, 18 (1): pp. 3–13.
- BOHNSACK, D., POTTEN, M., KÄSLING, H., THURO, K. & ZOSEDER, K. (2019): Geomechanical investigation of a geothermal aquifer in the South German Molasse Basin. – In: DA FONTOURA, S. A., ROCCA, R. J. & MENDOZA, J. P. (Eds.): *Proceedings of the 14th International Congress on Rock Mechanics and Rock Engineering (ISRM 2019)*, September 13-18, 2019, Foz do Iguassu, Brazil, *Proceedings in Earth and Geosciences*: pp. 3136–3143, Boca Raton (CRC Press).
- BOHNSACK, D., POTTEN, M., PFRANG, D., WOLPERT, P. & ZOSEDER, K. (2020): Porosity–permeability relationship derived from Upper Jurassic carbonate rock cores to assess the regional hydraulic matrix properties of the Malm reservoir in the South German Molasse Basin. – *Geothermal Energy*, 8, 12: pp. 1–47.
- BRAUNER, H.-J. & HOSE, K. (2019): Information about access to data of the German Oil and Gas Industry at LBEG-Hannover. – 23 p., [https://www.lbeg.niedersachsen.de/download/1392/information\\_about\\_access\\_to\\_data\\_of\\_the\\_German\\_Oil\\_and\\_Gas\\_Industry\\_at\\_LBEG-Hannover.pdf](https://www.lbeg.niedersachsen.de/download/1392/information_about_access_to_data_of_the_German_Oil_and_Gas_Industry_at_LBEG-Hannover.pdf) (last access on July 09, 2020).
- BROOK, N. (1993): The measurement and estimation of basic rock strength. – In: HUDSON, J. A. (Ed.): *Comprehensive Rock Engineering*: pp. 41–66, Oxford, New York, Seoul, Tokyo (Pergamon Press).
- BÜCHI, E., MATHIER, J. F. & WYSS, C. (1995): Gesteinsabrasivität - ein bedeutender Kostenfaktor beim mechanischen Abbau von Fest- und Lockergestein. – *Tunnel*, 5: pp. 38–43.
- BUDACH, I., MOECK, I., LÜSCHEN, E. & WOLFGGRAMM, M. (2018): Temporal evolution of fault systems in the Upper Jurassic of the Central German Molasse Basin: case study Unterhaching. – *International Journal of Earth Sciences*, 107 (2): pp. 635–653.
- CACACE, M., BLÖCHER, G., WATANABE, N., MOECK, I., BÖRSING, N., SCHECK-WENDEROTH, M., KOLDITZ, O. & HUENGES, E. (2013): Modelling of fractured carbonate reservoirs: outline of a novel technique via a case study from the Molasse Basin, southern Bavaria, Germany. – *Environmental Earth Sciences*, 70: pp. 3585–3602.
- CARMICHAEL, R. S. (1982): *Handbook of Physical Properties of Rocks*. – 1st ed., 414 p., Boca Raton (CRC Press).
- Cerchar (1986): The Cerchar Abrasiveness Index. – pp. 1–12, Verneuil.
- CHANG, C., ZOBACK, M. D. & KHAKSAR, A. (2006): Empirical relations between rock strength and physical properties in sedimentary rocks. – *Journal of Petroleum Science and Engineering*, 51 (3-4): pp. 223–237.
- COHEN, K. M., FINNEY, S. C., GIBBARD, P. L. & FAN, J.-X. (2013; updated): The ICS International Chronostratigraphic Chart. – pp. 199-204, <http://www.stratigraphy.org/ICSchart/ChronostratChart2020-01.pdf> (last access on July 09, 2020).

- DE WALL, H., SCHAARSCHMIDT, A., KÄMMLEIN, M., GABRIEL, G., BESTMANN, M. & SCHARFENBERG, L. (2019): Subsurface granites in the Franconian Basin as the source of enhanced geothermal gradients: a key study from gravity and thermal modeling of the Bayreuth Granite. – *International Journal of Earth Sciences*, 108 (6): pp. 1913–1936.
- DGGT (2004): Einaxiale Druckversuche an zylindrischen Gesteinsprüfkörpern. Neufassung der Empfehlung Nr. 1 des Arbeitskreises “Versuchstechnik Fels” der Deutschen Gesellschaft für Geotechnik e. V. – *Bautechnik*, 81 (10): pp. 825–834.
- DGGT (2008): Indirekter Zugversuch an Gesteinsproben - Spaltzugversuch. Empfehlung Nr. 10 des Arbeitskreises 3.3 “Versuchstechnik Fels” der Deutschen Gesellschaft für Geotechnik e. V. – *Bautechnik*, 85 (9): pp. 623–627.
- DGGT (2010): Punktlastversuche an Gesteinsproben. Empfehlung Nr. 5 des Arbeitskreises 3.3 “Versuchstechnik Fels” der Deutschen Gesellschaft für Geotechnik e. V. – *Bautechnik*, 87 (6): pp. 322–330.
- DGGT (2016): Bestimmung der Abrasivität von Gesteinen mit dem CERCHAR-Versuch. Empfehlung Nr. 23 des Arbeitskreises 3.3 “Versuchstechnik Fels” der Deutschen Gesellschaft für Geotechnik e. V. – *Bautechnik*, 93 (6): pp. 409–415.
- DIETL, C., KÄMMLEIN, M., DREWS, M., STOLLHOFEN, H., JAHNS, E., BAUMGARTNER, H. & DE WALL, H. (2017): Rock physics as a key for the productivity of geothermal reservoirs. – *Der Geothermiekongress 2017*, 12. - 14. September 2017, Munich: pp. 1–10.
- DILL, H. G. (2015): *The Hagendorf-Pleystein Province: the Center of Pegmatites in an Ensialic Orogen.* – 1st ed., 475 p., Cham (Springer).
- DIN 51220 (2003): *Werkstoffprüfmaschinen - Allgemeines zu Anforderungen an Werkstoffprüfmaschinen und zu deren Prüfung und Kalibrierung.* – Berlin (Beuth).
- DIN EN 12504-4 (2004): *Prüfung von Beton in Bauwerken - Teil 4: Bestimmung der Ultraschallgeschwindigkeit.* – Berlin (Beuth).
- DIN EN 14146 (2004-06): *Prüfverfahren für Naturstein - Bestimmung des dynamischen Elastizitätsmoduls (durch Messung der Resonanzfrequenz der Grundschiwingung).* – Berlin (Beuth).
- DIN EN ISO 7500-1 (2018): *Metallische Werkstoffe - Kalibrierung und Überprüfung von statischen einachsigen Prüfmaschinen - Teil 1 Zug und Druckprüfmaschinen - Kalibrierung und Überprüfung der Kraftmessrichtung.* – Berlin (Beuth).
- DOPPLER, G., GLASER, S. & SCHWERD, K. (2004): *GeoBavaria - 600 Millionen Jahre Bayern.* – 92 p., Munich (Bayerisches Geologisches Landesamt).
- DREWS, M., BAUER, W., FAZLIKHANI, H., EBERTS, A., POTTEN, M., DE WALL, H., THURO, K. & STOLLHOFEN, H. (2019a): *PetroTherm (GAB): Towards a regional geomechanical model of the Franconian Basin, SE Germany.* – *Der Geothermiekongress 2019*, 19. - 21. November 2019, Munich: pp. 1.
- DREWS, M., BAUER, W., FAZLIKHANI, H., STOLLHOFEN, H., KÄMMLEIN, M., POTTEN, M., THURO, K. & DE WALL, H. (2019b): *Ursachenforschung zur geothermischen Anomalie in Nordbayern.* – *Geothermische Energie*, 91: pp. 10–13.

- DREWS, M. C., BAUER, W., CARACCILO, L. & STOLLHOFEN, H. (2018): Disequilibrium compaction overpressure in shales of the Bavarian Foreland Molasse Basin: Results and geographical distribution from velocity-based analyses. – *Marine and Petroleum Geology*, 92: pp. 37–50.
- DREWS, M. C., BAUER, W., CARACCILO, L. & STOLLHOFEN, H. (2020): Corrigendum to “Disequilibrium compaction overpressure in shales of the Bavarian Foreland Molasse Basin: Results and geographical distribution from velocity-based analyses” [*Mar. Pet. Geol.* 92 (2018) 37–50]. – *Marine and Petroleum Geology*, 92: pp. 37–50.
- DREWS, M. C., SEITHEL, R., SAVVATIS, A., KOHL, T. & STOLLHOFEN, H. (2019c): A normal-faulting stress regime in the Bavarian Foreland Molasse Basin? New evidence from detailed analysis of leak-off and formation integrity tests in the greater Munich area, SE-Germany. – *Tectonophysics*, 755: pp. 1–9.
- DREXL, C. (2018): Geotechnical parameters of granites from the Fichtelgebirge mountain range. – Bachelorthesis (unpublished), Chair of Engineering Geology, Technical University of Munich, 79 p., Munich.
- DUNHAM, R. J. (1978): Classification of Carbonate Rocks According to Depositional Textures. – In: HAM, W. E. (Ed.): *Classification of carbonate rocks: a symposium*: pp. 108–121, Tulsa.
- DUSSEL, M., LÜSCHEN, E., THOMAS, R., AGEMAR, T., FRITZER, T., SIEBLITZ, S., HUBER, B., BIRNER, J. & SCHULZ, R. (2016): Forecast for thermal water use from Upper Jurassic carbonates in the Munich region (South German Molasse Basin). – *Geothermics*, 60: pp. 13–30.
- EDEL, J. B. & WEBER, K. (1995): Cadomian terranes, wrench faulting and thrusting in the central Europe Variscides: geophysical and geological evidence. – *Geologische Rundschau*, 84 (2): pp. 412–432.
- FALTENHAUSER, M. (2018): Zahlen und Fakten zur Stromversorgung in Deutschland. – 24 p., [https://www.wbu.de/media/news/positionen/publikationen/2018-08-02\\_wirtschaftsbeirat-bayern\\_strom.pdf](https://www.wbu.de/media/news/positionen/publikationen/2018-08-02_wirtschaftsbeirat-bayern_strom.pdf) (last access on July 09, 2020).
- FARQUHAR, R. A., SOMERVILLE, J. M. & SMART, B.G.D. (1994): Porosity as a Geomechanical Indicator: An Application of Core and Log Data and Rock Mechanics. – *European Petroleum Conference*, London, 25 October 1994: pp. 481–489, London (Society of Petroleum Engineers).
- FINGER, F., ROBERTS, M. P., HAUNSCHMID, B., SCHERMAIER, A. & STEYRER, H. P. (1997): Variscan granitoids of central Europe: their typology, potential sources and tectonothermal relations. – *Mineralogy and Petrology*, 61: pp. 67–96.
- FJÆR, E., HOLT, R. M. & RAAEN, A. M. (2008): *Petroleum Related Rock Mechanics*. – 2nd ed., *Developments in petroleum science*, 53: 514 p., Amsterdam (Elsevier Science).
- FLECHTNER, F. (2018): Tiefengeothermie-Forschung an der TU München. – 7 p., [https://www.geothermie.de/fileadmin/user\\_upload/Aktuelles/Presse/Pressemappe/Muenchen\\_2018/PPT\\_Ferdinand\\_Flechtner\\_-\\_Tiefengeothermie-Forschung\\_an\\_der\\_TU\\_Muenchen.pdf](https://www.geothermie.de/fileadmin/user_upload/Aktuelles/Presse/Pressemappe/Muenchen_2018/PPT_Ferdinand_Flechtner_-_Tiefengeothermie-Forschung_an_der_TU_Muenchen.pdf) (last access on July 09, 2020).
- FLÜGEL, E. & MUNNECKE, A. (2010): *Microfacies of Carbonate Rocks*. – 2nd ed., 984 p., Berlin, Heidelberg (Springer).

- FOLK, R. L. (1974): Petrology of sedimentary rocks. – 170 p., Austin (Hemphill Pub. Co).
- FÖRSTER, H.-J., RHEDE, D. & HECHT, L. (2008): Chemical composition of radioactive accessory minerals: implications for the evolution, alteration, age, and uranium fertility of the Fichtelgebirge granites (NE Bavaria, Germany). – *Neues Jahrbuch für Mineralogie - Abhandlungen*, 185 (2): pp. 161–182.
- FRANKE, W. (2006): The Variscan orogen in Central Europe: construction and collapse. – *Geological Society, London, Memoirs*, 32 (1): pp. 333–343.
- FREUDENBERGER, W. & SCHWERD, K. (1996): Erläuterungen zur Geologischen Karte von Bayern, 1:500 000. – 4th ed., 329 p., München (Bayerisches Geologisches Landesamt).
- GARDNER, G. H., GARDNER, L. W. & GREGORY, A. R. (1974): Formation velocity and density; the diagnostic basics for stratigraphic traps. – *Geophysics*, 39 (6): pp. 770–780.
- GASSMANN, F. (1951): Über die Elastizität poröser Medien. – *Vierteljahrsschrift der Naturforschenden Gesellschaft in Zürich*, 96 (1): pp. 1–23.
- GEBRANDE, H., KERN, H. & RUMMEL, F. (1982): Elasticity and inelasticity. – In: HELLWEGE, K.-H. (Ed.): *Landolt-Börnstein Numerical Data and Functional Relationships in Science and Technology, New Series: Group V. Geophysics and Space Research*, 1(b): pp. 1–233, Berlin; Heidelberg; New York (Springer).
- GOEMAN, U. E. (1972): Mineralbestand und petrographische Kennzeichnung der dem variskischen Fichtelgebirgsgranit vorgelagerten Granitstücke Reut bei Gefrees, Waldstein (mit Epprechtstein) und Kornberg. – *Tschermaks Mineralogische und Petrographische Mitteilungen*, 18 (3): pp. 243–272.
- GRIMM, W.-D. (1990): *Bildatlas wichtiger Denkmalgesteine der Bundesrepublik Deutschland*. – 1st ed., 250 p., München (Bayerisches Landesamt für Denkmalpflege).
- GUDDEN, H. (1973): Die Thermalwasser-Erschließungsbohrung Rodach 1/1972. – *Geologica Bavarica*, 67: pp. 80–118.
- GUDDEN, H. (1977): Die Thermal-Mineralwasser-Erschließungsbohrung Staffelstein 1975. – *bbr*, 28: pp. 85–92.
- GUDDEN, H. (1981): Über Thermal-Mineralwasser-Bohrungen im Coburger Umland. – *Jahresberichte und Mitteilungen des Oberrheinischen Geologischen Vereins*, 63: pp. 229–252.
- GUDDEN, H. (1983): Über Nutzungsmöglichkeiten von Erdwärme in Bayern. – *Geologische Jahresberichte*, C (33): pp. 5–25.
- HECHT, G. (1993): Die geothermischen Verhältnisse in der Bohrung Bad Colberg 1/1974. – *Geowissenschaftliche Mitteilungen aus Thüringen*, 1: pp. 121–128.
- HECHT, L. (1998): Granitoide des Fichtelgebirges (NE-Bayern): Magmengenese und hydrothermale Alteration. (Exkursion J am 18. April 1998). – *Jahresberichte und Mitteilungen des Oberrheinischen Geologischen Vereins*, 80: pp. 223–250.
- HECHT, L. & VIGNERESSE, J. L. (1999): A multidisciplinary approach combining geochemical, gravity and structural data: implications for pluton emplacement and zonation. – *Geological Society, London, Special Publications*, 168: pp. 95–110.

- HECHT, L., VIGNERESSE, J. L. & MORTEANI, G. (1997): Constraints on the origin of zonation of the granite complexes in the Fichtelgebirge (Germany and Czech Republic): evidence from a gravity and geochemical study. – *Geologische Rundschau*, 86 (S1): 93-109.
- HEDTMANN, N. (2020): Hydrogeomechanische Untersuchungen an Karbonaten des Oberen Juras des Süddeutschen Molassebeckens. – Ph.D.-thesis, Chair of Engineering Geology/Rock Engineering, Ruhr-University Bochum, 124 p., Bochum.
- HEDTMANN, N. & ALBER, M. (2017): Investigation of Water-permeability and Ultrasonic Wave Velocities of German Malm Aquifer Rocks for Hydro-Geothermal Energy. – *Procedia Engineering*, 191: pp. 127–133.
- HEDTMANN, N. & ALBER, M. (2018): Variation of laboratory test results with specimen size in carbonates of Bavarian Malm. – In: *ISRM Regional Symposium (Ed.): EUROCK 2018, 22-26 May, Saint Petersburg, Russia*: pp. 1–6, Saint Petersburg (International Society for Rock Mechanics and Rock Engineering).
- HEIDBACH, O., RAJABI, M., CUI, X., FUCHS, K., MÜLLER, B., REINECKER, J., REITER, K., TINGAY, M., WENZEL, F., XIE, F., ZIEGLER, M. O., ZOBACK, M.-L. & ZOBACK, M. (2018): The World Stress Map database release 2016: Crustal stress pattern across scales. – *Tectonophysics*, 744: pp. 484–498.
- HEIDBACH, O., RAJABI, M., REITER, K., ZIEGLER, M. & WSM Team (2016): World Stress Map Database Release 2016. – V. 1.1. GFZ Data Services, <https://dataservices.gfz-potsdam.de/wsm/show-short.php?id=escidoc:1680890> (last access on July 09, 2020).
- HEIDBACH, O., RAJABI, M., REITER, K. & ZIEGLER, M. O. (2019): World Stress Map. – In: *SORKHABI, R. (Ed.): Encyclopedia of Petroleum Geoscience*: pp. 1–8, Cham (Springer).
- HEIDBACH, O. & REINECKER, J. (2013): Analyse des rezenten Spannungsfelds der Nordschweiz. – 146 p., [https://www.nagra.ch/data/documents/database/dokumente/\\$default/Default%20Folder/Publikationen/NABs%202004-2012/d\\_nab12-005.pdf](https://www.nagra.ch/data/documents/database/dokumente/$default/Default%20Folder/Publikationen/NABs%202004-2012/d_nab12-005.pdf) (last access on July 09, 2020).
- HEIDBACH, O., TINGAY, M., BARTH, A., REINECKER, J., KURFEB, D. & MÜLLER, B. (2010): Global crustal stress pattern based on the World Stress Map database release 2008. – *Tectonophysics*, 482 (1-4): pp. 3–15.
- HEIM, F. (1932): Vom Gefreiser Granit. – *Der Siebenstern 1932*: pp. 143–146.
- HEINRICHS, T., GIESE, P. & BANKWITZ, E. (1994): DEKORP 3/MVE- 90 (West) - preliminary geological interpretation of a deep near-vertical reflection profile between the Rhenish and the Bohemian Massifs, Germany. – *Z. Geol. Wiss.*, 22 (6): pp. 771–801.
- HENNINGSEN, D. & KATZUNG, G. (2011): Einführung in die Geologie Deutschlands. – 7th ed., 234 p., Heidelberg (Springer Spektrum).
- HERGERT, T., HEIDBACH, O., REITER, K., GIGER, S. B. & MARSCHALL, P. (2015): Stress field sensitivity analysis in a sedimentary sequence of the Alpine foreland, northern Switzerland. – *Solid Earth*, 6 (2): pp. 533–552.
- HOEK, E. & MARTIN, C. D. (2014): Fracture initiation and propagation in intact rock – A review. – *Journal of Rock Mechanics and Geotechnical Engineering*, 6 (4): pp. 287–300.

- HOMUTH, S. (2014): Aufschlussanalogstudie zur Charakterisierung oberjurassischer geothermischer Karbonatreservoire im Molassebecken. – Ph.D.-thesis, Institute of Applied Geosciences, Technical University of Darmstadt, 310 p., Darmstadt.
- HOMUTH, S., GÖTZ, A. E. & SASS, I. (2015): Physical Properties of the Geothermal Carbonate Reservoirs of the Molasse Basin, Germany - Outcrop Analogue vs. Reservoir Data. – In: International Geothermal Association (Ed.): Proceedings World Geothermal Congress 2015, April 19-24, 2015, Melbourne, Australia: pp. 1–11, Melbourne.
- HOMUTH, S. & SASS, I. (2014): Outcrop Analogue Vs. Reservoir Data: Characteristics and Controlling Factors of Physical Properties of the Upper Jurassic Geothermal Carbonate Reservoirs of the Molasse Basin, Germany. – In: Stanford University (Ed.): Proceedings, 38. Workshop on Geothermal Reservoir Engineering, February 24-26, 2014, Stanford, USA: pp. 1–10, Stanford.
- HUENGES, E. (2010): Geothermal energy systems. – 463 p., Berlin (Wiley-VCH).
- HUENGES, E., KOHL, T., KOLDITZ, O., BREMER, J., SCHECK-WENDEROTH, M. & VIENKEN, T. (2013): Geothermal energy systems: research perspective for domestic energy provision. – *Environ Earth Sci*, 70: pp. 3927–3933.
- ILLIES, J. H. & GREINER, G. (1978): Rhinegraben and the Alpine system. – *Geological Society of America Bulletin*, 89: pp. 770–782.
- ISRM (1978): Suggested methods for the quantitative description of discontinuities in rock masses. – *International Journal of Rock Mechanics and Mining Sciences & Geomechanics Abstracts*, 15: pp. 319–368.
- ISRM (1985): Suggested method for determining point load strength. – *International Journal of Rock Mechanics and Mining Sciences & Geomechanics Abstracts*, 22 (2): pp. 51–60.
- KALTSCHMITT, M., STREICHER, W. & WIESE, A. (2013): Erneuerbare Energien. – 5th ed., 964 p., Berlin, Heidelberg (Springer).
- KÄMMLEIN, M. (2020): The Franconian Basin temperature anomaly, SE Germany: Methodologically aspects on the determination of rock thermal conductivity and modelling of potential heat sources. – PhD thesis, Chair of Geology, Friedrich-Alexander-Universität Erlangen-Nürnberg, 161 p., Erlangen.
- KÄMMLEIN, M., BAUER, W. & STOLLHOFEN, H. (2017): New thermophysical data pool for NE-Bavaria reveals exceptionally high local heat fluxes. – German Geothermal Congress GGC 2017, 12th–14th September 2017: pp. 1.
- KÄMMLEIN, M., BAUER, W. & STOLLHOFEN, H. (2020): The Franconian Basin thermal anomaly, SE Germany revised: New thermal conductivity and uniformly corrected temperature data. – *Zeitschrift der Deutschen Gesellschaft für Geowissenschaften*, 171 (1): pp. 21–44.
- KÄMMLEIN, M., DIETL, C. & STOLLHOFEN, H. (2019): The Franconian Basin thermal anomaly: testing its origin by conceptual 2-D models of deep-seated heat sources covered by low thermal conductivity sediments. – *International Journal of Energy and Environmental Engineering*, 10: pp. 389–412.

- KÄMMLEIN, M. & STOLLHOFEN, H. (2019): Pore-fluid-dependent controls of matrix and bulk thermal conductivity of mineralogically heterogeneous sandstones. – *Geothermal Energy*, 7:13: pp. 1–23.
- KÄSLING, H. & THURO, K. (2010): Determining abrasivity of rock and soil in the laboratory. – In: WILLIAMS, A. L. (Ed.): *Geologically Active: Proceedings of the 11th IAEG Congress*. Auckland, New Zealand, 5-10 September 2010: pp. 1973–1980, Boca Raton (CRC Press).
- KASSAB, M. A. & WELLER, A. (2015): Study on P-wave and S-wave velocity in dry and wet sandstones of Tushka region, Egypt. – *Egyptian Journal of Petroleum*, 24 (1): pp. 1–11.
- KOCH, A., JORAND, R., ARNOLD, J., PECHNIG, R., MOTTAGHY, D., VOGT, C. & CLAUSER, C. (2009): Erstellung statistisch abgesicherter thermischer und hydraulischer Gesteinseigenschaften für den flachen und tiefen Untergrund in Deutschland - Phase 2 - Westliches Nordrhein-Westfalen und bayerisches Molassebecken. – 202 p., [http://www.geophysica.de/Forschung/Petrophysik\\_Abschluss\\_Phase\\_2.pdf](http://www.geophysica.de/Forschung/Petrophysik_Abschluss_Phase_2.pdf) (last access on July 09, 2020).
- KOCH, R., BACHMANN, G. & MÜLLER, M. (2010): Fazies des Oberen Jura (Malm) der Bohrungen Scherstetten 1 und 2 (Molasse-Becken, Süddeutschland) und ihre Bedeutung für die geothermische Exploration. – *Zeitschrift für Geologische Wissenschaften*, 38 (5/6): pp. 327–351.
- KOCH, R., SENOWBARI-DARYAN, B. & STRAUSS, H. (1994): The Late Jurassic ‘Massenkalk Fazies’ of southern Germany: calcareous sand piles rather than organic reefs. – *Facies*, 31: pp. 179–208.
- KOSSMAT, F. (1927): Gliederung des varistischen Gebirgsbaues. – *Abhandlungen des Sächsischen Geologischen Landesamts*, 1: pp. 1–39.
- KUHLEMANN, J. & KEMPF, O. (2002): Post-Eocene evolution of the North Alpine Foreland Basin and its response to Alpine tectonics. – *Sedimentary Geology*, 152 (1-2): pp. 45–78.
- LEMCKE, K. (1979): Dreiig Jahre Öl- und Gassuche im süddeutschen Alpenvorland. – *Jahresberichte und Mitteilungen des Oberrheinischen Geologischen Vereins*, 61: pp. 305–319.
- LEMCKE, K. (1988): Das bayerische Alpenvorland vor der Eiszeit. – *Geologie von Bayern*, 175 p., Stuttgart (Schweizerbart).
- LfU (2016): Erdwärme – die Energiequelle aus der Tiefe. – 8 p., [https://www.lfu.bayern.de/buerger/doc/uw\\_20\\_erdwaerme.pdf](https://www.lfu.bayern.de/buerger/doc/uw_20_erdwaerme.pdf) (last access on July 09, 2020).
- LfU (2018): UmweltAtlas Bayern - Übersicht der Funktionalitäten. – 32 p., [https://www.lfu.bayern.de/umweltdaten/kartendienste/umweltatlas/hilfe/doc/hilfe\\_uab.pdf](https://www.lfu.bayern.de/umweltdaten/kartendienste/umweltatlas/hilfe/doc/hilfe_uab.pdf) (last access on July 09, 2020).
- LITTKE, R., BAYER, U., GAJEWSKI, D. & NELSKAMP, S. (2008): *Dynamics of Complex Intracontinental Basins*. – 519 p., Berlin (Springer).
- LUCIA, F. J. (1995): Rock-Fabric/Petrophysical Classification of Carbonate Pore Space for Reservoir Characterization. – *AAPG Bulletin*, 79 (9): pp. 1275–1300.
- LUCIA, F. J. (2007): *Carbonate reservoir characterization*. – 2nd ed., 336 p., Berlin, New York (Springer).

- LUCIA, F. J. & CONTI, R. D. (1987): Rock Fabric, Permeability, and Log Relationships in an Upward-Shoaling, Vuggy Carbonate Sequence. – Geological Circular 87-5, 22 p., Austin (University of Texas at Austin, Bureau of Economic Geology).
- MARTIN, C. D. & CHRISTIANSSON, R. (2009): Estimating the potential for spalling around a deep nuclear waste repository in crystalline rock. – *International Journal of Rock Mechanics and Mining Sciences*, 46 (2): pp. 219–228.
- MARTIN, C. D., KAISER, P. K. & MCCREATH, D. R. (1999): Hoek-Brown parameters for predicting the depth of brittle failure around tunnels. – *Canadian Geotechnical Journal*, 36 (1): pp. 136–151.
- MARTÍNEZ-MARTÍNEZ, J., BENAVENTE, D. & GARCÍA-DEL-CURA, M. A. (2012): Comparison of the static and dynamic elastic modulus in carbonate rocks. – *Bulletin of Engineering Geology and the Environment*, 71 (2): pp. 263–268.
- MARTINI, C. D., READ, R. S. & MARTINO, J. B. (1997): Observations of brittle failure around a circular test tunnel. – *International Journal of Rock Mechanics and Mining Sciences*, 34 (7): pp. 1065–1073.
- MAVKO, G., MUKERJI, T. & DVORKIN, J. (2009): *The Rock Physics Handbook*. – 2nd ed., 511 p., Cambridge (Cambridge University Press).
- MAYR, S. I. & BURKHARDT, H. (2006): Ultrasonic properties of sedimentary rocks: effect of pressure, saturation, frequency and microcracks. – *Geophysical Journal International*, 164 (1): pp. 246–258.
- MCPHEE, C., REED, J. & ZUBIZARRETA, I. (2015): *Core analysis: A best practice guide*. – *Developments in petroleum science*, 64, 852 p., Amsterdam (Elsevier).
- MEGIES, T. & WASSERMANN, J. (2014): Microseismicity observed at a non-pressure-stimulated geothermal power plant. – *Geothermics*, 52: pp. 36–49.
- MENSCHIK, F. (2015): *Analysis of Performance and Wear of Electrical Rock Hammer Drills*. – Ph.D.-thesis, Chair of Engineering Geology, Technical University of Munich, 165 p., Munich.
- MEYER, R. K. (1994): “Moosburg 4”, die erste Kernbohrung durch den Malm unter der bayerischen Molasse. – *Erlanger Geologische Abhandlungen*, 123: pp. 51–81.
- MEYER, R. K. & SCHMIDT-KALER, H. (1989): *Paläogeographischer Atlas des süddeutschen Oberjura (Malm)*. – *Geologisches Jahrbuch*, A 115: pp. 1–77.
- MEYER, R. K. & SCHMIDT-KALER, H. (1996): *Jura*. – *Erläuterungen zur geologischen Karte von Bayern 1:500000*: pp. 90–111.
- Micromeritics (2020): *AccuPyc II 1340 Brochure*. – 6 p., [https://www.micromeritics.com/Repository/Files/AccuPyc\\_Final\\_0.pdf](https://www.micromeritics.com/Repository/Files/AccuPyc_Final_0.pdf) (last access on July 09, 2020).
- MIELKE, H. (1982): *Erläuterungen zur Geologischen Karte von Bayern 1:25000 Blatt Nr. 6037 Ebnath*. – pp. 46-52, Munich (Bayerisches Geologisches Landesamt).
- MIELKE, H. & STETTNER, G. (1984): *Erläuterungen zur Geologischen Karte von Bayern 1:25000 Blatt Nr. 5838/5839 Selb/Schönberg*. – pp. 111, Munich (Bayerisches Geologisches Landesamt).

- MOECK, I. S. (2014): Catalog of geothermal play types based on geologic controls. – *Renewable and Sustainable Energy Reviews*, 37: pp. 867–882.
- MOECK, I. S., DUSSEL, M., WEBER, J., SCHINTGEN, T. & WOLFGRAMM, M. (2019): Geothermal play typing in Germany, case study Molasse Basin: a modern concept to categorise geothermal resources related to crustal permeability. – *Netherlands Journal of Geosciences*, 98, e13: pp. 1–10.
- MRAZ, E. (2019): Reservoir Characterization to Improve Exploration Concepts of the Upper Jurassic in the Southern Bavarian Molasse Basin. – Ph.D.-thesis, Chair of Engineering Geology, Technical University of Munich, 166 p., Munich.
- MRAZ, E., BOHNSACK, D., STOCKINGER, G., KÄSLING, H., ZOSSEDER, K. & THURO, K. (2018): Die Bedeutung von Analogaufschlüssen des Oberjura für die Interpretation der Lithologie der geothermalen Tiefbohrung Geretsried. – *Jahresberichte und Mitteilungen des Oberrheinischen Geologischen Vereins*, 100: pp. 517–548.
- MÜLLER, B. & PIPPING, U. (2011): Praktikable geotechnische Klassifikationen von Festgesteinen und Festgebirgen für das Bauwesen sowie den Bergbau. – *Felsbaumagazin*, 3 (1): pp. 10–31.
- MÜLLER, F. (1997): INSK kompakt. Die internationale Natursteinkartei für den aktuellen Markt. – 1st ed., Ulm (Ebener).
- MÜLLER, M., NIEBERDING, F. & WANNINGER, A. (1988): Tectonic style and pressure distribution at the northern margin of the Alps between Lake Constance and the River Inn. – *Geologische Rundschau*, 77 (3): pp. 787–796.
- NAVABPOUR, P., MALZ, A., KLEY, J., SIEGBURG, M., KASCH, N. & USTASZEWSKI, K. (2017): Intraplate brittle deformation and states of paleostress constrained by fault kinematics in the central German platform. – *Tectonophysics*, 694: pp. 146–163.
- NF P 18-579 (2013): Aggregate - Abrasiveness and grindability tests. – Berlin (Beuth).
- OBERT, L. & DUVAL, W. I. (1967): *Rock mechanics and the design of structures in rock*. – 650 p., New York (John Wiley & Sons Inc).
- OPPEL, A. (1858): *Die Juraformation Englands, Frankreichs und des südwestlichen Deutschlands*. – 857 p., Stuttgart (Ebner & Seubert).
- PASCHEN, H., OERTEL, D. & GRÜNWARD, R. (2003): Möglichkeiten geothermischer Stromerzeugung in Deutschland - Sachstansbericht. – 128 p., <https://www.tab-beim-bundestag.de/de/pdf/publikationen/berichte/TAB-Arbeitsbericht-ab084.pdf> (last access on July 09, 2020).
- PENG, S. & ZHANG, J. (2007): *Engineering Geology for Underground Rocks*. – 319 p., Berlin, Heidelberg (Springer).
- PICKETT, G. R. (1963): Acoustic Character Logs and Their Applications in Formation Evaluation. – *Journal of Petroleum Technology*, 15 (06): pp. 659–667.
- PIENKOWSKI, G., SCHUDACK, M. E., BOSAK, P., ENAY, R., FELDMAN-OLSZEWSKA, A., GOLONKA, J., GUTOWSKI, J., HERNGREEN, G.F.W., JORDAN, P., KROBICKI, M., LATHUILIERE, B., LEINFELDER, R. R., MICHALIK, J., MONNIG, E.,

- NOE-NYGAARD, N., PALFY, J., PINT, A., RASSER, M. W., REISDORF, A. G., SCHMID, D. U., SCHWEIGERT, G., SURLYK, F., WETZEL, A. & WONG, T. E. (2008): Jurassic. – In: MCCANN, T. (Ed.): *The geology of central Europe*: pp. 823–922, London (Geological Society).
- POTTEN, M., BOHNSACK, D., KÄSLING, H. & THURO, K. (2018): Geomechanische Reservoircharakterisierung anhand der gekernten Bohrung Moosburg SC 4. – *Der Geothermiekongress 2018*, 27- 29 November 2018, Essen: pp. 1.
- POTTEN, M., BOHNSACK, D., KÄSLING, H., ZOSSEDER, K. & THURO, K. (2019a): Geomechanische Untersuchungen im Bereich der bayerischen Geothermie. – *Fachsektionstage Geotechnik – Interdisziplinäres Forum*, 29–30 October, 2019, Würzburg: pp. 204–209.
- POTTEN, M., SELMEIER, B., MRAZ, E. & THURO, K. (2019b): Geomechanical Investigation of High Priority Geothermal Strata in the Molasse Basin, Bavaria, Germany. – In: SHAKOOR, A. & CATO, K. (Eds.): *IAEG/AEG Annual Meeting proceedings*, San Francisco, California, 2018: pp. 21–26, Cham (Springer).
- QUENSTEDT, F. A. (1858): *Der Jura*. – 842 p., Tübingen (H. Laupp).
- REINECKER, J., TINGAY, M., MÜLLER, B. & HEIDBACH, O. (2010): Present-day stress orientation in the Molasse Basin. – *Tectonophysics*, 482 (1-4): pp. 129–138.
- REITER, K., HEIDBACH, O., MÜLLER, B., REINECKER, J. & RÖCKEL, T. (2016): *Stress Map Germany 2016*. – GFZ Data Services., [http://doi.org/10.5880/WSM.Germany2016\\_en](http://doi.org/10.5880/WSM.Germany2016_en) (last access on July 09, 2020).
- REYNOLDS, J. M. (2011): *An introduction to applied and environmental geophysics*. – 2nd edition, 696 p., Chichester, West Sussex, Hoboken (Wiley-Blackwell).
- RICHTER, A. E. (1985): *Geologie und Paläontologie: Das Mesozoikum der Frankenalb - Vom Ries bis ins Coburger Land*. – 224 p., Stuttgart (Franckh'sche Verlagshandlung).
- RICHTER, P. & STETTNER, G. (1979): Geochemische und petrographische Untersuchungen der Fichtelgebirgsgranite. – *Geologica Bavarica*, 78: pp. 1–144.
- RÖCKEL, T. & WONIK, T. (2006): Strukturauswertungen von Bohrlochmessungen der Forschungsbohrung Lindau 1 (Bayreuth). – *Geologica Bavarica*, 109: pp. 151–183.
- RUMMEL, F., KLEE, G. & WEBER, U. (2002): *Stimulationsversuche in der Forschungsbohrung Lindau/Oberfranken*. – 30 p., Bericht Nr. 08.02 (unpublished).
- SCHAARSCHMIDT, A., DE WALL, H., DIETL, C., SCHARFENBERG, L., KÄMMLEIN, M. & GABRIEL, G. (2017): Geothermal Prospection in NE Bavaria - crustal heat supply by sub-sediment Variscan granites in the Franco-nian basin? – 77. Jahrestagung der Deutschen Geophysikalischen Gesellschaft 27–30 March 2017, Potsdam: pp. 316.
- SCHÄFER, F., ONCKEN, O., KEMNITZ, H. & ROMER, R. L. (2000): Upper-plate deformation during collisional orogeny: a case study from the German Variscides (Saxo-Thuringian Zone). – *Geological Society, London, Special Publications*, 179 (1): pp. 281–302.
- SCHARFENBERG, L. & DE WALL, H. (2016): *Natürliche Gammastrahlung von Graniten in der Oberpfalz (Nordost-Bayern) – Vergleich von aerogeophysikalischen und in situ gammastrahlungsmessungen*

- Messungen. – *Geologische Blätter für Nordost-Bayern und angrenzende Gebiete*, 66 (1-4): pp. 205–227.
- SCHARFENBERG, L., DE WALL, H. & BAUER, W. (2016): In situ gamma radiation measurements on Variscan granites and inferred radiogenic heat production, Fichtelgebirge, Germany. – *Zeitschrift der Deutschen Gesellschaft für Geowissenschaften*, 167 (1): pp. 19–32.
- SCHIMAZEK, J. & KNATZ, H. (1976): Die Beurteilung von Gesteinen durch Schneid- und Rollenbohrwerkzeuge. – *Erzmetall*, 29 (3): pp. 113–119.
- SCHMID, S. M., FÜGENSCHUH, B., KISSLING, E. & SCHUSTER, R. (2004): Tectonic map and overall architecture of the Alpine orogen. – *Eclogae Geologicae Helvetiae*, 97 (1): pp. 93–117.
- SCHNEIDER, M. (2012): Verbundvorhaben: Wissenschaftliche und technische Grundlagen zur strukturgeologischen und hydrogeologischen Charakterisierung tiefer geothermisch genutzter Grundwasserleiter am Beispiel des süddeutschen Molassebeckens: Endbericht- Laufzeit des Vorhabens 01.03.2008-29.02.2012. – 237 p., <https://www.tib.eu/de/suchen/id/TIBKAT:739284339/> (last access on July 09, 2020).
- SCHÖDLBAUER, S., HECHT, L., HÖHNDORF, A. & MORTEANI, G. (1996): Gesteinseinschlüsse in den peraluminösen Kösseinegraniten (Fichtelgebirge, NE Bayern). – *Geologica Bavarica*, 101: pp. 113–137.
- SCHÖDLBAUER, S., HECHT, L., HÖHNDORF, A. & MORTEANI, G. (1997): Enclaves in the S-type granites of the Kösseine massif (Fichtelgebirge, Germany): implications for the origin of granites. – *Geologische Rundschau*, 86 (S1): 125-140.
- SCHÖN, J. (2015): *Physical properties of rocks - Fundamentals and principles of petrophysics*. – 2nd ed., 512 p., 65, Amsterdam (Elsevier).
- SCHRÖDER, B. (1987): Inversion tectonics along the Western margin of the Bohemian Massif. – *Tectonophysics*, 137 (1-4): pp. 93–100.
- SCHRÖDER, B., AHRENDT, H., PETEREK, A. & WEMMER, K. (1997): Post-Variscan sedimentary record of the SW margin of the Bohemian massif: a review. – *Geologische Rundschau*, 86: pp. 178–184.
- SCHULZ, R. & THOMAS, R. (2012): Geothermische Charakterisierung von karstig-klüftigen Aquiferen im Großraum München- Endbericht. – 99 p., [https://www.leibniz-liag.de/fileadmin/user\\_upload/dokumente/Geothermische\\_Energie/BMU0325013A.pdf](https://www.leibniz-liag.de/fileadmin/user_upload/dokumente/Geothermische_Energie/BMU0325013A.pdf) (last access on July 09, 2020).
- SEHT, M. I.-V., PLENEFISCH, T. & SCHMEDES, E. (2006): Faulting style and stress field investigations for swarm earthquakes in NE Bavaria/Germany – the transition between Vogtland/NW-Bohemia and the KTB-site. – *Journal of Seismology*, 10: pp. 197–211.
- SEITHEL, R., GAUCHER, E., MUELLER, B., STEINER, U. & KOHL, T. (2019): Probability of fault reactivation in the Bavarian Molasse Basin. – *Geothermics*, 82: pp. 81–90.
- SEITHEL, R., STEINER, U., MÜLLER, B., HECHT, C. & KOHL, T. (2015): Local stress anomaly in the Bavarian Molasse Basin. – *Geothermal Energy*, 3:4: pp. 1–22.

- SEITHEL, R. J. (2019): Geomechanical characterization of geothermal reservoirs in the Bavarian Molasse Basin. – Ph.D.-thesis, Department of Geothermal Energy, Karlsruhe Institute of Technology, 144 p., Karlsruhe.
- SIBLEY, D. F. (1982): The origin of common dolomite fabrics: clues from the pliocene. – *Journal of Sedimentary Petrology*, 52: pp. 1087–1100.
- SIBLEY, D. F. & GREGG, J. M. (1987): Classification of dolomite rock textures. – *Journal of Sedimentary Petrology*, 57: pp. 967–975.
- SIEBEL, W., CHEN, F. & SATIR, M. (2003): Late-Variscan magmatism revisited: new implications from Pb-evaporation zircon ages on the emplacement of redwitzites and granites in NE Bavaria. – *International Journal of Earth Sciences*, 92: pp. 36–53.
- SIEBEL, W., HÖHNDORF, A. & WENDT, I. (1995): Origin of late Variscan granitoids from NE Bavaria, Germany, exemplified by REE and Nd isotope systematics. – *Chemical Geology*, 125 (3-4): pp. 249–270.
- SIEBEL, W., SHANG, C. K. & PRESSER, V. (2010): Permo-Carboniferous magmatism in the Fichtelgebirge: dating the youngest intrusive pulse by U-Pb, 207Pb/206Pb and 40Ar/39Ar geochronology. – *Zeitschrift für Geologische Wissenschaften*, 38 (2-3): pp. 85–98.
- SIEBEL, W., TRZEBSKI, R., STETTNER, G., HECHT, L., CASTEN, U., HÖHNDORF, A. & MÜLLER, P. (1997): Granitoid magmatism of the NW Bohemian massif revealed: gravity data, composition, age relations and phase concept. – *Geologische Rundschau*, 86: 45-63.
- SKIBA, P., GABRIEL, G., SCHEIBE, R., SEIDEMANN, O., VOGEL, D., KRAWCZYK, C. & VINNEMANN, C. (2010): Schwerekarte der Bundesrepublik Deutschland 1:1000000. – 1 p., [https://www.leibniz-liag.de/fileadmin/user\\_upload/S1/arbeitsbereiche/gravi\\_mag/schwerekarte.pdf](https://www.leibniz-liag.de/fileadmin/user_upload/S1/arbeitsbereiche/gravi_mag/schwerekarte.pdf) (last access on July 09, 2020).
- STETTNER, G. (1958): Geologische Karte von Bayern 1:25000, Erläuterungen zum Blatt Nr. 5937 Fichtelberg. – Bayerisches Geologisches Landesamt: pp. 116.
- STETTNER, G. (1977): Geologische Karte von Bayern 1:25000, Erläuterungen zum Blatt Nr. 5936 Bad Berneck. – Bayerisches Geologisches Landesamt: pp. 112–126.
- STETTNER, G. & SALGER, M. (1985): Das Schiefergebirge in der Forschungsbohrung Obernsees. – *Geologica Bavarica*, 88: pp. 49–55.
- STIER, P. & PRESTEL, R. (1991): Der Malmkarst im süddeutschen Molassebecken – Ein hydrogeologischer Überblick. – In: Bayerisches Landesamt für Wasserwirtschaft & Landesamt für Geologie, Rohstoffe und Bergbau (Ed.): Hydrogeothermische Energiebilanz und Grundwasserhaushalt des Malmkarstes im süddeutschen Molassebecken. – Schlussbericht zum Forschungsvorhaben 03E-6240 A/B (im Auftrag des Bundesministeriums für Forschung und Technologie): pp. 1–12, München, Freiburg.
- StMWi (2019a): Aktuelle Zahlen zur Energieversorgung in Bayern - Prognose bis zum Jahr 2018. – 80 p., [https://www.stmwi.bayern.de/fileadmin/user\\_upload/stmwi/Publikationen/2019/2019-08-19\\_Energiedaten\\_Bayern\\_Endbericht.pdf](https://www.stmwi.bayern.de/fileadmin/user_upload/stmwi/Publikationen/2019/2019-08-19_Energiedaten_Bayern_Endbericht.pdf) (last access on July 09, 2020).

- StMWi (2019b): Bayerischer Geothermieatlas - Hydrothermale Energiegewinnung. – 96 p., [https://www.stmwi.bayern.de/fileadmin/user\\_upload/stmwi/Publikationen/2019/2019-03-19\\_Bayerischer\\_Geothermieatlas\\_2019.pdf](https://www.stmwi.bayern.de/fileadmin/user_upload/stmwi/Publikationen/2019/2019-03-19_Bayerischer_Geothermieatlas_2019.pdf) (last access on July 09, 2020).
- STOBER, I. (2014): Hydrochemical properties of deep carbonate aquifers in the SW German Molasse basin. – *Geothermal Energy*, 2:13: pp. 1–20.
- STOBER, I. & BUCHER, K. (2014): *Geothermie*. – 2nd ed., 306 p., Berlin, Heidelberg (Springer).
- STOBER, I., FRITZER, T., OBST, K., AGEMAR, T. & SCHULZ, R. (2016): *Tiefe Geothermie*. – 88 p., 4th ed., [https://www.geotis.de/homepage/sitecontent/info/publication\\_data/public\\_relations/public\\_relations\\_data/LIAG\\_Broschuere\\_Tiefe\\_Geothermie.pdf](https://www.geotis.de/homepage/sitecontent/info/publication_data/public_relations/public_relations_data/LIAG_Broschuere_Tiefe_Geothermie.pdf) (last access on July 09, 2020).
- STOCKINGER, G., MRAZ, E., MENSCHIK, F. & THURO, K. (2019): Geomechanical Model for a Higher Certainty in Finding Fluid Bearing Regions in Non-porous Carbonate Reservoirs. – In: SHAKOOR, A. & CATO, K. (Eds.): *IAEG/AEG Annual Meeting proceedings*, San Francisco, California, 2018: pp. 193–198, Cham (Springer).
- STOLLHOFEN, H., BAUER, W., BERTERMANN, D., DREWS, M. & FAZLIKHANI, H. (2018): Oberflächennah bis kilometertief – Lehre und Forschung zur Geothermie an der FAU Erlangen. – *Geothermische Energie*, 89: pp. 30–32.
- SWM (2019): *Stadtwerke München: Gestalter der Wärmewende*. – 7 p., <https://www.swm.de/dam/swm/dokumente/m-fernwaerme/broschuere-gestalter-waermewende.pdf> (last access on July 09, 2020).
- SYMANK, A.-I. (2020): The use of seismic attributes to increase the reliability of geothermal prospects in the South German Molasse Basin. – Ph.D.-thesis, Chair of Engineering Geology/Rock Engineering, Ruhr-University Bochum, 197 p., Bochum.
- TAVAKOLI, V. (2018): *Geological Core Analysis: Application to Reservoir Characterization*. – 1st ed., 99 p., Cham (SpringerBriefs in Petroleum Geoscience & Engineering).
- THOMAS, K., CARLA, V., KATHRIN, W., HARRY, L. & KLAUS, M. (2010): *Energieziel 2050: 100% Strom aus erneuerbaren Quellen*. – 196 p., [https://www.umweltbundesamt.de/sites/default/files/medien/378/publikationen/energieziel\\_2050.pdf](https://www.umweltbundesamt.de/sites/default/files/medien/378/publikationen/energieziel_2050.pdf) (last access on July 09, 2020).
- THURO, K. (1996): *Bohrbarkeit beim konventionellen Sprengvortrieb. Geologisch-felsmechanische Untersuchungen anhand sieben ausgewählter Tunnelprojekte*. – Ph.D.-thesis, Münchner Geologische Hefte, B1, Chair of General Applied and Engineering Geology, Technical University of Munich, 149 p., Munich.
- THURO, K. & KÄSLING, H. (2009): Classification of the abrasiveness of soil and rock. – *Geomechanics and Tunneling*, 2 (2): pp. 179–188.
- THURO, K., SINGER, J., KÄSLING, H. & BAUER, M. (2006): Soil Abrasivity Assessment Using the LCPC Testing Device. – *Felsbau*, 24 (6): pp. 37–45.
- THURO, K., ZOSEDER, K., BOHNSACK, D., HEINE, F., KONRAD, F., MRAZ, E. & STOCKINGER, G. (2019): *Abchlussbericht zu den Arbeitspaketen der Technischen Universität München zum Verbundprojekt:*

Dolomitkluft - Erschließung, Test und Analyse des ersten kluftdominierten Dolomitaquifers im tiefen Malm des Molassebeckens zur Erhöhung der Erfolgsaussichten: Teilprojekt B: Geomechanische und hydro-geologische Parametrisierung und Modellierung. –

<https://www.tib.eu/de/suchen/id/TIBKAT:1687930376/> (last access on July 09, 2020).

TONDERA, D., KLAPPERICH, H., BLÖCHER, G., MOECK, I., STEIGER, T., BEMS, C. & HILD, S. (2013): Geothermie Forschungsprojekt "Allgäu 2.0" – Forschungsansätze, Laboruntersuchungen & Planungsschritte. – 19. Tagung für Ingenieurgeologie mit Forum für junge Ingenieurgeologen, 13. - 16. March 2013, Munich: pp. 285–293.

TRZEBSKI, R., BEHR, H. J. & CONRAD, W. (1997): Subsurface distribution and tectonic setting of the late-Variscan granites in the northwestern Bohemian Massif. – *Geologische Rundschau*, 86 (S1): pp. 64–78.

TUCKER, M. E. & WRIGHT, V. P. (1990): *Carbonate Sedimentology*. – 482 p., Oxford (Blackwell Scientific).

UECKERT, M. & BAUMANN, T. (2019): Hydrochemical aspects of high-temperature aquifer storage in carbonaceous aquifers: evaluation of a field study. – *Geothermal Energy*, 7:4: pp. 1–22.

UNGER, H. J. (1999): *Bayerische Molasse (Tektonik, Nomenklaturen, Ost-Westmolasse, pliozäne Stromsysteme)*. – 1st ed., 125, 97 p., München (documenta naturae).

VALLEY, B. C. (2007): The relation between natural fracturing and stress heterogeneities in deep-seated crystalline rocks at Soultz-sous-Forêts (France). – Ph.D.-thesis, Group of Engineering Geology, ETH Zurich, 193 p., Zurich.

VDI 4640: (2010): Part 1 - Thermal use of the underground - Fundamentals, approvals, environmental aspects. – Düsseldorf (VDI-Gesellschaft Energie und Umwelt).

WAGNER, W. & PRÜß, A. (2002): The IAPWS Formulation 1995 for the Thermodynamic Properties of Ordinary Water Substance for General and Scientific Use. – *Journal of Physical and Chemical Reference Data*, 31 (2): pp. 387–535.

WALTER, R. & DORN, P. (2007): *Geologie von Mitteleuropa*. – 7th ed., 511 p., Stuttgart (Schweizerbart).

WEBER, J., BORN, H. & MOECK, I. (2019): Geothermal Energy Use, Country Update for Germany 2016 - 2018. – 16 p., <http://europeangeothermalcongress.eu/wp-content/uploads/2019/07/CUR-12-Germany.pdf> (last access on July 09, 2020).

WEBER, J. & MOECK, I. (2018): Wärmewende mit Geothermie – Möglichkeiten und Chancen in Deutschland. – 12 p., [https://www.geotis.de/homepage/sitecontent/info/publication\\_data/public\\_relations/public\\_relations\\_data/Liag-Brosch-waermewende-de.pdf](https://www.geotis.de/homepage/sitecontent/info/publication_data/public_relations/public_relations_data/Liag-Brosch-waermewende-de.pdf) (last access on July 09, 2020).

WEKA (2013a): Diamant-Kernbohrständer KS 13. – 2 p., <http://www.betonfuras.net/PR-KS13.pdf> (last access on July 09, 2020).

WEKA (2013b): 3-Gang Diamant-Kernbohrmaschine DK17 Nass + Trocken. – 2 p., <https://www.weka-elektrowerkzeuge.de/download/english-pr-dk17/#> (last access on July 09, 2020).

- WELZEL, B. (1991): Die Bedeutung von K/Ar-Abkühlaltern an detritischen Muskoviten für die Rekonstruktion tektonometamorpher Einheiten im orogenen Liefergebiet - ein Beitrag zur Frage der variszischen Krustenentwicklung in der Böhmisches Masse. – *Göttinger Arbeiten zur Geologie und Paläontologie*, 49: pp. 1–61.
- WEST, G. (1989): Rock abrasiveness testing for tunnelling. – *International Journal of Rock Mechanics and Mining Sciences & Geomechanics Abstracts*, 26 (2): pp. 151–160.
- WHALEY, J. (2019): An Introduction to Geomechanics. – *GEO ExPro Magazine*, 16 (2): pp. 68–70.
- WIESER, C. (2016): Quantifying the Effect of Stress Changes on the Deformation and Cracking Behavior of Solid Rock using Acoustic Emission Techniques. – PhD thesis, Technical University of Munich, 190 p., Munich.
- WILFING, L. S. (2016): The Influence of Geotechnical Parameters on Penetration Prediction in TBM Tunneling in Hard Rock. – PhD thesis, Technical University of Munich, 191 p., Munich.
- WILLIAMS, A. L. (2010): *Geologically Active: Proceedings of the 11th IAEG Congress*. Auckland, New Zealand, 5-10 September 2010. – 4 p., Boca Raton (CRC Press).
- WOLFGRAMM, M., BIRNER, J., BUDACH, I., THIEM, S., THORWART, K., NOWAK, K., LENZ, G., BUSE, C., SEIBT, P. & ZIMMERMANN, J. (2018): Verbundprojekt MAFA: Parametrisierung von Fazies, Diagenese, Struktur- und Spannungsfeld sowie Optimierung der Testabläufe im Malm zur Verringerung des Erfolgsrisikos, Teilprojekt A- Sedimentologisch-fazielle Analyse, Testplanung- Forschungsvorhaben 0325673A-Revision 0001. – 231 p., <https://www.tib.eu/de/suchen/id/TIBKAT:1015388507/> (last access on July 09, 2020).
- WOLFGRAMM, M., BLOCH, T., BARTELS, J., KUHN, P., NAEF, H., VOIGT, H. D., SEIBT, P., SONDEREGGER, M., STEIGER, T. & UHLIG, S. (2015): Reservoir-geological Characterization of a Fractured Limestone: Results Obtained from the Geothermal Well St. Gallen Gt-1 (Switzerland). – *Proceedings World Geothermal Congress 2015*, Melbourne, Australia, 19-25 April 2015: pp. 1–12.
- ZANG, A. & STEPHANSSON, O. (2010): *Stress Field of the Earth's Crust*. – 324 p., Dordrecht (Springer).
- ZHANG, J. (2013): Borehole stability analysis accounting for anisotropies in drilling to weak bedding planes. – *International Journal of Rock Mechanics and Mining Sciences*, 60: pp. 160–170.
- ZHANG, L. (2016): *Engineering properties of rocks*. – 2nd ed., 394 p., Oxford (Butterworth-Heinemann).
- ZIEGLER, M. O. & HEIDBACH, O. (2020): The 3D stress state from geomechanical–numerical modelling and its uncertainties: a case study in the Bavarian Molasse Basin. – *Geothermal Energy*, 8:11: pp. 1–21.
- ZIEGLER, M. O., HEIDBACH, O., REINECKER, J., PRZYBYCIN, A. M. & SCHECK-WENDEROTH, M. (2016): A multi-stage 3-D stress field modelling approach exemplified in the Bavarian Molasse Basin. – *Solid Earth*, 7 (5): pp. 1365–1382.
- ZIEGLER, P. A. (1982): Triassic rifts and facies patterns in Western and Central Europe. – *Geologische Rundschau*, 71 (3): pp. 747–772.

ZOBACK, M. D. (2010): Reservoir geomechanics. – 2nd ed., 449 p., Cambridge (Cambridge University Press).

ZOBACK, M. D. (2016): Reservoir Geomechanics. – unpublished lecture document: pp. 1–75.

ZOBACK, M. D., BARTON, C. A., BRUDY, M., CASTILLO, D. A., FINKBEINER, T., GROLLIMUND, B. R., MOOS, D. B., PESKA, P., WARD, C. D. & WIPRUT, D. J. (2003): Determination of stress orientation and magnitude in deep wells. – *International Journal of Rock Mechanics and Mining Sciences*, 40: pp. 1049–1076.

ZOBACK, M. L. (1992): First- and second-order patterns of stress in the lithosphere: The World Stress Map Project. – *Journal of Geophysical Research*, 97 (B8): pp. 11703–11728.

## URL references

- www-01: [https://www.praxisforum-geothermie.bayern/sites/default/files/181022\\_pm\\_100\\_terawattstunden\\_geothermale\\_waerme.pdf](https://www.praxisforum-geothermie.bayern/sites/default/files/181022_pm_100_terawattstunden_geothermale_waerme.pdf) (last access on May 04, 2020).
- www-02: <https://www.geotis.de/geotisapp/geotis.php> (last access on March 03, 2020).
- www-03: [https://www.energieatlas.bayern.de/thema\\_geothermie/tiefe/daten.html](https://www.energieatlas.bayern.de/thema_geothermie/tiefe/daten.html) (last access on June 05, 2020).
- www-04: <https://www.erdwerk.com/en/schaftlarnstrasse> (last access on February 19, 2020).
- www-05: [www.mse.tum.de/en/geothermal-alliance-bavaria](http://www.mse.tum.de/en/geothermal-alliance-bavaria) (last access on February 19, 2020).
- www-06: [https://www.geotron.de/tl\\_files/geotron/media/Messverfahren/Bestimmung\\_elastischer\\_Konstanten\\_1961.pdf](https://www.geotron.de/tl_files/geotron/media/Messverfahren/Bestimmung_elastischer_Konstanten_1961.pdf) (last access on March 23, 2020).
- www-07: [https://www.geotron.de/tl\\_files/geotron/media/Informationen/Datenblatt\\_USG%2040.pdf](https://www.geotron.de/tl_files/geotron/media/Informationen/Datenblatt_USG%2040.pdf) (last access on March 04, 2020).
- www-08: <https://www.picotech.com/oscilloscope/picoscope-4000-series> (last access on March 04, 2020).
- www-09: [https://www.geotron.de/tl\\_files/geotron/media/Informationen/Datenblatt\\_UP-DW.pdf](https://www.geotron.de/tl_files/geotron/media/Informationen/Datenblatt_UP-DW.pdf) (last access on March 04, 2020).
- www-10: [https://www.geotron.de/tl\\_files/geotron/media/Informationen/Datenblatt\\_LHUMPC.pdf](https://www.geotron.de/tl_files/geotron/media/Informationen/Datenblatt_LHUMPC.pdf) (last access on March 04, 2020).
- www-11: [https://www.geotron.de/tl\\_files/geotron/media/Informationen/Datenblatt\\_LHDW.pdf](https://www.geotron.de/tl_files/geotron/media/Informationen/Datenblatt_LHDW.pdf) (last access on March 04, 2020).
- www-12: <https://www.lfu.bayern.de/umweltdaten/kartendienste/umweltatlas/index.htm> (last access on March 03, 2020).
- www-13: <http://www.bgs.ac.uk/lexicon/lexicon.cfm?pub=PB> (last access on April 02, 2020).
- www-14: <https://www.braun-baustoffe.de/produkte/reinersreuth-waldstein-hell/> (last access on April 16, 2020).
- www-15: [https://www.bamberger-natursteinwerk.de/fileadmin/user\\_upload/Steine/KoesseineGranit/Koesseine\\_Granit\\_Beschreibung.pdf](https://www.bamberger-natursteinwerk.de/fileadmin/user_upload/Steine/KoesseineGranit/Koesseine_Granit_Beschreibung.pdf) (last access on April 11, 2020).
- www-16: <https://www.braun-baustoffe.de/produkte/reinersreuth-granitporphyr/> (last access on April 16, 2020).
- www-17: <https://www.umweltatlas.bayern.de/mapapps/resources/reports/geotope/generateBericht.pdf?additionallayerfieldvalue=479A004> (last access on April 13, 2020).
- www-18: [https://www.natursteinonline.de/index.php?id=205&user\\_dnsdatenbank\\_pi1\[steinID\]=1013&user\\_dnsdatenbank\\_pi1\[pdf\]=5](https://www.natursteinonline.de/index.php?id=205&user_dnsdatenbank_pi1[steinID]=1013&user_dnsdatenbank_pi1[pdf]=5) (last access on April 16, 2020).

www-19: <https://www.umweltatlas.bayern.de/mapapps/resources/reports/geotope/generateBericht.pdf?additionallayerfieldvalue=479A009> (last access on April 16, 2020).

www-20: <https://www.umweltatlas.bayern.de/mapapps/resources/reports/geotope/generateBericht.pdf?additionallayerfieldvalue=479A006> (last access on April 17, 2020).

www-21: <https://www.umweltatlas.bayern.de/mapapps/resources/reports/geotope/generateBericht.pdf?additionallayerfieldvalue=472A006> (last access on November 8, 2019).

www-22: <http://www.world-stress-map.org/casmo/> (last access on July 11, 2020).

www-23: [https://commons.wikimedia.org/wiki/File:Karte\\_Bundesrepublik\\_Deutschland.svg](https://commons.wikimedia.org/wiki/File:Karte_Bundesrepublik_Deutschland.svg) (last access on July 12, 2020).

www-24: [https://www.flora.uni-bayreuth.de/Bilder/Karten/2010\\_Bayern-Reliefkarte.png](https://www.flora.uni-bayreuth.de/Bilder/Karten/2010_Bayern-Reliefkarte.png) (last access on July 12, 2020).

www-25: <https://www.slb.com/resource-library/oilfield-review/defining-series/defining-geomechanics> (last access on April 22, 2020).

## Appendix

**Due to the large amount of data collected,  
the data are not included in this version's appendix.**